Filamentary nanosecond surface dielectric barrier discharge at elevated pressures. Streamer-to-filamentary transition and application for plasma assisted combustion.

Sergey Shcherbanev

THESE DE DOCTORAT

DE

L'UNIVERSITE PARIS-SACLAY

PREPAREE A

L'ECOLE NORMALE SUPERIEURE PARIS-SACLAY

ÉCOLE DOCTORALE № 572
Ondes et Matière

Spécialité de doctorat : Physiques des Plasmas

Par

Sergey Shcherbanev

Décharge Filamentaire Nanoseconde en Surface à Barrière Diélectrique. Transition Streamer-Filamentaire et Application pour Combustion Assistée par Plasma

Thèse présentée et soutenue à l'École Polytechnique, le 16 décembre 2016 :

Composition du Jury :

M Christophe LAUX Ecole Centrale, Paris, Président du Jury
Mme Svetlana STARIKOVSKAIA Ecole Polytechnique, Paris, Directrice de thèse
M Pierre TARDIVEAU Université Paris-Sud, Paris, Rapporteur
M Epaminondas MASTORAKOS Cambridge University, UK, Rapporteur
M Pere ROCA i CABARROCAS Ecole Polytechnique, Paris, Examinateur
M Guillaume VANHOVE Université de Lille 1, Lille, Examinateur
M Marc BELLENOUE PPRIME, Poitiers, Examinateur
M Jean-Michel POUVESLE CNRS-GREMI, Orléans, Examinateur

To my mother

Contents

Acknowledgements

I would like to express my sincere appreciation to my supervisor Svetlana Starikovskaia for her guidance and encouragement, without which this work would not be possible. I am truly thankful for her unwavering support. During the last three years she was always very patient and consistent during our discussions. She taught me a great deal as in the field of experimental physics, so how to properly present my results. I am extremely grateful to Svetlana for the opportunities to participate in a variety of international conferences around the world. Finally, I am sincerely grateful for the fact that throughout our collaboration, she treated me like a full-fledged colleague trusting me and relying on me.

I would also like to express my deepest gratitude and respect to Nikolay Popov (Moscow State University) for his productive and fruitful discussions. Thanks to these discussions I improved my knowledge in plasma physics, physics of combustion and hydrodynamics.

I thank my co–authors and collaborators: Mohamed Boumehdi, Guillaume Vanhove and Pascale Desgroux from University Lille 1 (laboratory PC2A), for cooperation of plasma–assisted combustion in RCM with nanosecond surface DBD; Viktor Soloviev (Moscow Institute of Physics and Technology) for the interacting discussions of 2D numerical simulation of nSDBD; Sergey Pancheshnyi and Lorenz G. Hermann (ABB Switzerland) for interesting experiment and common publication; all the interns, master and PhD students I worked with: Issatay Nadinov, Andrey Khomenko, Yifei Zhu, Brian Baron, Nicolas Couchot, Alexandre De-Martino, James Williams.

I am really thankful to Dr. Pierre Tardiveau from Laboratoire de Physique des Gaz et des Plasmas of University Paris Sud and to Prof. Epaminondas Mastorakos from Hopkinson Lab of Department of Engineering, University of Cambridge, who accepted to be reviewers of my Thesis; I would like also to thank all members of my Jury : Prof. Christophe Laux from Ecole Central Paris, Prof. Jean-Michel Pouvesle from University of Orleans, Dr. Guillaume Vanhove from University Lille 1, Prof. Marc Bellenoue from Ecole Nationale Superieure de Mecanique et d'Aerotechnique

(Poitiers), Prof. Pere Roca i Cabarrocas form Ecole Polytechnique (LPICM).

Je souhaiterais tout particulièrement remercier M. Ali Mahjoub ingénieur de recherche. Sans son aide, pour le développement de nouveaux composants travailler sur mon projet aurait été impossible. Je lui suis également extrêmement reconnaissant pour son soutien dans des nombreuses difficultés administratives que j'ai rencontré lors de mes études doctorales. De plus, grâce aux trois années durant lesquelles nous avons collaborés, je considère Ali comme un ami et tiens à le remercier.

My appreciation also extends to other laboratory colleagues Philippe Auvray for technical advices, Bruno Dufour for mechanical assistance, Olivier Guaitella for his help and advices, Pascal Chabert for his encouragements and valuable recommendations.

I wish to thank my colleague and friend Nikita Lepikhin. His stay in the lab certainly brightened everyday life. Some ideas generated during our discussions were realized during the experiments and during the data treatment.

I am very grateful to the woman I love, Olga Permiakova, who was always there. Her support and patience never left me during my emotional highs and lows. Her help in page–making of my work, as well as her help in writing some programs greatly helped me in the processing and presentation of my results.

I would love to thank my family: father, brother and my Mom. Her sincere faith in me never let me down. For all of the times I never said thank you because I thought you knew, I thank you now more than ever, Mom.

Abstract

Non-equilibrium plasma is one of the most attractive and promising tool for many plasma-assisted applications. Production of active species (excited species, radicals, high energetic photons covering UV and IR spectral range) is important for gas pollution control, surface treatment, plasma actuators for aerodynamics application, biomedical applications and more recently the field of plasma medicine. For atmospheric and elevated gas densities the mainstream of the non-thermal plasma applications is the ignition of combustible mixtures or so-called Plasma-Assisted Ignition (PAI).

Surface dielectric barrier discharges (SDBDs), widely used for aerodynamic flow control, were recently suggested as distributed initiators of combustion in different systems. A principal possibility of using the SDBD igniters at as high pressure as tens of bars has been demonstrated during the last 4-5 years. At the moment of the beginning of the thesis, the set of experimental data on the discharge and of ignition of fuels with SDBD was insufficient for detailed analysis. Therefore, the experimental study of the surface DBD at atmospheric and elevated gas densities and the study of flame initiation with nanosecond SDBD were the object of the presented thesis.

The results in the Thesis are presented in three parts. In the first part the nSDBD in a single shot regime at atmospheric air is investigated. The analysis of energy deposition, discharge current, intensity distribution and consequent energy release is performed. The positive and negative polarity pulses are used to produce surface discharge. The physics of anode and cathode-directed streamers is discussed. For both polarities of the applied pulses the electron density and reduced electric field are estimated and compared with calculations and/or 2D modeling results.

The second part is devoted to the study of nSDBD at elevated pressures, up to 12 bar, in different gas mixtures (N_2, air, N_2:CH_4, N_2:H_2, Ar:O_2, etc.). Two morphologically different forms of the nSDBD are considered: a "classical" streamer DBD at relatively low pressures and voltages, and a filamentary DBD at high pressures and/or voltages. The emission spectroscopy is used to obtain quantitative

data about the discharge at high pressures (1–12 bar). The possible nature of the discharge filamentation is described.

Finally, the third part describes the experiments of plasma-assisted ignition with nanosecond SDBD at elevated pressures. The discharge morphology in lean combustible (H_2:air) mixtures and following ignition of the mixtures are studied. The comparison of ignition by filamentary and streamer discharge at the pressures 1–6 bar is performed. Kinetic modeling of plasma assisted ignition for the electric fields typical for nSDBD, $E/N = 100 - 200$ Td is used for analysis of experimental data. Complex study of the discharges at atmospheric pressure, discharge at high pressures and ignition allow detailed description of the high-pressure, distributed in space ignition by non–equilibrium plasma.

Chapter 1

Literature review

1.1 Surface dielectric barrier discharge in atmospheric air

Over the last 15 years, increasing interest to physics of surface dielectric barrier discharge (SDBD) in air at atmospheric pressure has been observed. Applications of strong research interest include plasma-based flight control, namely generation of lift and turbulization of flow around the airfoil [1–4], plasma assisted combustion, where generation of radicals and fast heat release due to relaxation of highly excited levels decrease dramatically ignition delay time [5–8] and also flame stabilization with surface or volumetric DBDs [9]. Both periodic-pulse excitation and sinusoidal power of $1 - 10$ kHz frequency are typically used for flow control and/or combustion experiments. In periodic mode, a series of microdischarges of $20 - 50$ ns duration is observed at increasing of absolute value of voltage. These microdischarges are separated by $1 - 10$ μs periods of plasma decay.

SDBD excited by a single pulse of a few tens of nanoseconds is an efficient system to study physics of surface DBDs because only one discharge "plane", consisting on parallel propagating streamers, is generated over the pulse time. The discharge propagation along the non–charged surface at the leading front of the pulse simplifies the interpretation of experimental data. Moreover the nSDBD in a single shot regime produces a discharge simultaneously starting from the edge of HV electrode, whereas SDBD initiated by sinusoidal applied voltage produces a few streamers during each half–period and starting randomly from one to another discharge initiation.
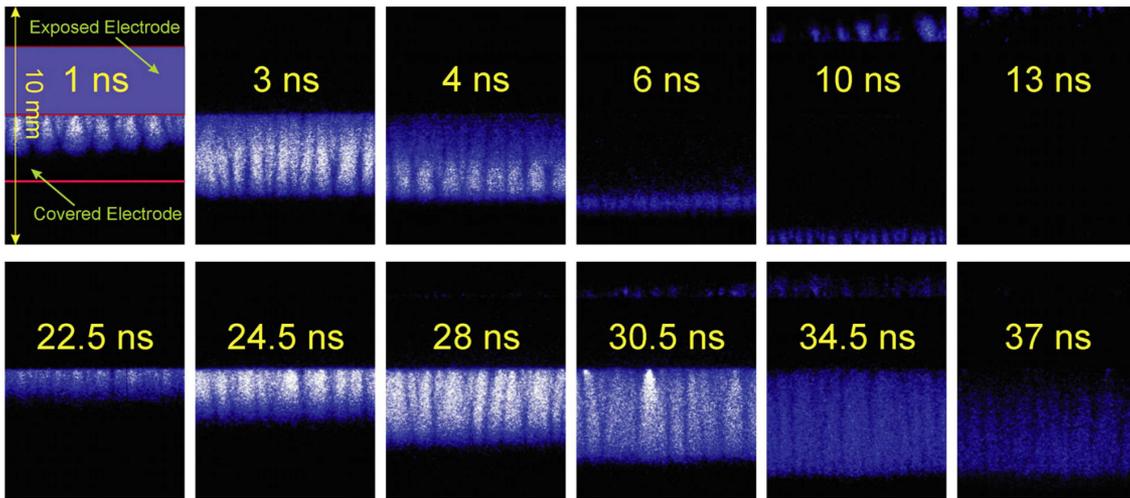
Figure 1.1: Images of surface nanosecond barrier discharge development taken with nanosecond time resolution. Camera gate is 0.5 **ns. Voltage on the HV electrode is** 14 **kV. The half-width time of pulse is** $\tau_{1/2} = 25$ **ns,** $P = 1$ **bar. Cathode-directed streamer discharge [10].**

One of the most distinctive features of nSDBD is the stability at high pressures (repeatability from one to another experiment) and operation at high values of reduced electric field values $E/N \sim 10^2 - 10^3$ Td, where 1 Td=10^{-17} V/cm^2. Under these conditions, a significant fraction of energy deposited into the discharge goes to electronic excitation of atoms, molecules and dissociation of molecules by direct electron impact. As a result, efficient generation of active species takes place.

The detailed morphology of the nSDBD was for the first time studied in [10]. It was also shown that the dominant effect of nSDBD plasma actuators on the flow is due to the fast localized heat release. The compression waves in quiescent air generated by localized heating during the nanosecond pulse were detected experimentally. The typical images of the nSDBD for positive polarity of applied pulses are demonstrated in figure 1.1. The pulse width was about 25 ns. The discharge propagates as two successive ionization fronts, developing on the leading front and on the trailing edge of the high-voltage pulse. In the first ionization front, hereinafter we will call it a first stroke, and the second ionization front, the second stroke, the polarity of the high-voltage electrode is positive related to the surface of the dielectric. The reason is that, during the first stroke, a surface of the dielectric is charging and the potential of the surface finally becomes a fraction of the voltage amplitude. Decrease of voltage on the trailing edge causes a change of the sign of the difference of potentials between the electrode and the surface of the dielectric.

It was demonstrated in [11] that both first and second stroke of a single voltage pulse produce a current peak. Each of the peaks leads to the production of the pres-
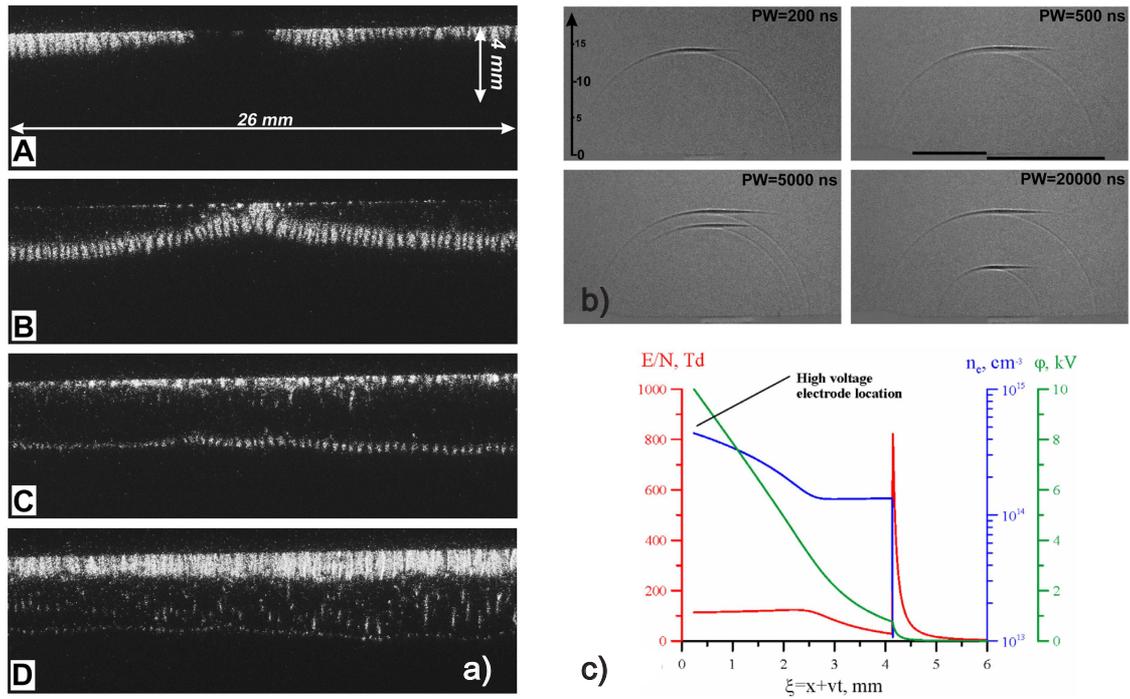
Figure 1.2: (a) Plasma formation and propagation in the rising and trailing edge of HV pulse; (b) pressure waves propagation for different pulse widths at +10 kV amplitude (scale in mm, images taken in 10 μs, PW stands for pulse width) [11]; (c) predicted reduced electric field and electron density distributions in a positive polarity discharge [12].

sure wave propagating in the medium. The results also indicate that the intensity of the pressure wave can be changed by the amplitude of applied pulse, by the rise time of the leading edge or by the period of HV pulses. The waves corresponding to the first and second strokes are presented in figures 1.2. The pressure waves are different for the different pulse widths. For a low pulse width, a single trace is observed. This trace correspond to the superposition of the waves produced by first and the second stroke of the applied pulse. By increasing the pulse width, two waves separated in time and become visible in the shadowgraph image. Both traces propagate with approximately same velocities close to sound speed 340 m/s. However, as it was demonstrated in [10], the slightly supersonic velocities of compression waves have been detected for different width of applied pulses 7 and 50 ns, 420 and 480 m/s respectively.

More detailed morphology and energy release study is described by Nudnova et al [13]. It was shown that energy deposition does not significantly depend on the polarity of applied pulses. At the same time, the discharge structure significantly depends on the polarity on exposed electrode. The negative polarity discharge is

more uniform than positive polarity discharge in the transverse direction. It was also mentioned that the maximum electric field is higher for positive polarity discharge. Whereas, the gas heating is higher (at the small time periods up to 1 μs) for negative polarity discharge. The velocities of the discharge propagation were also analyzed. It was assumed that due to higher values of propagation velocity V and radius of the streamer head R for positive polarity streamers, the time of the residence of the discharge electrons in the regions with high E/N values is lower. Therefore, the specific energy that goes to the heat release on the considered time scale is higher for negative polarity pulses.

Until recently, the reduced electric field distribution and electron density in the plasma channel have been studied only numerically. One or two dimensional models require experimental data of integral discharge parameters such as: energy deposition, current, applied voltage pulse shape, discharge propagation velocity. These parameters were uploaded into computational model and then, the calculations of reduced electric field and/or electric density have been performed. For volumetric and surface DBD, an interesting analysis was done by the team of professor Adamovich *et al* [12]. The physics of the discharge was analyzed on the basis of experimental results. The self-similar, local ionization kinetic model predicting energy coupling to the plasma in the surface ionization wave discharge produced by a nanosecond voltage pulse was developed. The model predicts the key discharge parameters such as: propagation velocity, electric field, electron density and the thickness of the plasma layer. The results presented in [12] describe pretty well the discharge parameters for volumetric discharge and also satisfactorily coincides with more advanced simulation models for SDBD configurations [14–17]. The results of surface DBD calculations are shown in figure 1.2(c).

The *in situ* electric field and electron density measurements is a challenging task for nSDBD discharge configuration. The fineness of the plasma layer and presence of the dielectric surface in close proximity of the discharge region complicates the diagnostics of SDBD discharge type. It is complicated to use the laser beam as a diagnostic probe. In spite of the complexity of the discharge geometry some experimental data concerning charge and field distribution exist. Leonov *et al* [18] has measured the surface charge and surface potential with the sequences of charge sensors (Kelvin probes) implemented into the dielectric layer of SDBD. It was done for pulse periodic microsecond discharge with positive and negative bias and polarity of applied pulses. The similar diagnostics has been used for the sinusoidal applied voltage in [2]. One more method of diagnostics is based on the Pockels effect, that is on the dependence of optical birefringence on the electric field [19]. This method is used to perform quantitative measurements of surface charge density potential distribution in both volumetric DBD [20] and surface DBD [21] arrangements.
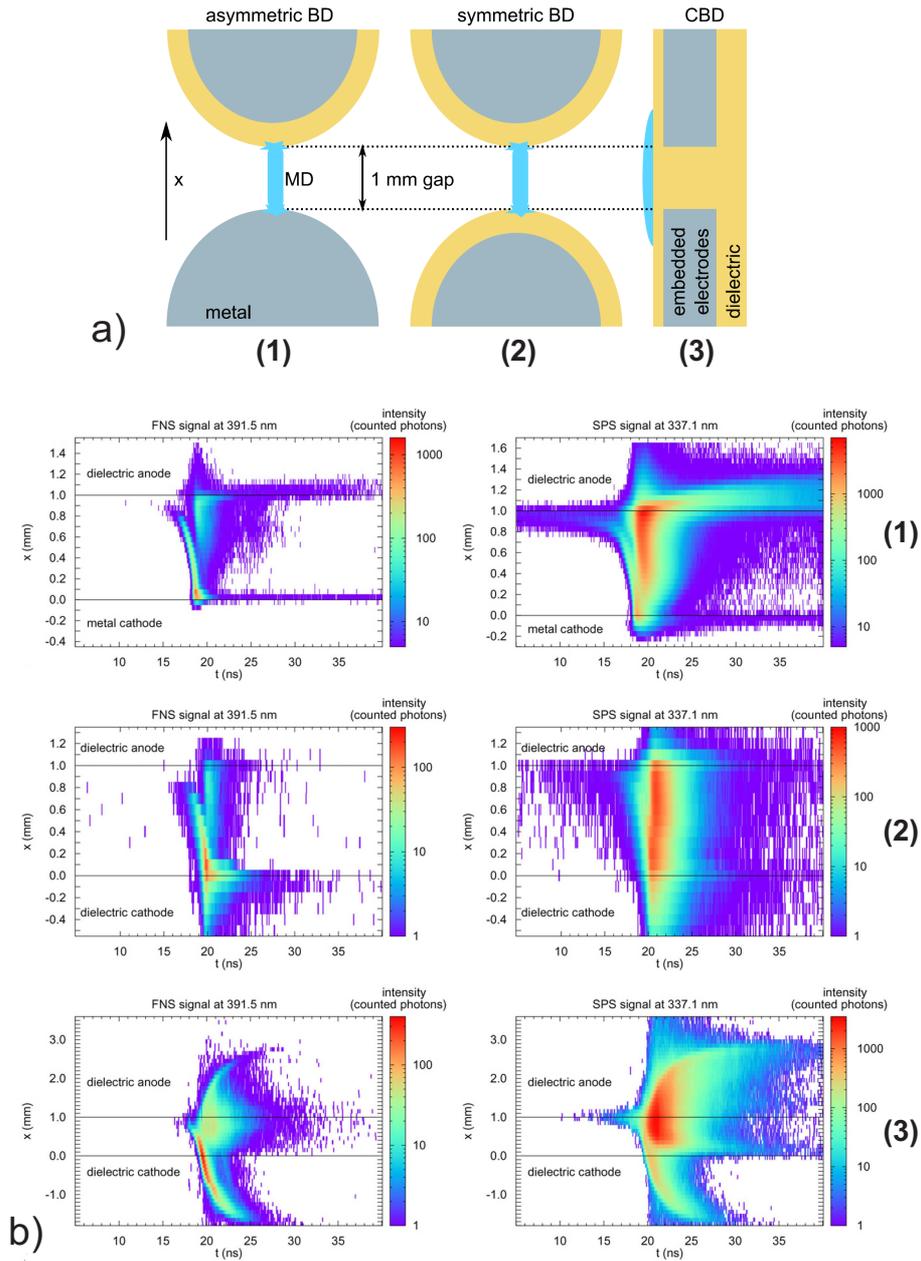
Figure 1.3: (a) Electrode arrangements for investigated barrier discharges (BD); (b) Spatio-temporal distributions of the discharge luminosity of FNS and SPS in asymmetric BD with metal cathode, in symmetric BD and in CBD. Positions of the electrode tips are denoted by the black lines [22].

Both volume and surface DBDs are spatially distributed systems and some special efforts are needed to measure or at least estimate the electric field in the discharge gap. The analysis of the spatial intensity of the first negative (FNS) $(N_2^+(B^2\Sigma_u^+)_{\nu'=0} - N_2^+(X^2\Sigma_u^+)_{\nu''=0}, \lambda = 391.4$ nm) and the second positive systems

(SPS) $(N_2(C^3\Pi_u)_{\nu'=0} - N_2(B^3\Pi_g)_{\nu''=0}$, $\lambda = 337.1$ nm) for three different arrangements of electrode system was performed in [22]. The electrode systems are shown in figure 1.3(a):asymetric BD, symmetric BD, coplanar BD.

The results of spatio-temporal analysis of intensities of SPS and FNS [22] show that the mechanisms of electrical breakdown for the three BDs are quantitatively similar. The discharge consist of three pases: (i) the pre–breakdown Townsend phase; (ii) the phase of ionization wave propagation; and (iii) the decay phase. The Townsend phase demonstrate itself as a weak continuously growing glow in front of the anode. This glow is clearly seen on the plots of SPS in figure 1.3(b) for $t < 15 \; ns$. In the first pre–breakdown phase the electric field is quasi-stationary, the electron density and thus the intensity increases exponentially in time due to the electron avalanches. The accumulated discharge leads to the distortion of the electric field and formation of cathode-directed ionization wave (CDIW). In the case of the coplanar discharge the CDIW is accompanied by another ionization wave propagating over the anode surface in the opposite direction. Both ionization waves gradually slow down and decay outside the inter–electrode region. The thickness of the cathode layer for the asymmetric BD was estimated from the experiment and was found to be about 30 μm. This value correlates with the simulation results of [16].

Another effort of the resolution of the surface discharge spatial structure was done in [23]. The intensity analysis on the different distances from the dielectric surface has been performed for emission of the SPS and the FNS. The spatial analysis of SDBD fine structure showed that the maximum intensity for both polarities of applied pulses correspond to the region of the discharge front at the distance a few hundreds of microns above dielectric layer. When approaching to the dielectric surface, intensity decreases. The results of the work [23] is the only set of experimental results of intensity analysis of SDBD microdischarges. The discharge was initiated with alternating voltage with a frequency 5-14 kHz.

In the quasi–uniform discharge where FNS and SPS emission goes from the same discharge area, the reduced electric field strength can be determined from the intensity ratio I_{391}/I_{337} or I_{391}/I_{394}. A technique of E/N measurement is described in [24, 25]. This method is widely used in the volumetric discharge at low pressures. However for more complex structures of the discharge this method can give unreliable values of E/N. For example, Kosarev *et al* [5] measured the E/N in nSDBD at different gas pressures (1-5 bar). The reduced electric field for considered condition was in the range $350 - 600$ Td. Later, it was demonstrated from the experimental results and from 2D modeling that the nSDBD is highly nonuniform and that the methodic of E/N measurement with intensity ratio of SPS and FNS cannot be applied for sliding discharge [26].
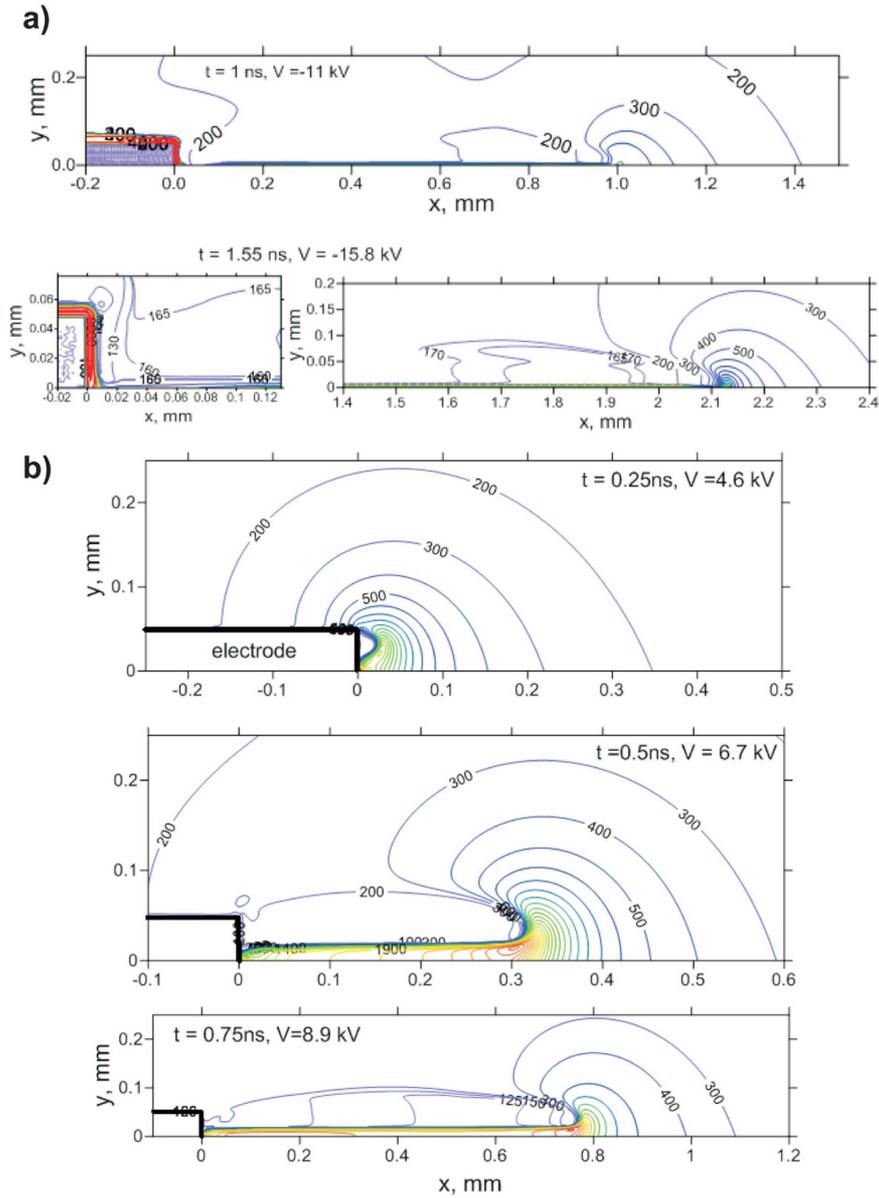
Figure 1.4: Calculated isolines of E/N: (a) negative polarity discharge, $U = -24$ kV; (b) positive polarity discharge, $U = +24$ kV [26].

In the nSDBD, the electric field and electron density change significantly in the normal to dielectric surface direction. Figure 1.4 demonstrates the E/N isolines calculated with 2D simulation model of Dr. Soloviev in the work [26]. The difference of isolines morphology for positive and negative streamers is that for positive polarity streamer the "gap" of rather high E/N can be clearly seen between the streamer body and the dielectric surface. This "gap" is formed because the charge surplus concentrates near the surface. Indeed, this gap is also present in negative polarity streamer. But comparing to positive streamer the characteristic thickness of this gap is an order of magnitude less than for positive polarity streamer. Paper [26]

17

presents the detailed analysis of the electron density, intensities on $\lambda = 337.1$ and $\lambda = 391.4$ nm, and E/N distribution over the plasma layer thickness.

The direct comparison of calculated 2D plots with experimental data is not possible, so the authors [26] suggested a following scheme: 2D distribution of the electric field and of the SPS were calculated and considered as input data for comparison. The 2D distribution of the FNS was calculated from known E/N and I_{337} for any point in space and time [26,27]. Further, the emission intensities I_{337} and I_{391} were integrated in the direction perpendicular to the dielectric surface, to imitate the data collection in the experiments.

The schematic representation of experimental results acquisition is given in figure 1.5(a). The obtained signal is the integrated signal over the discharge thickness. The comparison for the positive and negative polarity streamers is shown in figure 1.5(b). Two dashed rectangles demonstrate the calculated intensity ratio $R_{391/337}$ for all possible set of parameters (x, t) except the discharge front. Two pairs of dashed horizontal lines correspond to the range of E/N values measured experimentally with the method described in [25]. From figure 1.5(b) it can be concluded that for the negative polarity streamer numerical simulations and experimental results are in a good agreement. However, for positive polarity discharge no correlation between theoretical and experimental results is observed. The authors [26] analysed 3D effect, namely the fact that in the modeling the nSDBD is a uniform layer in z–direction (figure 1.5(a)), while in reality it is a set of separated streamers, well–pronounced for positive polarity and relatively diffuse for negative polarity. Nevertheless, the suggested idea was not able to explain the observed difference between the experiment and the numerical modelling.

Additional information about spatial distribution of plasma parameters in the non-uniform discharges can be obtained from the analysis of the work of numerical modeling [15,17,27–30]. All the works present the results of numerical simulation of SDBD in a flat (air–flow) configuration. The modeling is performed in 2D-geometry similar to the results presented in figure 1.4.

Numerical modeling of parameters and dynamics of the surface discharge is usually based on the transport equations for the charged species and Poisson's equation for potential of self-consistent electric field in 2D geometry (fluid model). The detailed modeling of the surface DBDs using this approach is presented in publications of a few groups: Center of Plasma Physics and Applications in Toulouse [31–33], Moscow Institute of Physics and Technology [14, 15, 27], and Princeton University [28, 34, 35]. The majority of these papers consider the SDBD modeling for constant, linear or sinusoidal applied voltage waveform, and only [15, 26, 27, 33, 36] deal with driven voltages in the form of few tens nanosecond pulse. In general, the results of modeling are in good qualitative correlation with available experi-
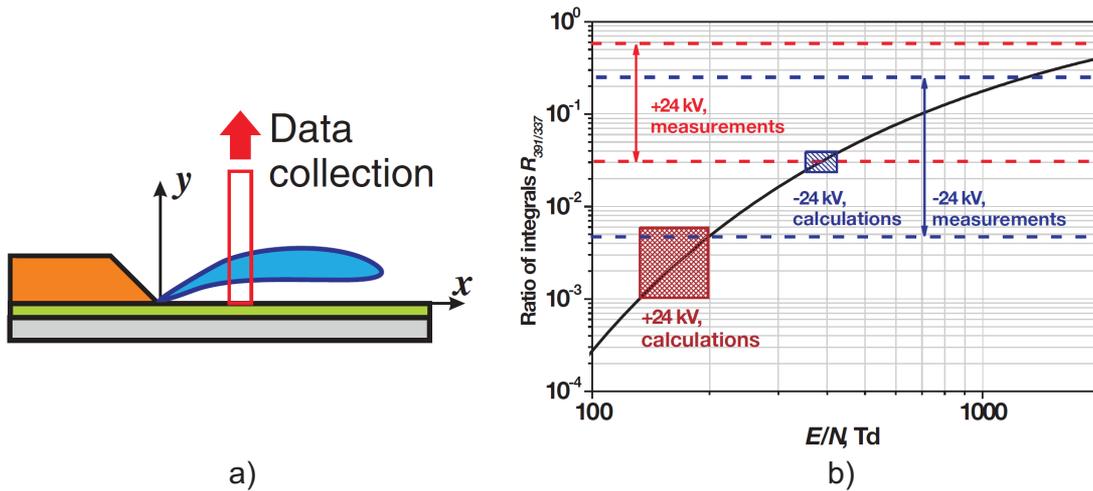
Figure 1.5: (a)Scheme of data collection in the experimental procedure and integration of the numerical result. The window marked in red corresponds to the region of integration; (b) Comparison of experimental and theoretical results for different polarities of applied pulses [26].

mental data. The calculations are time-consuming, and so a comparison of models suggested by different authors is hindered. A few significant distinctions can be mentioned here. For positive polarity discharges, the pre–ionization of gas from the discharge region is important. Calculations without UV pre-ionization [31–33] result in shorter streamer length and modified spatial distribution of charged species. For negative polarity discharges, the results of calculations are strongly influenced by boundary conditions on electron density on the surface of the dielectric. If the boundary condition for electrons on the dielectric surface is set in the form of equalizing their fluxes in hydrodynamic and kinetic approach [14], then a thin high positive ion density and high-electric-field layer is created above the dielectric surface. For simplified boundary condition like an approximation of instantaneous electron attachment to the dielectric surface resulting in n_e=0 the near–surface layer is not created. For this condition the numerical modeling does not predict a high electric field observed in experiment [26]. So, the experiment [26] implicitly confirms the validity of a boundary condition, proposed in [14] and not a simplified version [37], confirming that even non-direct comparison of the results of calculation with the experiments provides extremely important information for further development of discharge models.

The important issue is that the positive and negative polarity nSDBDs differ significantly. According to [38–40], in SDBD flow control problem the most significant effect is generated mainly during the negative half-period of AC voltage. It was
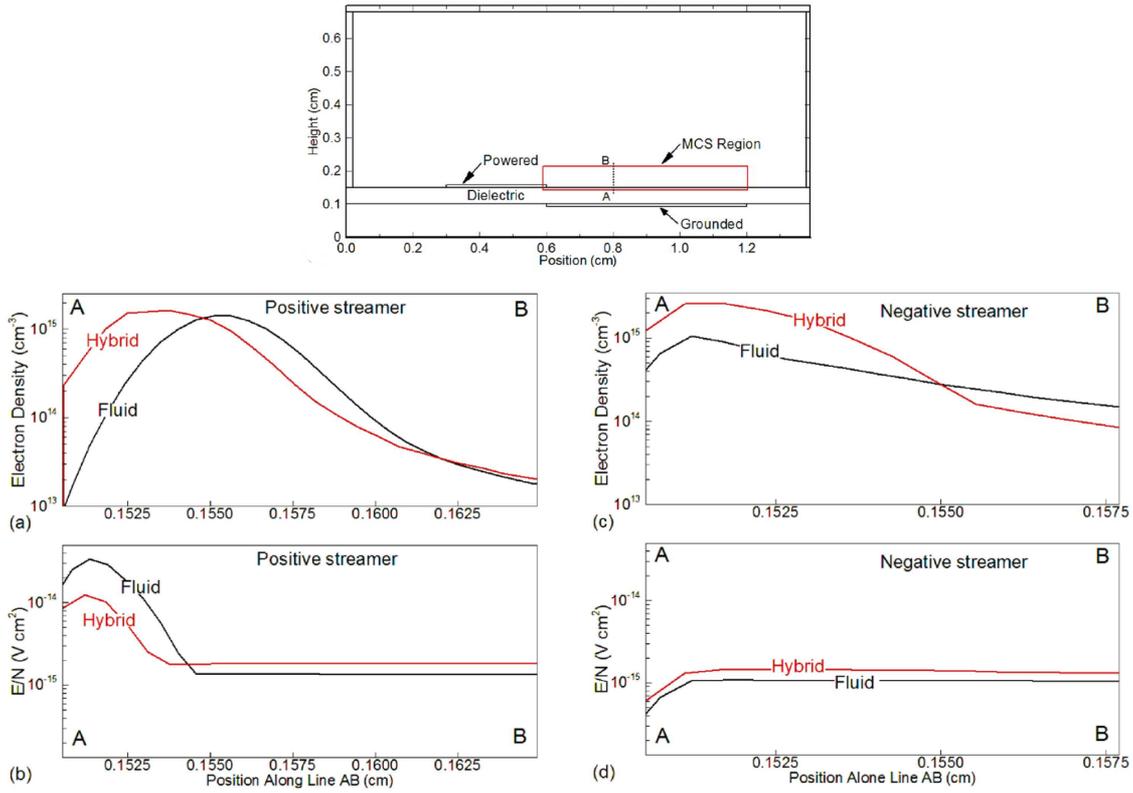
Figure 1.6: Profiles of discharge parameters along the line A–B calculated with fluid and hybrid models. (a) and (b) positive polarity streamer, 3 ns; (c) and (d) negative polarity streamer, 6 ns [41].

reported [6,7] that initiation of combustion of hydrocarbons is easier when acting by a negative polarity nanosecond pulse. A principal difference between a volumetric streamer discharge and surface dielectric barrier discharge modeling is that the fine computational grid should be used not only on the head of the streamer but in the entire zone along the dielectric. For atmospheric air the grid cell size should be not greater than $1 - 2$ μm to resolve the aforementioned thin near-surface layers in the discharge structure. Positive polarity discharge typically propagates at long distances, as a result, the time consuming calculations in [15] with a mentioned fine grid were able to simulate only the discharge at the leading front of the pulse; the trailing edge was not modeled.

One of the first modeling of the nanosecond surface discharge, carried out by Boeuf [33] for the SDBD driven by positive 35 ns voltage pulse of 14 kV amplitude succeeded using an order of magnitude greater grid cell size (18.75 μm). Because of such a rough grid these calculations did not resolve a thin discharge structure and it is not clear how accurate the obtained results are, both because of grid size and not–accounted for air photo-ionization by UV–radiation from discharge region

mentioned above.

A comprehensive numerical modeling of the SDBD driven by both positive and negative voltage nanosecond pulse has been fulfilled recently [41] using both conventional fluid model and combined fluid-Monte-Carlo model with kinetic Monte-Carlo description of high energy secondary electrons. Babaeva and Naidis [41] present the results of comparative numerical modeling with 2D fluid model and fluid-EMCS hybrid model. The results are summarized in figure 1.6. It was also demonstrated like in aforementioned works, that for positive polarity streamers, the intense sheath region is formed near the surface. This sheath is responsible for high value of E/N near the dielectric surface. It was demonstrated that the negative polarity streamers have a more diffuse structure with a lower E/N in the discharge front than the positive streamers. It was found that the effect of secondary electron emission induced by photons can be neglected for both positive and negative polarities of applied pulses. However, for higher values of secondary emission coefficients for photons, the influence of photoemission can be essential.

Unfortunately, the obtained results refer only to the leading front of the voltage pulse and do not describe the discharge transformation at the trailing edge of the pulse. Simulations presented both in [33] and [41] were performed without binding to experimental data and analysis how the obtained results are close to observed ones. Thus, despite an intense and well thought numerical modeling performed by different authors we still have some ambiguous treatments of the SDBD physical model details, which could be clarified only by experimental validation.

1.2 Contraction of surface dielectric barrier discharge

One of the most important advantages of surface DBD is that it produces active species not in one point like a nanosecond spark discharge but in the uniform layer along the dielectric surface. The size of plasma region depends on the applied voltage, gas density and composition. The main reason of the high efficiency for airflow control application is a synchronous energy release on a sub–microsecond time scale.

Nanosecond SDBD as a tool for plasma–assisted ignition has been suggested for the first time by Starikovskaia *et al* [42]. The electrode system in cylindrical geometry has been proposed for the following reasons: (i) to avoid edge effects as in flat configuration; (ii) to produce active species along entire dielectric surface of electrode system with the aim to get efficient 2D ignition of combustible mixtures; (iii) to adapt SDBD configuration for cylindrical combustion chamber of Rapid Compression Machines (RCM) [43, 44]. The experimental conditions of RCMs reproduce
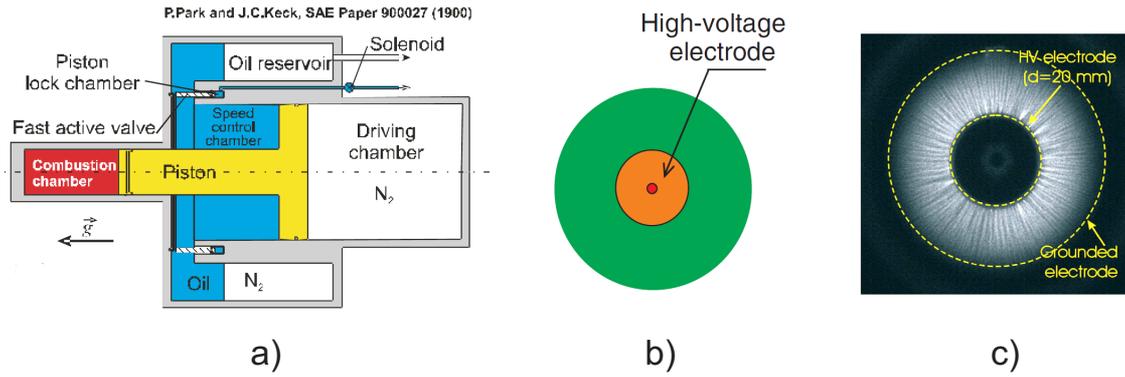
Figure 1.7: (a) Chamber and compression system of rapid compression machine [45]; (b) cylindrical electrode system (top view), dielectric is given by green colour; (c) Discharge initiated in cylindrical configuration of SDBD ($P = 1$ bar, $U = -25$ kV) [42].

the conditions of internal combustion engines ($P = 10 - 50$ bar, $T = 500 - 1500$ K) in a single shot experiment. The schematic view of RCM chamber and compression systems is demonstrated in figure 1.7(a). The upper view of the electrode system [42] and corresponding image of the discharge at $P = 1$ bar are demonstrated in figure 1.7(b) and (c). It is clearly seen that the discharge covers entire dielectric surface.

Therefore, it was necessary to understand how the discharge behaves at elevated gas densities. The nanosecond SDBD discharge in a single shot regime was studied experimentally in air at high pressure (1-6 bar) by Stepanyan *et al* [46]. The width of applied HV pulses was ~ 20 ns with the pulse rise time 0.5 ns. It was found that with increase of voltage and/or pressure the streamer surface discharge transforms to constricted mode. The constricted mode of the discharge represents a periodic structure of bright filaments starting from the edge of HV electrode and propagating in radial direction.

The discharge contraction is the phenomenon that has been first detected in AC, RF and pulse periodic surface DBD [2, 18, 47] and later in nanosecond SDBD discharges [11, 46]. Visually, the filaments of surface discharge for all aforementioned cases are similar, however the mechanisms of transition in constricted phase are not the same. The majority of early experiments was carried out in ambient air in repetitive mode or for the long pulses.

Corke *et al* [2, 3] describe the experimental investigation of SDBD initiated with sine wave AC applied voltage. It was demonstrated that transition from quasi–uniform discharge to filamentary mode is directly related to the frequency of applied voltage. The number of well-pronounced filaments per unit of electrode length

increases with the frequency as it is demonstrated in figure 1.8.
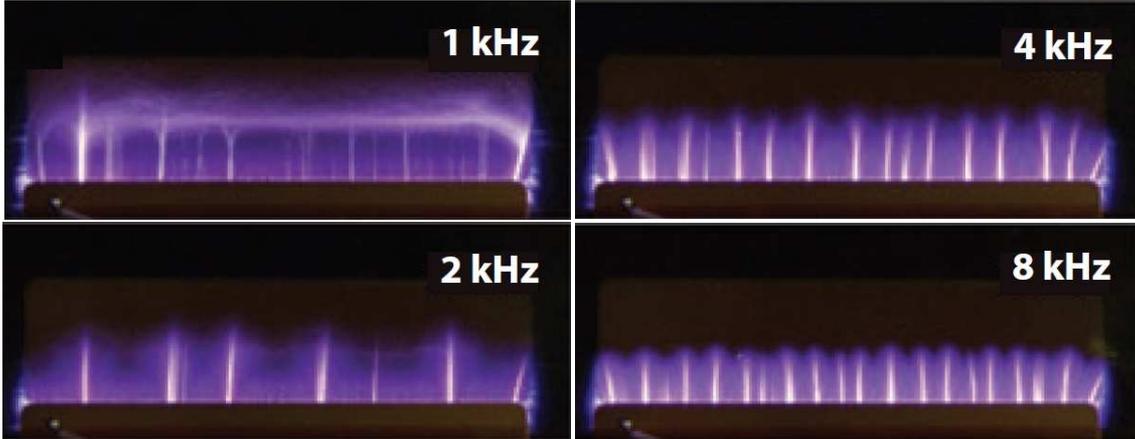
Figure 1.8: Images of surface discharge initiated by AC applied voltage with different frequencies [3].

In a single shot regime with a rather long width of applied pulses ($\sim 1\ \mu$s) several consecutive microdischarges take place [48]. The duration of each microdischarge is of the order of tens of nanoseconds. The negative polarity microsecond pulse with the current peaks corresponding to the discharge events is shown in figure 1.9(a). The corresponding images of the discharge are demonstrated in figure 1.9(b). It is clearly seen that discharge starts propagating in a quasi-uniform mode. For this mode the current increases gradually. As far as the applied voltage reaches the threshold of the transition into filamentary mode the discharge contraction takes place and well–pronounced current peaks are clearly seen. The filaments are not attached to the fixed plane from one to another microdischarge initiation. Each following filament is connected to the strip with individual cathode spot.

For a shorter time of applied pulses the filamentation of discharge was also observed in atmospheric air. Moreau *et al* [11] showed that single pulsed nanosecond SDBD discharge constricts at the trailing edge of applied pulses. During the decaying period of positive polarity pulse, as it is shown in figure 1.10, the second stroke of the discharge take place. The discharge is formed as a quasi-uniform front (figure 1.10 moment A). The plasma propagates with relatively low speed of 0.1 mm/ns. Further, filaments are organized and the length of propagation exceeds the latter of the first stroke discharge. The filamentary discharge structure is different comparing to the discharge of Akishev *et al* [48]. Filaments are formed as a periodic structure but not as randomly appeared channels.

One more important example of surface DBD discharge contraction was observed in nanosecond pulse periodic regime of alternating polarity of applied pulses. It was found by Leonov *et al* [18] that discharge transforms to well–developed filamentary
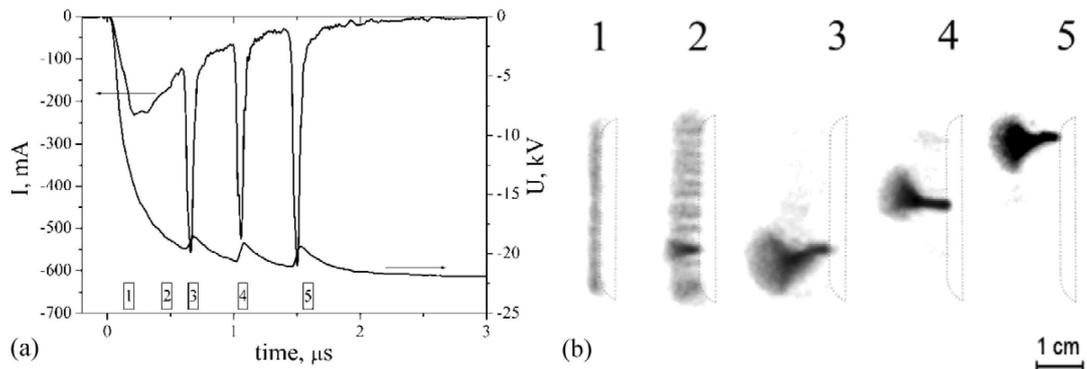
Figure 1.9: (a) Discharge current and voltage waveforms, and (b) plasma emission images at different moments of time in strip-to-half-plane SDBD plasma in air at atmospheric pressure. Camera gate is 100 ns. The dielectric barrier is a ceramic plate 2 mm thick ($\varepsilon \approx 6.8$). Labels indicate image timing [48].
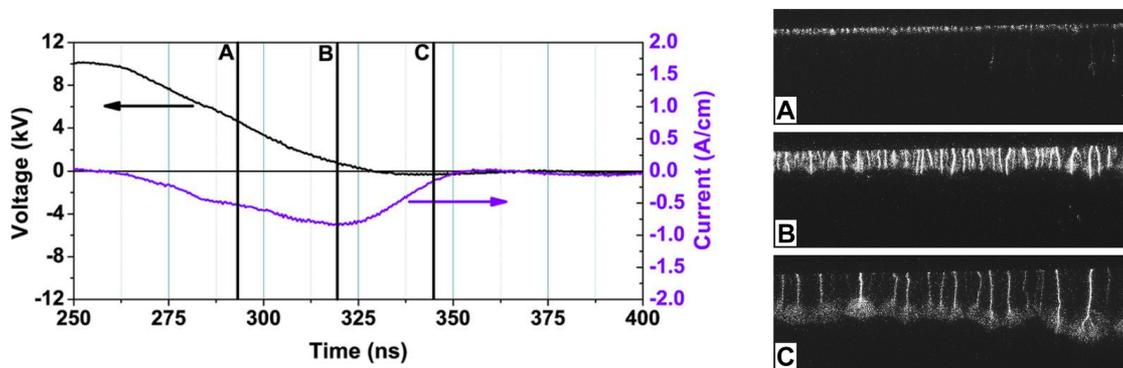
Figure 1.10: Plasma formation and propagation during the decaying period of a positive polarity applied pulse. Real size per frame 26x9.7 mm^2. [11].

phase within a few tens of nanoseconds when alternative polarity pulse train is used. At the same time the discharge remains diffuse when only negative polarity pulses are used, and a week filamentation takes place on a trailing edge of applied pulses when exposed electrode has positive polarity. The typical images of constricted and diffuse discharges are shown in figures 1.11(a) and (b). The corresponding schlieren images of produced shock waves are represented in figures 1.11(c) and (d). It is clearly seen that contraction significantly affects the compression wave amplitude and structure. For filamentary discharge, the compression wave length more than 2 times exceeds the latter produced by diffuse discharge. It was found [18] that the wave amplitude correlates directly with the coupled discharge energy. When the electrode is powered by a single (negative) polarity burst the appeared shock wave

is much weaker comparing to the wave generated by alternative polarity pulses.
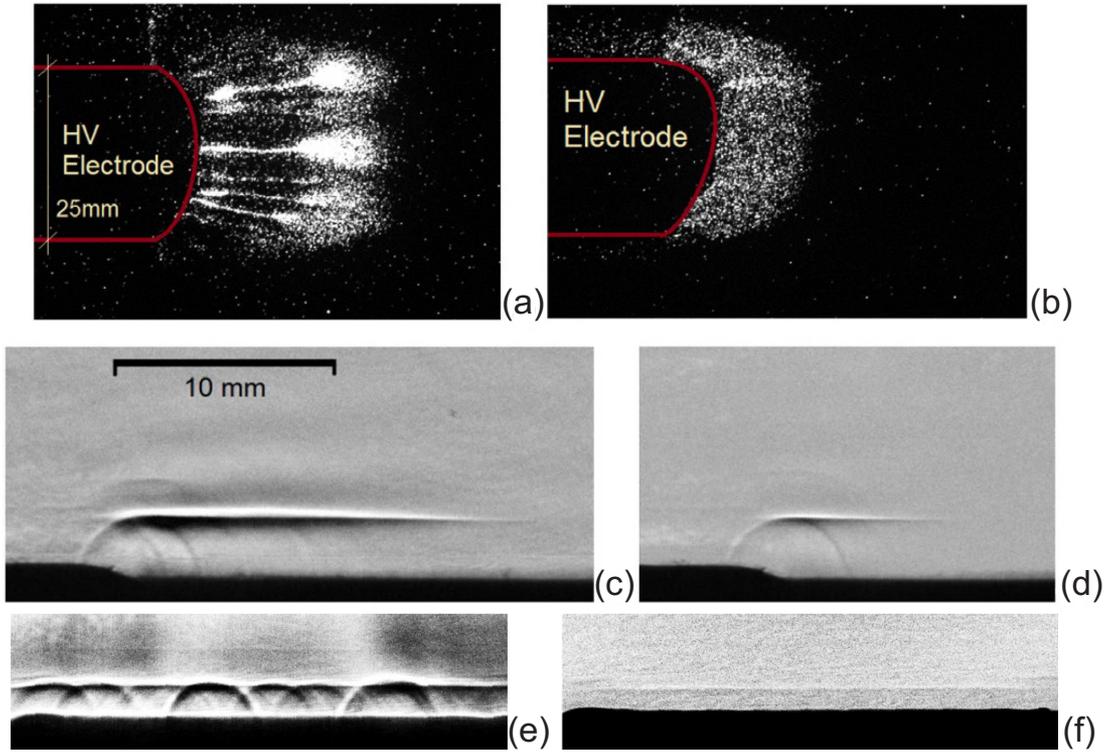
Figure 1.11: Direct correlation between negative polarity discharge images 60 ns after the pulse voltage rise, and schlieren images of the shock wave take 7.5 μs after the discharge pulse: (a,c) alternating polarity pulse train, (b,d) single (negative) polarity pulse train. "Side view" (high voltage electrode in on the left), $U_{psmax} = 14$ kV. (e,f) schlieren images of the shock wave generated by pulse surface DBD plasma, taken 4 μsafter the discharge pulse for different pulse peak voltages: (e) $U_{psmax} = 14$ kV, where strong contraction is observed and (f) $U_{psmax} = 8$ kV [18].

Figures 1.11(e) and (f) demonstrate how the amplitude of the applied voltage influences on the discharge structure and the structure of the generated shock waves. It is clearly seen, that the wavefront from the diffuse discharge ($U_{psmax} = 8$) kV seems to be quite flat and uniform, whereas the waves generated by the constricted discharge of $U_{psmax} = 14$ kV amplitude has a well pronounced cylindrical structure. The front becomes flat relatively fast with the distance from the electrode plane.

Despite the fact that the detailed mechanism of the surface DBD contraction in the works of Leonov is not well understood, it was shown [18, 49] that the discharge contraction and thus the amplitude of the shock wave is directly related to the morphology of the surface charge transfer. The discharge contraction results in significant release of energy stored on the dielectric surface during and after discharge

a) U=-26 kV, P=1 atm **b) P=3 atm, U=-47 kV**
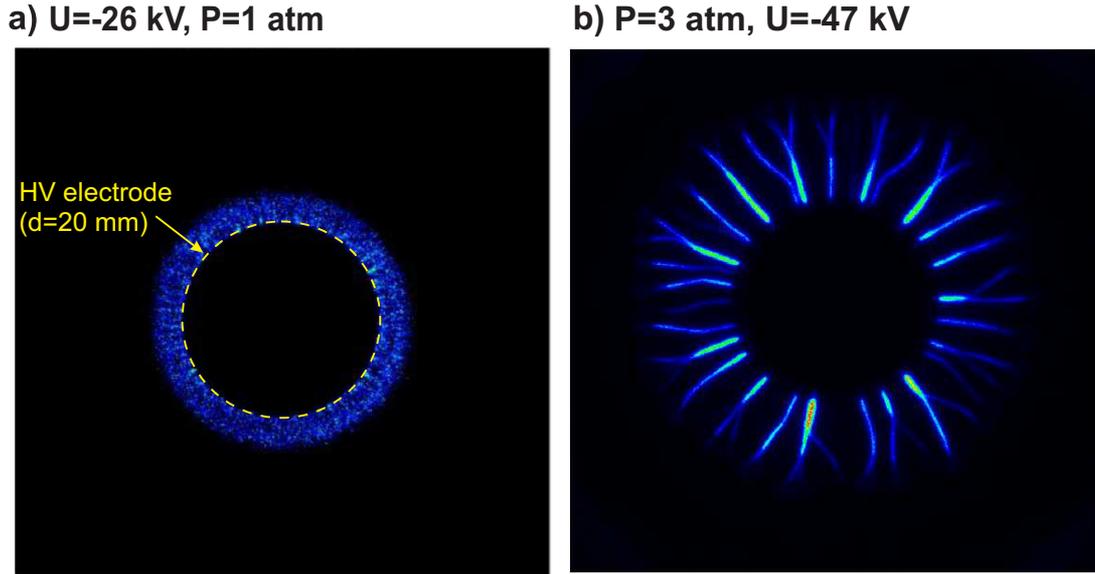
Figure 1.12: Streamer and filamentary nanosecond SDBD discharge. Camera gate 0.5 ns.

pulse, which in considered case exceeds the energy dissipated as Joule heat up to factor of 3–4. The stored energy is released as a heat if the discharge pulse is followed by an opposite polarity pulse. In discharge powered by a single polarity pulse, substantial accumulation of the surface charge limits the energy coupled to the plasma by subsequent pulses. therefore the filamentation is hindered.

The surface discharge filamentation in air in a single shot regime, when filaments appeared on the plateau of nanosecond pulses, was observed for the first time in [46]. The transition in filamentary mode has a threshold pressure P_{th} and threshold voltage U_{th}. The quasi–uniform and filamentary discharge phases are shown in figure 1.12. The discharge images were obtained for 1 and 3 bar pressure. Filamentary discharge at $P = 3$ bar and $U = -47$ kV appears abruptly 6 ns after the discharge start as a set of bright filaments propagating from HV electrode edge. The filamentary mode of nSDBD in a single pulse regime was observed, in considered conditions only for negative polarity of applied pulses [46]. The filaments were not observed for pressures $P < 3$ bar. During filamentary phase the discharge current, the discharge intensity and the maximum propagation length were higher than for streamer discharge.

Ionization–heating instability in the cathode layer was suggested [46] as a reason for the filamentation. Although, fast gas heating is able to provide significant temperature increase on the scale of a parts of micron during a few nanoseconds, the heated layer will have a longitudinal dimension of the cathode layer (sub–micron) and will be equal to a streamer radius in a lateral direction. There is no explana-

tion how the suggested shape of perturbation can initiate the ionization wave in the longitudinal direction (along the radius of the electrode system).

No experimental study of filamentary nSDBD at $P \geq 6$ bar is available; the discharge has been studied only in air; very limited information about plasma parameters in the filaments can be found.

1.3 Plasma–assisted ignition/combustion at elevated gas densities

Equilibrium plasma initiated by spark discharge has been used for ignition of combustible mixtures for over a hundred years, the millisecond sparks are widely used in spark ignition engines. Low temperature non–equilibrium plasma is an efficient tool for initiation of the combustion chemistry. It can influence both acceleration of ignition and sustaining/stabilisation of combustion. For the very first time, nanosecond discharges were suggested for PAI in [50]. During the last two decades significant advance in understanding of kinetics of ignition by non-thermal plasma has been made. The PAI domain was enlarged by a huge set of experimental data summarized in [51]. Figure 1.13 presents a summary of the initial thermodynamic parameters $\{P; T\}$ for the experiments on PAI/PAC with the help of nanosecond discharges. Only the experiments in combustible mixtures were taken into account.

Showing the initial gas number density (before ignition) and temperature for each of the experiments, the $P - T$ diagram in figure 1.13 allows comparison of the data related to the discharge development and combustion kinetics obtained by different scientific groups. The numbers on the right-hand side of the plot are linked to the appropriate papers in the table 1.1. Dashed lines in the diagram represent the isolines of the gas density, normalized to the atmospheric gas density at normal conditions, N_{atm}.

It is clearly seen in figure 1.13, that the experiments at ambient initial temperature cover a wide range of pressures $P =$ from ~ 1 Torr [58–60] to 30 bar [72]. For higher temperatures the experiment are performed in different systems and conditions: (i) the reactors with preliminary gas heating are used for pressures $25 - 100$ Torr and temperatures < 700 K [52,53]; (ii) shock tubes [57,61] are used for pressures $0.5 - 2$ bar and temperatures $800 - 1700$ K; (iii) the rapid compression machines for pressure ranges $2 - 50$ bar and temperatures $700 - 1500$ K [6,55,56]; (iv) low and atmospheric pressure burners are used in intermediate range of temperatures [64,66,67]. It can be noticed that the majority of the experiments is performed below atmospheric gas densities $N < N_{atm}$. At the same time, the domain of high gas densities is extremely important for PAI/PAC applications.
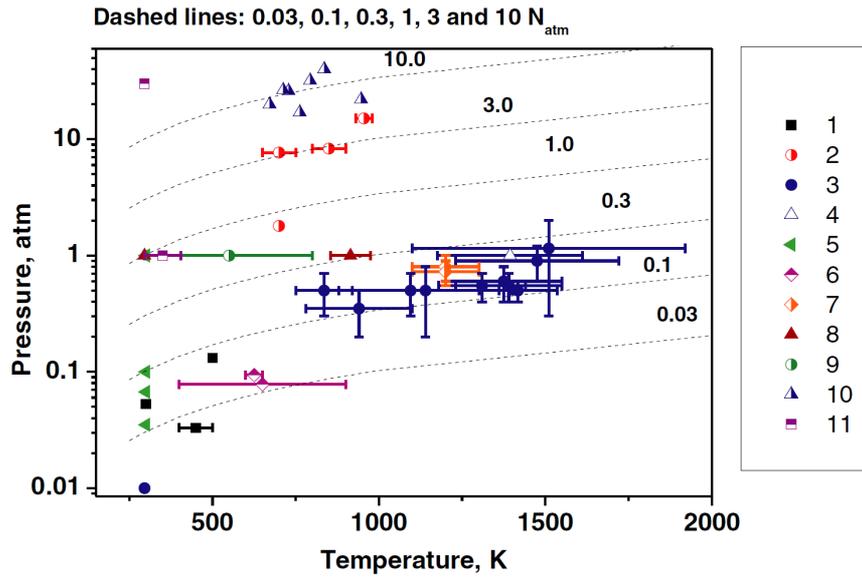
Figure 1.13: $P - T$ diagram of results available in the literature from experiments on combustion initiated or assisted by nanosecond discharges. The details of the symbols in the legend are given in table 1.1. Dashed lines represent the isolines of the gas density N_{atm} for normal conditions. Diagram is taken from review of *Starikovskaia* [51].

Table 1.1:   Reference and mixtures under study for the data presented in the $P - T$ diagram in figure 1.13 [51].

Number in fig. 1.13	Reference	Composition of the mixture
1	[52–54]	$H_2,CH_4,C_2H_4,C_3H_8/O_2/N_2,Ar$
2	[6, 55, 56]	$CH_4,C_4H_{10},C_7H_{16}/O_2/N_2,Ar$
3	[57–60]	$H_2,C_nH_{2n+2},n = 1 - 6,C_{10}H_{22}/O_2/N_2O/N_2,Ar,He$
4	[61]	$C_2H_6/O_2/N_2,Ar$
5	[62, 63]	$CH_4,C_2H_4,C_3H_8/O_2/N_2,Ar$
6	[64]	$CH_4,DME/O_2/He,Ar$
7	[65]	$C_2H_2/O_2/Ar$
8	[66, 67]	$CH_4/O_2/N_2$
9	[68]	$C_nH_{2n+2},n = (1 - 5)/O_2/N_2$
10	[69]	$C_3H_8/O_2/N_2$
11	[70–72]	$C_2H_2,CH_4/O_2/N_2$

The discharge morphology is very sensitive to both gas density and gas composition. It was demonstrated by Pendleton *et al* [73] that the discharge morphology changes considerably with gas composition. The discharge becomes more branched
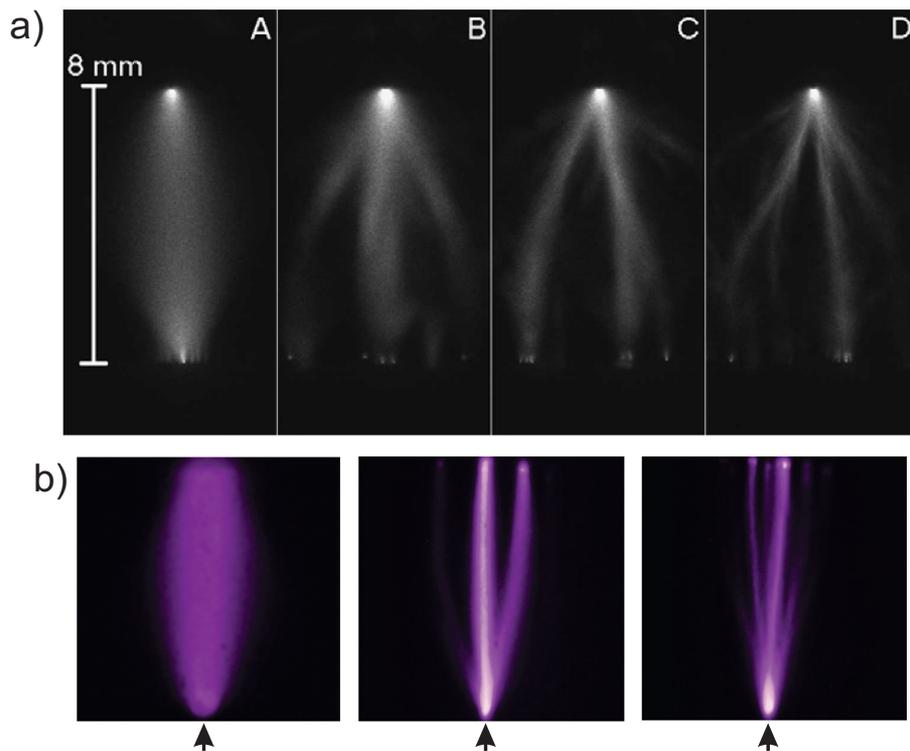
Figure 1.14: (a) Images of the discharge in: A-air, $\Phi = 0$; B-air:CH$_4$, $\Phi = 0.3$; C-air:CH$_4$, $\Phi = 0.6$; D-air:CH$_4$, $\Phi = 1.2$ **[73]**. (b) Diffuse nanosecond discharge in pure air (left) and filamentation effect in air:propane (middle) and air:n-heptane (right) mixtures with 6% of hydrocarbon additives. The black arrows give the locations of the pin HV electrode **[74]**.

with increase of fuel part in the gas mixture on the level of a few percent. The discharge [73] was initiated in point–to–plane geometry of electrode system. The tip radius was about 75 μm and the interelectrode distance was 8 mm. Nanosecond pulses with ~ 20 ns pulse width were used. Figure 1.14(a) demonstrates the discharge imaging in air and air:methane mixtures with different equivalence ratios.

Another independent group has observed similar behavior of the discharge in air and air:hydrocarbons. Figure 1.14(b) demonstrates the results of nanosecond discharge in a similar point–to–plane electrode geometry. Discharge was initiated with $20-40$ ns and $40-50$ kV pulses at atmospheric gas densities [74,75]. It is clearly seen how the diffuse discharge in air becomes "filamentary" in air:propane and air:n-heptane mixtures with 6% of hydrocarbon additives. Energy deposition and current in these two works are of the same order of magnitude. The discharge morphology is an extremely important parameter for the following ignition of combustible mixtures. It provides the information about the distribution of temperature and active species in the volume and/or surface where discharge is initiated. In general, the volume occupied by the discharge decreases when pressure is increased. Therefore, to provide
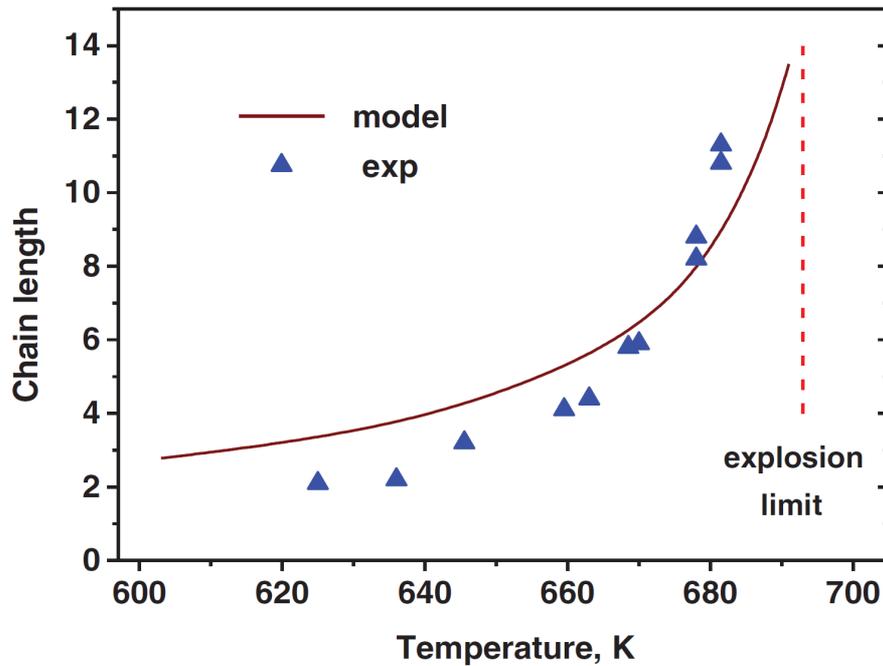
Figure 1.15: The chain length in a stoichiometric H_2:O_2 mixture at $P =$ 20 Torr and current $I = 150$ mA as a function of initial temperature: the symbols correspond to the experiment [76], the curve correspond to the calculation [77]. And the dashed vertical line to the ignition threshold for the conditions in [76]. Plot is taken from [78].

efficient ignition at high pressure is a challenging task.

One of the pioneering and unique for nowadays work of ignition with transient plasma was done by Gundersen *et al* [70]. The results of ICCD images of nanosecond discharge and following flame initiation in a quiescent C_2H_2:air mixture at $P = 1$ bar and $T = 300$ K are presented in [70]. Two different nanosecond pulses of 10 and 50 ns pulse widths were used to compare the efficiency of ignition regarding to conventional spark plug. The experiments were carried out at extremely high gas pressure, up to 30 bar at ambient temperature. The experiments were carried out in the cylindrical combustion reactor with constant volume. The stainless steel wire in the axis of cylindrical chamber served as the HV electrode. The discharge was initiated by 10 and 50 ns pulses in a single shot regime.

The efficiency of plasma–assisted combustion is directly related to three key points: (i) the production of active species and fast gas heating (FGH) during the discharge phase; (ii) the combustion chemistry that includes chain branching and development and that is exponentially dependent on the gas/flame temperature, and (iii) the hydrodynamics of combustion waves propagation. There is a number of theoretical works considering the FGH during non–equilibrium discharge [79–

82]. Experimentally fast gas heating is considered in [83, 84]. In spite of some mismatches in fraction of energy, transferred rapidly into heating due to FGH, in general the mechanisms are equivalent. Two–step processes are responsible for the rapid heat liberation: 1) $N_2(X)+e \rightarrow N_2(A,B,C,...)+e$, and 2) $N_2(A,B,C)+O_2 \rightarrow N_2(X)+2O+heat$.

The combination of the heat release due to FGH and production of active species determines the basis of ignition chemistry. As an example, the possibility of ignition temperature threshold decreases with production of active species in H_2:O_2 mixture in photolysis was studied experimentally in [76] and later calculations for the same conditions were performed in [77]. The efficiency of the chain–branching reactions depending on the initial gas temperature was investigated. It was demonstrated that absorption of the radiation in the Schumann-Runge continuum of oxygen molecules is accompanied by O_2 dissociation and the production of active $O(^1D)$ atoms, that significantly increases the chain length. Figure 1.15 shows the experimental and the calculated chain length for different temperatures. It is clearly seen how temperature increase provided by FGH can increase the chain branching.

High reduced electric field in the discharge leads to efficient production of atomic particles. It was shown [82] that for $E/N = 100 - 300$ Td in air:fuel mixtures, up to 50% of the discharge energy is spent on the dissociation of molecules. The addition of atomic oxygen and/or atomic hydrogen to combustible mixtures causes the reduction of ignition delay time and ignition threshold. There are different channels of active atomic particles production: (i) dissociation by UV radiation [76, 85]; (ii) by direct electron impact [57, 86]; (iii) quenching of electronically excited molecules [80, 87, 88], *etc.* On the other hand, chain combustion reactions exponentially accelerate with gas temperature. Therefore, while considering the most optimal way of efficient flame initiation it is necessary to "play" with a balance of active species production and fast gas heating, as far as the energy branching over internal degrees of freedom is determined by E/N values in the discharge. A few recent reviews devoted to the ignition with non–thermal plasma of hydrogen combustion [77, 78, 89] discuss all these aspects regarding to low temperature oxidation of hydrogen:air mixtures.

The combustion chemistry plays a crucial role on both stage of the flame initiation and of the propagation of combustion wave. Seeding of active species produced by non-thermal plasma changes the kinetic pathways and thus changes the ignition and extinction limits [90]. The changes of these limits can be represented as a transition of S–curve into a monotonic curve as it is shown in figure 1.16(a). It can lead to the situation when no flame extinction limit will exist between ignition and flame [91]. To prove experimentally the so–called S–curve transition by plasma, nanosecond pulsed discharge experiment was carried out in methane/air mixture in counterflow diffusion flames [92]. The S-curve transition that is demonstrated in
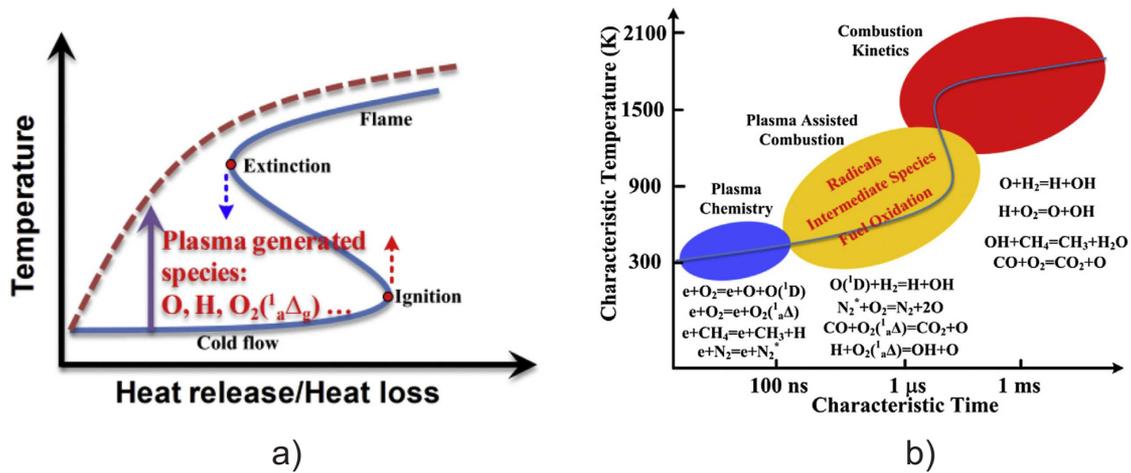
Figure 1.16: (a) Schematic of the plasma assisted transition from the classical ignition and extinction S–curve (solid blue line) to the monotonic stretched S–curve (red dashed line). [91]; (b) Schematic of timescale and key kinetic pathways at different stages of plasma assisted ignition and combustion [93].

figure 1.16(a) due to the action of plasma is equivalent to a decrease of the activation energy of the fuel oxidation reaction at low temperature. It happens because plasma can produce radicals faster than the fuel oxidation chemistry alone.

It is schematically illustrated by *Ju* and *Su* in their review [93] and shown in figure 1.16(b), that the plasma–assisted combustion chemistry can be represented as three stages: (i) plasma chemistry, where the discharge produces active species and the electron impact excitation and dissociation play the main role; (ii) plasma–assisted combustion stage, where the radicals are produced in collisions with excited species $N_2(A,B,C,...)$, $O(^1D)$, $O_2(a^1\Delta_g)$, *etc.*; (iii) combustion kinetics, where chain branching reactions lead to pressure/temperature increase and flame enhancement. In spite of rather well developed plasma kinetics during the initial period (~ 100) ns, the energy transfer and kinetic interaction of plasma generated active species and other reactants at intermediate timescale at low temperatures (100 ns$< t < 1$ ms, $T = 300 - 1000$ K) remain unclear. The current plasma–assisted combustion kinetic models cannot predict the behavior of key species at low temperatures and high pressure conditions. One of the still poorly understood phenomenon is the interaction of the plasma with cool flames [94].

Figure 1.17 demonstrates the theoretical results of Filimonova *et al* [95] concerning the study of the low–temperature plasma action on the negative temperature coefficient behavior in C_3H_8:air mixtures. Negative temperature coefficient (NTC) is a region in the coordinates "Induction time" *vs* "temperature" where the ignition
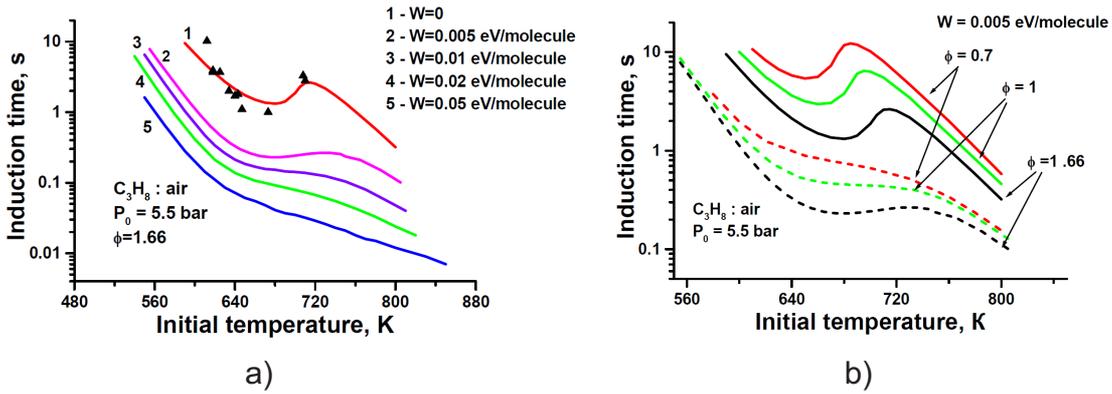
Figure 1.17: (a) Induction time as a function of initial temperature and input energy of the discharge; (b) Induction time as a function of initial temperature for different equivalence ratio of the C_3H_8:air mixture. [95].

delay increases with temperature. This happens when the chain branching is governed by a density of relatively stable intermediate radicals (so–called degenerate chain branching). The discharge effect on the negative temperature coefficient is illustrated by figure 1.17(a). It is clearly seen that the discharge even with relatively small deposited energy $W = 0.005$ eV/molecule significantly reduces the amplitude of the NTC. For $W = 0.02$ eV/molecule the NTC completely disappears. The difference of discharge operation with $W = 0.005$ eV in mixtures with different equivalent ratio is demonstrated in figure 1.17(b). It is shown that for lean mixture with ER=0.7, the NTC region is totally eliminated by non–thermal plasma action. The worse a mixture ignites due to auto–ignition, the more efficient the influence of the discharge. This fact was experimentally confirmed in [96].

One more key point of combustion processes is related to the propagation and interaction of combustion waves. The gas dynamics and the thermochemical coupling between non–thermal plasma and the reactive flows are still unclear. One of the pioneering work demonstrating the impact of flow recirculation induced by nanosecond spark discharge on the ignition kernel is done by Castela *et al* [97]. 3–D DNS computations, with detailed combustion chemistry and a plasma model developed in [97], for understanding of the plasma–flow–combustion interaction during the ignition by nanosecond repetitively pulsed (NRP) spark discharges. The results of a 3–D DNS was compared by experimental schlieren images of reactive kernel dynamic. The study was performed for methane-air mixture.

Figure 1.18(a) demonstrates the radial profiles of the key species in the middle of the gap between tip electrodes for the cases with and without gas recirculation at three time moments, and figure 1.18(b) shows radial temperature profiles for considered time instants. Starting from $t \sim 80$ μs the recirculation plays an important role
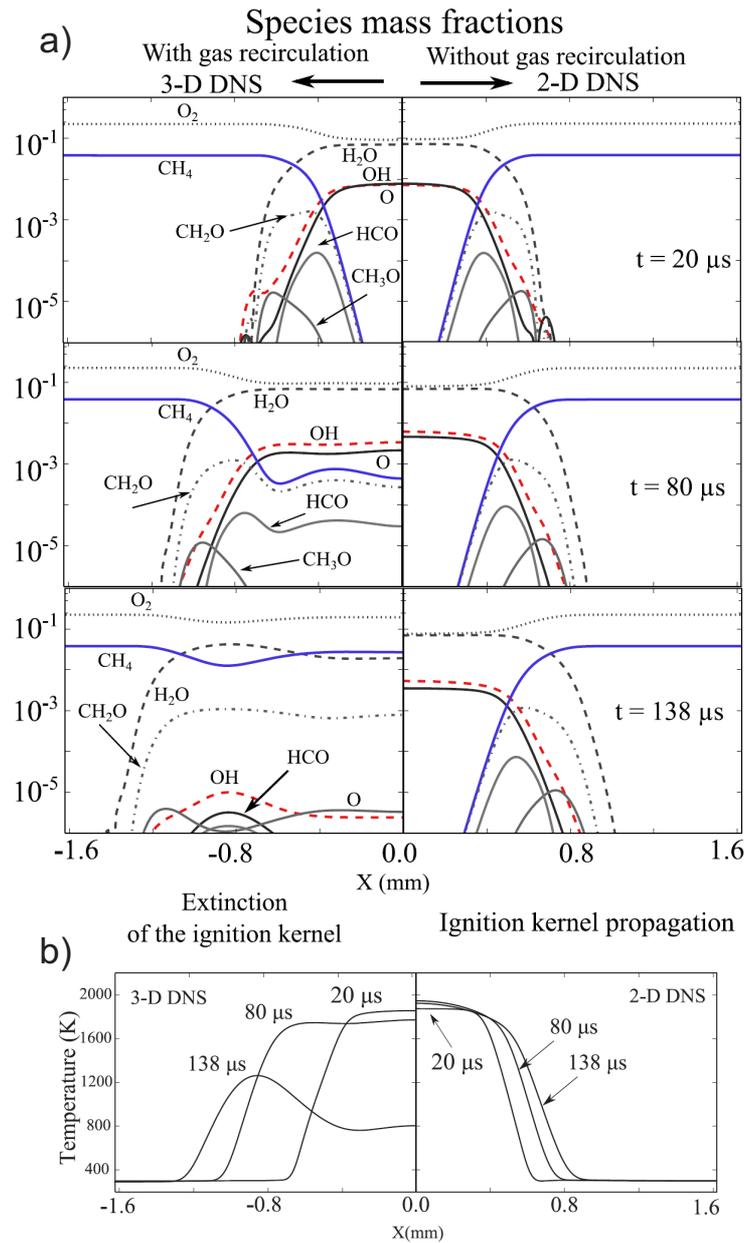
Figure 1.18: (a) Species mass fraction profiles along the radius of the nanosecond spark channel: on the left side refer to the case with gas recirculation (3-D DNS); on the right side refer to the case without gas recirculation (2-D DNS); (b) Temperature radial profiles with (on the left) and without (on the right) recirculation. [97].

in ignition processes. It decreases the temperature, however the diffusion length of the reactive species is increased by ~ 1.5 times. The spreading of the intermediate species may lead to increase of the gas energy around the discharge zone, and to appearance of more favorable thermochemical conditions. This may influence on the flame speed enhancement observed previously by the same scientific group [98].

It was demonstrated in [98], that the flame wrinkling induced by the NRP discharges seems to accelerate the flame propagation. The comparison between ignition initiated by conventional Audi coil and NRP discharges has been performed. The flame propagation strongly depends on the frequency and number of initiated discharge pulses. It was found that, the flame ignited by NRP discharge has more wrinkling structure than that initiated by conventional spark. The turbulization of the flame front by plasma, although not clearly understood yet, can be an important issue of PAI/PAC problem.

1.4 Plasma–assisted ignition with surface DBDs

Non–equilibrium plasma can be produced by different ways. One of the most popular discharge for plasma–assisted ignition is nanosecond spark either a single spark or in pulse periodic regime [97–99]. However, there are a few other ways to initiate low temperature ignition, as corona or microwave discharges [96, 100, 101]. One of the most promising advantages of nSDBD for PAI is the distributed ignition along entire surface of the electrode. And as it was mentioned above, the nSDBD in cylindrical configuration was suggested for this purpose [42].

Some previous studies describe the ability of ignition with nSDBD in the constant volume chamber [5] and in the rapid compression machines [6]. The considered nSDBD provided two–dimensional low–temperature plasma in the vicinity of the end plate of the combustion chamber. The experiments in rapid compression machine described in [6] were carried out in methane–oxygen and n–butane–oxygen mixtures with equivalence ratios between 0.3 and 1 diluted by $70 - 76$ % of Ar or N_2 for temperatures and pressures in top dead center between 600 to 1000 K and $6-16$ bar respectively. The study provides evidence of the efficiency of nanosecond SDBD to ignite combustible mixtures. A direct comparison of autoignition and PAI by nSDBD demonstrated a stable ignition and subsequent flame propagation in the combustion chamber of RCM for nanosecond pulse duration 20 ns in a single shot regime.

Figure 1.19 demonstrates the comparison of ignition delays for autoignition and ignition by nSDBD. The results were obtained for methane and n–butane containing mixtures. It can be observed that plasma–assisted ignition delay time is practically constant with initial temperature of the mixture and comprises about 6 ms for the $CH_4/O_2/Ar$, and about 0.5 ms for the n-$C_4H_{10}/O_2/Ar$ mixtures. The analysis of flame propagation was also performed. The resulting combustion waves were recorded by fast imaging. A single combustion wave propagating from the electrode system is clearly distinguished. The energy deposition per one streamer to initiate a
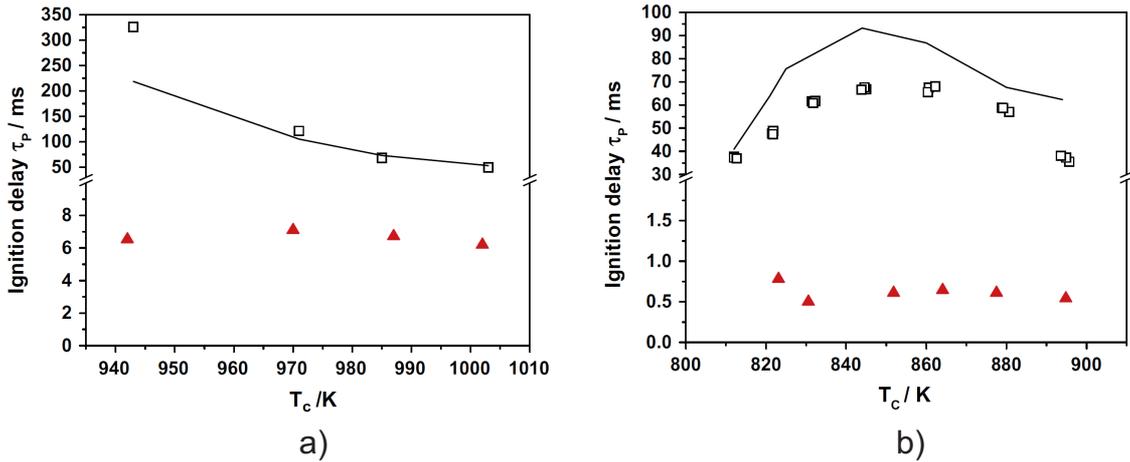
Figure 1.19: **Evolution of the autoignition delay (white squares) and plasma assisted ignition delay (red triangles) with initial temperature. Lines: calculated autoignition delays using the mechanism from Healy et al [102]. (a) $CH_4/O_2/Ar$, ER=0.5, $U = -24$ kV. P_{TDC} ranges from 15.4 to 16.0 bar; (b) stoichiometric $n\text{-}C_4H_{10}/O_2/Ar$ mixture. $U = -52$ kV. P_{TDC} ranges from 8.3 to 9.6 bar [6].**

stable combustion wave was estimated to be in the range $5-10$ μJ. Such a small value proves the efficiency of distributed (multi–point) ignition by non–thermal plasma at high pressures and intermediate temperatures.

Later [56] the experiments were carried out in n–$C_7H_{16}/O_2/N_2$=1.8/19.6/78.6 mixture at $P_{TDC} = 1.8$ bar and $T_C = 630$ K. At this conditions no autoignition is observed. The discharge was initiated by double 20 ns pulses: first at top dead center point, the second 60 ms after. Starting from the certain amplitude of applied voltage $U = -40$ kV, the pressure trace is modified and demonstrate a low, about 0.1 bar rise of the pressure. This pressure rise corresponds to plasma–assisted cool flame. At the considered conditions no autoignition and no cool flame without discharge initiation were observed. With increase of voltage amplitude, the pressure rise also increased and when the voltage was about $U \sim 47$ kV the second pulse initiated the sharp pressure increase corresponding to explosion of gas mixture. So, well pronounced two–stage ignition was controlled experimentally [56].

The chemical analysis of intermediate species of plasma–assisted cool flame at $P_{TDC} = 1.5$ bar and $T_C = 650$ K was studied experimentally by Vanhove *et al* [103] with the help of gas chromatography. It was demonstrated that under particular conditions of the RCM experiment ($N \simeq 0.9N_{atm}$), despite the aforementioned electrode configuration the initiated discharge was volumetric with streamers that cross the combustion chamber of RCM. Comparison of the plasma–assisted cool flame
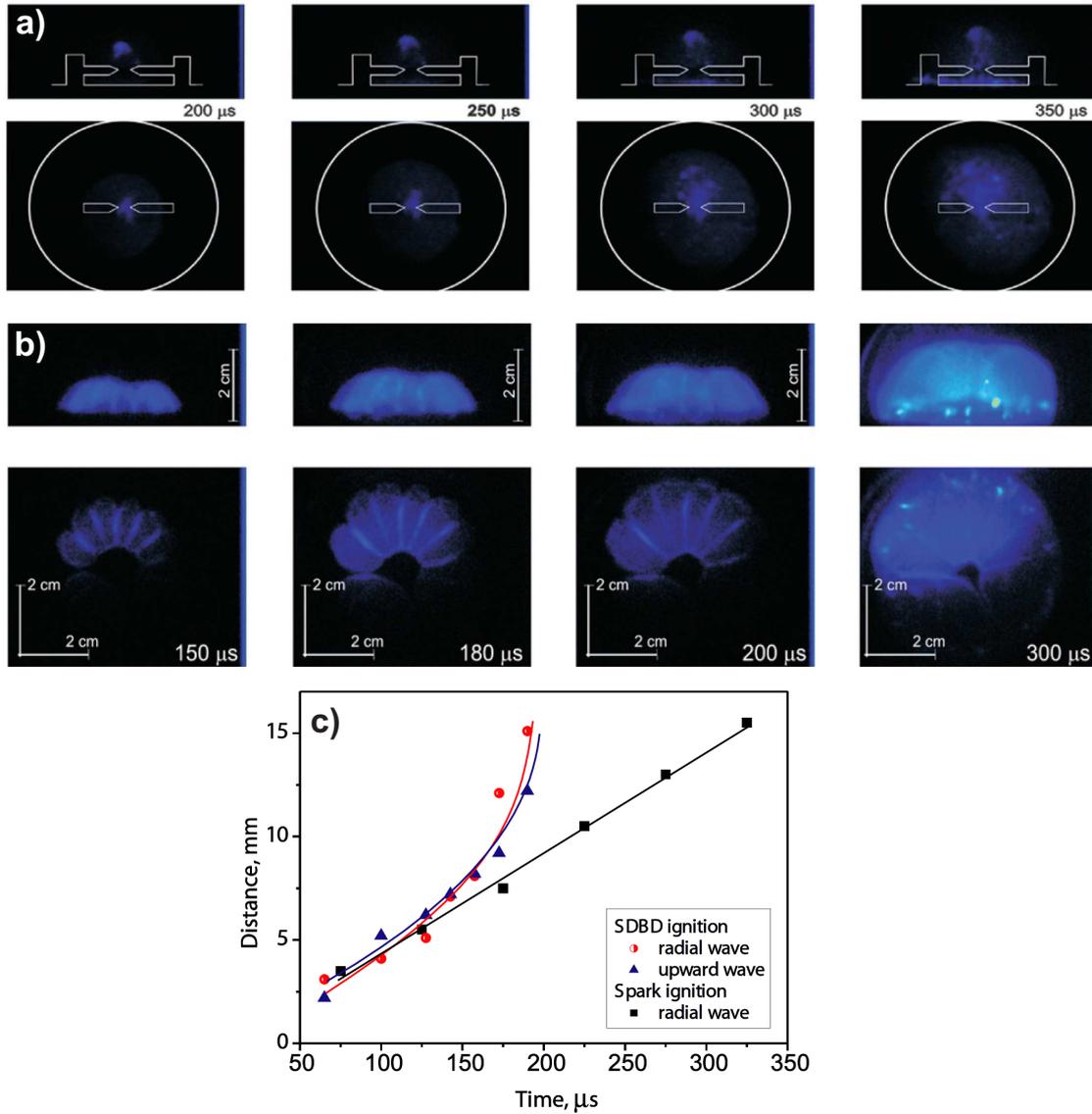
Figure 1.20: ICCD images of C_2H_6:O_2=2:7 mixture ignition by (a) a nanosecond spark discharge; (b) a nanosecond SDBD. Camera gate for both cases is 0.5 μs. (c) Flame propagation $x - t$ diagrams for the SDBD and for spark ignition [5].

with spontaneous cool flame at somewhat higher pressure ($P_{TDC} = 2.4$ bar) showed that no new products are formed. Gas chromatography analysis of the cool flame at different time instances after the discharge demonstrates that the main reaction pathways of low–temperature combustion (LTC) chemistry are not changed under plasma action. It is concluded [103], that discharge mostly influence on the formation of a radical pool that accelerates the LTC chemical mechanism.

Despite the fact that the discharge effect on ignition in RCM is well pronounced and demonstrated in [6, 56, 103], the optical access did not allow performing the
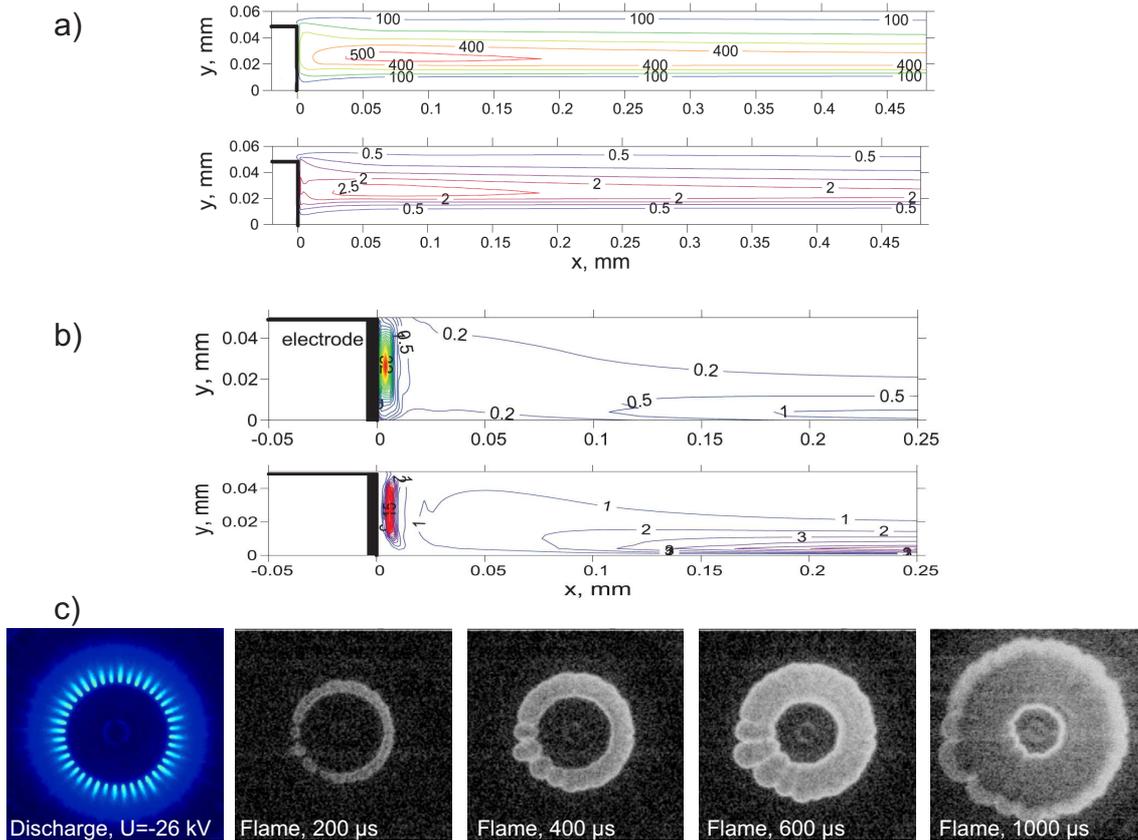
Figure 1.21: The specific energies deposition (mJ·cm^{-3}) contours (top plots) and the contours of O-atom densities (10^{17}cm^{-3}) near the high–voltage electrode edge at the end of streamer discharge formation ($t = 13$ ns) for (a) positive and (b) negative polarity of applied pulses with $|U| = 14$ kV; (c) image of the discharge and consequent flame initiation and propagation of combustion wave (top view) [7].

detailed study of the discharge in combustible mixtures and of the morphology of ignition pattern. For the very first time the morphology of ignition pattern initiated by nSDBD was studied in [5] on the example of stoichiometric C_2H_6/O_2 mixtures ($P = 1$ bar) in a constant volume chamber. It was demonstrated, that the nSDBD can be considered as a multi-point ignition system. The pulses of negative polarity with $25-30$ ns FWHM and 10–15 kV amplitude were used to trigger the discharge in the same cylindrical SDBD geometry as described above and the nanosecond spark. To initiate the nanosecond spark, the two pin electrodes separated by 2 mm were used.

Figure 1.20(a) and (b) show the ICCD images of the flame propagation initiated by nanosecond spark and SDBD respectively. The energy of the incident pulse was kept the same, $W = 60$ mJ. It can be noticed that during the same period the flame

from the nSDBD occupies bigger volume that that initiated by the nanosecond spark. Figure 1.20(c) shows the $x - t$ diagrams of combustion waves. During the first 150 μs, the velocities of the combustion waves initiated by SDBD and spark are identical. However, at $t > 150$ μs the flame front initiated by SDBD moves significantly faster. The reason of such propagation velocity increase can be linked with the processes related to the interaction of several combustion waves. To our knowledge, for the moment there is no qualitative explanation of this phenomenon confirmed by simulation results.

One more recent study devoted to the plasma-assisted ignition with SDBD was carried out by the same scientific group of Moscow Institute of Physics and Technology [7]. In this work the stoichiometric C_2H_2/air mixture was ignited at $P \leq 1$ bar with a single pulsed nSDBD. Discharge was produced by both positive and negative polarity. It was found that negative polarity discharge ignites the mixture "easier" (smaller energy deposition) than the discharge of positive polarity. Anokhin *et al* [7] showed that for both polarities of applied pulses the ignition takes place at the edge of the high voltage electrode.

2-D modeling of the discharge in air was performed by Soloviev *et al* [7] and the results of this modeling are shown in figure 1.21(a) and (b). It is clearly seen that for negative polarity of applied pulses the energy deposition and O-atoms density in the vicinity of the HV electrode is significantly higher than the values provided by positive polarity of applied pulses. Subsequent flame initiation by the discharge of negative polarity is demonstrated in figure 1.21(c). Indeed, it is clearly seen that flame propagates from the HV electrode.

So, the question of the spatial distribution of energy in the discharge is very important for following chemistry, heating and finally for the ignition/combustion development.

Chapter 2

Problem formulation

As it was described in literature review, the nanosecond surface dielectric barrier discharge (nSDBD) in a single pulsed regime in atmospheric air has been widely studied experimentally and with the help of numerical 2D simulation. It is known that the nSDBD starts from the edge of the HV electrode for both polarities of applied pulses. The velocity of positive polarity streamers is higher than the velocity of propagation of negative polarity. The synchronous start of the set of streamers leads to the synchronous energy release and to the generation of the compression wave. Attempts to measure E/N, although giving different results, indicate that the region of high electric field exist in the vicinity of the dielectric layer. The complexity of nSDBD structure is basically related to the highly nonuniform distribution of the reduced electric field both with the radius and along the length of the plasma channel. Validation of numerical schemes under these conditions is a challenge.

It is known that with increase of pressure and/or amplitude of applied voltage a single pulsed nSDBD transforms to contracted – filamentary mode. No information is available about transition parameters in different gases. No filamentation was observed at positive polarity of the high voltage pulse. The lack of the experimental data does not allow development of a reliable mechanism describing the transition to filamentary mode. The parameters of plasma in the filaments are not known.

As it was demonstrated, the surface discharge in the contracted mode is of particular interest for aerodynamic and combustion applications. The nSDBD has a significant advantage regarding to other discharge types (f.e. spark, microwave discharge *etc.*) that can be applied for ignition of combustible mixtures. It is the ability to provide a regular structure of ignition kernels at high gas densities. All

previous studies of PAI with nanosecond surface dielectric barrier discharge either were performed at atmospheric or lower gas densities or were performed in the chambers with poor optical access. Therefore, there is no self–consistent experimental results of the discharge in combustible mixtures and the following flame initiation by nSDBD at high gas densities.

The present work is focused on the following tasks:

1) On the basis of the direct visualisation of the discharge with the help of ICCD imaging, measurements of discharge current, energy deposition and emission spectra, to obtain a consistent set of the plasma parameters of the streamer nSDBD in ambient air. To compare experimentally the discharge development for anode– and cathode–directed streamers. To provide the information of time–resolved spatial structure of the discharge and to compare the discharge morphology and parameters with the results of numerical simulation presented in literature.

2) To study the parameters of the nSDBD at high pressures (up to 12 bar) in different non–combustible mixtures (air, N_2, N_2:CH_4, N_2:H_2, Ar:O_2) for both polarities of HV pulses. To study the conditions and parameters of the streamer-to-filament transition. To investigate plasma parameters in the channels of the filaments and to compare them to plasma parameters in the streamers.

3) To study the development of nSDBD in combustible mixtures at elevated pressures. To find the conditions for streamer–to–filament transition. To learn the efficiency of flame initiation in lean mixtures. To compare the ignition by streamer and filamentary nSDBD. To check the efficiency of distributed in space plasma–assisted ignition and interaction of combustion waves at high pressures.

Chapter 3

Experimental equipment and measuring methods

This section provides the description of the experimental facilities used in the present Thesis. Section 3.1 presents the geometry of the electrodes. Three different discharge cells were used to study the discharge in nSDBD configuration. For the experiments in ambient air the classical "flat" electrode system was used. A cubic constant volume chamber with nSDBD in cylindrical symmetry was used for experiments at high (up to 9 bar) pressure. Finally, High-pressure and high-temperature discharge/combustion chamber was developed for experiments at pressures up to 15 bar and high temperatures up to 700 K and also for the combustion experiments. Section 3.2 presents the synchronisation scheme and the description of experimental methods used in the present work: deposited energy and current measurement methods, optical methods of discharge and flame diagnostics including the shadowgraphy, the schlieren, the emission spectroscopy and ICCD imaging techniques.

3.1   Surface dielectric barrier discharge cells

3.1.1   Electrode configurations

Dielectric barrier discharge (DBD) is a discharge originating in a discharge gap at the conditions when at least one of the electrodes is covered by a dielectric layer. The current in the DBD is limited by charging of the dielectric. One of the modifications of DBDs is a surface DBD (SDBD). In this case, the electrode system
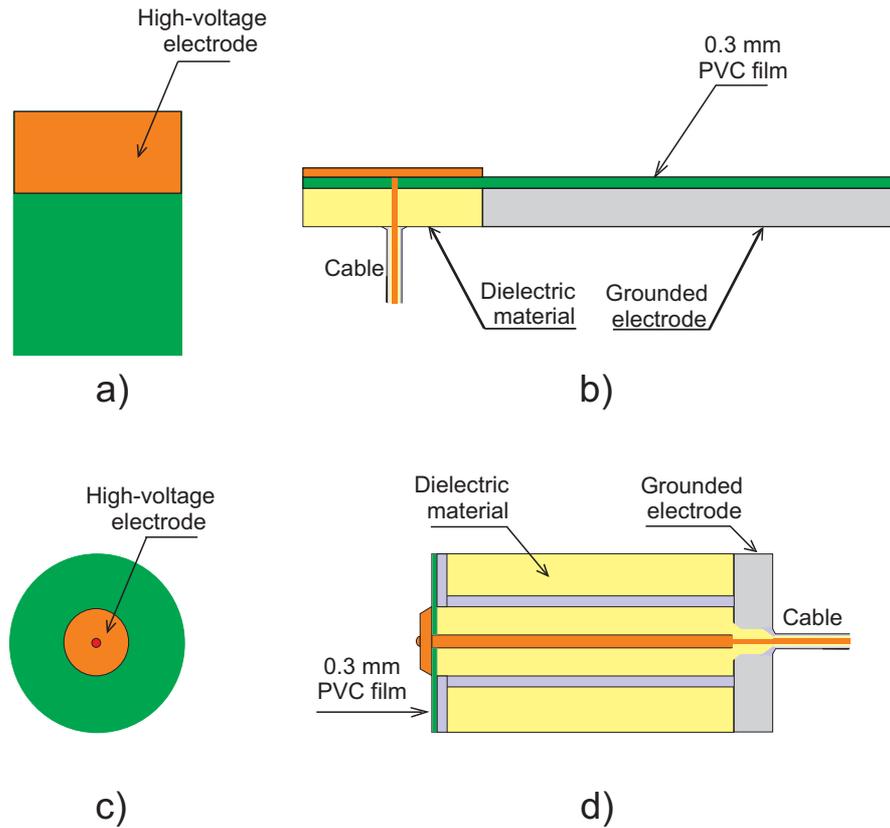
Figure 3.1: Flat electrode system (a),(b) and cylindrical electrode system (c),(d).

has a "sandwich-like" structure, consisting of the low-voltage electrode, covered with a thin (fraction of mm) dielectric layer, and high-voltage (HV) electrode of a smaller surface, glued on the dielectric. The discharge starts from the HV electrode and propagates along the dielectric surface.

The used configurations of the electrode systems are presented in figure 3.1. In a "classical" air-flow control geometry (figure 3.1(a) and (b)) with a metal strip as the high voltage electrode, the SDBD starts as a set of synchronous streamers propagating along the dielectric in the direction perpendicular to the HV electrode. In this case all streamers propagate in parallel. The second, the cylindrical configuration is presented in figure 3.1(c) and (d). The HV electrode has a disk–like shape. In such electrode geometry the discharge propagates in the radial direction from the edge of HV electrode. This configuration was developed for the cylindrical chamber of Rapid Compression Machine [43] for the very first experiments of plasma–assisted ignition with nanosecond SDBD [42].

3.1.2 High-pressure discharge cell

To study the discharge in non–combustible mixture at high pressure the cubic chamber was used. The schematic representation of the high–pressure chamber is demonstrated in figure 3.2. The general view is demonstrated on the top of the figure. The chamber and all flanges are made of stainless steel. The chamber is equipped with three optical quartz windows, with a thickness of 15 mm and a diameter of 50 mm. One optical window is situated in front of the electrode. The imaging of the discharge as well as emission spectroscopy study were performed through the frontal window. Two other windows allow the observation of the discharge from the side. These side windows are used for schlieren and shadowgraphy diagnostics.
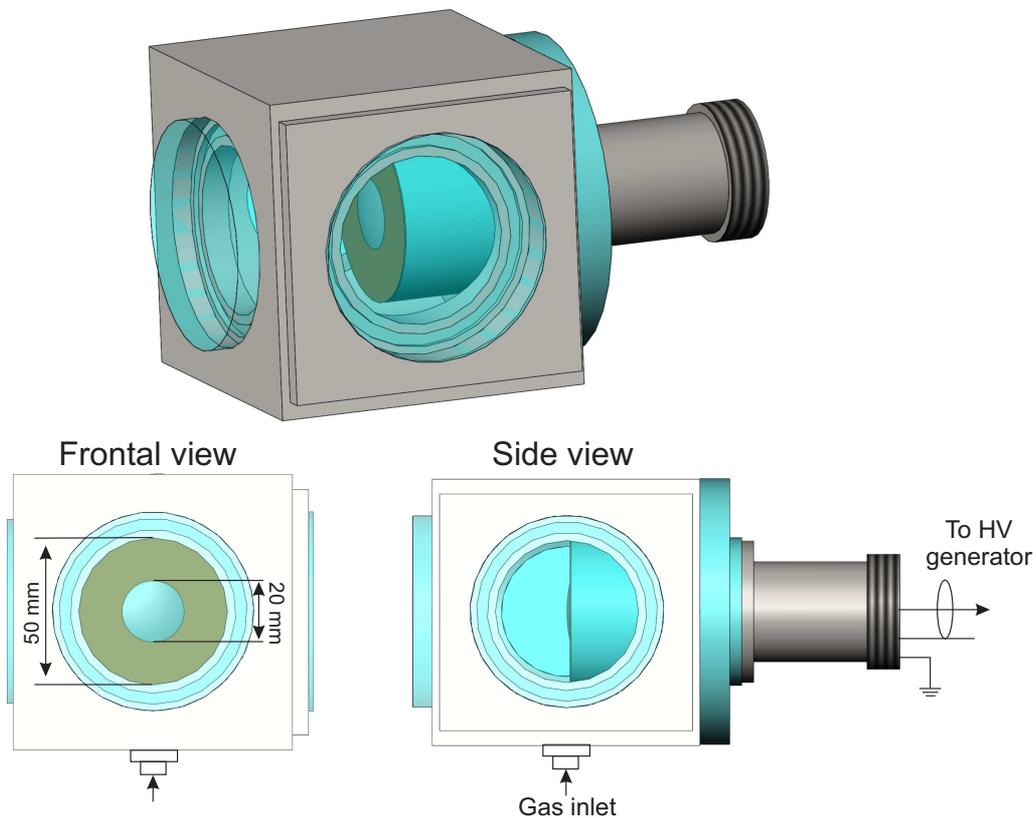
Figure 3.2: Cubic high pressure chamber.

The gas is uploaded from the bottom of the chamber (black arrows in figure 3.2). The system of the gas inlet is described below. The experiments in the cubic high–pressure chamber were performed for ambient temperatures and for gas pressures up to 9 bar.

3.1.3 High-pressure high-temperature plasma/combustion setup

To study the discharge in combustible and non–combustible mixtures at higher pressures up to 15 bar and with possibility of preheating the investigated gas, and also to study consequent ignition of combustible mixtures by nanosecond SDBD under controlled initial parameters, the High Pressure and High Temperature (HPHT) cell was developed. The design of the chamber allows observation of optical discharge emission and at the same time the emission of the flame at initial stage of combustion.
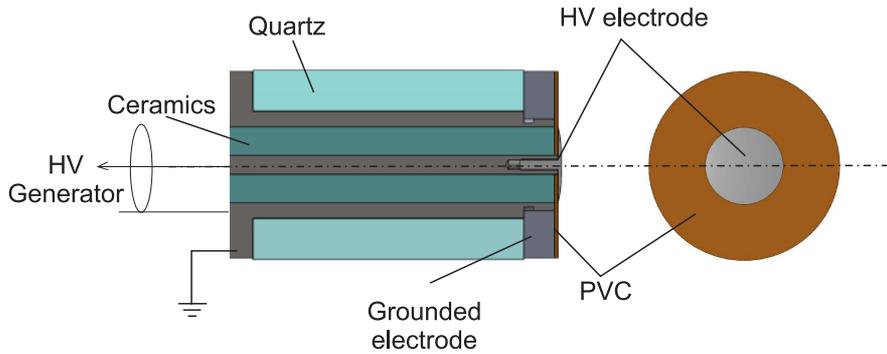
Figure 3.3: Cylindrical SDBD electrode used in HPHT.

Table 3.1: Dielectric constants of used material

Material	Dielectric constant
Silicon glue	(2.8-3.2)
HT silicon glue	(2.2-2.9)
PVC	(3.3-3.5)
Teflon	(2-2.3)
Ceramic (MACOR)	(5.8-6.3)

The coaxial electrode system, similar to the system used in experiments in a HP discharge chamber described in previous section is mounted into HPHT chamber. The details of the electrode system are shown in Figure 3.3. The high-voltage electrode is represented by a segment of sphere 2 cm in diameter and 5 cm of a curvature radius, made of stainless steel. The inner diameter of the low-voltage electrode is equal to the outer diameter of the HV electrode, and the outer diameter of the low-voltage electrode is equal to 48 mm. The cylindrical electrode system used in HPHT cell is adapted for the high temperature experiments. First of all, the
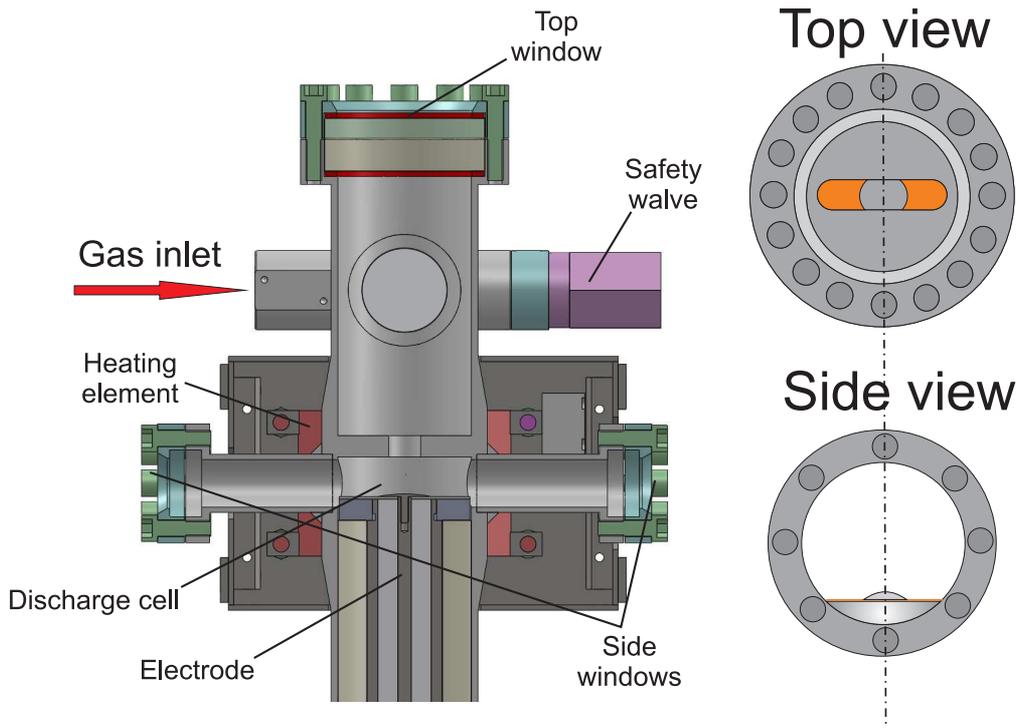
Figure 3.4: The schematic representation of High-Pressure High-Temperature (HPHT) chamber and the views of the flanges (top, side).

dielectric parts made of PVC or teflon in the electrode system shown in figure 3.1(d) were replaced by the identical parts made either of quarts or of ceramic. Depending on the experiments the different dielectric layers separating the high voltage and grounded electrode were used. The dielectric materials used as layer interlayer (glue between the dielectric and electrode) are summarized as a table (see table 3.1). In all cases the thickness of the dielectric layer (dielectric film + glue) does not exceed 0.6 mm.

A scheme of HPHT chamber is shown in Figure 3.4. The walls of the chamber are made of stainless steel. The chamber is surrounded with a heating jacket to keep the initial gas temperature between 300 and 700 K. The temperature is controlled with three thermocouples: two thermocouples of type K (270-1400 K chromel-alumel) are installed directly into the heating jacket to follow the dynamics of heating, and the third one, mounted into the chamber wall, is used to measure gas temperature before the experiment (thermocouple type J 270-1000 K iron-constantan). One more thermocouple can be installed from the side window. This thermocouple (of type J) is used to measure radial profile of the temperature at the distance 0.5 mm above the electrode.

Ignition is initiated in the volume in the center of HPHT chamber indicated as "discharge cell" in figure 3.4. the volume represents a cylinder of 50 mm in

diameter and 15 mm in high. Two quartz optical windows, 10 mm in diameter each, provide a side view. A top view through the 50 mm in diameter top quartz window is partially closed by the upper flange of the discharge cell (see figure 3.4). When the HPHT chamber is filled with a gas mixture under study combustion is initiated by the nanosecond discharge near the lower flange of the discharge cell. All experiments either study of the discharge or plasma–assisted ignition experiments were performed in a single shot regime.

3.1.4 General scheme of the experimental setup and synchronization system

General scheme of the experimental setup

The general scheme of the experimental setup including the gas inlet system, the evacuation system and the discharge and/or combustion cell is demonstrated in figure 3.5. Two different (cubic discharge cell and HPHT cell) chambers are connected to the gas inlet system (GIS) depending on the investigated problem.

The chamber is pumped down to 10^{-2} Torr before filling with gas mixture under study. The pressure of the gas mixture can be up to 15 bar (for HPHT) or 9 bar (for HP cubic cell) in stationary regime. Pressure in the chamber is controlled with three pressure gauges: (1) low pressure detector Pfeiffer Vacuum D-35614 Asslar to control a residual pressure between the experiments; (2) stationary membrane gauge SMC ISE300-01-65 to measure initial pressure before the experiment and (3) KULITE high temperature IS pressure piezo-transducer (XTEH-10L-190 series, with
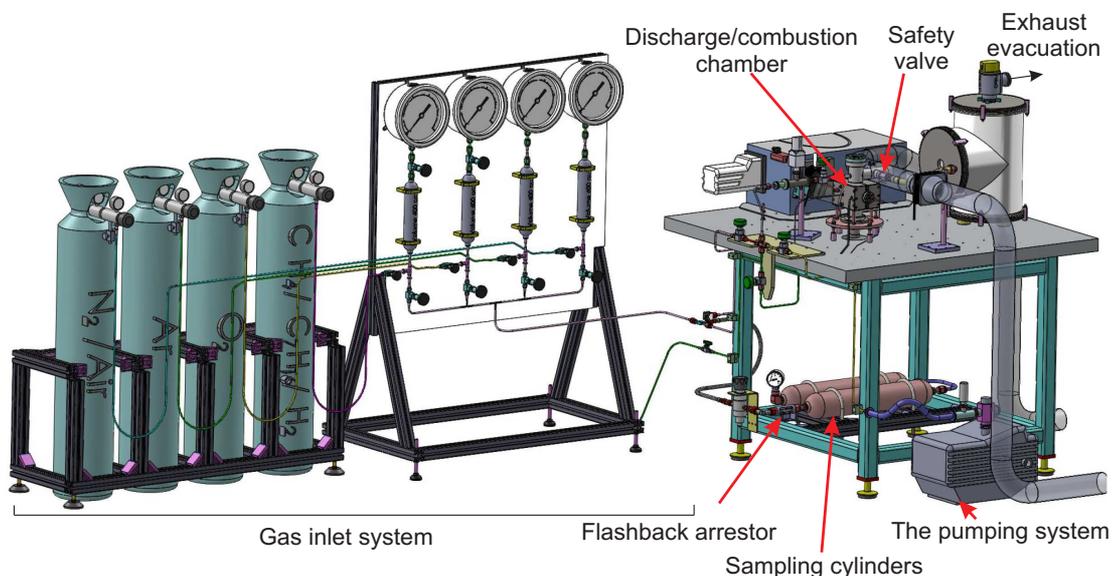

Figure 3.5: The general scheme of the experimental setup (HPHT).

500 kHz natural frequency) to measure pressure profile during ignition processes in the HPHT cell.

During the experiments different gas mixture were prepared using: synthetic air (80% N_2 and 20% O_2), N_2, Ar, O_2, H_2, CH_4, C_7H_{16} gases. The impurities of all gases do not exceed 3 ppm. The gas mixtures were prepared in the sampling cylinders (P_{max} = 20 bar). For combustion experiments the system is equipped with a safety valve through which the burned gas was transmitted to the exhaust collector. The flashback arrestor, installed on the sampling cylinders, prevents the flame penetration into the latter.

Synchronization scheme

All experiments presented in the Thesis were performed in a single–shot regime. The scheme of synchronization is shown in figure 3.6. All electrical signals (BCS signals, pressure transducer) and optical signal from the photomultiplier (PMT) were registered by two LeCroy WaveRunner 600MHz oscilloscopes, separately for nanosecond and for millisecond time scale. The optical emission of the discharge/flame was obtained with the ICCD camera or with the PMT. To study the temporal behavior of selected molecular bands, monochromator ANDOR SR-300i with 600 l/mm grat-
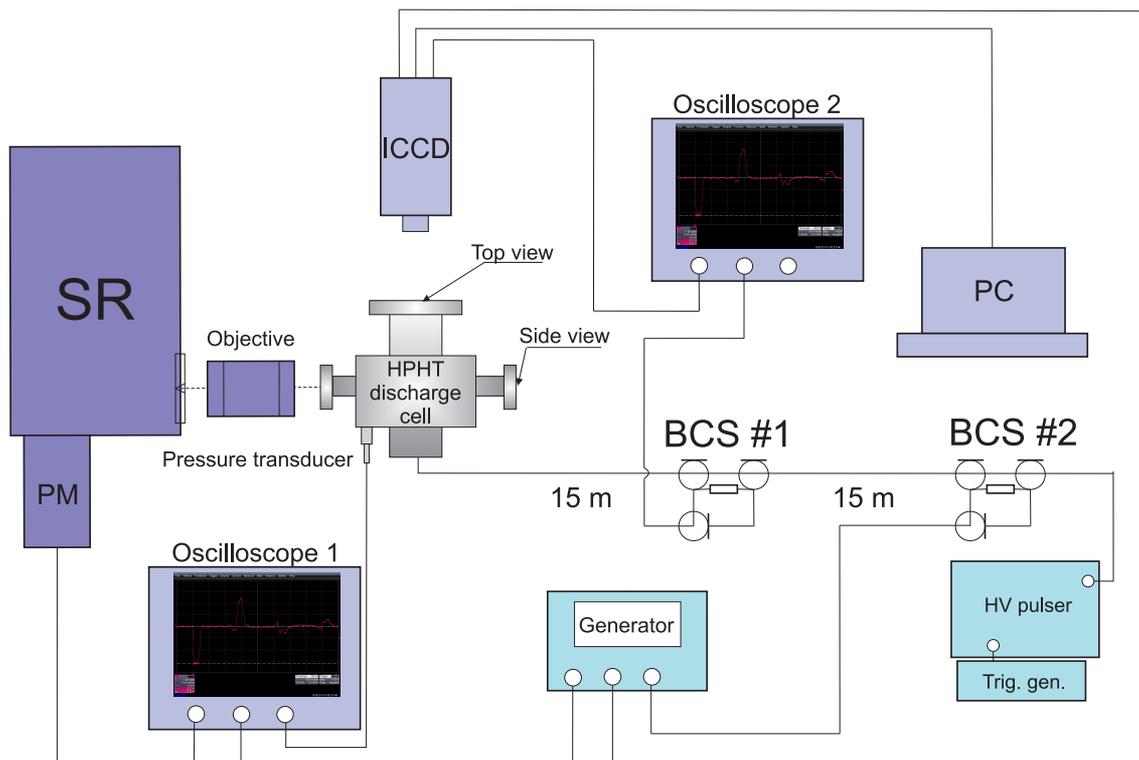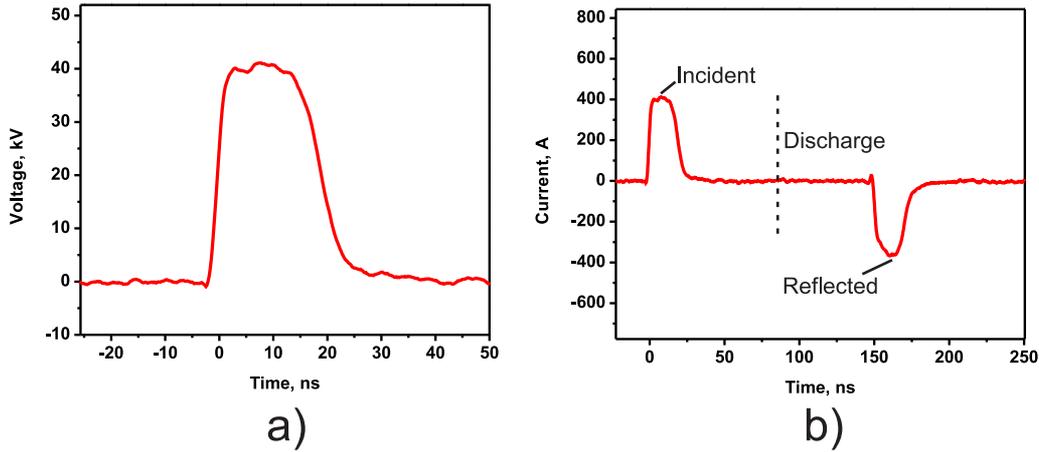

Figure 3.6: **Synchronization scheme. SR - spectrograph, ICCD - PiMax 4 ICCD camera, PM - Photomultiplier tube, BCS - back current shunt.**

Figure 3.7: Applied and reflected HV pulses. The oscillogram is obtained with BCS1 installed in the middle of 30 m coaxial cable.

ing combined with H6610 photomultiplier tube (Hamamatsu) was used. To study the detailed structure of the discharge and flame the ICCD imaging (see details below) was used.

The high-voltage pulses of positive and negative polarities with 2 ns rise time and 10-30 kV amplitude (see figure 3.7(a)) were generated by a commercial pulsers FID Technology, FPG20-03PM and FPG20-03NM. The pulse is transmitted to the electrode system via 50 Ohm high voltage coaxial cable. Two calibrated custom made back current shunts (BCS) are soldered in the shield of the cable: one, BCS1 in the middle of the cable, and another, BCS2 1 m apart from the FID generator (see figure 3.6). The length of the cable, 30 m, is selected to separate the incident pulse and the pulse, reflected from the discharge cell, on the BCS1 shunt (see figure 3.7(b)). The BCS1 is used to measure pulse shape and absolute values of electrical current. The energy deposited into the plasma is calculated as a difference between the energies stored in the incident and in the reflected pulses taking into account energy losses in the cable and the losses on charging of the electrode system. The details of the technique can be found elsewhere [60]. The BCS2 is used to synchronize optical diagnostics with the discharge.

3.2   Experimental techniques

3.2.1   Voltage, current and energy deposition measurements

Voltage in the cable is measured via BCS1. The signal corresponds to the current passing through the outer sheath of coaxial cable. According to the distributed

element model, the current passing through the core and sheath of coaxial cable are equal to each other in magnitude but they have different sign. The back current shunt is represented as a set of 14 resistors of 2.2 Ohm each, soldered in parallel into the sheath of the cable. A typical oscillogram obtained with BCS1 including incident pulse produced by FID high voltage generator and consequent reflected pulse from the electrode system is presented in figure figure 3.7(b)). The amplitude of the incident and reflected waves are related as:

$$\frac{U_{\text{ref}}}{U_{\text{inc}}} = \frac{Z - Z_0}{Z + Z_0}, \tag{3.1}$$

where Z_0 - the impedance of the cable (50 Ω), Z - the impedance of the load on the end of the cable.

To distinguish in time the incident and reflected pulses the following conditions must be fulfilled:

$$L \geq \frac{c_{el}\tau}{2}, \tag{3.2}$$

where L - the distance from the discharge cell (end of the cable) to BCS. τ - pulse width, c_{el} - the velocity of EM signal propagation in the cable (for the 50 Ohm coaxial cable used in present work $c_{el} = 0.2$ m/ns).

BCS1 was calibrated experimentally. The gate-shape pulses produced by TGP110 generator were applied to the exit of coaxial cable and were registered with oscilloscope from BCS1. The division coefficient acquired experimentally coincides quite well with calculated one:

$$K = \frac{Z_0 N_{res}}{R_{res}} = \frac{50 \cdot 14}{2.2} = 318.18, \tag{3.3}$$

$$K_{exp} = \frac{V_0}{V_{BCS}} = \frac{2.12}{0.006.7} = 316.4. \tag{3.4}$$

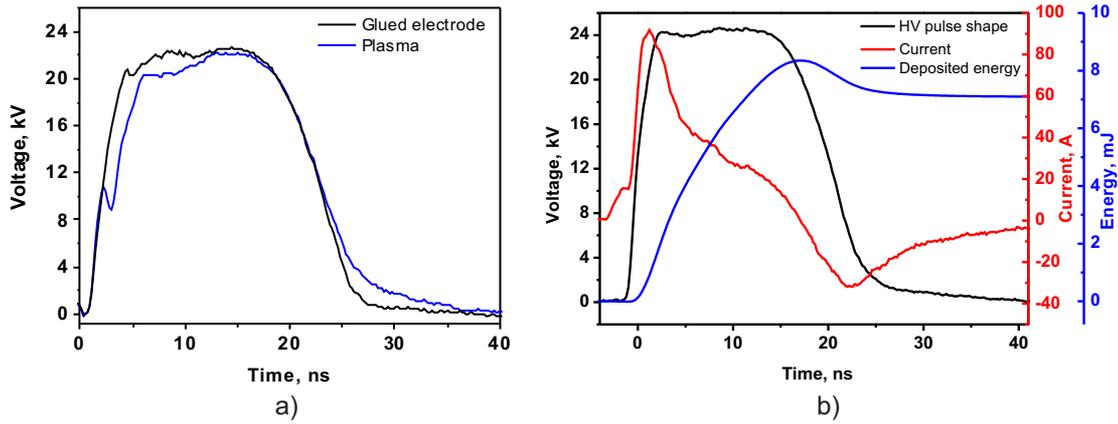The voltage and current of the signal propagating in the long coaxial cable are coupled with the expression :

$$U = I \cdot Z_0, \tag{3.5}$$

The corresponding power of the pulse is:

$$P = I \cdot U = \frac{U^2}{Z_0}, \tag{3.6}$$

therefore the energy of the pulse of any shape can be calculated as:

$$W = \int_0^\infty \frac{U^2(t)}{Z_0} dt. \tag{3.7}$$

Figure 3.8: Measured with BCS1: (a) reflected pulses from the electrode system with discharge generation and from glued electrode system (no plasma); (b) applied voltage, current and energy deposition.

Finally, the total energy that is consumed by plasma while discharge is produced can be measured as a difference between the energy of incident pulse and reflected one taking into account losses in the cable during the HV pulse propagation and charging of the electrode system capacity:

$$W_{dep} = W_{inc} - W_{ref} - W_{losses} = \int_0^{\tau_{pulse}} \frac{U_{inc}^2(t)}{Z_0} dt - \int_0^{\tau_{ref}} \frac{U_{inc}^2(t)}{Z_0} dt - W_{losses}, \quad (3.8)$$

where W_{inc}, W_{ref}, W_{losses} are energy of incident pulse, energy of reflected pulse, energy dissipated in the cable and energy of capacity charging, respectively. All losses and energy of capacity charging can be measured together, without plasma generation. Two possible methods can be applied to do it: i) the electrode system can be covered with few mm silicon layer, or ii) the discharge cell can be pumped down to the pressure $\sim 10^{-3}$ bar. In the second case we are in the conditions of the left branch of Paschen's curve where breakdown voltage increases dramatically with pressure decrease and no discharge is observed. The difference between the energies of incident and reflected pulses is equal to W_{losses} and practically gives the same values for the conditions i) and ii).

The current in the discharge can be calculated in the following way. If we consider two cases: i) with plasma and ii) without plasma ("glued" electrode or pumped chamber) then the current of capacity charging and current in the discharge can be determined as:

$$I_{capacity} = \frac{U_1^{inc} - U_1^{no}}{Z_0}, \quad (3.9)$$

$$I_{capacity} + I_{discharge} = \frac{U_2^{inc} - U_2^{discharge}}{Z_0}. \tag{3.10}$$

For the same applied voltages $U_1^{inc} = U_2^{inc}$. Subtracting the first equation from the second one we get:

$$I_{discharge} = \frac{U_1^{no} - U_2^{discharge}}{Z_0}. \tag{3.11}$$

Thus the discharge current can be calculated as a difference between reflected pulses from the discharge cell with and without plasma generation. The characteristic oscillograms of the reflected pulses from "glued" electrode and from the electrode producing discharge are presented in figure 3.8(a). The characteristic energy deposition and current shape are presented together with applied HV pulse in figure 3.8(b).

3.2.2 ICCD imaging of the discharge and flame propagation

To study the spatial structure and the development of the discharge and of the following combustion, the images of the discharge and/or combustion patterns were obtained with Pi-Max4 Princeton Instruments ICCD camera with Edmund Optics 50 mm FL high resolution lens. Three types of images were acquired and analyzed: (i) time resolved images (camera gate $0.5 - 2$ ns); (ii) integrated over the pulse width (camera gate $20 - 50$ ns); (iii) the images of flame propagation (camera gate $10 - 200$ μs). The camera was triggered externally and the trigger of the camera was synchronized with the discharge initiation via BCS2. The TGP110 generator was used to transform the irregularly–shaped signal from the BCS to a long ~ 1 μm TTL signal, that is sent to the input trigger of the ICCD camera. The camera has its own internal nonregulated delay that is equal to 31.2 ns. The length of the cables connecting the camera, TGP110 generator and BCS2 shunt should be selected correctly in order overpass this internal unchangeable camera delay.

3.2.3 Optical emission spectroscopy

The main part of the results presented in the present work was obtained with optical emission spectroscopy. The spectra of the discharge and of the flame were acquired in the wavelength range $200 - 800$ nm. To collect the radiation in the considered wavelength the ACTON SP-2500i Princeton Instruments Spectrometer has been used. The spectrometer is based on the Czerny-Turner optical scheme that has two outputs: first, the micrometer centered entrance slit ; and the second is the socked for ICCD camera. The spectrometer is equipped with three diffraction

gratings 600 (blaze on 300 nm), 1200 (blaze on 500 nm) and 2400 (blaze on 240 nm) lines per mm. The nominal dispersion of the optical system is 0.5 nm/mm and 0.006 nm/pixel.

The very important parameters, which can be acquired with emission spectroscopy, are rotational, vibrational and electronic temperatures. The spectra of a few certain molecular bands were analysed during in the present work: different electro–vibro–rotational bands of second positive system of molecular nitrogen corresponding to the transition $N_2(C^3\Pi_u)(\nu')\rightarrow N_2(B^3\Pi_g)(\nu'')$; the emission of hydroxyl radical corresponding to the transition $OH(A^2\Sigma^+$, v'=0 $\rightarrow X^2\Pi$, v''=0) on the wavelength 307 nm and the emission of the cyano radical $CN(B^2\Sigma^+) \rightarrow CN(X^2\Sigma^+)$ in the wavelength range $382 - 389$ nm. The rotational and vibrational temperatures were measured by fitting the experimental spectra with the calculated ones. For this purpose the SPECAIR [104, 105] software was used.

3.2.4 Schlieren and shadowgraphy methods

The ordinary detectors and cameras cannot distinguish the phase difference in a light beam. Using PMT tubes and CCD/ICCD devices it is possible to get the information only about the intensity, contrasts and in some particular cases - polarization. However, the schlieren and shadowgraphy methods transform the phase difference into amplitude of the detected light, since the light passes through the transparent medium its propagation speed depends on refractive index of this medium $n = c_0/c$, where c is a light speed in the considered medium, c_0 is a light speed in vacuum.
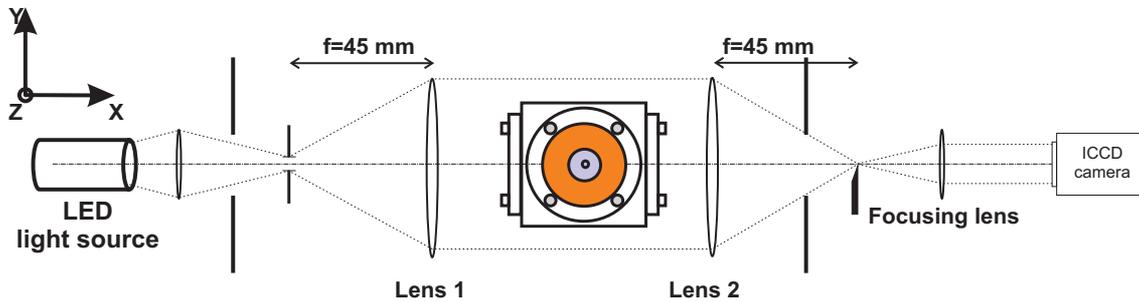
Figure 3.9: Scheme of schlieren system.

Schlieren method is widely used for visualisation of optical inhomogeneities in transparent refractive media [106]. This method was for the first time realized by A. Toepler. The detailed explanation of schlieren method can be found elsewhere [106, 107], the base formulas used in this work will be described during the data analysis. A classical two–lens schlieren photography system was used for visualising the hydrodynamic perturbations produced by nanosecond surface dielectric

barrier discharge at high pressures in cubic HP chamber. The scheme of the schlieren system is shown in figure 3.9. The nSDBD discharge produces the compression wave propagates from the plane of electrode system. While propagating the wave causes the local changes of gas density that lead to inhomogeneities of the refractive index. The schlieren images were captured by a Pi-Max4 ICCD camera. Two 45 mm focal length lenses were used in the systems. As a light source the Thorlabs LED M505L3-C at 505 nm central wavelength and 30 nm bandwidth was used. The results of schlieren analysis of the discharge at high pressures are presented in chapter 5.
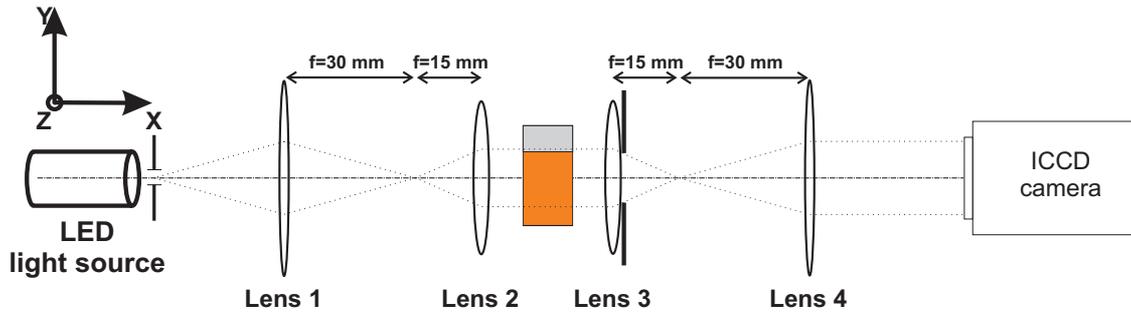
Figure 3.10: Scheme of shadowgraphy system with 2x magnification.

As it was mentioned above, for the experiments in atmospheric air, the discharge was produced in "flat" SDBD configuration. The hydrodynamic perturbations as well as the discharge itself was detected by the shadowgraphy system with 2x magnification presented in figure 3.10. This system provides a spatial resolution of 7 μm/pixel and temporal resolution of 0.5 ns. Such high spatial resolution has been used for visualizing the fine structure of the surface streamers and the hydrodynamic effects, characterizing the local heat release, in the very proximity to the edge of high voltage electrode. The results of the measurements are presented in chapter 4.

Chapter 4

Nanosecond surface dielectric barrier discharge at atmospheric gas density

The extensive study of nanosecond surface DBD lasts already more than a decade. Originally a deep interest was caused by application of SDBDs for control of laminar-to-turbulent transition and for separation of boundary-layer zone in aerodynamic applications [1, 2, 108, 109]. The flat SDBD configuration that is described in this section is called "classical air-flow configuration", because this is the configuration that has been first proposed for air flow control. Further it was suggested to use the non–equilibrium plasma for PAI. And for the very first time the experiments of PAI with nSDBD and the comparison with nanosecond spark were performed in [5].

Despite the fact that nSDBD has been investigated during long time, some questions remain open. They are streamer structure difference of positive and negative polarity, why and how streamers stop, the physics of return stroke appearing at the trailing edge of high-voltage pulse and so on. The importance of these unanswered questions is aimed at forming the complete picture of processes and physics of nSDBD. A full understanding of what is happening will give an opportunity to extract the information concerning the nature of instabilities in SDBDs and to transform nSDBD to filamentary mode, that is discussed in chapter 5.

The first part of this section is devoted to the experimental investigation of nSDBD in flat electrode configuration in ambient air. The discharge propagation, intensity of the discharge of both polarities as well as energy deposition and energy release during the discharge and in the afterglow are described here. The influence

of the geometry on discharge structure is also analyzed.

4.1 nSDBD in classical air-flow control configuration. General characteristics and morphology

A typical flat SDBD geometry or so-called classical airflow configuration was chosen for investigation because of its simplicity and because of the possibility to compare the experimental results and calculations for 2D approximation. The SDBD electrode is constructed in the following way: the dielectric layer (PVC film, $\varepsilon \approx 3$) of 0.3 mm thickness is glued (by a silicon sealant, $\varepsilon \approx 3$) on the metal bar that serves as a grounded electrode. The copper strip with a thickness of 0.1 mm is attached to the dielectric surface (see figure 4.1). Two electrode systems with different widths, 25 and 50 mm marked as W in figure 4.1(a), are considered below.

The nanosecond surface barrier discharge develops as a set of streamers propagating synchronously and in parallel. In general, surface streamers represent a complex 3D structure with strong gradient of electric field and electron density in the direction perpendicular to the surface. Despite the fact that the integral characteristics, like velocity of propagation on ICCD imaging, are widely presented in the literature [13, 26, 110], still there is a lot of knowledge to extract from the experimental data about energy deposition, heating or spectral characteristics with a sub-nanosecond resolution. Furthermore, a self-consistent set of experimental data is of particular interest for specialists involved in discharge modeling.
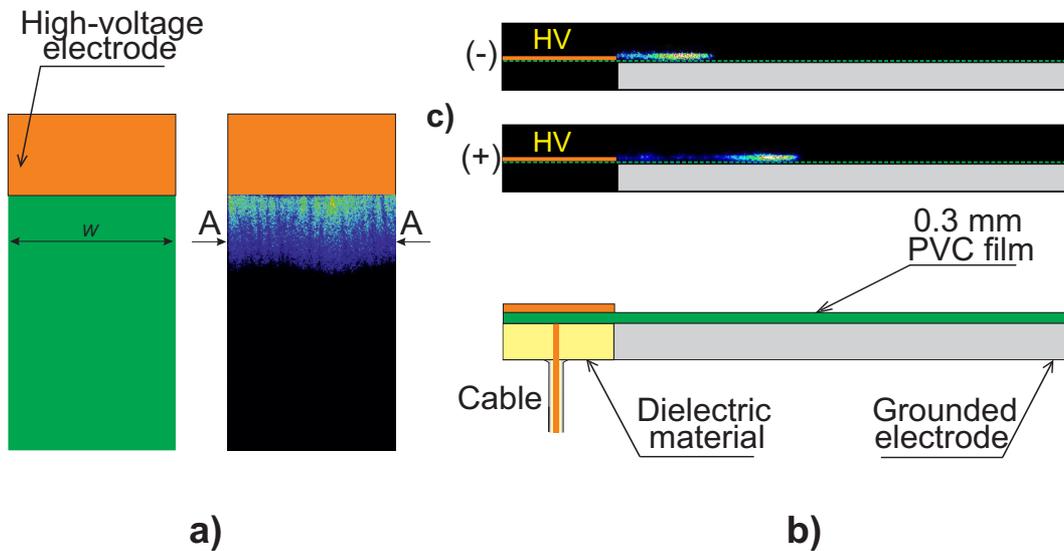
Figure 4.1: Scheme of the electrode system in flat air–flow geometry: (a) frontal view; (b) side view; (c) side view of the discharge propagation.

So, the discharges propagate as a set of parallel streamers (see figure 4.2) along the surface of dielectric layer. The dimensions of the streamers and their velocities of propagation are different in the case of positive and negative polarity. The mechanisms of anode- and cathode-directed streamers formation and development are fundamentally different and are the cause for the discussions of various groups involved in the modeling. First of all lets analyze how the nanosecond SDBD is described by the various theoretical works [14, 15, 17, 27, 41].

The dynamics of the anode-directed or negative polarity streamer basically consists of the formation of the cathode layer that is formed on the vicinity of high–voltage (HV) electrode of negative polarity (cathode). From the very beginning electrons collide with heavy particles producing the electron avalanche and causing the photon flux in the direction of the discharge propagation. The photon flux generates secondary electrons. The presence of the photoemission is a fundamental issue for the discharge propagation. Without photoemission the discharge would be too slow comparing with the experimental data [16].

The mean reduced electric field strength and electron density in the channel of negative streamer are about 100 Td and $(2-5)\cdot10^{13}$ cm^{-3} respectively [17, 46]. These values are determined by the equilibrium between the rates of electron attachment and ionization. Because of this equilibrium the effective multiplication coefficient of the electrons is close to 1. At the same time the conductivity of the negative streamer remains relatively high. Thus, the anode-directed streamer is a non-self-sustaining structure. Electrons from the channel sustain its propagation. The main source of electrons is the cathode layer.

The main difference of the positive and negative polarity streamers is the field values in the streamer channel. If E/N remains quite high (~ 100 Td) along the entire length for the negative streamer, for the positive one it decreases practically to zero behind the streamer head. Photoemission is essential for the cathode-directed streamer development along the dielectric surface. The main source of photons is in the streamer head. Photons, reaching the dielectric surface in front of the streamer, produce electrons from the near dielectric region. These electrons move upwards and reach their maximum density in the streamer head. Electron collisions with heavy particles not only multiply the electrons number but also generate new portion of photons. The photons reach the dielectric surface and so on, forming the positive feedback. This feedback supports the propagation of the cathode-directed streamers. Therefore, the positive streamer is a self-sustaining phenomenon and does not need any additional electron source for the development. Moreover, the streamer head is a powerful source of electrons, which is more efficient than the cathode layer for negative polarity streamer. According to simulation results [17] the electron density in the channel of positive polarity streamer is about $2\cdot10^{14}$ cm^{-3}.
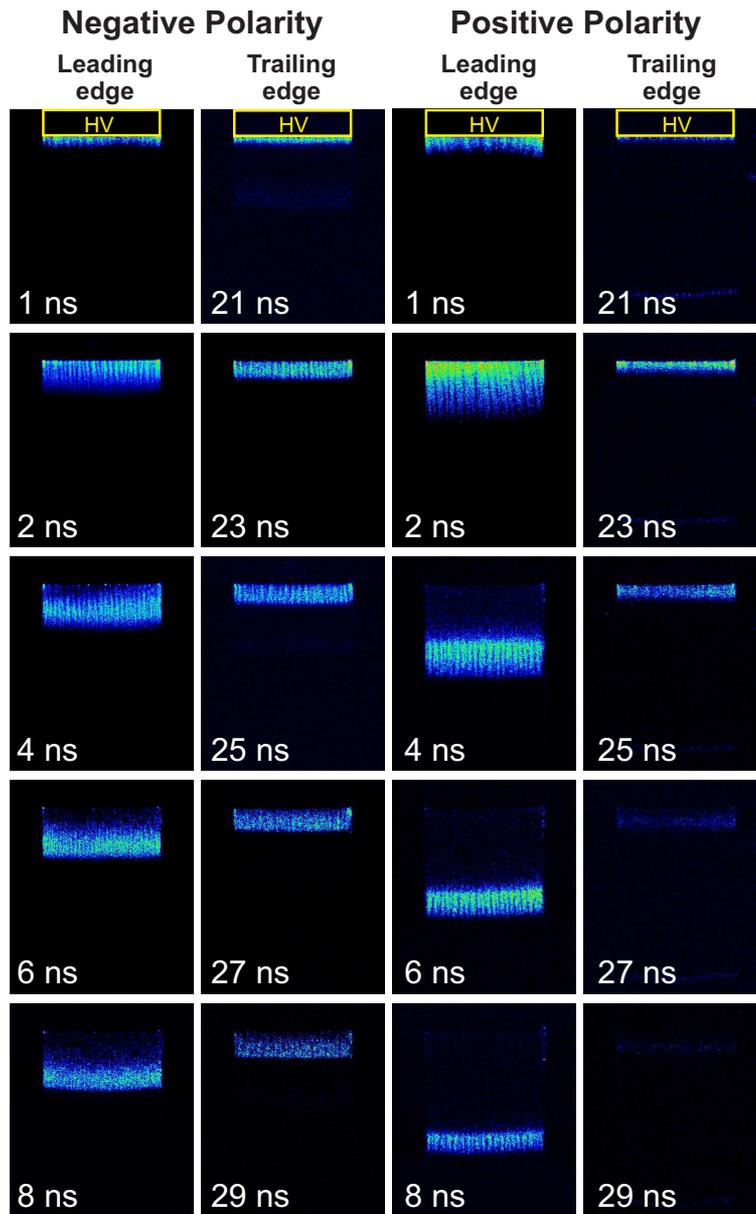
Figure 4.2: ICCD images for the discharges of positive and negative polarities (frontal view). Discharge in ambient air, voltage amplitude on the electrode is $U = +24$ kV, $P = 1$ bar, ICCD camera gate is 1 ns. Width of the electrode system is 2.5 cm.

The ICCD images of the discharge development are presented in figure 4.2. The diameter of the streamers of positive and negative polarity are different. For positive polarity pulses the diameters are $1.5 - 2$ times higher than for negative polarity streamers. These diameters hardly depend on the applied voltage. The velocities of discharge are also different. As one can see, 4 ns after the discharge start positive polarity streamers pass the distance almost 2 times longer than the negative polarity

streamers. For the trailing edge of the discharge, the return stroke propagates at longer distance for the case of negative polarity streamers. Streamer structure of the discharge is clearly seen for the second stroke of negative polarity, whereas for positive streamers the second stroke seems to be more diffuse. The nature of the second or return stroke will be described below. The most general statement can be formulated as follows: the discharge morphology is related to the direction of electron flux. If the electrons move from the HV electrode, the discharge is more diffuse, whereas they move toward the HV electrode, the discharge channels are well pronounced.

The thickness of the steamers depends on a few parameters, such as applied voltage (a magnitude of the applied voltage determines the longitudinal and transverse dimensions of the structure of the electric field), polarity of applied pulses, pressure of the gas where the discharge is initiated, material of the dielectric layer etc. To determine the thickness of the fine structure of streamers with high precision is a challenging task because of complex collective structure of the discharge and the existence of a nonzero correlation between streamers [111]. The typical side view of the discharge propagation is presented in figure 4.3. The thickness of the discharge does not exceed 0.5 mm, that correlates well with previous works [10, 13, 26].
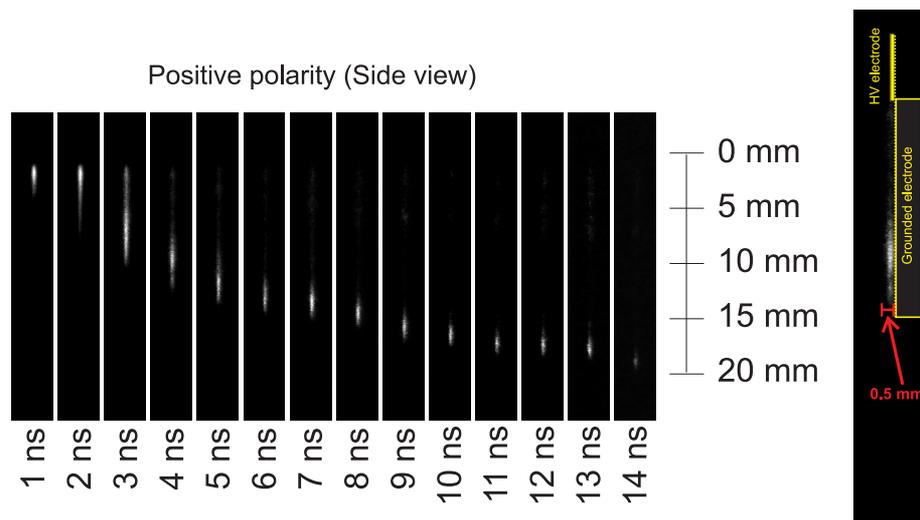
Figure 4.3: Positive polarity streamers propagation (side view); $U = +24$ kV, ambient air.

The experiments in this paragraph were performed for two electrodes of different dimensions in the air–flow configuration. The widths of the HV electrodes were equal to 2.5 and 5 cm. Figure 4.4 demonstrates an integral ICCD image of the discharge in the configuration with 5 cm electrode width. It is clearly seen that the negative polarity discharge stops at the certain distance from the HV electrode, whereas the positive streamers propagate much longer. We know that positive streamers are self–

sustained structures that propagate for a rather long distance (several cm) without any connection to HV electrode, the charged species are basically generated in the head of streamer. The image of the positive polarity discharge shown in figure 4.4 demonstrates that. It is clearly seen, that discharge of positive polarity propagated to the distance a few times longer comparing to the propagation length of negative polarity. More than that, we see that the luminescence intensity decreases gradually with distance from the high voltage electrode. We do not see the sharp intensity drop corresponding to the streamers stop. That confirms the hypothesis of self–sustained mechanism of positive streamer development.
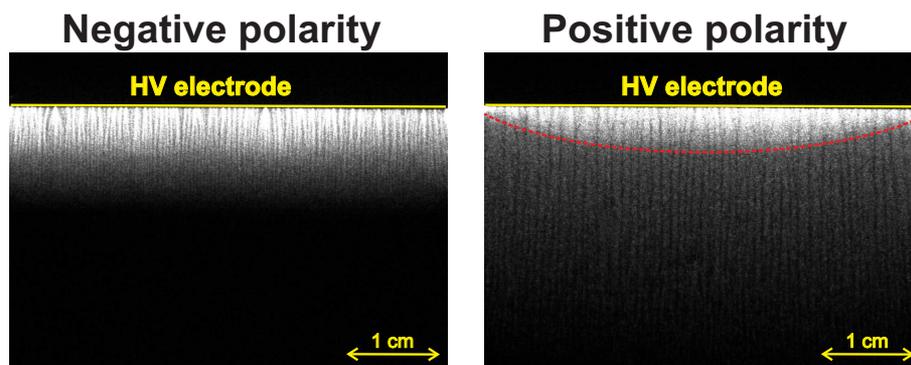
Figure 4.4: Integral ICCD images of positive and negative streamers. Camera gate is 50 ns. Width of electrode system is 5 cm.

One more important point must be taken into account for the electrode system with 5 cm width. Both positive and negative polarity discharge have a flat front propagating from the HV electrode during the leading edge and on the plateau of the HV pulses. However, the shape of the discharge fronts are different for second stroke at the trailing edge of the HV pulse. For the case of positive polarity, the shape of the front of the second stroke is not flat anymore. The front is formed in the central part of the high voltage electrode, and then is pulled along the edge of electrode to form a front with finite radius of curvature. It can be seen even at integral ICCD images represented in figure 4.4, the middle part of HV electrode for positive polarity is brighter than the edge regions. The red dashed curve underlines this effect. It can be caused by edge effects that can play an important role when the width of electrode system increases. With an even greater increase in the size of the electrode system the front of the first stroke of the discharge will become less and less flat as well. For bigger electrode systems (a few meters), this effect will be seen as a traveling wave of the discharge along the edge of HV electrode [112]. When the negative polarity pulses are used to generate the discharge, the front of second stroke remains flat. As it was demonstrated in [7], the energy deposition is concentrated near the edge of HV electrode. Therefore, the negative nSDBD might
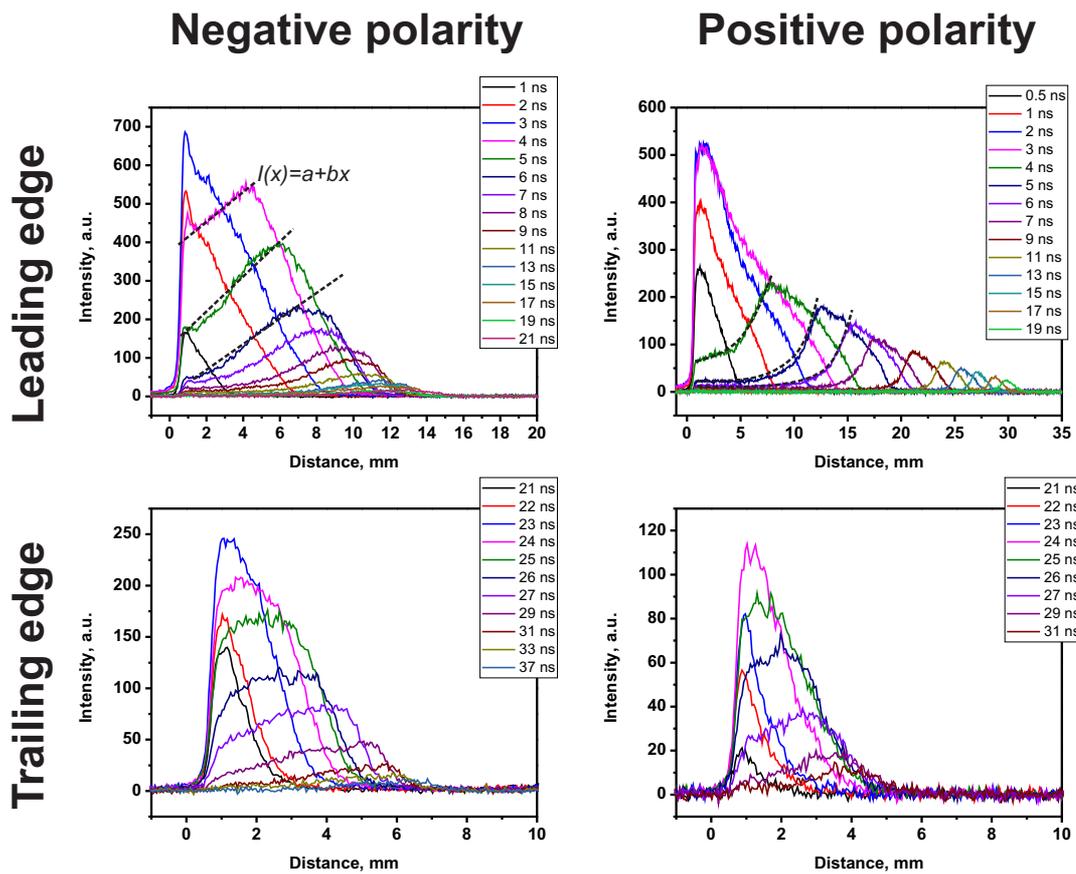
Figure 4.5: Profiles of the discharge intensity at different time instances for negative and positive polarity of applied pulses. Upper line corresponds to first stroke of the discharge. Lower line corresponds to second stroke. Width of electrode system is 2.5 cm. Voltage amplitude $|U| = 24$ kV.

be a more efficient tool for the control of the laminar-turbulent transition.

Further information can be obtained from the quantitative analysis of emission profiles. A spectral sensitivity of the ICCD camera used in experiments is in the range $300 - 800$ nm. In this spectral range the spectrum consists mainly of bands of the second positive system of molecular nitrogen, $N_2(C^3\Pi_u)$–$N_2(B^3\Pi_g)$ transition. The efficient lifetime of $N_2(C^3\Pi_u)$ state is caused by quenching on molecular oxygen and equal to 0.7 ns at atmospheric pressure [46], limiting the resolution of ICCD images. Intensity of mentioned transition indirectly gives the information about combination of electron density with electric field as well as the information about conductivity of the channels.

The intensity profiles of the discharge in the direction of its propagation are presented in figure 4.5. These profiles correspond to the discharge propagation at positive and negative polarity of applied pulses. It is clearly seen that starting from
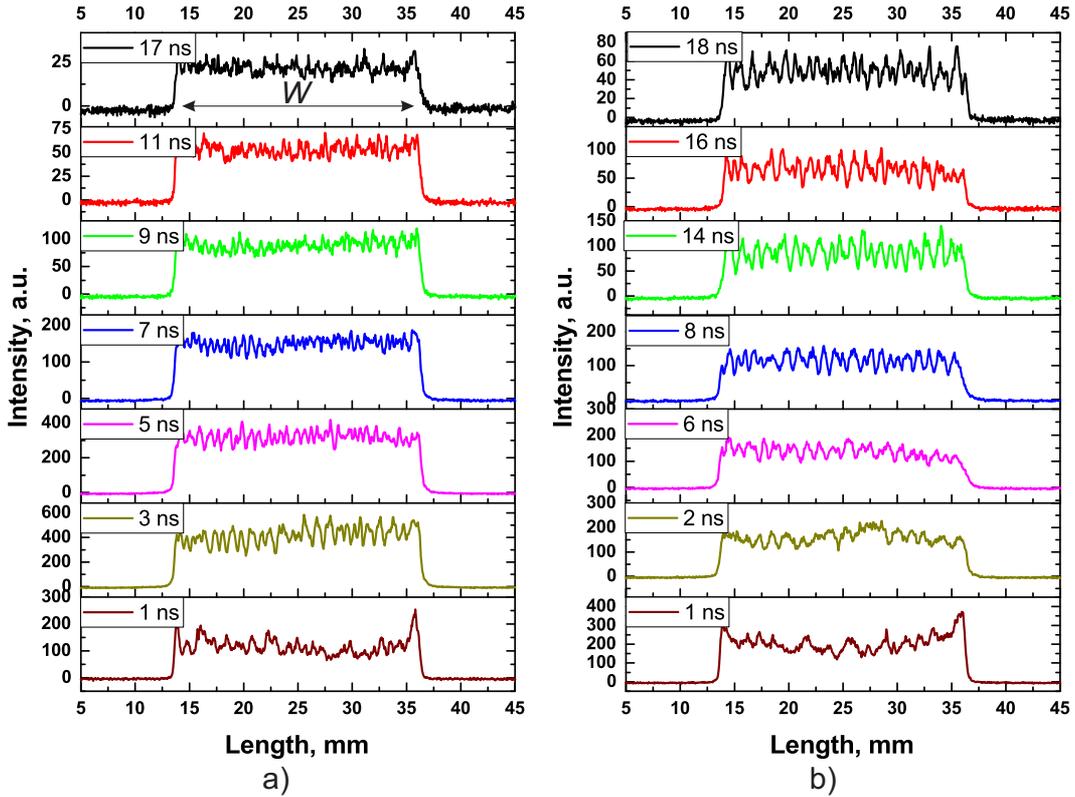
Figure 4.6: Intensity profiles along the line AA (see figure 4.1) across the streamers. (a) Negative polarity; (b) Positive polarity. Width of the electrode system is $W = 2.5$ cm. Voltage amplitude $|U| = 24$ kV.

~ 4 ns the shapes of the profiles differ dramatically for different polarities. For negative polarity streamers, the intensity along the channels in the first approximation can be represented as a linear function $I(x) = a + bx$ from the near HV electrode region to the streamer head. For positive polarity streamers, a sharp drop of intensity along the channels is observed. Direct excitation of $N_2(C^3\Pi_u)$ level by an electron impact demands at least 11.03 eV of energy. So, it is possible to conclude that, behind the streamer head, electric field in the streamer body is higher for negative polarity than that of positive polarity. This fact is in correlation with numerical modelling [17,27] reporting close to zero electric field in the body of positive polarity streamer.

The shape of intensity profiles corresponding to the trailing edge of applied pulses seems to be similar for both polarities. However, the absolute value of the maximum intensity and the length of propagation of return stroke are different. The intensity is approximately two times higher for negative polarity. It means that the current and/or reduced electric field is higher for second stroke of negative polarity streamers.
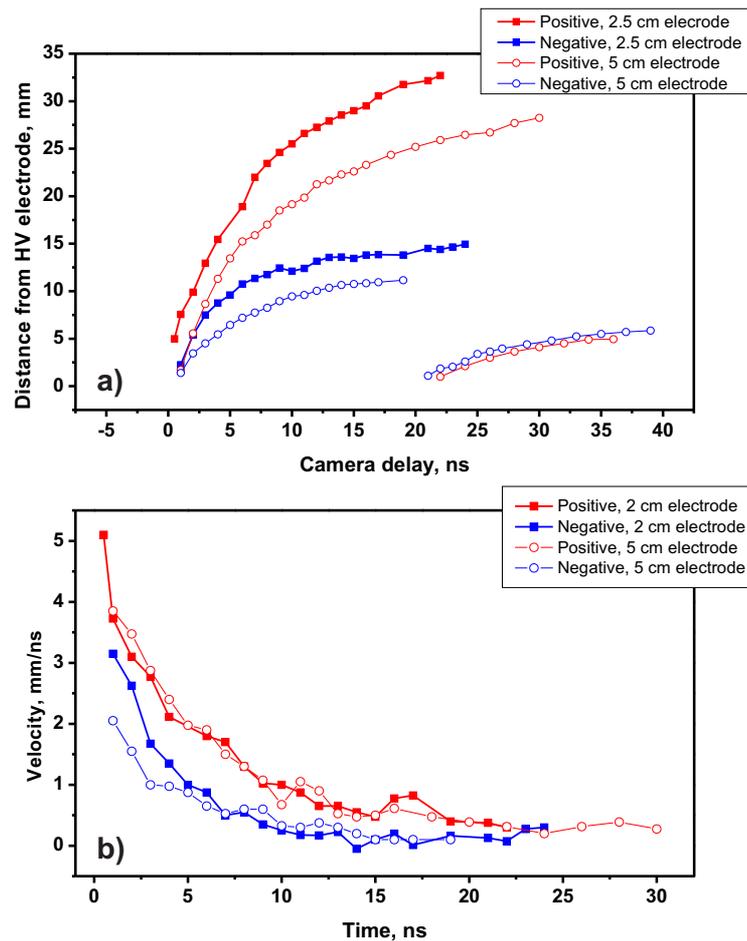
Figure 4.7: (a) x-t diagrams of the discharge propagation for two configuration of electrode system with 2.5 and 5 cm of HV electrode width; (b) velocities of discharge propagation for electrode systems with 2.5 and 5 cm of the HV electrode width.

The intensity of the discharge across the direction of the propagation is demonstrated in figure 4.6. Each profile is averaged over 2 mm of the length of streamer. The diameters of the streamer body and/or streamer head were measured for the amplitude of the voltage ± 24 kV on the high–voltage electrode. The diameters of streamers change monotonically with time or distance from the HV electrode from 0.68 ± 0.2 mm to 0.38 ± 0.2 mm for positive polarity and from 0.3 ± 0.2 mm to 0.26 ± 0.2 mm for negative polarity of applied pulses. The structure of the front part of the negative polarity streamers become diffuse $9 - 11$ ns after the discharge start. Whereas, well pronounced channels structure is seen for the positive polarity streamer even at 18 ns time instance. As it was mentioned above, in the return stroke of the discharge the situation is reverse: for positive polarity pulse, the discharge is more diffuse.

The x-t diagrams and velocities of streamer propagation for electrode configuration with different width are demonstrated in figure 4.7(a,b). It is clearly seen that the velocities of the discharge of both positive and negative polarity practically does not depend on the width of electrode system.

The velocities of the discharge propagation as a function of time are presented in figure 4.7(b) for both electrodes (25 and 50 mm) and both polarities. The velocity does not depend on the electrode size but considerably depends on polarity of applied pulses. The velocities of positive polarity discharge are almost two times higher than that of negative polarity. It can be explained by the fact that for positive polarity streamers the main source of electrons is a streamer head, while for negative polarity streamers it is a cathode layer. For cathode-directed streamer the electric field in the head is much higher than that in the head of the anode-directed, negative polarity discharge. The high E/N values (up to 2000 Td) in the discharge front produce electrons and positive ions in the streamer head sustaining high electric field during the propagation at far enough away distance from the high-voltage electrode. For negative polarity streamers the situation is inverse. High electric field is "locked" in the near cathode region and decreases with channel length. When the potential in the front of negative polarity streamer becomes lower than the value of breakdown voltage, anode-directed streamer stops. More detailed analysis of anode– and cathode–directed streamer propagation is described below.

4.2 Anode-directed (negative polarity) streamer.

As we see, the structure of the streamers for positive and negative polarities are fundamentally different. The mechanism of anode-directed (negative polarity) streamer propagation is accompanied by relatively high-values of reduced electric field in the streamer channel [46]. The electric field in the channel of negative polarity streamer can be estimated on the basis of the measurements of applied voltage and of the maximum streamer propagation length. Assuming that at the time instant when streamers stop, the potential drop in the head of the streamer U_h is much less than potential on HV electrode, and that the main potential drop takes place along the channel, the average longitudinal electric field in the anode–directed streamer channel can be estimated as:

$$(E/N)_{ch} \approx \frac{(U - U_{cath})}{L_{max}N} = 72 \ Td, \tag{4.1}$$

where $U_{cath} \approx 0.2$ kV is the voltage on the cathode layer [113], N is the gas number density at $P = 1$ bar and $T = 300$ K, and $L_{max} \approx 13$ mm is the streamer length at the moment of stopping.
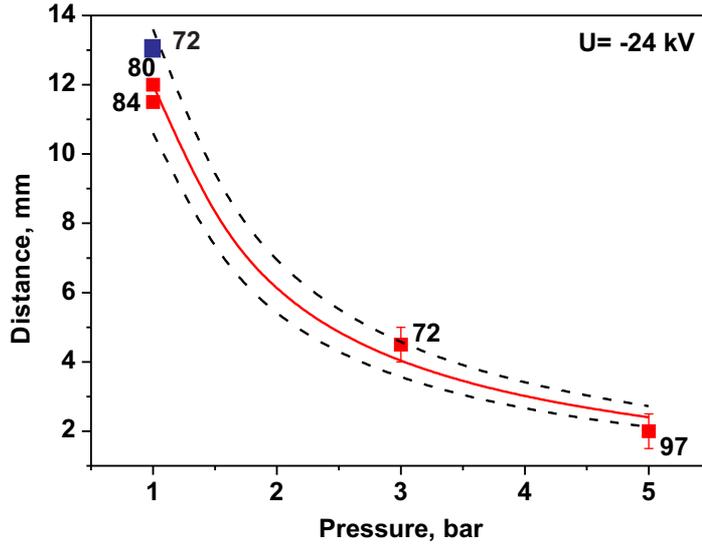
Figure 4.8: Maximal length of the discharge propagation as a function of gas pressure. Numbers near the curves correspond to the longitudinal electric field estimated as described in the text. The solid red curve corresponds to calculations with E/N=80 Td. Dashed curves correspond to E/N=70 Td and E/N=90 Td. Red points correspond to experiments in [46], blue point is experimental result obtained in the present work.

Production of active species in the discharge in 0 D approximation is unambiguously described by a set of parameters $\{\rho_{gas}, E/N, n_e\}$, where ρ_{gas} is a gas density, E/N is a reduced electric field, and n_e electron number density. In any particular case, a inverse problem of $E/N(t)$ behavior can be solved if density of the discharge species and electron density are known.

The flowchart representing the steps of $E/N(t)$, $[N_2(C)](t)$ and $n_e(t)$ in the channel of the anode–directed streamer is shown in figure 4.9. The blue rectangles signify the input experimental data, green - intermediate steps and red - the results.

As it was mentioned, the main source of light radiation of nSDBD in air in visible and UV range of spectrum is the second positive system of molecular nitrogen. The kinetics equation for excited $N_2(C^3\Pi_u)$ state density can be written as:

$$\frac{d[N_2(C)]}{dt} = k_{exc} \cdot n_e \cdot [N_2] - [N_2(C)](\frac{1}{\tau_0} + \sum_{i=1} k_q^i[M_i]), \tag{4.2}$$

where k_{exc} is the rate constant of excitation by direct electron impact, n_e is an electron density, τ_0 is a life time of excited nitrogen molecules, k_q^i are the quenching coefficients, $[M_i]$ is the density of quenching molecules (N_2 and O_2 for the discharge in air). Table 4.1 represents the quenching rate constants of excited molecular
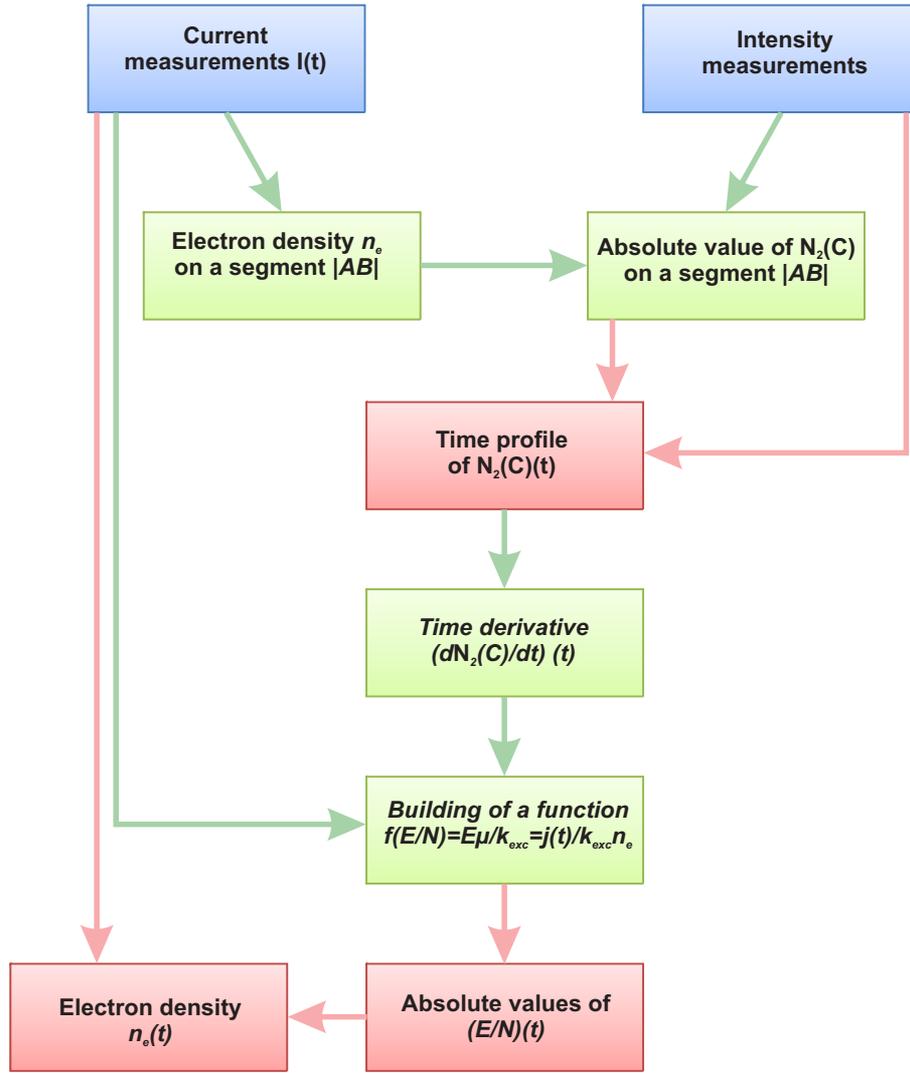
Figure 4.9: The flowchart of $E/N(t)$, $[\mathbf{N_2(C)}](t)$ and $n_e(t)$ determination for anode–directed streamer.

nitrogen and the radiative life time.

Table 4.1:   Rate constants

Number	Reaction	Rate constant, cm^3/s	Reference
R1	$N_2(C^3\Pi_u)+O_2 \rightarrow Products$	$3{\cdot}10^{-10}$	[114]
R2	$N_2(C^3\Pi_u)+N_2 \rightarrow Products$	$1.0{\cdot}10^{-11}$	[114]
R3	$N_2(C^3\Pi_u) \rightarrow N_2(B^2\Sigma_g^+) + h\nu$	$1/\tau_0 = 2.4 \cdot 10^7\ s^{-1}$	[114]

The rate constant of excitation of $N_2(C^3\Pi_u)$ state by electron impact strongly depends on reduced electric field value. In [46] it was derived that $k_{exc} \sim (E/N)^5$.

The equation (4.2) contains electron density that can be estimated from the experiment. The time dependent profile of experimental absolute current per streamer value is demonstrated in figure 4.10(a) - red solid line. If we know the geometry of the streamer and if we assume that the current is constant along the streamer length, we can estimate the average electron density. The current density j depends on the electric field in the plasma channel as follows:

$$j = \sigma \cdot E, \tag{4.3}$$

where $j = I/S$, $\sigma = en_e\mu_e(E)$ is a plasma conductivity, μ_e is the electron mobility, $S = \pi d_{cr}^2/4$ is the cross section of a streamer. The current density from one side depends on the streamer diameter and from another side depends on electron number density. The diameter of the streamer channel can be determined from the lateral intensity profiles as it is shown in figure 4.10(b). The optical diameter of the negative streamer is $d \simeq 260\ \mu$m. Indeed, it was demonstrated for volumetric streamer that the current diameter of the channel differs from the optical one [115]. The analysis of (0–0) transition of 2^+ system on the wavelength 337.1 nm showed that the ratio between optical emission radius and current radius is about $R_{em}/R_{cr} \sim 2$ [115]. This phenomenon can be explained in the following way. The electric field in the streamer channel is a function of the channel radius $E(r)$. The behaviors of the rate constants of $N_2(C^3\Pi_u)$ excitation and of ionization rate (production of electrons) are different with E/N. The current is related to electron density distribution, whereas the emission is related to $N_2(C)(r)$ distribution. Thus, in general $R_{em} \neq R_{cr}$.

According to the equation (4.3), the electron density can be expressed as:

$$n_e = \frac{I}{v_{dr}eSZ}, \tag{4.4}$$

where v_{dr} is the electron drift velocity, I is a total discharge current, Z is a number of streamers. From the electron balance equation including the ionization, recombination and attachment processes the characteristic decay time of the plasma is about 10^{-8} s under considered conditions. So, during the period of time < 10 ns, we can assume that electron density in the streamer body does not change significantly.

The electron mobility and thus, the drift velocity depends on E/N value. Here we consider that electric field in the channel is determined from the equation (4.1) and equal $E/N \approx 70$ Td. Figure 4.10(d) demonstrates the k_{exc}, electron mobility and drift velocity as the functions of E/N. For considered value 70 Td the drift velocity is $v_{dr} = 8.8 \cdot 10^6$ cm/s. Therefore, the electron density at the moment of streamer stopping, according to the equation (4.4), is equal to $n_e \simeq 1.1 \cdot 10^{14}$ cm^{-3}.

The concentration of $N_2(C^3\Pi_u)$ state and emission intensity are related by the equation:
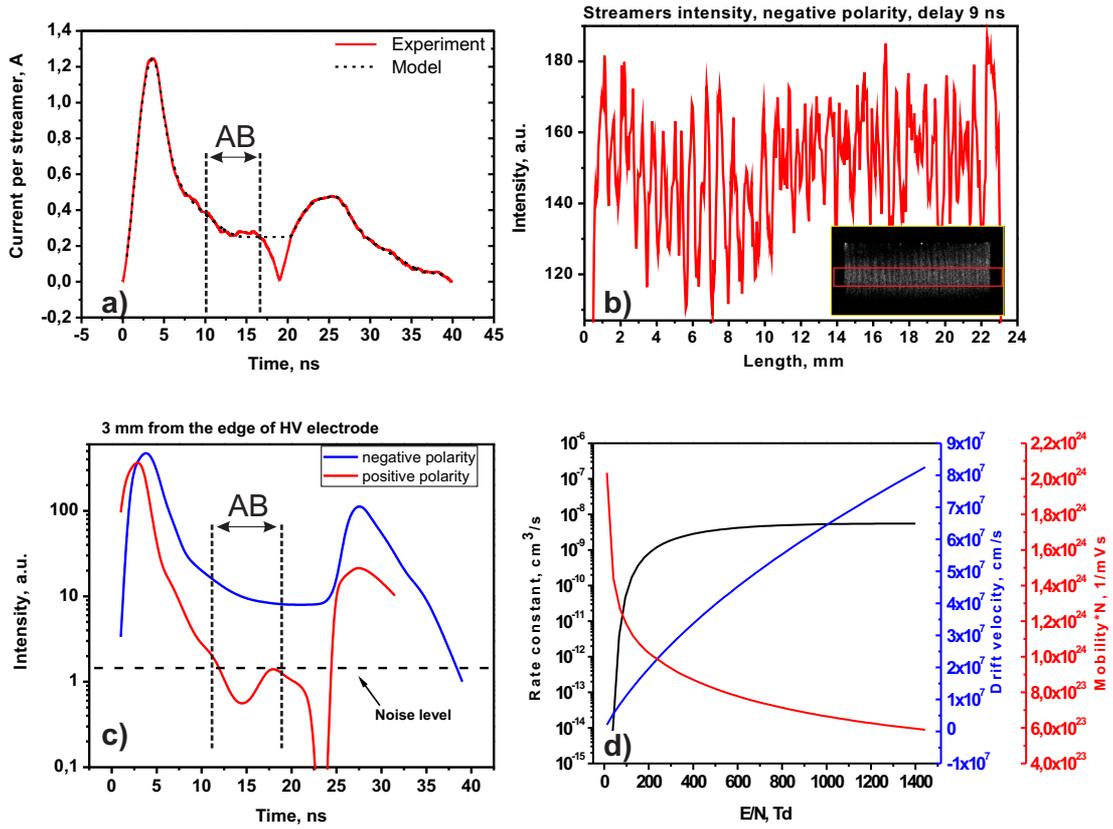
Figure 4.10: (a) Absolute value of current during the discharge of negative polarity. Red curve - experimental current, dashed black curve - current used for modeling; (b) transverse structure of negative streamers, time instant is 7 ns; (c) time resolved intensity profiles for positive and negative polarities. 3 mm from HV electrode; (d) rate constant of $N_2(C^3\Pi_u)$ state excitation (11.06 eV), mobility of electrons and electron drift velocity as a functions of reduced electric field.

$$Int = h\nu_{ij}\frac{[N^*]}{\tau_0}A_{ij}, \tag{4.5}$$

Due to the typical behavior of emission and electrical current in 1 atm pressure nSDBD, the information about absolute density of $N_2(C^3\Pi_u)$ can be obtained without absolute spectral calibration of the system. The corresponding time dependent intensity profiles at $x = 3$ mm are shown in figure 4.10(c) for positive and negative streamers. According to these profiles it is clearly seen, that for positive polarity the emission at the period $8-10$ ns and later is lower than a noise level of the system. Unlike the negative streamers, the emission intensity drops down two orders of magnitude with respect to maximum value but still can be detected. It is clearly seen that during the period 10-20 ns the intensity in the negative streamer channel

remains almost constant. It means, according to the equation (4.5), that during considered period of time the concentration of $N_2(C^3\Pi_u)$ excited molecules remains also constant.

Let's consider this period, where intensity remains approximately constant, as $|AB|$. Taking into account that $dN_2(C)/dt = 0$ at the segment $|AB|$, equation (4.2) can be rewritten as follows:

$$[N_2(C)] = [N_2] \cdot \frac{k_{exc} \cdot n_e}{1/\tau + \sum_{i=1} k_q^i [M_q^i]},\tag{4.6}$$

The rate constant of $N_2(C)$ excitation by electron impact is $k_{exc}(70\ Td) \simeq 5 \cdot 10^{-12}$ cm^3/s. All other rate constants of quenching processes in air can be taken from table (4.1). Therefore, the concentration $N_2(C^3\Pi_u)$ on segment $|AB|$ can be calculated with equation (4.6) and is equal to $[N_2(C)]_{AB} = 5.6 \cdot 10^{12}$ cm^{-3}.

When the absolute value of $N_2(C)$ during the segment $|AB|$ is calculated, it is easy to calculate the concentration of $N_2(C)$ in any time moment.

$$[N_2(C)](t) = [N_2(C)]_{AB} \cdot \frac{I(t)}{I(AB)},\tag{4.7}$$

Figure 4.11(b) presents the time dependent concentration of $N_2(C)$ acquired with equation (4.7). Also the derivative $dN_2(C)/dt$ is given in the same plot.

To analyze the reliability of the experimental results of $N_2(C)$ and electron density concentrations, the numerical kinetic modelling has been performed. Figure 4.11(a) presents the simulation results of negative polarity streamer. The calculations were carried out in the framework of the 1-D radial model with a given current dynamics. The shape of the current pulse used during calculations presented in figure 4.10(a) - black dashed line. The initial diameter of the discharge channel was varied from 100 to 300 μm. The value $d = 250\ \mu$m corresponds to the diameter at which the current density roughly corresponds to the normal current density in the cathode layer. The black square in figure 4.11(a) correspond to the experimental value of n_e.

When the values of $[N_2(C)](t)$ and $\frac{d[N_2(C)](t)}{dt}$ are found from experiment, it is possible to resolve the inverse problem for E/N determination. According to equation (4.2) it is possible to derive the following combination $k_{exc} \cdot I$:

$$k_{exc} I(t) = (k_{exc} \cdot n_e) \cdot eE(t)\mu(E(t))SZ\tag{4.8}$$

We can divide both part of equation (4.8) on $(k_{exc}^2 n_e \cdot eSZ)$. And finally, the can get the following function:

$$f(E/N) = (\frac{E}{N}) \cdot \frac{\mu(E/N) \cdot N}{k_{exc}(E/N)} = \frac{I(t)}{eSZ} \cdot \frac{1}{k_{exc} \cdot n_e},\tag{4.9}$$
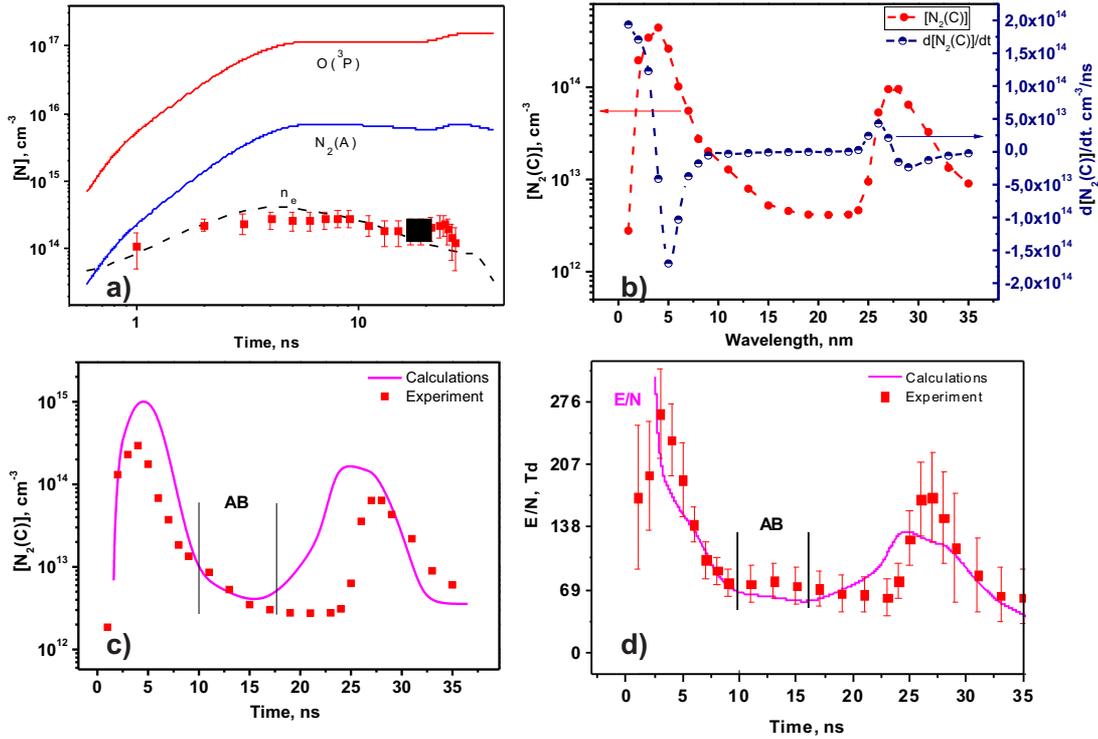
Figure 4.11: (a) Calculated density of $O(^3P)$, $N_2(A)$ and n_e. Black square correspond to experimental value of n_e on a segment $|AB|$, and red scatter the experimentally determined n_e (see text); (b) The experimental values of $N_2(C)$ and $dN_2(C)/dt$; (c) Calculated and experimental values of $N_2(C)$ concentration; (d) Calculated and experimental values of E/N. The conditions are the same as in figure 4.10. All numerical calculations were performed by Dr. Nikolay Popov.

In this expression the right part can be considered as a function of time and can be measured experimentally, taking into account the knowledge about absolute values of $[N_2(C)](t)$. The combination $(k_{exc} \cdot n_e)$ in the denominator of the right side of equation (4.9), can be calculated from kinetic equation (4.2). At the same time, the left part of the equation (4.9) depends only on E/N and can be calculated via BOLSIG+ package [116]. In this way we determine the $E/N(t)$ as a function of time in the streamer channel.

Finally, if we know the reduced electric field $E/N(t)$ and current per channel $I(t)$, it is easy to calculate the $n_e(t)$. The result of electron density in the channel of anode–directed streamer as a function of time is presented in figure 4.11(a) as a red scatter. The error is mostly caused by the inaccuracy of determination of the streamer diameters.

Figures 4.11(c) and (d) present the experimental and calculated dynamics of
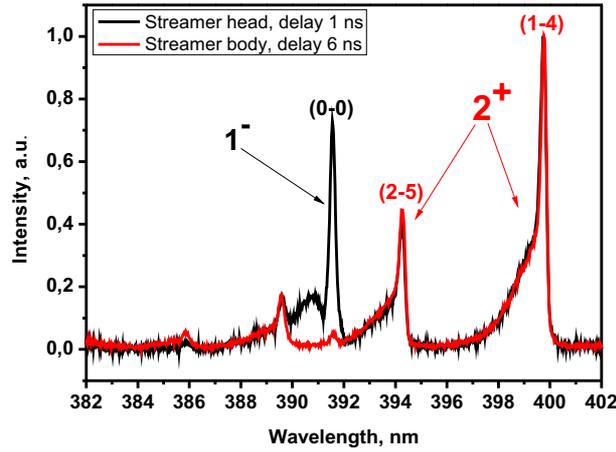
Figure 4.12: Emission spectrum of the discharge in the wavelength range $382 - 402$ **nm. Applied voltage** $U = -24$ **kV. Camera gate 2 ns, number of accumulations 100. Emission is accumulated along entire discharge volume.**

$[N_2(C)](t)$ and $E/N(t)$ respectively. The behavior and absolute values of $[N_2(C)](t)$ density correlates with calculations pretty well on the segment $|AB|$. The main uncertainties of the measured value are related to the errors of determination of streamer radius while calculating the electron density as far as $n_e \sim (r_{st})^{(-2)}$. On the other hand, the current approximation used in simulation fits well just during the situation when the total current reaches a fixed value, that takes place on the segment $|AB|$. At the initial period $(0-5$ ns) the intensity rise reflects the dynamics of emission at certain position $x = 3$ mm from the HV electrode: the arrival of the ionization wave in the considered point, then the decrease of the electric field, transitions to the channel and, consequently, decrease of the intensity of 2^+ system. The current dynamics, which is used during the calculations defines the processes in the near electrode region, such as the formation of the space charge layer and the ionization processes in the near electrode zone. At initial stages of the discharge propagation the current dynamics and emission dynamics reflect different physical processes. A similar situation takes place at final stages of the discharge development - on the trailing edge of applied pulse. Whereas, at the plateau of HV pulse the current approximation used in calculation must be valid. The main result is the agreement between the experimentally determined and calculated minimal value of $N_2(C)$ density.

Additional evidence of the high electric field on the first stages of discharge propagation is a presence of the intense band of the first negative system of $N_2^+ (B^2 \sum_u^+$-

71

$X^2 \sum_g^+$) ion (391.4) nm. The intensity ratio between this band and (0–0) band of second positive system is widely used as a methodic of E/N determination in uniform discharge [25]. In the case of nSDBD, the intensity distribution of the first negative and of the second positive systems of molecular nitrogen is highly non–uniform. Nevertheless, comparison of numerical modeling and experimental results taking into account the spatial non-uniformity, demonstrate reasonable agreement for E/N in the nSDBD for the negative polarity discharge.

Figure 4.12 shows the emission spectra acquired from entire surface of the discharge. The spectra were obtained in two different time instances 1 and 6 ns after the discharge start, and so represent the emission "mainly from the streamer head" or "mainly from the streamer body". Camera gate was equal to 2 ns. It is clearly seen that the intensity of the band 391 nm is almost two times higher than the intensity of 394 nm for 1 ns delay. After 5 ns the relative intensity of 1^- system decreases dramatically. Ratio of $v' = 2 \rightarrow v'' = 5$ at 394 nm and of 391.4 nm emission can also be used for electric field measurements. The calibration is given in [25], and the corresponding expression is the following:

$$\frac{I_{391}}{I_{394}} = R_{391/394}(E/N, N_0) = 46exp\left[-89\left(\frac{E}{N}\right)^{-0.5}\right], \qquad (4.10)$$

where E/N is in Td (10^{-17} V·cm^2), I_{391} and I_{394} the intensity integrals over considered band. Estimated electric field in 0-D approximation via equation (4.10) for 1 ns and 6 ns delays are equal 570 and 190 Td respectively. Although, this estimate cannot be directly transmitted onto complex 2-D or even 3-D geometry of the surface streamer, a significant drop of maximum possible E/N with elongation of the negative streamer is evident.

4.3   Cathode-directed (positive polarity) streamer.

For the cathode–directed streamers, the main reason of propagation is ionization by electron impact in the streamer head. The ionization rate, e.g. the number of electrons produced in 1 cm^3 per 1 s is defined as:

$$\frac{dn_e}{dt} = \int\limits_{I}^{\infty} Nv\sigma_i(\varepsilon)f_e(\varepsilon)d\varepsilon = k_i Nn_e \qquad (4.11)$$

where $\sigma_i(\varepsilon)$ is the ionization cross–section by electrons with energy ε; $f_e(\varepsilon)$ - electron energy distribution function (EEDF); I - ionization potential; k_i - ionization rate constant.
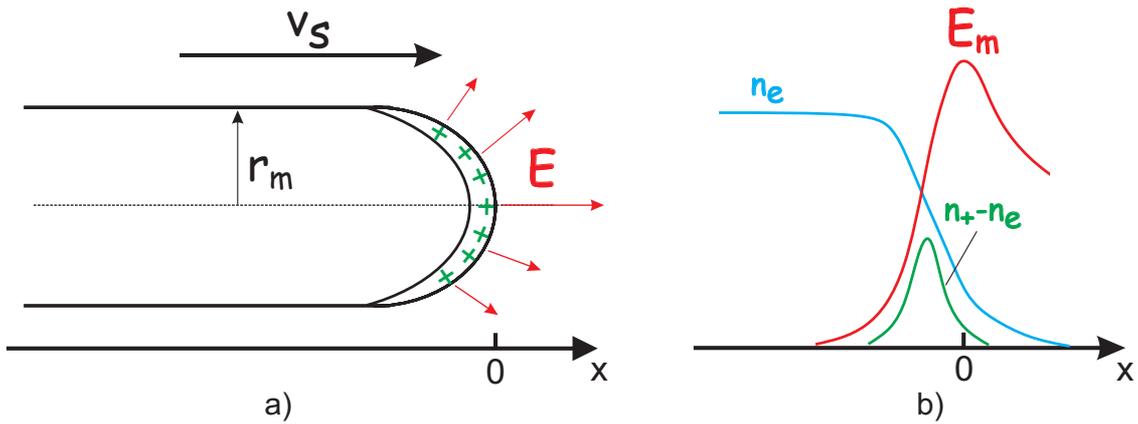
Figure 4.13: **(a) Schematic representation of the cathode-directed streamer and (b) qualitative behavior of electron density n_e, space charge density $(n_+ - n_e)$ and electric field E on the axis near the head of streamer.**

Another key process for the cathode–directed streamer is the photoionization. Excited species produced in a streamer head emit photons absorbed by the molecules ahead of the streamer. In air, the photoionization is due to absorption, by O_2 molecules, VUV–radiation of molecular nitrogen, $b^1\Pi_u$; $b'^1\Sigma_u^+$; $c'^1\Sigma_u^+ \to X^1\Sigma_u^+$, $980 - 1025$ A. Before the front of the ionization wave, the density of the seed electrons is $n_0 \ll n_c$, where n_c is an electron density in the streamer channel. The distribution of seed electrons in front of the streamer head can be approximated as $n_0 \sim r^{-2} exp(-r/\lambda)$ [113], where λ is the characteristic length of absorption of ionizing radiation. A scheme of the cathode–directed streamer is given by figure 4.13.

In the framework of some simplified models it is possible to get the information about the causal connections between the characteristics of the ionisation wave and to make the estimations of the corresponding parameters. The problem of the cathode–directed streamer can be represented as two independent problems. The first problem concerns the propagation of ionization front (about its velocity and the ionization degree in the front). Due to the quasi–stationarity of the wave in the reference system associated with the discharge front, the characteristics of the streamer head basically depend on the processes that occur inside the front of the ionization wave and also depend on some "external" parameters. Such parameters are U - the potential of streamer head and E_m the field in the head. These values are connected by the radius of the head r_m. Indeed, the mechanisms of setting of the head radius are not well known, we will consider the r_m as measured parameter from the experiment, taking into account the error of determination. The second problem is about the structure and processes in the streamer channel. The processes in the body can be considered as slow regarding to the characteristic time of streamer

propagation. Thanks to the slowness of the kinetic, plasmic and electric processes in the long streamer channel ($l \gg r_m$), e.g. due to the relative slowness of the charge changing rate in the middle of the streamer, we can consider the ionization wave as quasi-stationary. Moreover, in the frame of considered problem formulation the surface–plasma interaction is also neglected. In the frame of quasi-stationary approximation, we can estimate the n_m, electron density in the head of positive streamer as well as its behavior in time. The streamer propagation velocity v_s and the electron density behind the head n_c are set as a result of some self–regulated processes, which depend on external parameters: E_m, the maximum electric field in the streamer head and r_m, the head radius. The streamer propagation velocity v_s provides enough time to get, in the high electric field zone, electron density n_c enough to displace the streamer channel. The field in the channel must be decreased to the value insufficient for ionization with high rate as in the head. What is clearly seen in experiment - a sharp drop of the emission intensity behind the streamer head.

Despite the fact that attachment plays the main role in discharge kinetics in air, in high electric field ($E/N \geq 1500$ Td) the attachment processes can be neglected. Therefore, the balance of charged species can be represented in the form of the following continuity equations:

$$\frac{\partial n_e}{\partial t} + div\Gamma_e = \nu_i n_e - \beta n_e n_+, \tag{4.12}$$

$$\frac{\partial n_+}{\partial t} + div\Gamma_+ = \nu_i n_e - \beta n_e n_+, \tag{4.13}$$

$$\Gamma_e = -n_e \mu_e \mathbf{E} - D_e grad n_e, \tag{4.14}$$

$$\Gamma_+ = n_+ \mu_+ \mathbf{E} - D_+ grad n_+, \tag{4.15}$$

where ν_i is an ionization frequency by electron impact, $\Gamma_{e,+}$ are electron and ion fluxes respectively, β is a recombination rate constant. Among the various mechanisms of recombination, the fastest one corresponds to dissociative recombination $A_2^+ + e \rightarrow A + A^*$. Typical coefficient of dissociative recombination is $\beta_{dis} \sim 10^{-7}$ cm^3/s [117], and it decreases with the electron temperature rise as $\beta_{dis} \sim T_e^{-3/2}$. Therefore in quasi–stationary approximation, the recombination in high enough E/N can be also neglected. Being interested in distributions $E(r)$, n_e and $\Delta n = (n_+ - n_e)$ only in the direction parallel to propagation, and neglecting the transverse motion of electrons, we can consider the streamer head as a flat wave. In such wave $E = E(x - v_s t)$, $n_e = n_e(x - v_s t)$, e.g. the distributions are stationary in the coordinate system associated with the streamer head. In this case the equations (4.15) can be re-written as follows:

$$-\frac{d}{dx}[n_e(v_s + v_e)] = \nu_i n_e, \qquad -v_s\frac{dn_+}{dx} = \nu_i n_e, \tag{4.16}$$

where $v_e = \mu_e E$ - module of the drift velocity. Multiplying equations (4.16) on e - electron charge and subtracting them from each other we get:

$$\frac{d}{dx}(en_e v_e - e\Delta n v_s) = 0, \tag{4.17}$$

where $\Delta n = (n_+ - n_e)$. Equation (4.17) is equivalent to the conservation law of the total current. The electric field produced by streamer head in a fixed point in space is changing while streamer propagating. This changes of electric field produces the displacement current in any space point. In the coordinate system associated with the streamer head the gas flows in with the velocity v_s - streamer propagation velocity. And if there is a space charge ρ before the head, it flows into the head with gas. Taking into account that:

$$div(\mathbf{j} + \varepsilon_0\frac{\partial\mathbf{E}}{\partial t}) = 0, \qquad div\mathbf{E} = \rho/\varepsilon_0 = \frac{e}{\varepsilon_0}(n_+ - n_e). \tag{4.18}$$

During the transition to the moving coordinate system of streamer head, the displacement current becomes the convection current flowing into the head: $\rho v_s = e\Delta n v_s$. As far as there are neither electrons nor space charge before streamer head, while integrating the equation (4.17) the integrating constant that is equal to total current density in the following approximation is equal to zero.

$$j_{total} = en_e v_e - e\Delta n v_s = 0, \qquad n_e v_e = \Delta n v_s, \tag{4.19}$$

The streamer body can be approximated as a cylinder with a head that is hemisphere with the same radius r_m. In this case for the spherical front end of the head the Poisson's equation can be written as:

$$\frac{1}{r^2}\frac{d(r^2 E)}{dr} = \frac{e}{\varepsilon_0}(n_+ - n_e), \qquad \frac{dE}{dr} = \frac{e\Delta n}{\varepsilon_0} - \frac{2E}{r}, \tag{4.20}$$

The maximum of the electric field, $E = E_m$ is reached at the tip of the streamer head. For $E = E_m$ the following condition must be fulfilled: $dE/dr = 0$. According to equation (4.20), the maximum electric field value depends on r_m and on the space charge density in this point $\rho = e\Delta n_m$:

$$E_m \approx \frac{e\Delta n_m r_m}{2\varepsilon_0}. \tag{4.21}$$

a)   b)
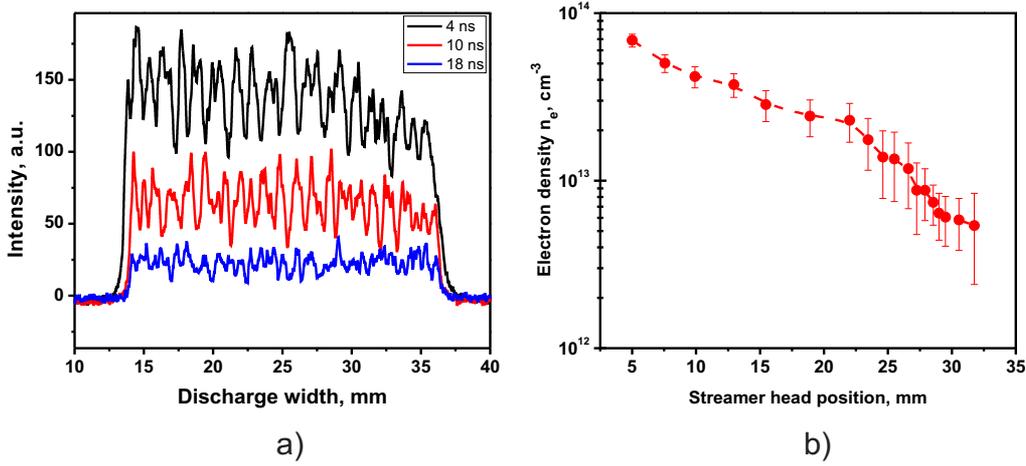
Figure 4.14: (a) Lateral intensity profile for r_m measurements; (b) Electron density in the head of cathode-directed streamer as a function of streamer head position.

Taking into account expressions (4.21) and (4.19), the streamer velocity can be estimated as:

$$v_s \approx \frac{e\mu_e n_m r_m}{2\varepsilon_0}, \tag{4.22}$$

Equation (4.22) shows the dependence between the streamer propagation velocity and the electron density in the streamer head. In the approximation of cylindrical channel with semi–spherical streamer head this dependence is linear.

To calculate the electron density, it is necessary to know the r_m - radius of the streamer head and μ_e. Figure 4.14(a) shows the lateral intensity profiles of the streamer head averaged over 1 mm. The statistical analysis shows that $1-3$ ns after the discharge start the size of the streamer head does not change significantly, and r_m is in the range $(300-400)$ μm.

According to simulation results [17,27,41] the electric field values in the streamer head, E_m, are in the range $(800-1600)$ Td. Therefore, according to figure 4.10(d) the electron mobility $\mu_e(E/N = 800-1600) \simeq 320-260$ cm^2/V·s. Figure 4.14(b) presents electron density in the cathode–directed streamer head as a function of distance between the streamer head and edge of HV electrode. The errors in the calculation of the head radius and the electron mobility are taken into account.

Also, it is possible to estimate the electron density value in the streamer channel n_{ch}. For this estimation, two assumptions can be done: (i) the drift velocity in the considered range of reduced electric field is $v_e = 0.4-0.8$ mm/ns (see figure 4.10(d)). In this case, in the initial stages of propagation the streamer can be represented as a so–called "strong wave", $v_e << v_s$; (ii) we can neglect the curvature of the streamer

head front. The second assumption is reasonable, because the thickness Δx of the space charge region is much smaller: $\Delta x \sim r_m/ln(n_m/n_0)$ [113], n_0 is a density of seed electrons that are always present in the atmosphere (according to different sources [15,113,118] $n_0 = 10^5 - 10^6$ cm^{-3}). From equations (4.19) and (4.20), behind the front of streamer head

$$\frac{dE}{dx} = \frac{e\Delta n}{\varepsilon_0} = \frac{e\mu_e E n_e}{\varepsilon_0 v_s}. \tag{4.23}$$

Dividing equation (4.23) by the first from equations (4.16), and taking into account $v_e << v_s$, we get the differential equation of $n_e(E)$ and implicit dependence $x(E, n_e(E))$. It is also possible to approximate the ionization frequency by a power function [46]: $\nu_i = \nu_i^m(E/E_m)^l$, where $l = 5/2$. Integrating the equation for $n_e(E)$ along the entire wave front, from the point where $E = E_m$, $n_e = n_m$, to the area behind the wave where $E \approx 0$ and $n_e = n_{ch}$, we get:

$$n_{ch} = n_m + \frac{\varepsilon_0 \nu_i^m}{e\mu_e l}. \tag{4.24}$$

Here n_{ch} is an average electron density in the channel during the time period where the approximation of "strong wave" is valid and is $n_{ch} \simeq (7.5\pm1.0)\cdot10^{14}$ cm^{-3}. If comparing with the electron density in the channel of anode–directed streamer it is $5 - 7$ times higher.

It is clearly seen from figure 4.15 that a few nanosecond after the discharge start the intensity in the streamer head correlates with the velocity of the discharge propagation. The intensity is proportional to the concentration of excited molecular nitrogen and, thus, according to equation (4.6), is proportional to excitation rate constant. It was demonstrated in [46] that for atmospheric air $k_{exc} \sim (E/N)^{5/2}$. Finally from figure 4.15 we can conclude that $v_{st} \sim I \sim [N_2(C)] \sim k_{exc}$, therefore $E \sim (v_{st})^{2/5}$. As we see, the velocity depends only slightly on the field in the streamer head. For example, if the velocity decreases two times $v(t_2)/v(t_1) = 1/2$, the field will decrease $2^{2/5}$ times. It correlates with the simulation results of different groups [27, 41].

4.4 Spatial fine structure of the streamers

The nSDBD in classical air–flow arrangement has been studied numerically. Physical reasons and dynamics of streamer slowing down were analyzed in [27]. Independently in [41] for the first time hybrid numerical model consisting of fluid model and Monte-Carlo methods was used for nSDBD. All scientific groups have demonstrated good correlation of integral characteristics, such as emission intensity (e.g. N$_2$(C) concentration) and velocity of streamer propagation, with experimental

values. But internal kinetic characteristics, such as electron number density and electric field, are different in the calculations of different authors. Debates on this issue do not cease up to date.

Table 4.2: Electric field in the streamer channel.

Author	Positive polarity streamer	Negative polarity streamer	Reference
Soloviev	130-150 Td	110-120 Td	[26]
Gibalov	$\leq$20 Td	100 Td	[17]
Babaeva	100 Td	100 Td	[41]

Table 4.2 demonstrates the values of reduced electric field in the channel of cathode and anode directed streamers. According to the model of Prof. Soloviev, the E/N does not differ significantly for positive and negative polarity of applied pulses, and its values slightly exceed 100 Td. This value is achieved by the balance between the production of electrons (ionization) and attachment processes to oxygen atoms in the discharge channel. Very close values were obtained by the team of Dr.Babaeva and Prof. Naidis. However, the analysis performed by Dr. Gibalov shows that the electric field in the streamers of negative polarity remains rather high behind the
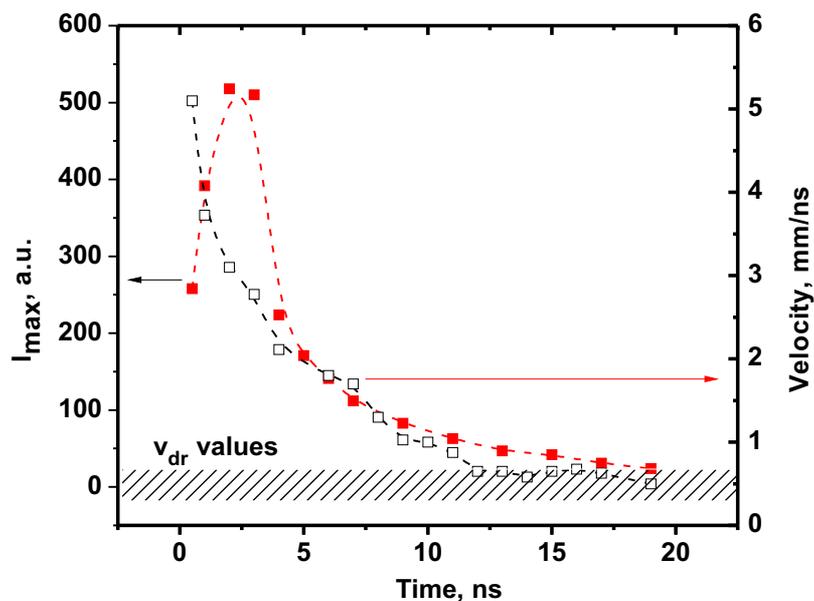
Figure 4.15: Time dependent emission intensity in the cathode–directed streamer head and the propagation velocity of the streamer.
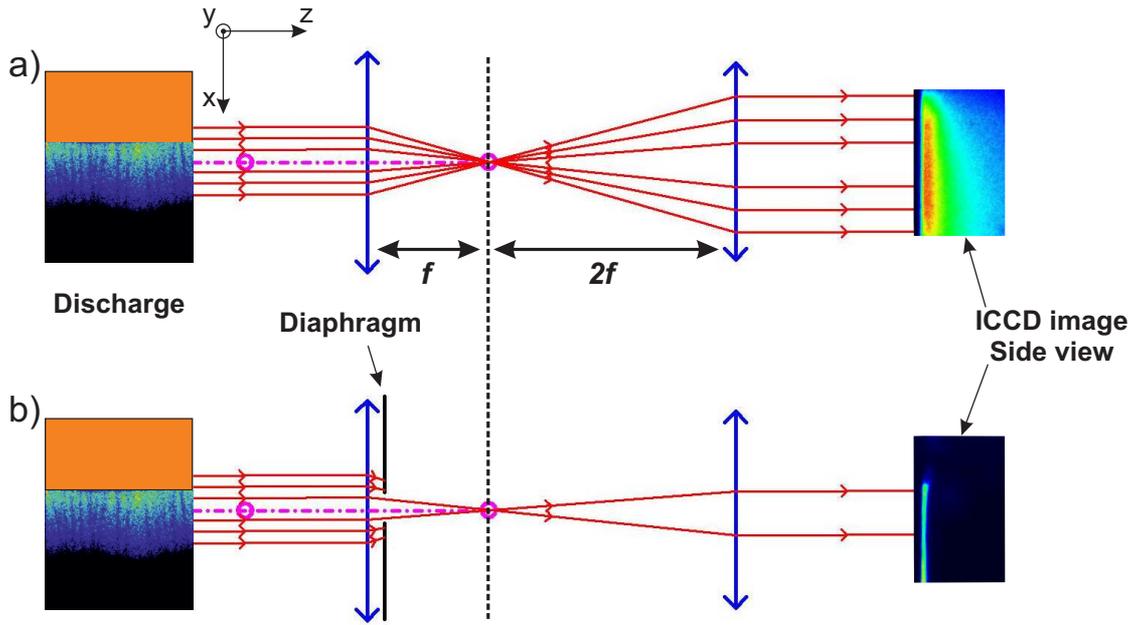
Figure 4.16: The schemes of the ICCD images (side view) acquisition (a) without and (b) with diaphragm increasing the depth of field.

front of ionization wave, but the field in the body of positive streamers drops down dramatically and does not exceed ~ 20 Td until the trailing edge of the applied HV pulse.

As it was mentioned above, the nSDBD streamer is a complex 3D structure. The reliable experimental measurements are complicated by the small thickness of the plasma layer produced in a close proximity to the dielectric surface. The knowledge, even qualitative, about the thin structure of the nSDBD can help understanding the physics of the discharge.

To get time- and space–resolved 2-D images of a streamer propagation, a x2 magnification optical system consisting of two lenses of focal distances 150 mm and 300 mm was used. The scheme of the system is presented in figure 4.16. To increase the depth of field, the diaphragm was placed after the first lens. Figures 4.16(a) and (b) give the examples of a "blured" side discharge view, when a light from different streamers comes out of focus, and an image with the diaphragm was chosen so that no significant changes in the discharge morphology was observed at further diaphragm closing. The images were taken by a Princeton Instruments Pi-Max 4 1024i ICCD camera with a pixel size of 12.4×12.4 μm^2. Mainly the emission of $N_2(C^3\Pi_u) \rightarrow N_2(B^3\Pi_g)$ transition is recorded.

ICCD images of the discharges in the space region $(0-5)$ mm from the high–voltage electrode are given in figure 4.17 for negative and in figure 4.18 for positive
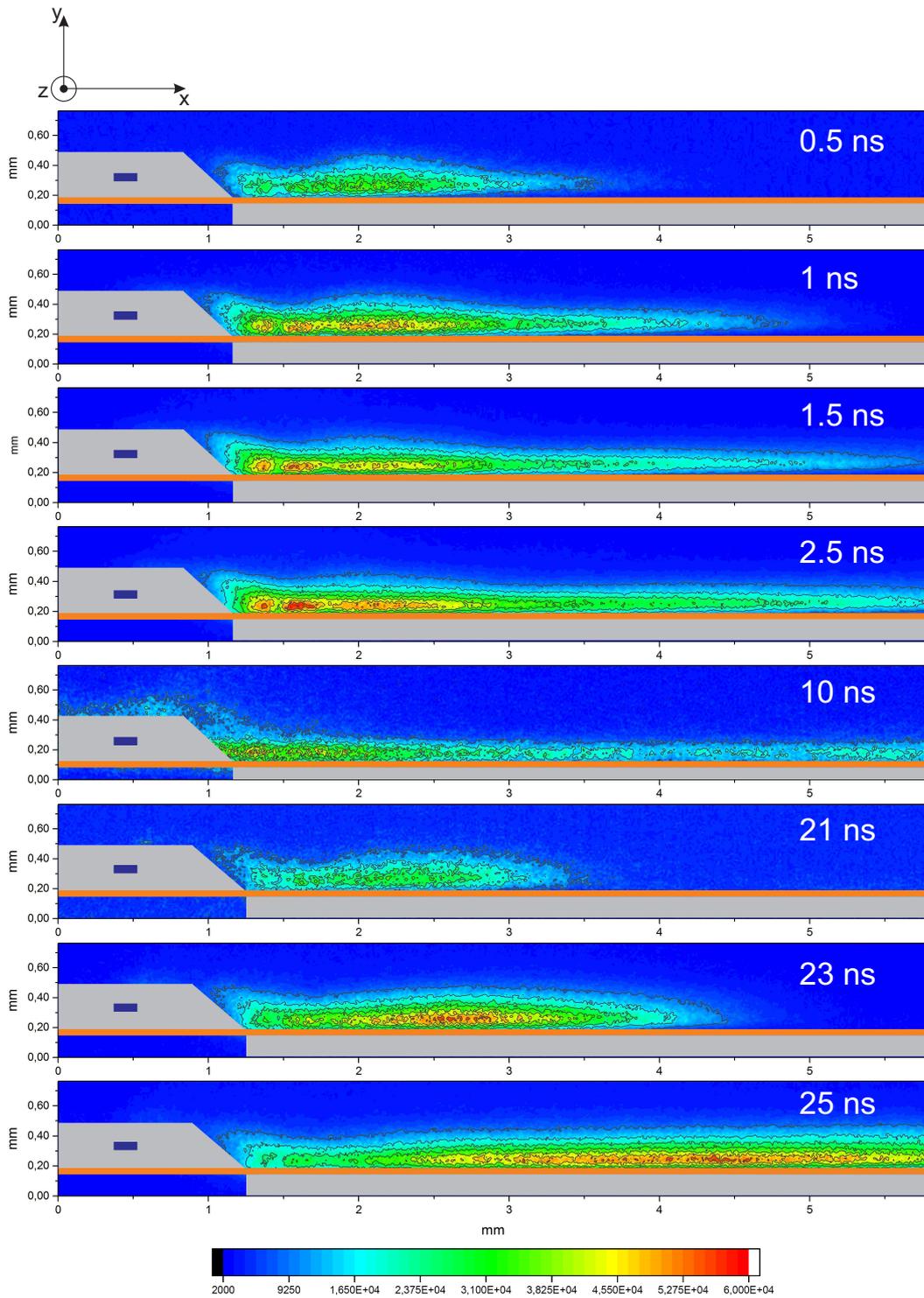
Figure 4.17: Side view of negative polarity discharge propagation. $W = 25$ mm electrode width. Camera gate 0.5 ns. Time delay relative to the start of the discharge is mentioned in the upper right corner of each frame. Amplitude of applied voltage $U = -24$ kV.
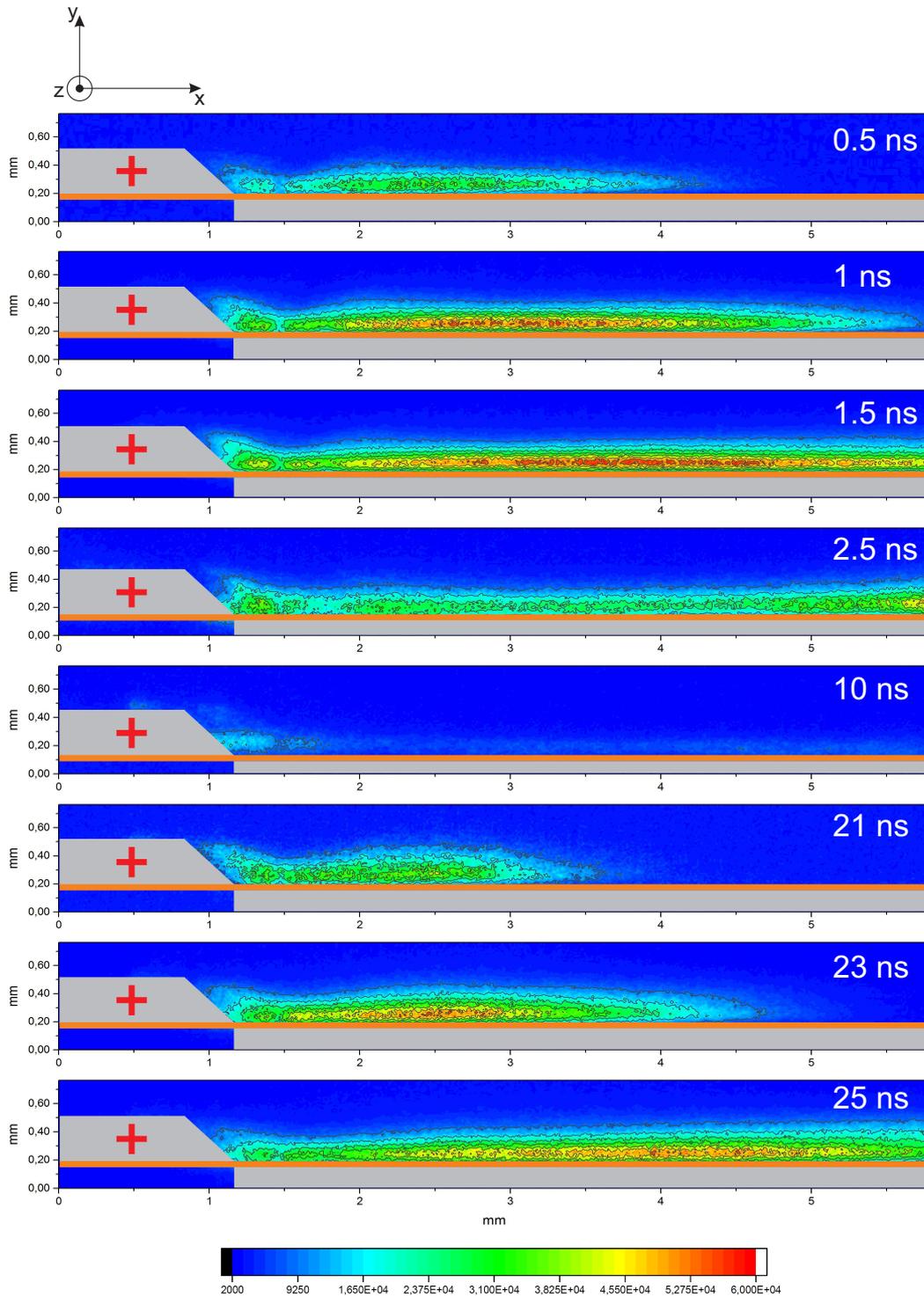
Figure 4.18: Side view of positive polarity discharge propagation. $W = 25$ mm electrode width. Camera gate 0.5 ns. Time delay relative to the start of the discharge is mentioned in the upper right corner of each frame. Amplitude of applied voltage $U = +24$ kV.

polarity of HV pulse. Each frame is a result of accumulation of 10 images with a camera gate of 0.5 ns taken with a given time delay respective to the start of the discharge.

A few important observations can be made basing on the ICCD images. The velocity of the streamer propagation calculated on the interval $(0 - 2.5)$ ns is about 5 mm/ns for a positive polarity streamer and about 2.5 mm/ns for a negative polarity streamer, in a good agrement with previous measurements (compare with figure 4.7). Although numerical modelling reports "diffusive" thin attached to the surface structure of a negative streamer and separate streamer structure with a gap ~ 50 μm between the streamer body and dielectric surface for positive polarity discharge [27]. However, no significant difference between the thickness (in $z-$direction) of the negative and positive polarity streamers is observed. The negative polarity streamers are a little bit more diffuse. It is well seen that the maximum of emission is located in the central part of the streamer $0 < z < z_h$, where z_h is a thickness of the HV electrode, and that the zone of a high uniform emission intensity from the central part of the streamer can be as long as a few millimeters.

A peculiar feature never presented in numerical modelling can be noticed in first $2.5 - 3$ ns of the discharge development. The structure of the discharge along $x-$axis is not uniform demonstrating a bright emission kernel $200 - 300$ μm apart from the HV electrode. The kernel is more bright for the negative polarity nSDBD. The difference in physics of streamer propagation for different polarities is the most evident from the images at 2.5 ns: bright emission near the HV electrode of the negative polarity streamer underlines the importance of the near-electrode processes, while high intensity of emission in the forehead part of the positive streamer proves that this is a self–sustained structure.

If measured by PMT (compare to figure 4.10(c)), the nSDBD emission is characterized by a high intensity peak with a FWHM about 5 ns. This is in correlation with ICCD images in figure 4.18: already 9 ns after the discharge start the emission is gone from the near–electrode region.

On the trailing edge of the pulse $(21 - 30$ ns), the secondary emission wave (the second stroke) propagating from the HV electrode is clearly seen. The properties of the discharge at this interval illustrate changing of the potential of the electrode relative to low–voltage electrode: The negative polarity streamer has more "streamer–like" appearance, while the positive polarity streamer is more "diffuse–like".

4.5 Return stroke of nSDBD

As it can be noticed above, at the nSDBD initiation with pulse duration of a few tens of nanoseconds, two waves of optical emission propagate from the high-voltage electrode, corresponding to the leading and trailing edges of the high-voltage pulse. It happens at any polarity of applied HV pulses. It is shown experimentally and by means of numerical modeling [15, 16, 33] that a glow-like discharge slides along the surface of dielectric at the leading edge of the pulse slowing down on the plateau of the pulse. When the trailing edge of the pulse arrives to the high-voltage electrode, a second emission wave starts and propagates in the same direction from the edge of UH electrode. As it was demonstrated above, depending on the polarity of applied pulses, the structure of the secondary wave (on the trailing edge of HV pulses) can be either diffuse (for $+U$) or well–pronounced streamer like (for $-U$). In the following paragraph we consider only negative polarity streamer to analyze the physics of the second stroke.

Generally speaking, the SDBD is a 3D phenomenon: both for positive and negative polarity streamers the discharge consists of a set of thin channels normal to the electrode edge [13, 46]. However, the relative simplification of the discharge modeling by the quasi-uniform mode, when the discharge at different positions along the high-voltage electrode looks as a uniform plasma layer, not like a set of streamers, is usually accepted [41]. As a result, the electric field inside the ionization region can be considered as 2–components: (i) parallel to streamer propagation, x–component; (ii) perpendicular to the dielectric surface, y–component. Accordingly, we can approximate the discharge zone as a plane sheet above the dielectric surface with uniform parameters along z-axis in the direction of the electrode edge normal to x-y plane. The kinetic model used for calculations is described in [14, 15].

4.5.1 Results of numerical modeling

To understand the nature of the glow on the trailing edge of the applied HV pulse, we analyze the electrical current in the discharge. The calculated current, corresponding applied voltage pulse and energy deposition as a function of time is presented in figure 4.19. According to different applied voltage behavior we can distinguish three areas on the current plot: (i) linear voltage increase, corresponding to leading edge of applied pulses $0-2.5$ ns; (ii) constant voltage region $2.5-15$ ns; and (iii) linear decrease corresponding to the trailing edge of applied pulse $15-22.5$ ns. The time dependent energy deposition is shown by the dashed curve.

The transient cathode layer is demonstrated in figure 4.20a. The electric field in the cathode layer achieves rather high values, $E/N > 2000$ Td. Due to so elevated
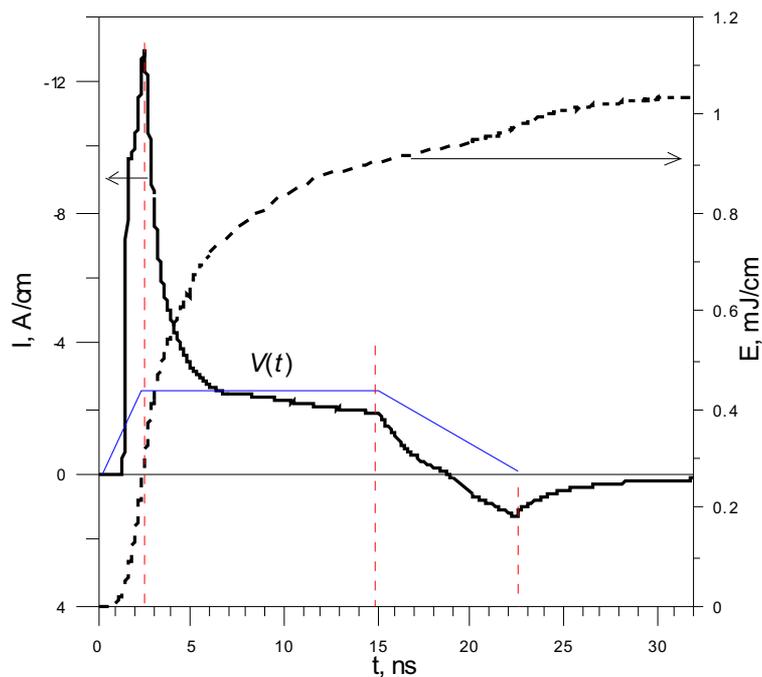
Figure 4.19: The time dependence of calculated electrical current in the circuit and the energy deposited into a discharge region. $U = -14$ **kV. Calculations of Dr. V. Soloviev.**

E/N values the electron and ion densities are of the order of 10^{15} cm^{-3}. Ions produced in the cathode later drift to the electrode edge causing the peak of the current in figure 4.19 at $t = 2.5$ ns time instant. The electrons produced in cathode layer are repelled from the edge of HV electrode and drift to the dielectric surface charging the surface negatively. As a result, the y–component of the external electric field and the flux of electrons on the surface decrease with time. The x–component of the electric field decreases as well, reducing ionization in the cathode layer. the electrical current through the cathode goes down (at $t = 2.5$ ns in figure 4.19).

The next stage of the discharge current corresponds to the slowing down of decrease of the current and formation of the plateau in the time interval $2.5 < t < 15$ ns. This behavior of the current wave form is caused by formation of the near-surface plasma layer and its development. This layer is demonstrated on the lower plot of figure 4.20a. Lets consider a fixed position, cross–section of the plasma sheet, at $x = 0.5$ mm demonstrated as black dashed line. The behavior of y-component of the electric field is demonstrated in figure 4.20b. Initially ($t = 1$ ns), the E_y is positive, when there is no surface and volumetric charges. When the discharge front comes to the considered x–position, electric field increases in the dielectric and becomes negative above the surface because of the formation of negative surface charge caused by electron flux towards the dielectric surface. The negative electric
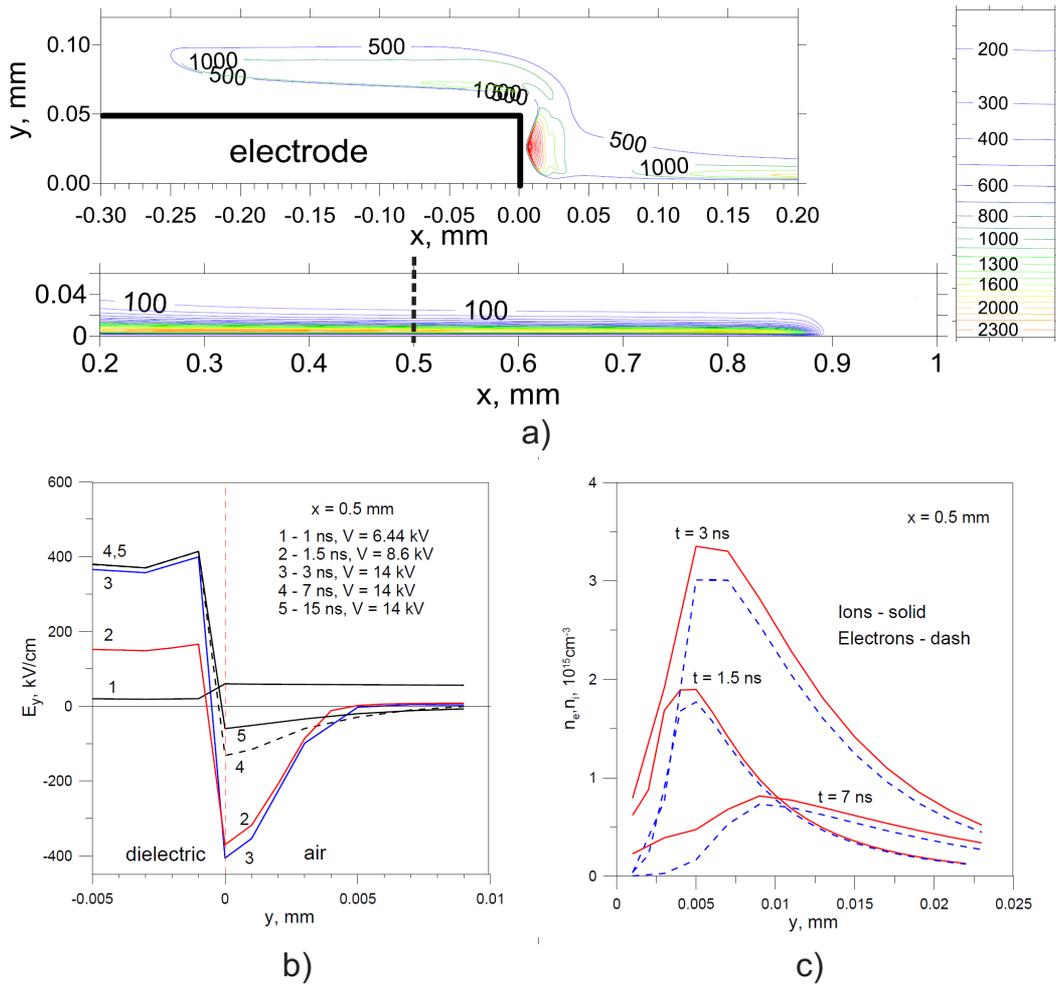
Figure 4.20: (a) Contours of normalized electron density n_e/n_0 for SDBD discharge at the leading edge of the high-voltage pulse (t=1.5 ns). Upper contour - the near-electrode region with a cathode layer; lower contour - the near-surface sliding discharge region; on the right, the color scale for n_e/n_0 is demonstrated, $n_0 = 0.82 \cdot 10^{12}$ cm^{-3}. (b) Normal electric field E_y and (c) evolution of the electron-ion density in cross section x=0.5 mm for leading edge sliding discharge (first stroke) Calculations of Dr. V. Soloviev.

field above the dielectric is much higher than the value necessary to equalize the electron diffusion flux to the surface mentioned in [15]. This is explained by 2D electron motion. When electrons reach the edge of the surface charge layer, the negative extra charge arises. The part of the extra charge comes to the dielectric surface, and the rest generates the aforementioned E_y component managed by the negative charge surplus at the discharge front and, consequently, by the rate of electron-ion production in a cathode layer.
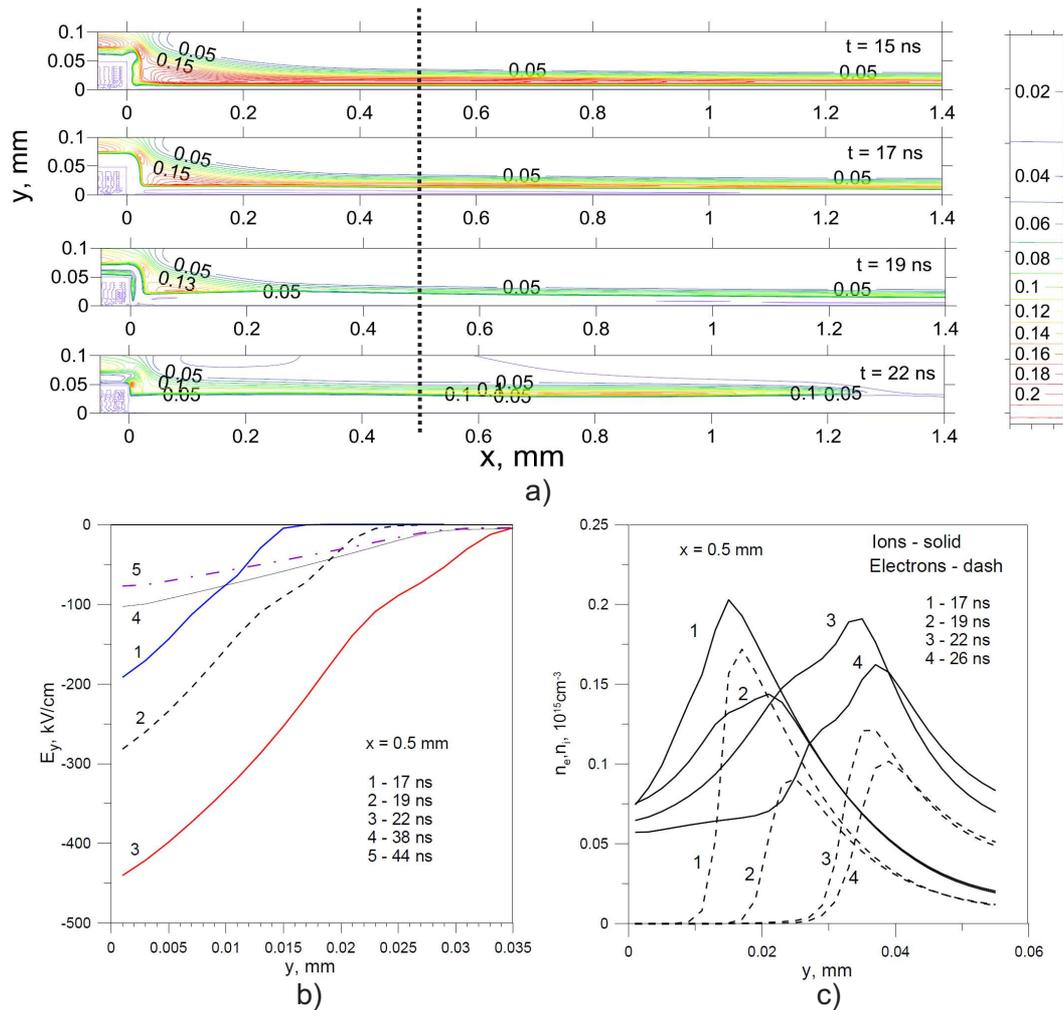
Figure 4.21: (a) Contours of electron density in units 10^{15} cm^{-3} for trailing edge of the voltage pulse (second stroke): near electrode discharge modification; color scale of electron densities in units of 10^{15} cm^{-3} is on the right. (b) Normal electric field $\mathbf{E}_y$ and (c) evolution of the electron-ion density in a cross section x=0.5 mm for trailing edge discharge. Calculation of Dr. V. Soloviev.

Figure 4.20(c) demonstrates the behavior of near–surface charge of electrons and ions in a fixed $x = 0.5$ mm position. The electron and ion densities increase initially (1.5 and 3 ns), afterwards they decrease. High electron and ion densities in the near–surface layer can be described by additional ionization in high electric fields: a conducting layer is formed near the dielectric surface at the stage of the leading edge of the applied pulse.

Figure 4.21 shows the behavior of the discharge during the trailing edge of the applied HV pulse. When the electrode potential decreases ($t > 15$ ns), the balance

between the field creating by surface charge and the external field of HV electrode is disturbed and the negative electric field above the dielectric surface starts to grow up again (figure 4.21(b)). This electric field moves the electrons apart from the surface and ions - toward the surface. As a result, a narrow gap of electron density between the dielectric surface and conducting discharge layer becomes wider (figure 4.21(a) and (c)), and the electrons move from the surface to the HV electrode, decreasing positive current values and finally creating a negative current peak.

4.5.2 Experimental observations

Experimentally measured electrical current flowing through the plasma is presented in figure 4.22(a). The obtained waveform is typical for streamer and uniform nanosecond SDBDs at atmospheric pressure: a sharp peak, about 14 A per centimeter, is observed on the rise front of the pulse, then current decays to the trailing edge, and then a small peak of current of the opposite polarity is observed.
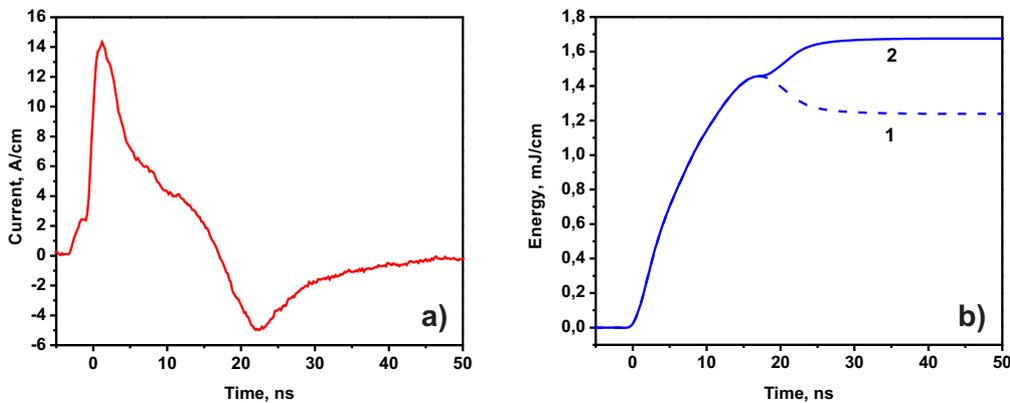
Figure 4.22: **Measured (a) current per unit length of the high-voltage electrode and (b) integrated over time voltage-current product for external circuit per unit length of the high-voltage electrode. Applied voltage** $U = -24$ **kV.**

Integrated over time the voltage–current product is given by figure 4.22(b). The energy increases in a monotonic way during the pulse, reaching the value of about 1 mJ/cm. A small drop on the curve after the $t = 18$ ns is due to changing of the sign of the current (see figure 4.22(a)). The energy input into a gas monotonically increases and the curve of the energy deposition into a discharge increases and similar to that one shown in figure 4.19. A visible secondary peak, about 10% of the energy, is observed at the moment when the trailing edge of the pulse comes to the high–voltage electrode.
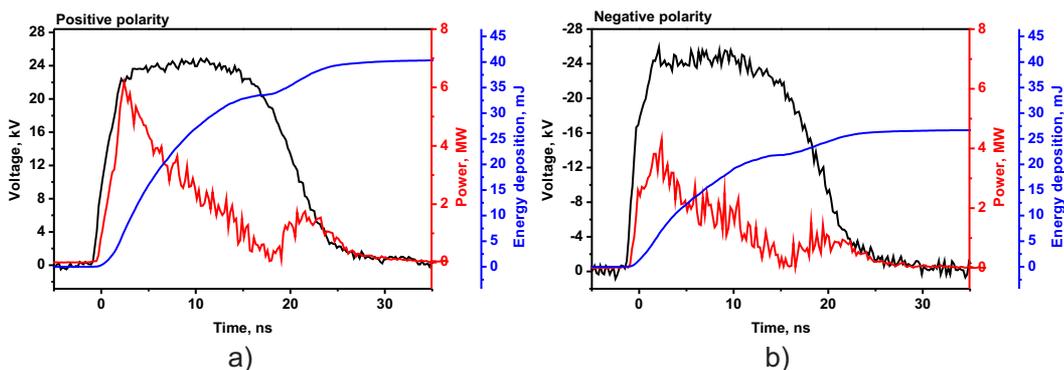
Figure 4.23: Power and energy deposited into the discharges for (a) positive and (b) negative polarities. Discharge in air, $P = 1$ bar, $U = \pm 24$ kV. The width of the HV electrode is $W = 25$ mm.

4.6   Energy release in the discharge

Energy release in the discharge and afterglow is a very important parameter for gas discharge plasma. The energy is deposited in a gas during the discharge phase, at high reduced electric fields, providing ionization, excitation of electronic and vibrational degrees of freedom and dissociation. In the discharge and early afterglow, energy relaxation in chemical reactions and E-T–exchange leads to a so–called fast–gas heating (FGH) [79, 82, 119] providing at $P = 1$ atm, depending an initial energy stored in the volume, heating release up to $\sim$kK/tens of ns [83]. On a longer time scale, microseconds and more, the V–T relaxation is important.

Different experimental techniques allow the determination of the energy release from units of nanoseconds to tens–hundreds of microseconds, and this will be demonstrated in section 4.6.2.

Energy deposited in a gas during the discharge phase can be measured by the technique of calibrated back current shunts (BCS) described in details in chapter 3.

The absorbed power, energy deposition and applied HV pulses are shown in figure 4.23 for U=$\pm$24 kV. To the end of HV pulses, 32 mJ is deposited into the discharge for positive and 22 mJ — for negative polarity. The surface covered by the plasma sheet is different for different polarities. If to calculate the energy by the units of streamer length, it gives 1 mJ/mm for a positive polarity streamer and 1.5 mJ/mm for a negative polarity streamer, e.g. if the total energy deposition is higher for positive polarity, energy deposition per unit length is higher for negative. It seems to be reasonable. As it was demonstrated above, the electron density in the streamer body for negative and positive polarity is about ~ 5 times higher for positive polarity, however, the electric field E/N is significantly higher in the body

of negative streamer. The energy deposition per volume unit is $w = jE$. Thus, the specific energy is higher for negative polarity streamers. A question about the specific deposited energy and the influence of energy distribution on the efficiency of initiation of combustion by nSDBD will be discussed in chapter 6.

The most considerable power dissipates in the gas during first $5 - 7$ ns of the pulse, corresponding to a fast propagation of the streamers along the dielectric and charging of a dielectric surface. Then, power decreases and streamers slow down.

4.6.1 Spatial time-resolved temperature distribution

The rotational temperature T_{rot} for the same HV pulse parameters was measured from the emission spectra of (0–0) line of 2+ system of molecular nitrogen, superimposing a plot calculated by Specair code [104] with experimentally obtained spectra. The spectra were obtained over the regions 0–2, 2–4 and 4–6 mm counting from the HV electrode with the ICCD camera gate equal to 1 ns. The evolution of rotational temperature at different distances from the HV electrode with corresponding applied HV pulses are shown in figure 4.24. For both positive and negative polarities of the high voltage pulse the temperature increase does not exceed 100 K respectively to the initial temperature that was equal to 290 K.

The simple estimate demonstrates that this result is reasonable. The longitudinal electric field in the surface streamer channel of negative polarity does not change with time and is equal to $E/N \approx 70 - 90$ Td. In assumption that the distance between the streamer channels is comparable with streamer diameters, for the experimental values of current (60 A) and for the thickness of a plasma layer of 250 μm, the current
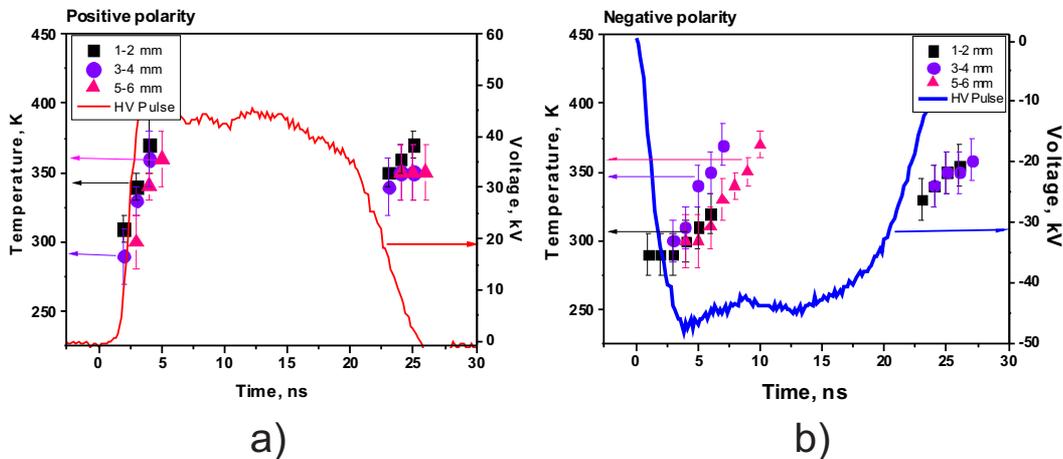
Figure 4.24: Time resolved rotational temperature for (a) positive and (b) negative polarity of applied pulses, taken at different distances from the high-voltage electrode.
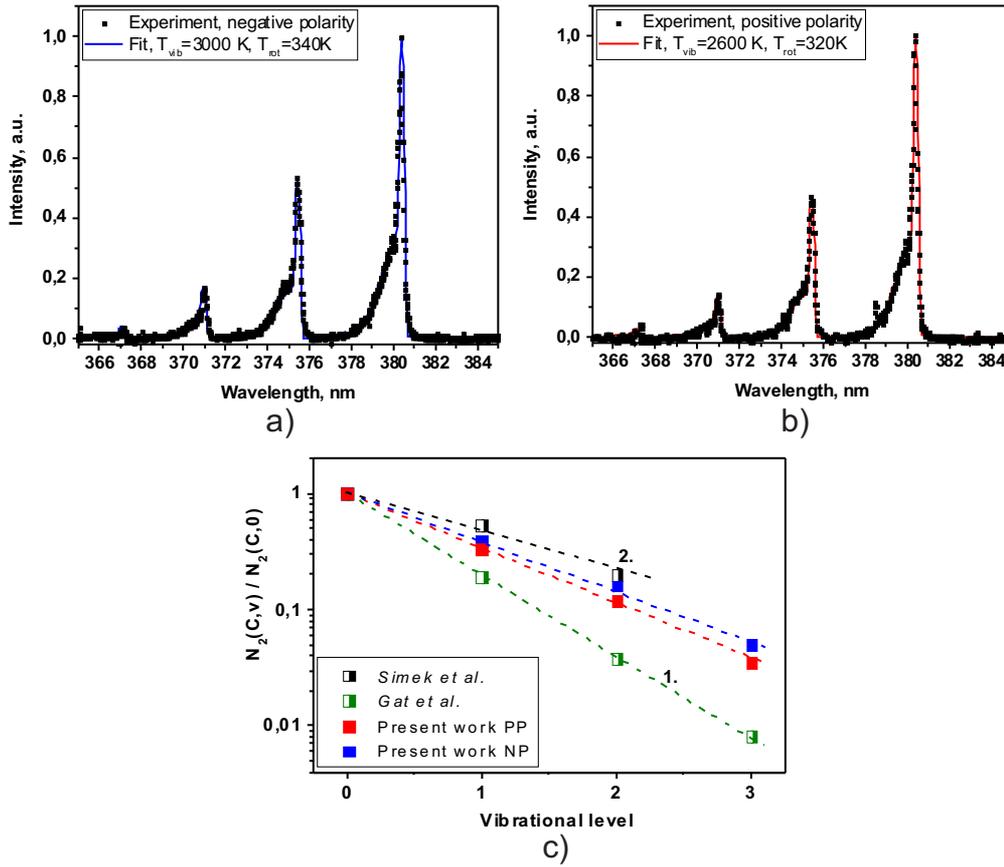
Figure 4.25: Emission spectrum of 2^+ system of molecular nitrogen corresponding to the vibrational transitions (0-2), (1-3) and (2-4) for (a) negative and (b) positive polarity of applied pulses. (c) Normalized maximum intensities of (0-2), (1-3) and (2-4) vibrational lines. Comparison of normalized intensities with corresponding values taken from [120] and [121].

density can be estimated as $j \approx 3$ kA/cm^2. At $E/N = 75$ Td the corresponding electron density is equal to $n_e \approx 2 \cdot 10^{14}$ cm^{-3}, and the energy deposited during first $5-6$ ns can be estimated as 0.1 eV/mol. At $E/N = 75$ Td about 15% of the discharge energy goes to gas heating via fast exchange processes [79], and so, the gas heating in isochoric approximation can be estimated as $\Delta T \approx 50$ K, what is in reasonable agreement with the measured values. It should be noted that similar values of fast gas heating in the discharge were obtained for nSDBD in air at atmospheric pressure in [13], where, moreover, the additional gas heating due to relaxation of vibrational energy has been recorded in a microsecond time scale.

Despite the fact that the rotational temperatures are rather similar for different polarities of applied pulses, the difference in vibrational temperatures can be seen.

Figures 4.25(a) and (b) present the experimental spectra of (0-2), (1-3), (2-4) and (3-5) lines of 2^+ system for negative and positive polarities. The vibrational temperatures are different and equal to 3000 K for negative and 2600 K for positive polarity of applied pulses.

Figure 4.25(c) represents the comparison of the results obtained in present work and in [121] and [120]. Gat *et al* [121] studied volumetric DBD in nitrogen ($P = 1$ bar). The discharge was initiated between two plane electrodes (4 cm in diameter), the gas gap was varied from 1 to 20 mm. The electrodes were covered by alumina layer. The power supply delivered sinusoidal high voltage in the kilohertz range. Vibrational temperature measured in this paper was in the range $1000 - 2000$ K depending on interelectrode distance. Simek *et al* [120] reported the results of corona discharge in N_2, N_2/O_2 and N_2/NO mixtures. The corona was generated in coaxial geometry with central wire anode with diameter 0.75 mm and grounded cylinder cathode, internal diameter of the cylinder was 56 mm. The pulsed positive HV power supply (Marx type with maximum ranging 100 kV/1 kA/7 ns rise time/$\sim$ 100 ns fall time) delivered pulses with repetition rate up to 10 Hz. The vibrational temperature in the discharge phase was about $3500 - 4000$ K. As we can see, the vibrational temperature in our nSDBD discharge is higher than for volumetric, but lower than for corona discharge in near anode region.

4.6.2 Energy release in the afterglow

It is a known fact that the nanosecond discharges at elevated pressures produce hydrodynamic perturbation in the region where the discharge is initiated. One of the most simple and impressive examples is the production of the shock wave that during a few microseconds turns into acoustic one by nanosecond spark in pin–to–pin electrode configuration [122]. One–dimensional hydrodynamic expansion model fits well with experimental results.

In the case of nSDBD the discharge is a complex structure consisting of numerous channels and each channel produces its own shock wave. The shock waves interact with each other and propagate in the direction perpendicular to the dielectric surface. Figure 4.26 demonstrates the shadowgraphy images of the shock wave produced by nSDBD of negative polarity. At 500 ns the perturbation caused by the discharge is already clearly seen. Afterwards, this perturbation detaches from the surface and propagates as a quasi–uniform sheet in the direction perpendicular to the dielectric surface.

It should be noted that, for positive and negative polarity nSDBD, the pictures of hydrodynamic perturbation at $t > 1$ μs is practically identical. The synchronous start of the streamers from the high–voltage electrode causes a cylindrical compres-
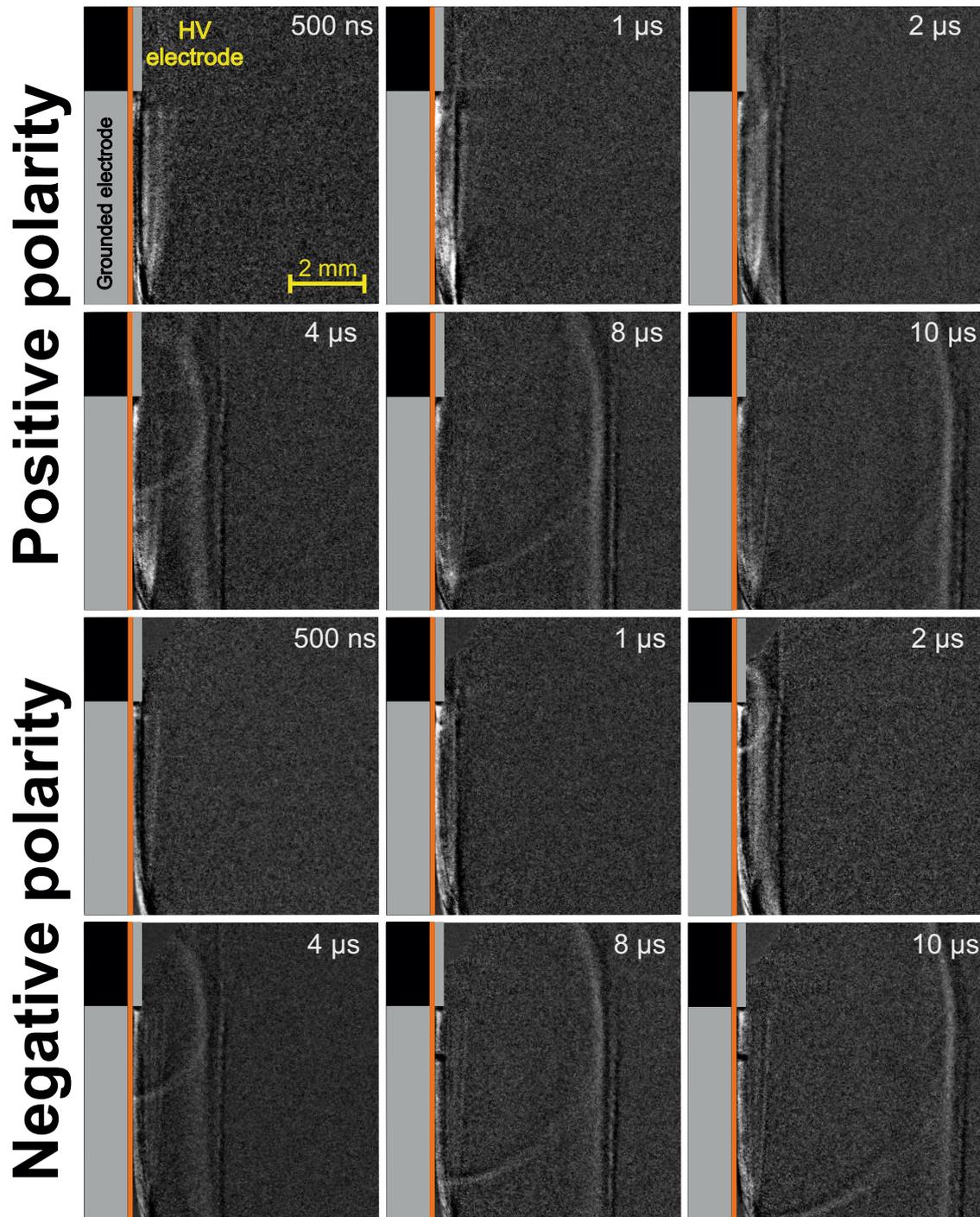
Figure 4.26: Shadowgraphy imaging of the compression wave propagation. Positive polarity of applied pulses. Applied voltage |U| = 24 kV. The width of HV electrode is 25 mm.

sion wave starting from the electrode and representing a superposition of individual waves generated by each streamer. The appearance of a compression wave is an interaction of a few physical processes, namely non–uniform excitation and distribu-
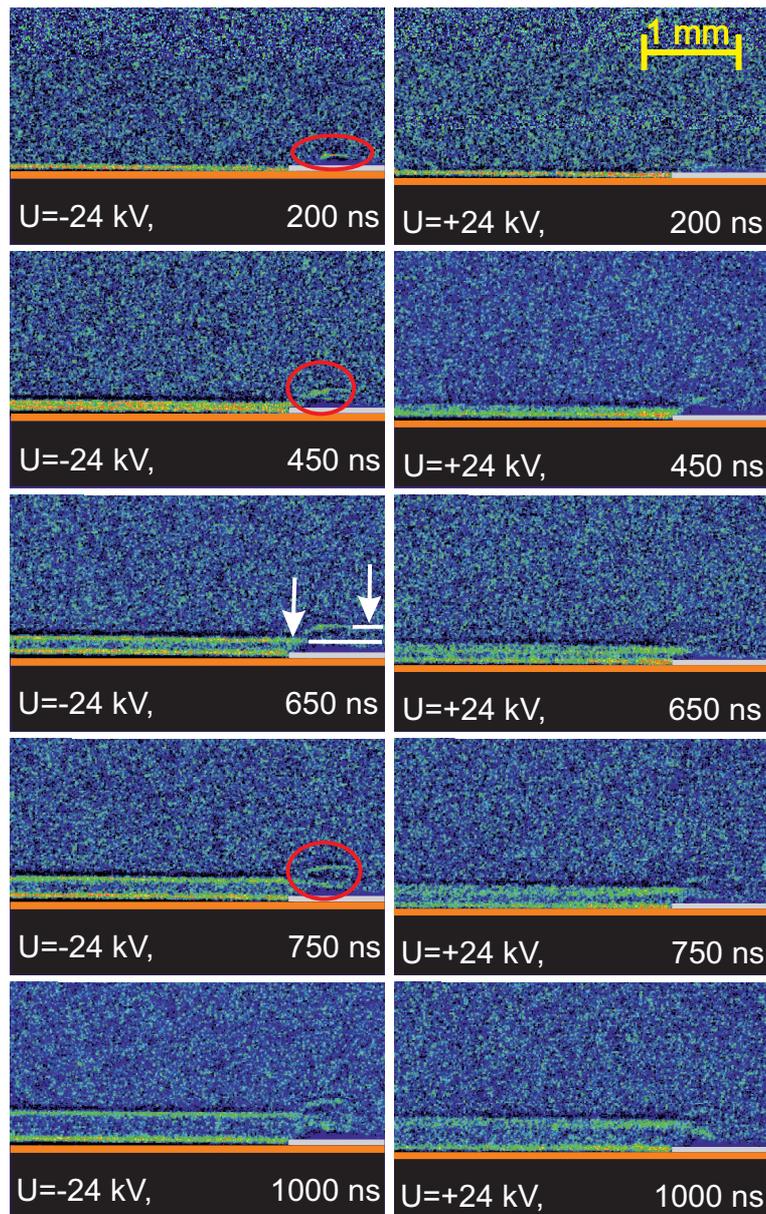
Figure 4.27: Shadowgraphy imaging of the perturbation in the afterglow of the discharge for positive and negative polarities of applied pulses. |U| = 24 kV. Camera gate 10 ns.

tion of active species, fast energy relaxation and hydrodynamics on a sub–millimeter scale. The velocities of propagation of produced compression waves exceed the sound speed in the ambient air and are equal to 385 ± 5 m/s for both positive and negative polarities of applied pulses, but within $6-8$ μs the shock wave transforms to acoustic wave. The velocity of the cylindrical wave is slightly higher than the velocity of the flat front.

The appearance and evolution of the perturbed near–surface region with higher spatial resolution are presented in figure 4.27. It is clearly seen that thin region

can be distinguished ~ 200 ns after discharge initiation. The main difference of this two series of positive and negative polarity streamers is that additional weak wave near the HV electrode can be seen from the shadowgraphy images of negative polarity discharge. It is clearly seen that this wave is absent for positive polarity. For negative polarity streamers the main source of the active species is the cathode layer. It was demonstrated in [7], that the main part of deposited energy is concentrated in the near electrode region for negative polarity. This concentrated energy near the electrode edge produces aforementioned cylindrical wave.

4.7 nSDBD in different electrode configurations

"Classical" airflow configuration nSDBD is a kind of self–regulating system, where a distance between the streamers, the electric field, and the velocity propagation are the parameters strongly influenced by interaction of individual microdischarges – streamers. A question of modification of the nSDBD under artificially produced perturbation of electric field is of special interest.

As it was mentioned above, nowadays the nSDBD in the planar geometry is simulated by 2D plasma sheet. To our knowledge, more complex geometries of nSDBD were not analyzed before. To study the possibility of optimization of the energy release and of the discharge configuration, adapting the last one to a particular combustion system, three different electrode configurations have been tested: classical airflow configuration, a configuration with an artificial perturbation and pin–to–pin surface configuration. All three systems are schematically represented in the upper line of figure 4.28(a), (b) and (c) respectively. The SDBD was initiated by 20 ns positive polarity high voltage pulses with a 30 kV amplitude on the electrode. The experiments were carried out in a single–shot regime.

The ICCD images taken with a camera gate of 1 ns and corresponding to the emission of the second positive system of molecular nitrogen are given by figure 4.28. Time delay relative to the start of the emission in the system is given for each frame.

In the classical airflow geometry (figure 4.25(a)) with a metal strip as the high–voltage electrode, the SDBD starts as a set of synchronous streamers propagating along the dielectric in the direction perpendicular to the HV electrode, the average velocity of propagation is being (2.0 ± 0.5) mm/ns. The picture changes for the HV electrode with a sharp tip. The SDBD develops as a combination of "classical" set of parallel streamers with the same velocity and the discharge initiated at the point of the high electric field, at the vicinity of the electrode tip (figure 4.25(b)). The discharge starts from the pin with a higher velocity (8.0 ± 0.5) mm/ns, then slows down to (2.0 ± 0.5) mm/ns. In a few nanoseconds, both parts of the discharge merge

and propagate as a single structure. This configuration can be interesting for the applications when it is necessary to start the chemical process in the local point(s) and to sustain it further along all the surface of the electrode. Finally, in the pin–to–pin configuration (figure 4.25(c)) the discharge develops in the direction parallel to the axis of the pins, but relatively bright glow is observed around, consisting
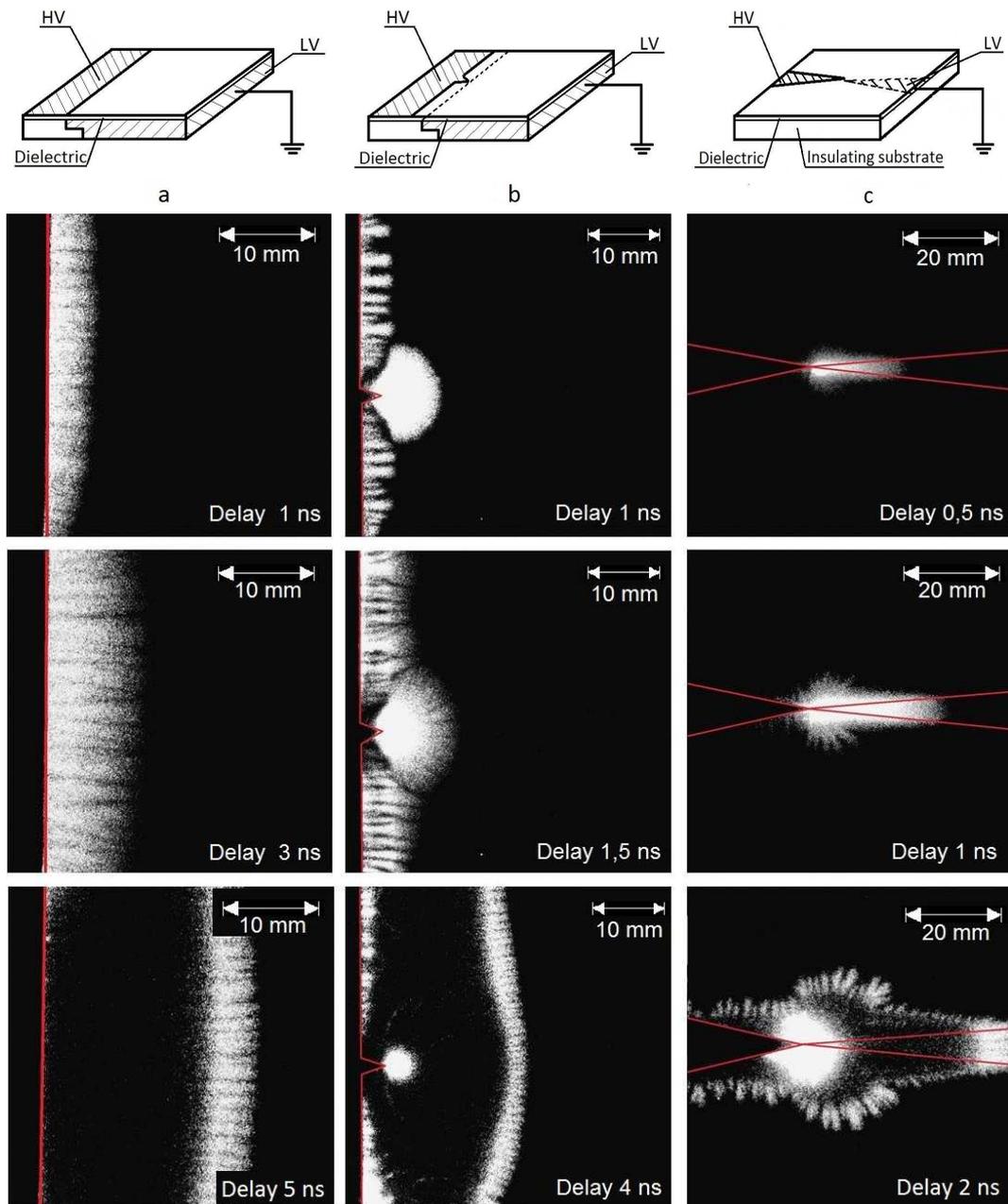
Figure 4.28: Evolution of SDBD in air for different geometries of the high voltage electrode in the system of flat electrodes. For all experiments the voltage of applied pulses was 30 kV on the electrode. ICCD camera gate is 1 ns.

of the streamers propagating in perpendicular direction. This fact underlines a complex structure of the nanosecond SDBD, proving that pin–to–pin geometry does not represent a single streamer but another discharge with different characteristics. The velocity of the main part of the discharge propagating along the pin axis is equal to (15 ± 2) mm/ns. So, modification of the electrode system can result in a significant redistribution of specific deposited energy for different zones of the discharge. Combination of production of active species, heat release and following hydrodynamic perturbations should be optimally chosen to accelerate the ignition in the combustion chamber.

4.8   Conclusion

Systematic experimental studies of morphology, development and plasma parameters for nanosecond surface dielectric barrier discharge (nSDBD) in atmospheric pressure air have been performed. Discharges initiated by high voltage pulses of negative and positive polarities $(24 - 30$ kV amplitude on the electrode, 2 ns pulse rise time, 20 ns pulse duration) in a single shot regime were compared.

It was found that negative and positive polarity nSDBDs propagate as a set of parallel streamers in the direction perpendicular to the high–voltage electrode. The optical diameters of surface streamers are equal 250 μm for negative and 400 μm for positive polarity discharge respectively. Measured velocities of the streamers, ~ 2 mm/ns for negative polarity and ~ 5 mm/ns for positive polarity discharge in the near–electrode zone are in a good correlation with the known results for nSDBDs.

A consistent set of plasma parameters for negative polarity (anode–directed) surface streamers was for the first time obtained on the basis of experimental data. Propagation of negative streamer is supported by intensive ionization in the cathode layer. Significant potential drop along the streamer channel is accompanied by a strong emission of the second positive system of molecular nitrogen. Electric field in the channel, $E/N \sim 70$ Td, was calculated from a maximum length of a streamer propagation. Finally, absolute time–dependent profiles of $E/N(t)$, $n_e(t)$ and $[\mathrm{N_2(C)}](t)$ were obtained for the anode–directed streamer. Measured densities of $\mathrm{N_2(C)}$ are $\sim 7 \cdot 10^{14}$ cm^{-3} in the streamer front and $\sim 10^{13}$ cm^{-3} in the streamer channel and are in a good correlation with the results of calculations.

Electron densities in the streamer head and in the channel for positive polarity streamer were calculated on the basis of experimentally measured streamer velocity. The average electron densities in streamer channels for positive and negative polarity were estimated and are equal to $(7 \pm 0.5) \cdot 10^{14}$ and $(1.5 \pm 0.5) \cdot 10^{14}$ respectively.

The n_e in the head of cathode–directed streamer is significantly lower than in the streamer channel, and decreases during the applied HV pulse duration from $6.5 \cdot 10^{13}$ to $5 \cdot 10^{12}$ cm^{-3}.

The spatial fine structures of cathode– and anode–directed streamers is analyzed with high spatial resolution $(5-10)$ μm. During the first stage of discharge development $(0-4)$ ns, the bright zone corresponding to high energy deposition was detected in near electrode region when negative polarity pulses are applied. Whereas, for positive polarity streamers the intensity is distributed more homogenously along the channel.

Spatial time resolved temperature distribution for positive and negative polarity streamers was measured. The rotational temperature increase does not exceed ΔT= 50 K for both polarities during the applied HV pulse. The vibrational temperature was measured for streamers of different polarities. It was found that the vibrational temperature is not changing significantly during the discharge and is equal to 3000 K for negative polarity and 2600 K for positive polarity of exposed electrode.

It was shown that the discharge morphology can be optimized by changing the configuration of the electrode system: size of streamers, direction of the discharge propagation, energy release and velocity of the discharge front can be optimized with the help of the electrodes geometry changes.

Chapter 5

Nanosecond SDBD at elevated gas densities

Physics of glow discharges at high pressure is a symbiosis of the complicated processes describing the behavior of the discharge and complex kinetics of active species including, at elevated pressures, three-body reactions. In the case of nanosecond SDBD the situation is even more complex because of the presence of the dielectric surface, which contributes to the development mechanisms and characteristics of the discharge.

The morphology of the transient discharge is very sensitive to the gas density, composition of gas mixtures and the polarity and/or frequency of applied pulses. It was found recently [46] that at pressure and/or voltage increase, a single-shot nSDBD transforms into a filamentary form. Streamers start from the HV electrode, slow down and stop. At this instant, a few nanosecond after the discharge start, a set of equidistant channels – filaments – start from HV electrode as a secondary ionization wave. Previous results of nSDBD transformation to filamentary mode were obtained for the discharge of negative polarity in air. At the moment of beginning of the work, no strict explanation of filamentary nSDBD discharge appearance or filaments propagation could be found. Insufficient amount of experimental data does not allow building a complete model. For the moment nothing is known about the electric field, the electron density and spectral composition of optical emission of the filamentary nSDBD.

This chapter describes the experimental results of the discharge transformations at elevated gas pressures (up to 12 bar) in different non–combustible gas mixtures for discharges of both positive and negative polarity of applied pulses. The first part of the chapter is devoted to the overview of so-called streamer–to–filamentary tran-

sition of nSDBD in a single pulse regime that was for the first time seen in the [123]. Also, the experimental results on the positive and negative polarity discharges in different mixtures (air, N_2, N_2/H_2, N_2/CH_4, Ar/O_2, etc.) are described. The second part of the chapter presents the time and space resolved emission spectroscopy study of filamentary nSDBD. The positive and negative polarity filaments are analyzed. A possible mechanism of the discharge contraction is described. The last part of the chapter is devoted to the schlieren spectroscopy study of the hydrodynamic perturbations produced by streamer and filamentary discharges at high pressures.

5.1 Streamer-to-Filamentary transition of nSDBD at high pressures

5.1.1 nSDBD at elevated pressures in air

As it was demonstrated in chapter 4, the atmospheric pressure nSDBD in air consists of hundreds of thin streamers, starting synchronously from the high-voltage electrode and covering in a 'quasi–uniform' manner the dielectric surface. Typical "density" of streamers is about a few streamers per millimeter of the length of the electrode. It depends on the surface properties - material, roughness, thickness and on the parameters of applied high–voltage pulses. Here we will discuss how the gas density and composition of the mixture influence the discharge parameters.

Quasi-uniform phase of the positive column of the glow discharge is often unstable when pressure increases, with fluctuations of the current density and/or as a consequence the heat release. Under certain conditions, the contracted state of the discharge is the most advantageous for several reasons. The formation of filaments is associated with the formation of streamers, but these "streamer–to–filament/spark/leader" transitions are poorly understood and still are the topics of interest for many research groups.

In some particular case it was demonstrated that the contraction of the quasi–uniform (streamer) mode of the nSDBD can be observed in frequency regime [18] of applied voltage. In this case the characteristic time of V-T relaxation correlates with characteristic time of the applied pulses (hundreds of μs) and their periodicity. In this case the temperature of gas increases causing the instabilities and contraction of a quasi-uniform plasma layer.

For the first time the fast contraction of the surface nanosecond discharge was observed in [46,123]. It was found that, starting from a certain values of voltage and pressure, the negative polarity discharge transforms into a regular filamentary structure, when each 4-6 streamers "merge" into one filament, and so, a linear "density"

Filamentary mode,
V=-46 kV, 4 bar, Air

HV electrode

Streamer mode
(quasi-uniform),
V=-35 kV, 2 bar, Air

a)

b)
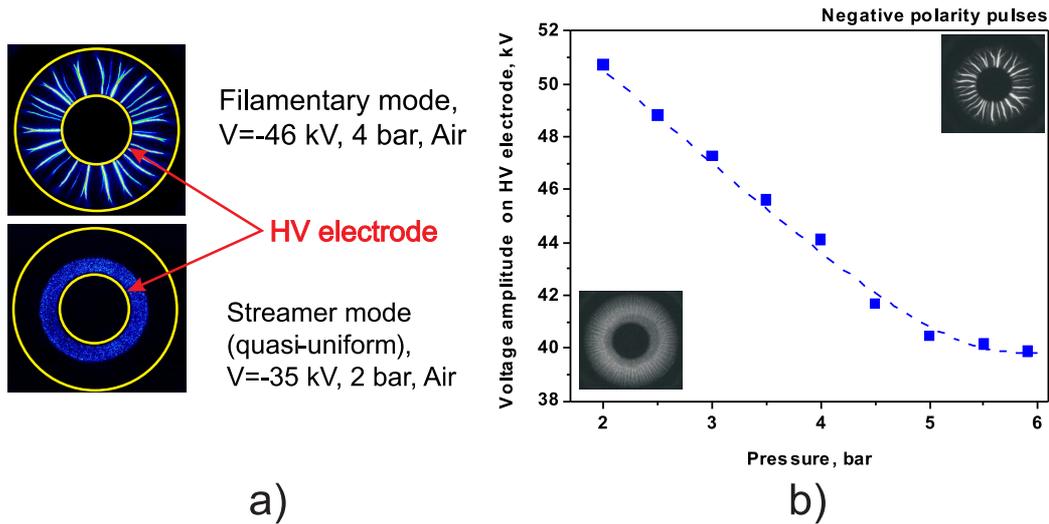
Figure 5.1: (a) Two modes of nSDBD in air. Camera gate 1 ns. (b) Filamentation curve [46]: quasi-uniform (below the curve) and filamentary (above the curve) discharges as a function of pressure and applied voltage (negative polarity, synthetic air).

of filaments is a few times lower than the linear density of streamer channels. No sharp changes of the deposited energy, current and electric field are observed at transition point. Similar to streamers, the filaments start from the near–electrode zone. Morphologically, the picture is close to contraction observed in pulsed–periodical nanosecond discharges, $1-2$ kHz in frequency, at times hundreds of microseconds [18], but a typical time of streamer–to–filament transition comprises a few nanoseconds.

The "streamer–to–filament" transition has been studied in a wide range of parameters (1-6 bar pressure and 12-50 kV pulse amplitude at pulse duration 20-30 ns and rise time dt=0.5 ns) for the negative polarity of HV pulse [46]. Figure 5.1(a) presents ICCD images of the filamentary and of the streamer nSDBDs. In filamentary phase there is no closing of the discharge gap, so the filamentary discharge is not a multi-spark but a kind of transient plasma.

Figure 5.1(b) demonstrates a filamentation curve in air. This curve separates two modes of the nSDBD in (P, U) diagram, where P is a pressure of the gas, U is an absolute value of applied voltage on the HV electrode. Below the curve the discharge propagates like a set of streamers (quasi-uniform discharge), and above the curve the contraction of the discharge is observed. The time instant of contraction depends on pressure and applied voltage. No filamentation was observed for the

positive polarity of the pulse.

So, previous investigations of the nSDBD at high pressure can be summarized in the following way [123]:

1. When positive polarity of applied pulses was used, the discharge remained in a streamer mode within the pressure range $P = 1 - 6$ bar and voltage amplitudes $U < 60$ kV, while negative polarity provokes streamer-to-filamentary transition.

2. The transition is a function of voltage amplitude and gas pressure: if gas pressure is fixed, voltage increase leads to the transition; if voltage is fixed, gas pressure increase leads to the filamentary mode (see figure 5.1b).

3. At the transition point, the streamers decelerate and stop at a certain distance from HV electrode. The bright channels (filaments) start from HV electrode and propagate radially.

4. The number of filaments is 4-6 times lower than the number of streamers and optical diameter of each filament is 3-5 times higher than that of streamer.

5. The rotational gas temperature in the filaments is only 10-20 K higher than rotational temperature in channels during streamer mode.

6. No sharp changes of the energy deposition in plasma is observed at the transition point.

The ionization-heating instability of the cathode layer was suggested [46] as a mechanism of filamentation. The temperature in the cathode layer ($d \sim 1$ μm at P= 3 bar) increases due to the fast gas heating (FGH) processes. The temperature increase leads to decrease of gas density $\rho \sim 1/T$ in the cathode layer that cause the increase of the reduced electric field E/N. The increase of the reduced electric field provokes the electron density increase and thus the current increase as well. The Joule heat $j \cdot E$ is generated and temperature increases again. The positive feedback takes place and it leads to the instability in the cathode layer and to appearance of bright channels propagating from the edge of HV electrode.

The ICCD images of three typical cases of nSDBD at atmospheric and elevated pressures are given in Figure 5.2(c). The first (1 atm, +20 kV) case corresponds to "traditional" morphology of nanosecond surface discharge presented in previous chapter with the only difference that the geometry is coaxial. The velocity of the streamer propagation is in a good correlation with the velocities for the flat electrode system. It should be noted that no visible changes were detected for different edges of the high–voltage electrode, so its sharpness does not seem to be an important parameter.

The third case (6 atm, -47 kV) was described for the first time in [46]. This case corresponds to well developed filamentary discharge. The filaments are distributed uniformly along the perimeter of HV electrodes and their number varies between $20 - 50$ depending on applied voltage and gas pressure. All the filaments have ap-

1 atm, +20 kV

3 atm, +20 kV, reflected

6 atm, -47 kV
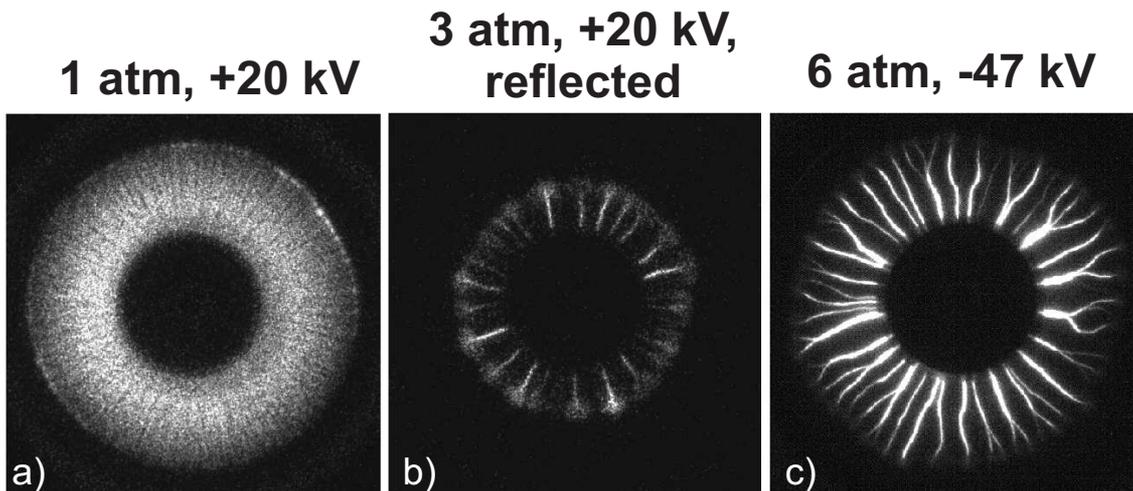
Figure 5.2: ICCD images for the discharges of positive and negative polarities. Discharge in synthetic air, ICCD camera gate is 2 ns.

proximately the same length and in some cases are branched. In the developed filamentary discharge the intensity of filaments is significantly higher than the intensity of aforegoing streamer discharge. As it will be described further, this sharp intensity increase occurs abruptly with the start of filamentary phase. In under-developed filamentary discharge just a few filaments are observed during the pulse duration, they are distributed chaotically along the edge of the exposed electrode and the intensity of the filaments just a few times higher than the emission intensity in the streamers.

The second case represented in Figure 5.2c (3 atm, +20 kV) is the only case corresponding to a "double pulse". "Reflected" in the caption of the figure means that the ICCD image is recorded during the reflected pulse of negative polarity coming, because of mismatching of the cable and the generator, to the discharge system 250 ns after the first pulse of positive polarity (see chapter 3). This case is similar with the stratified structure presented in [11].

Figure 5.3(a) presents the $x-t$ diagram for a few typical regimes where streamer–to–filament transition has been observed. After the transition, filaments in air propagate with a constant velocity, below 1 mm/ns, for a distance of tens of mm. The transition point, where streamers slow down and stop, is indicated in the figure.

It was assumed [46] that the streamers stop when the potential drop on the channel is equal to the voltage on the electrode. At transition point, 3 atm and -47 kV, the longitudinal E/N value was estimated to be approximately equal to 100 Td (which corresponds to electric field value of 25 kV/cm at $P = 1$ atm). Figure 5.3(b) gives a few plots of the position of the streamers head as a function of time for the negative polarity nSDBD fronts at atmospheric pressure together with calculated
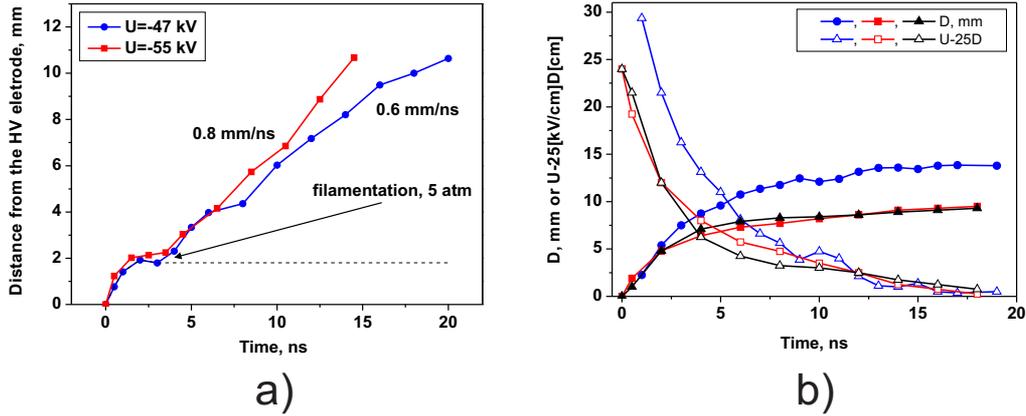
Figure 5.3: **(a) Position of a streamer/filament head in time. Synthetic air, 5 atm, -47 kV and -55 kV; (b) Distance between a streamer head and the HV electrode, D, and $(U - 25 \cdot D)$ value for different voltages U and different lengths of the ground electrode for ambient air, $P = 1$ atm. Blue curves correspond to $U = -35$ kV, length of the ground electrode 70 mm; black and red curves – to $U = -24$ kV and length of the electrode 20 and 7 mm respectively.**

$U - 25 \cdot D$ value ($25[\mathrm{kV/cm}] \cdot D$ representing the rest of potential on the streamer channel under the assumption that the cathode fall is negligible comparing to the voltage amplitude). It is seen that the streamers stop when the voltage drop on the channel is equal to the potential on the high voltage electrode. Similar consideration leads to the conclusion that in filaments and in positive polarity streamers the longitudinal electric field in the channel should be, in any case, significantly lower than in the negative polarity streamers.

5.1.2 The behavior of the nSDBD in different gas mixtures

Transition to filamentary regime, if it exists in the combustible mixtures, can be extremely important for re–distribution of energy in the discharge during the ignition processes. The experiments of the present work, conducted at higher pressures, up to 12 bar, and at lower rise time of the high voltage pulse, $dt = 2$ ns, show that filamentation in air happens at both negative and positive polarity of applied HV pulses; for positive polarity nSDBD at elevated pressures in air, the transition is hindered and observed at higher pressures and amplitudes than for negative polarity. In general, the picture of the filamentation is similar for both polarities (see figure 5.4(c),(d) and figure 5.2(c)). The characteristic times of the discharge filamentation are of the same order of magnitude. The velocities of filamentary discharge
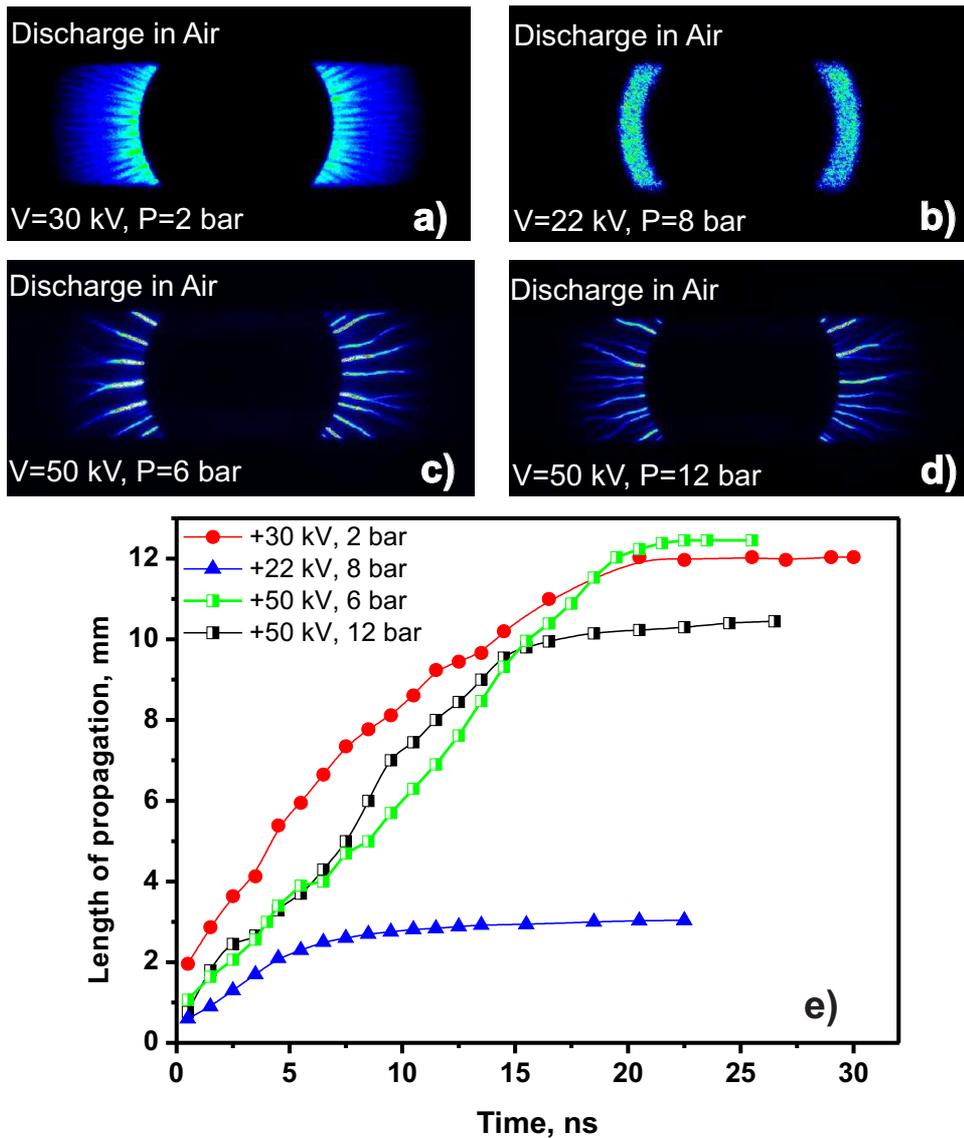
Figure 5.4: Integral ICCD images of positive polarity nanosecond surface barrier discharge (nSDBD) in air for different voltage of applied pulses and pressures: (a) $U = +30$ kV, $P = 2$ bar, (b) $U = +22$ kV, $P = 8$ bar, (c) $U = +50$ kV, $P = 6$ bar, (d) $U = +50$ kV, $P = 12$ bar. ICCD camera gate is 100 ns, pressure and voltage are indicated at each frame. (e) Selected x-t diagrams. ICCD gate is 0.5 ns.

propagation are also close to each other for negative and positive polarity discharges. These velocities, under different gas pressures, can be determined from figure 5.4(e). It is clearly seen, that filamentary discharge at 12 bar propagates almost to the same distance as the streamer discharge at 2 bar.

The filamentation curves that give the information about the range of conditions (P, U) of streamer–to–filamentary transition in different gases and for different
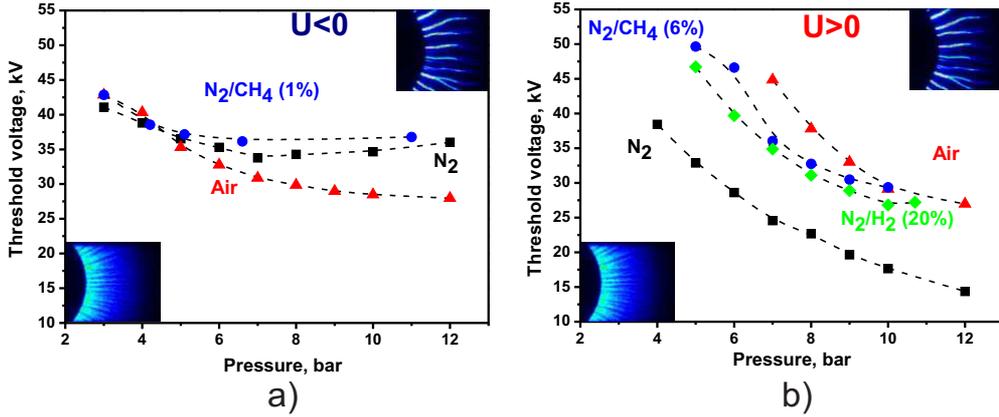
Figure 5.5: Threshold pressure and voltage for streamer–to–filament transition in different gases: (a) negative polarity of applied voltage; (b) positive polarity. Typical ICCD images of streamer and filamentary nSDBD (camera gate is 20 ns) are presented below and above the transition curve. The criterion for streamer–to–filament transition was that the transition happens within first 13 ns of the discharge.

polarities for the pressure range $P = (2 - 12)$ bar and voltage amplitude on the electrodes $U = \pm(10 - 50)$ kV are given in Figure 5.5. The curves are obtained in the following way. The ICCD images were taken with the gate of $\tau = 15$ ns and time delay $\Delta t = -2$ ns relative to the high–voltage pulse coming to the electrode, so that 13 ns of the discharge were captured by the ICCD image. Voltage increased progressively in each experiment. In the case when at least $2 - 5$ filaments were observed in ICCD image, this voltage was considered as a threshold voltage for the filamentation. The experiments were repeated at least 2-3 times, the uncertainty of the threshold did not exceed, depending upon pressure, $\pm(1 - 3)$ kV.

It is clearly seen that, for a wide range of parameters, the transition depends upon pressure and gas nature. At negative polarity, in air and CH_4/N_2 mixture, the threshold voltage decreases with pressure, while for pure nitrogen a minimum is observed at $P \approx 7$ bar. For pressures $P > 4$ bar the negative polarity nSDBD becomes filamentary in air at the lowest U_{th} as compared with the discharge in N_2 and CH_4. The threshold parameters (P_{th}, U_{th}) of streamer–to–filament transition in air slightly differ from the results presented in figure 5.1(b). This can be connected with the difference in pulse shape. In [46] the front rise time of the pulse was 0.5 ns, whereas the generator used in present study delivers the pulses with 2 ns front rise time. However, the difference between the results of present work and the results from [46] does not exceed 3 kV.

When positive polarity was used the picture of filamentary curve is different.

Between the studied mixtures, the nitrogen gas without any additives has the lowest (P_{th}, U_{th}) parameters for positive polarity nSDBD. Addition of oxygen, CH_4 or H_2 to N_2 results in significant increase of the filamentation threshold. In nitrogen the threshold of filamentation is close for positive and negative polarities within the pressure range $P = 2 - 5$ bar; at higher pressures $5 - 12$ bar, the filamentation occurs "easier" for positive polarity nSDBD.

The filamentation occurs within a few nanoseconds after the discharge start. The time instant of the discharge contraction depends on pressure, polarity of applied pulses and composition of gas mixture. Figure 5.6 demonstrates the time of filamentation start τ_f in air and N_2 for positive and negative polarities as a function of gas pressure. It is clearly seen that τ_f decreases linearly with gas pressure. As it will be discussed further, the filamentation occurs due to the formation of anode and cathode spots. The filamentation time is determined by the total time of the formation of the cathode layer (anode region) and the time of the formation of cathode (anode) spots τ_{spot}. According to [124], τ_{spot} is determined by the time of the cathode layer zone passage by the ions. As it is shown in figure 5.6, the rate of the discharge transformation into filamentary mode is opposite in air and nitrogen. Filamentation happens faster for negative polarity in air, and for positive polarity in nitrogen. The presence of the electronegative gas - oxygen, influence significantly the formation of the near electrode region.

A typical behavior of the nSDBD discharge in different gases is represented as a table in figure 5.7. The discharges in air, Ar, N_2, N_2:CH_4 and in ArO_2 are shown to demonstrate how the discharge morphology depends on the composition of gas mixture. The images were obtained with the camera gate 20 ns to capture whole period of applied pulse. The sensitivity of the camera remains the same for all images.

The first column in the figure 5.7 shows the streamer discharge in air and argon at different applied voltages and pressures. Under the pressure of $P = 1$ bar and voltage on the electrode $U = -20$ kV the discharge propagates as streamers covering homogenously the dielectric layer. The length of streamer propagation is rather sensitive to the gas pressure. The cases of $P = 1$ and 5 bar for a fixed applied voltage $U = -20$ kV demonstrate how the propagation length decreases almost 5 times for elevated pressure. For positive polarity pulses, the behavior of the discharge is similar with pressure increase. However at relatively high applied voltages f.e. $U = +50$ kV, the bright channels can be emphasized upon the diffuse glow of streamers. This bright channels appear at the trailing edge of HV pulse. The last image in the first column correspond to the discharge in argon. The discharge in argon develops with significantly higher velocity and, in the considered electrode configuration, entirely covers the surface of the electrode within a few nanosecond.
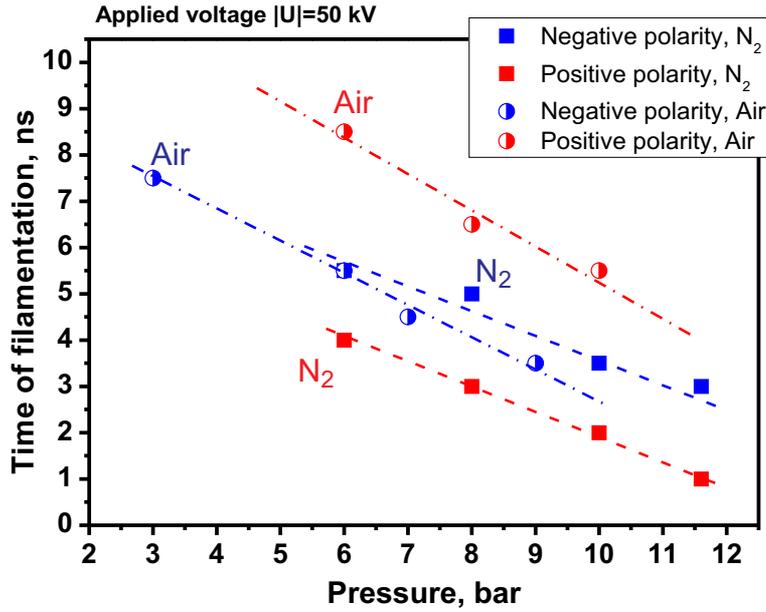
Figure 5.6: The time moment of filamentation (starting from the discharge appearance) in air and N_2 as a function of gas pressure. Applied voltage for both positive and negative polarity is |U|=50 kV.

The emission intensity of the nSDBD is significantly higher than in air or N_2, even if applied voltage is lower.

The first two images of second column of the table (figure 5.7) present the discharge morphology just below the filamentation threshold. In this case the bright channels on the trailing edge appear, but no filaments on the plateau of the HV pulse are observed. If we increase a little bit the voltage of the applied pulse, we get a so–called transitional mode, e.g. the filamentation takes place, but regular structure of filaments is not yet organized ($P = 3$ bar, $U = -50$ kV). The images of well developed filamentary discharge are shown in two last pictures of the second column (Air, $P = 7$ and 6 bar, $U = +55$ and -50 kV respectively). It is clearly seen, that the filaments are arranged periodically along the edge of the HV electrode.

Third and fourth columns of the figure 5.7 demonstrate the discharge at fixed gas pressure and applied voltages, but in different gas mixtures and polarities of applied pulses. The third column shows the images of positive polarity nSDBD and fourth column shows the negative polarity nSDBD at $P = 8$ bar. The amplitudes of applied pulses are $U = \pm 50$ kV. The following gas mixtures are used: N_2, air, N_2H_2 (7:1), N_2CH_4 (15:1), ArO_2 (5:3). Both positive and negative polarity filamentary nSDBDs either in N_2 or in air are well developed. The difference in discharge morphology is related to the length of filaments propagation and the linear density of filaments
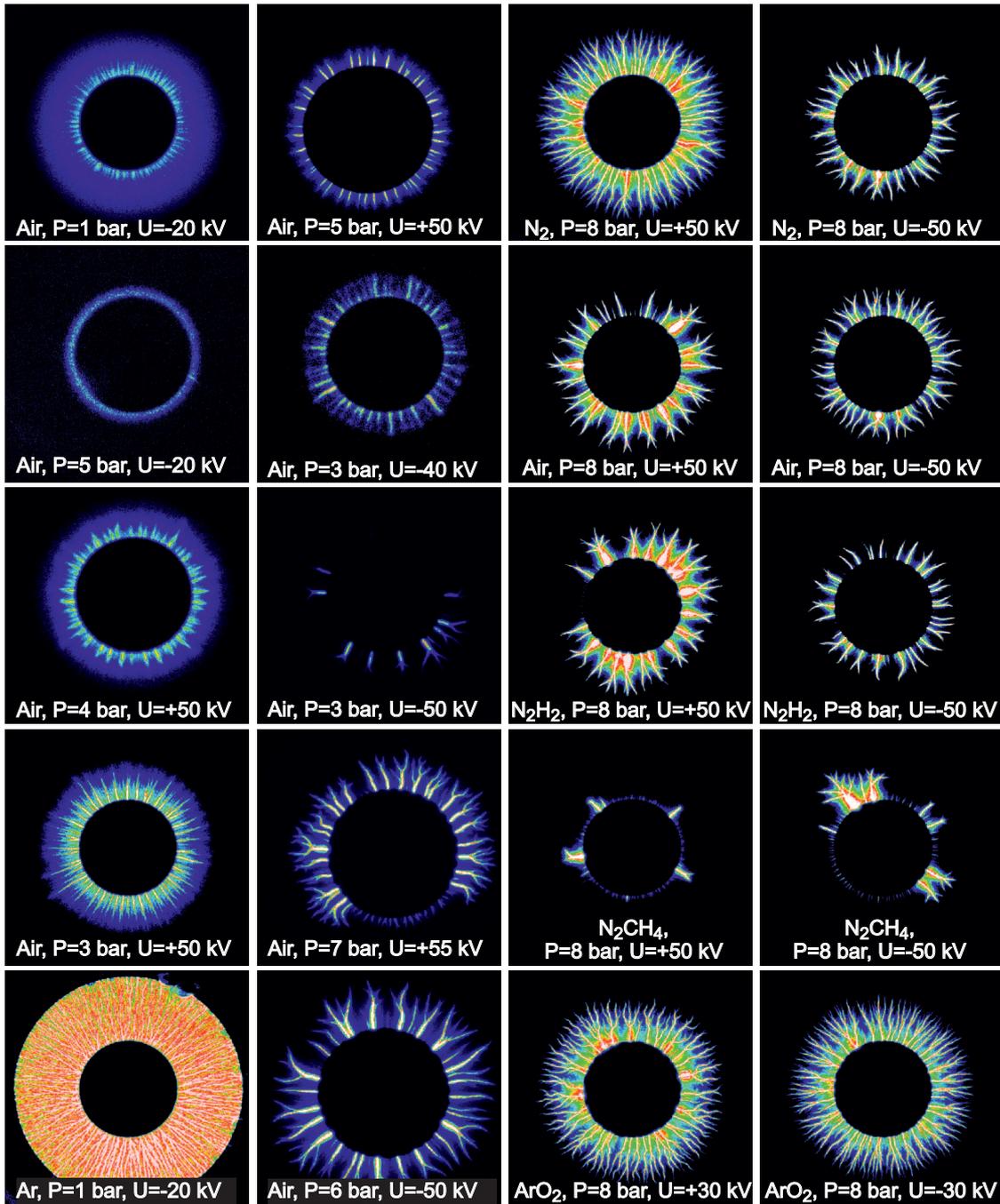
Figure 5.7: Integral ICCD images of the discharge in different gases. The applied voltage, pressure of the mixture and gas are indicated in the images. Camera gate is 20 ns.

per length unit of the HV electrode edge. Additives of hydrogen or methane in pure nitrogen hinders the filamentation processes for both polarities. A well developed and branched filamentary discharge can be also observed in ArO_2 and ArH_2 mixtures. Any additives of diatomic gases into argon lead to discharge transformation

into filamentary phase at high pressures. In pure argon the filamentation of nSDBD was not observed up to $P = 15$ bar and $U = \pm 55$ kV.

We believe that the nature of the filamentation of nSDBD considered in present work is cardinally different from the filamentation in [72] and in [74]. For volumetric discharge in pin–plane configuration the homogenous discharge in air becomes filamentary with 6% of methane and n-heptane additives [74]. For the discharge considered in [74] the photoionization may play an important role. Typically, addition of hydrocarbons or other molecules with a large cross-section of UV–absorption decreases the photo–ionization length [83] and so, decreases the discharge uniformity [5, 72]. Transition of the volumetric diffuse discharge in air in a multichannel discharge structure has been observed for atmospheric pressure at small addition of hydrocarbons corresponding to lean mixtures (CH_4 at ER=0.3 and C_3H_8 at ER=0.8) [72]. This is in correlation with experimental results of [5], where a multichannel discharge structure was observed at C_3H_8 additions on the level of 2% (ER=0.52). This correspond to the following densities of hydrocarbons: $[CH_4] \approx 7 \cdot 10^{17}$ cm^{-3}, and $[C_3H_8] \approx 5 \cdot 10^{17}$ cm^{-3}. For the radiation at the wavelength range $\lambda = 98 - 103$ nm, this gives, taking into account the cross–sections from [13], the absorption coefficient $20 - 30$ cm^{-1}atm^{-1}. Another important issue is a decrease of ionizing UV radiation because of quenching of the emitting states, $N_2(b^1\Sigma)$. These factors are very important for the problem of plasma–assisted combustion by nanosecond discharges, as far as densities of hydrocarbons and H_2O molecules, absorbing efficiently UV–radiation, can be high in combustible mixtures.

The energy deposition in the discharge significantly depends on the discharge structure and composition of the gas mixture. Figure 5.8(a) summarizes measured total energy deposition in different gas mixtures. The corresponding images of the discharge are presented in figure 5.7, third and fourth columns. For all cases the pressure and applied voltages are equal $P = 8$ bar and $|U| = 50$ kV respectively. It is clearly seen that in air and N_2 for fixed voltage, energy deposition is higher for positive polarity of applied pulses. However, if compare the energy depositions (ED) for $P = 6$ bar, the situation is changed: ED= 45 mJ for negative and 40 mJ for positive.

The discharge transformation leads to change of total electrical current. Figure 5.8(b) shows the total current of the discharge in air at different pressures. As one can see, when discharge propagates as streamers (2 bar, green curve), the sharp peak of the current can be seen at the very beginning and then the current decreases and takes a fixed value on the HV pulse plateau and then return current stroke takes place at the trailing edge of the pulse. This case is described in detail in section 4.5. In this case no filamentation is observed. When pressure is increased to 4 bar (black curve), the current peak at the very beginning still takes place, but further one

a)	Air	N$_2$	N$_2$:H$_2$=(7:1)	N$_2$:CH$_4$=(15:1)	Ar:O$_2$=(5:3)
+U	47 mJ	50 mJ	26 mJ	9 mJ	33 mJ
-U	33 mJ	36 mJ	28 mJ	13 mJ	34 mJ
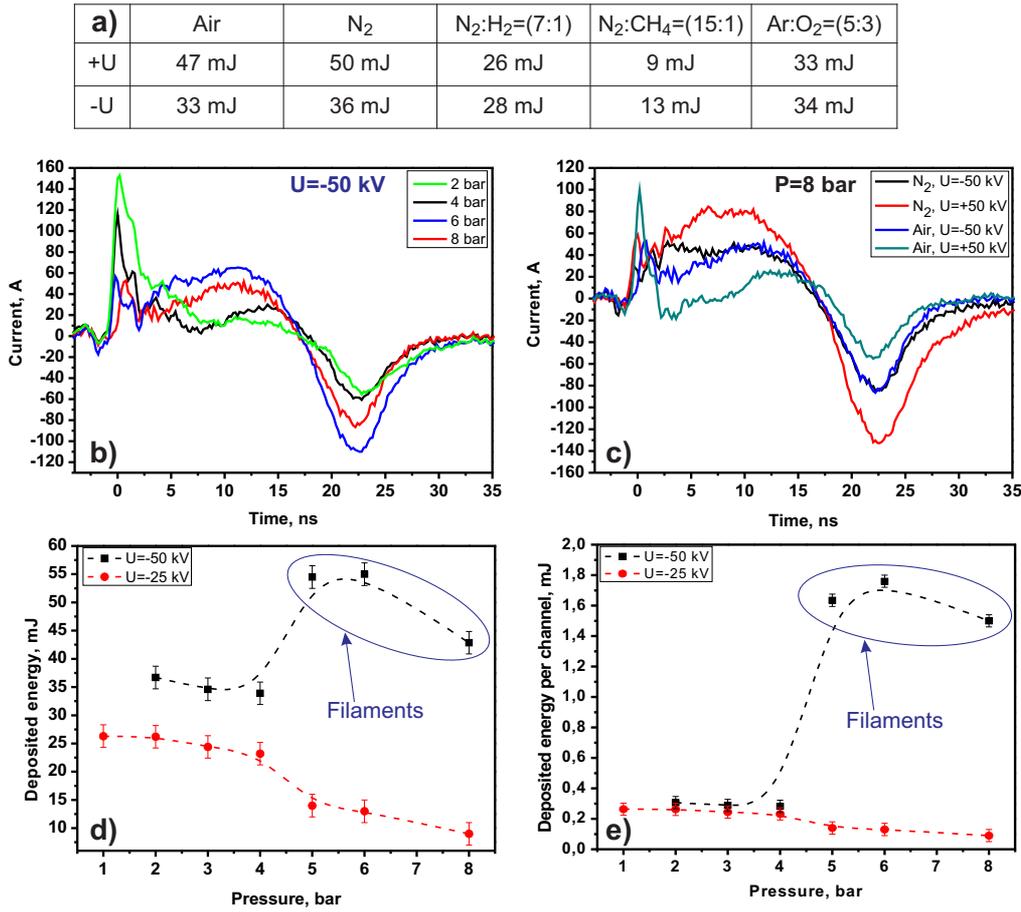
Figure 5.8: (a) Table of energy depositions in different mixtures. Pressure is 8 bar for all the mixtures. Applied voltage is 50 kV for all mixtures except Ar:O$_2$. For Ar:O$_2$ $|U| = 30$ kV; (b) Total current of the discharge in air for different pressures. Applied voltage is $U = -50$ kV; (c) Total current of the discharge in air and N$_2$ for positive and negative applied pulses ($|U| = 50$ kV); (d) Total energy deposition of the discharge in air for different pressures. Two cases: $U = -50$ and -25 kV; (e) Energy deposition per discharge channel in air for different pressures. Two cases: $U = -50$ and -25 kV.

more region of current increase can be seen during the period $10 - 15$ ns, on the plateau of the HV pulse. This peak corresponds to the current passing through the filaments, as far as with increase of pressure (6 and 8 bar) the current changes with two geometric parameters: number of the filaments and the propagation length of the filaments.

It can be seen by comparing the current curves corresponding to pressures 6 and 8 bar in figure 5.8(b) that both current on the plateau and current of return stroke on trailing edge are higher for $P = 6$ bar. The power dissipated in the discharge does not

depend on the direction of the current flow, thus the return stroke of applied pulses significantly influence the total energy deposition. Figure 5.8(c) demonstrates the comparison of total current of the discharge in air and N_2 for fixed absolute value of applied voltage. This current picture correlates with the discharge images presented in figure 5.7. The most developed filamentary phase correspond to the discharge of positive polarity in N_2.

The total energy deposition for two applied voltages $U = -25$ and -50 kV for the discharge in air and energy deposition per discharge channel as a function of gas pressure are shown in figure 5.8(d) and (e) respectively. In the first case, when applied voltage is $U = -25$ kV, the discharge always is in quasi–uniform mode. When the voltage amplitude is $U = -50$ kV, the discharge in air at pressures 5, 6 and 8 bar is filamentary. It is clearly seen that the total deposited energy is higher for the filamentary discharge and is not very dependent on gas pressure for streamer SDBD in the pressure range $1 - 4$ bar. It can be noticed, that for filamentary discharge the energy deposition has a maximum at $P = 5 - 6$ bar, and then decreases with pressure, despite that the discharge remains filamentary. As far as the deposited energy is proportional to the product $\mathbf{j} \cdot \mathbf{E}$, there are two possibilities to get high deposited energy in the filamentary mode: (i) the electric field in the filaments is higher than in streamers; (ii) the electron density n_e is higher in filaments. These points will be discussed when analysing the filaments optical emission.

In surface discharges, the electron emission from the surface of dielectric under the action of UV radiation of the streamer head can be an important additional process sustaining the discharge propagation. So, the experimental study of parameters and of a structure of the surface dielectric barrier discharge with a different fraction of hydrocarbons or H_2O molecules in the mixture at fixed high voltage pulse characteristic, pressure and temperature is an important task in the problem of plasma–assisted combustion.

Summarizing current experimental knowledge of a nanosecond discharge at high pressures at different mixtures, it is possible to conclude the following: filamentation is a fundamental property of nSDBD in a single shot regime at elevated pressures and voltages, for both polarities of the high–voltage pulse. With pressure increase, the velocity and the maximal distance of the discharge propagation decrease. With voltage increase at constant pressure, the velocity of the discharge and the maximal length of propagation increase, but no scaling on PU parameter is observed: pressure increase typically causes significant morphological changes of the discharge. The process of streamer–to–filamentary transition is triggered passing some combination of (P_{th}, U_{th}) that depends on the gas nature. The optical emission of the filaments is significantly higher than the emission of streamers. The analysis of the emission of the discharge at elevated pressures is considered in the next section.

5.2 Emission spectroscopy of the nSDBD at elevated pressures

5.2.1 Analysis of the emission intensity and electrical current

As it was shown in the previous chapter, the electric field in the plasma channel can be analyzed on the basis of the intensity of optical emission and electrical current. Figure 5.9 presents ICCD images together with measured electrical current. The ICCD images of a sector of the discharge are presented by figure 5.9(a); total electrical current through the discharge is given by figure 5.9(b); and finally, integral ICCD images of the discharge in streamer and filamentary modes are shown in figure 5.9(c).

Figures 5.9(a) compares the time resolved ICCD images of streamer and filamentary discharges. The images were taken with the same sensitivity of the camera, that is with the same camera gate and gain. It is clearly seen that the intensity of the streamer at $P = 2$ bar is higher than the streamer intensity at the beginning of the discharge at $P = 6$ bar. After 4 ns bright channels with higher intensity, filaments, start from the HV electrode. When filaments appear (4 ns), the week glow of the streamers along the perimeter of HV electrode fills the inter–filamentary space. When filamentary phase of the discharge is quite well developed (7 and 9 ns), the week glow between the filaments disappears, and only bright channels can be distinguished.

As it was mentioned above, no sharp changes of the power absorbed by SDBD is observed at the moment of quick change of the discharge spatial structure. However, the current changes can be observed by comparing the total current of filamentary and streamer discharges. The temporal evolution of the total current is demonstrated in figures 5.9b for two considered cases ($P = 2$ and 6 bar, with the same applied voltage $U = -47$ kV on electrode). The current at the very beginning of the streamer discharge at $P = 2$ bar is twice higher than for the discharge at 6 bar. That correlates with the difference in the emission intensity. But afterwards, when filamentation starts, the current increases (black curve) and a few nanoseconds after (7-9 ns after the discharge start) it exceeds the current of streamers (red curve). After 12-15 ns, the current of filaments significantly higher than that of streamers. If the current of streamers is $I_{st}(12\ ns) \simeq 15$ A, the current of filamentary discharge is about $I_{fil}(12\ ns) \simeq 60$ A. More than that, the current per channel increases also due to the fact that the number of filaments at $P = 6$ bar is $3 - 5$ times smaller than the number of streamers at $P = 2$ bar. Assuming that there is no current between filaments or that it can be neglected comparing to the current in the fila-
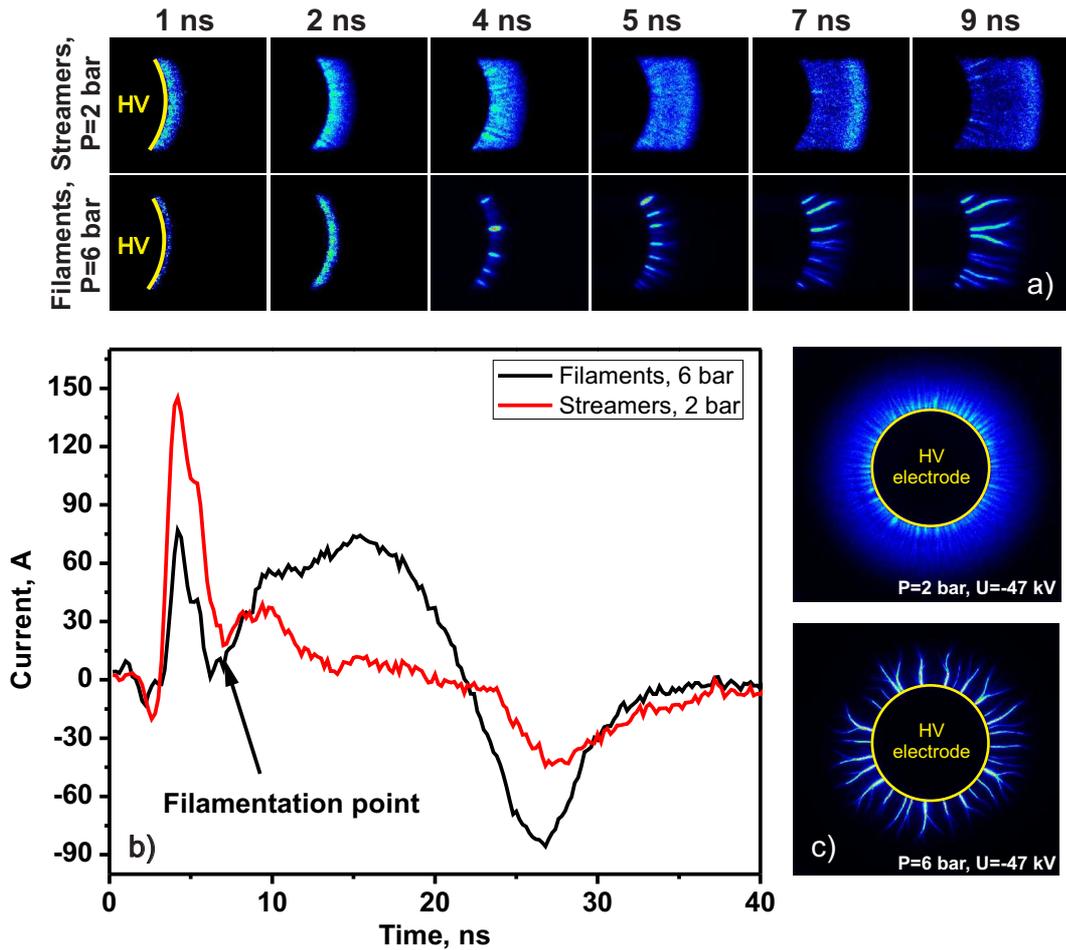
Figure 5.9: (a) ICCD images of the streamer ($P = 2$ bar, $U = -47$ kV) and filamentary ($P = 6$ bar, $U = -47$ kV) discharges in air. Camera gate is 0.5 ns; (b) Current in the discharge; (c) integral ICCD images of the streamer ($P = 2$ bar, $U = -47$ kV) and filamentary ($P = 6$ bar, $U = -47$ kV) discharges in air. Camera gate is 30 ns.

ments, the ratio between the current per filament and the current per streamer is $(I_{fil}/N_{fil})/(I_{st}/N_{st}) \approx 10$.

The emission from the filamentary discharge is bright comparing to the streamer discharge. To compare the emission quantitatively, a custom–made code was developed to analyze automatically the intensity of 2D picture of optical emission [125]. Figures 5.10(a) and (b) demonstrate a typical ICCD image of the discharge in air and corresponding intensity profile as a function $I(\alpha)$, where $\alpha = [0; 360]$ is an azimuthal angle in the plane of electrode. The background was subtracted from the ICCD image of the discharge. It can be noticed from figures 5.10(b) that the intensities of the filaments are different but have the same order of magnitude and also,

a)   b)
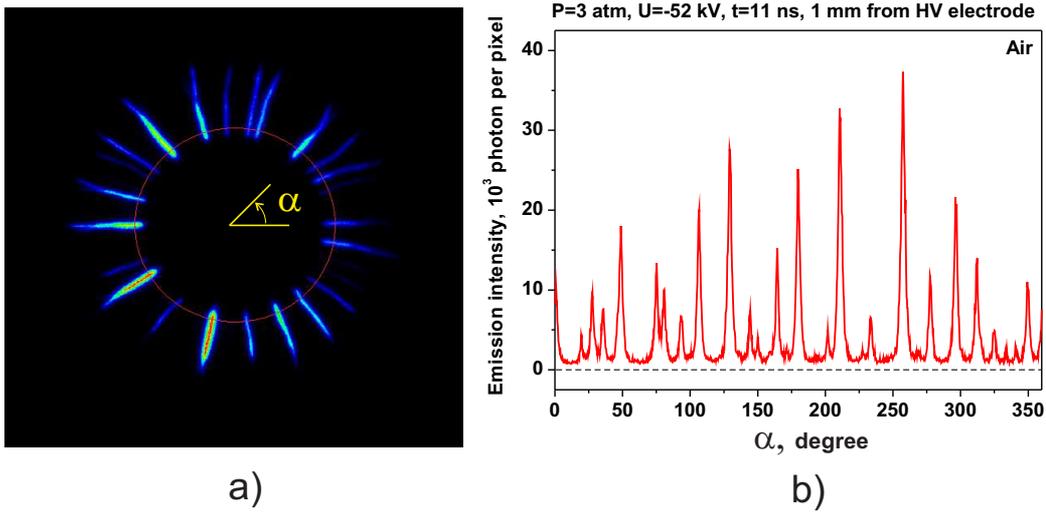
Figure 5.10: a) Frontal ICCD image of the discharge at P=3 atm, U=-46 kV, t=11 ns. Red circle notes the distance 1 mm from HV electrode; b) Angular distribution of the frontal emission intensity at 1 mm from HV electrode; Synthetic air. Single pulsed discharge [125].

a non–zero level of intensity can be detected between filaments.

To separate streamer and filament discharges on the ICCD images, we used the facts that a few first nanoseconds the nSDBD develops in a streamer mode, and that the transition happens within even shorter period of time. Pictures in the upper line of figure 5.11 give the ICCD images of the nSDBD in air for the conditions of the streamer–to–filament transition ($P_c = 3$ bar, $V_c = -46$ kV). The difference between the set of images (a), (b) and (c) is a time delay from the beginning of the discharge; all the images are taken with the camera gate $\Delta t = 2$ ns. Plots in the lower line of the figure show treated automatically relative intensity of emission in streamer (a) and filamentary ((b) and (c)) phase of the discharge. It is clearly seen that the intensity in the streamer (diffuse) mode is relatively weak, 300 counts is a typical averaged value; in the filamentary mode, the intensity of diffuse emission between the filaments (not seen because of the contrast with emission from the filaments) is close to the intensity in the streamers before transition (b); finally, intensity of optical emission in the filaments is more than one order of magnitude higher, 15000 counts (c):

$$I^{dif}_{4\ ns}/I^{dif}_{10\ ns}/I^{fil}_{10\ ns} \approx 1/1.8/50 \qquad (5.1)$$

where I^{fil}_{10ns} and I^{dif}_{10ns} are intensities in filaments and between them at the time moment $t = 11$ ns, I^{dif}_{4ns} - the intensity of streamers before filamentation. It should be also noted that the distribution of the emission intensity in radial direction in
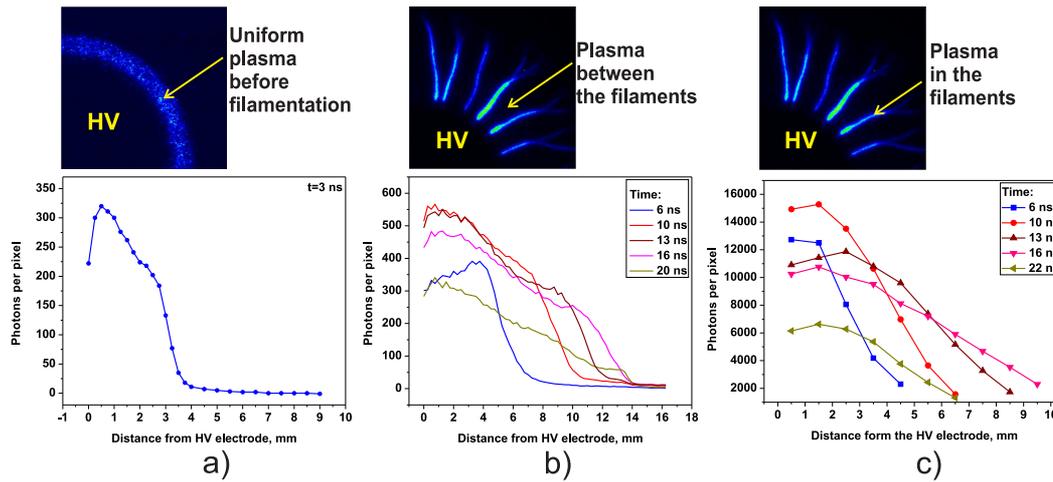
Figure 5.11: Radial distribution of the frontal discharge emission: (a) quasi-uniform discharge at $t = 4$ ns before filamentation; (b) filamentary discharge at different instances. Radial distribution of the emission intensity in the filaments; (c) filamentary discharge at different instances. Radial distribution of the emission intensity of the plasma between the filaments. $P = 3$ bar, $U = -47$ kV.

both filamentary and inter-filamentary regions of the discharge is quite smooth and the sharp changes do not occur at any distance from HV electrode.

All previous ICCD images of the frontal view of the discharge presented in the chapter are the result of the emission accumulation from the entire thickness of plasma layer. A sequence of side ICCD images was done in order to estimate at least the upper limit of the plasma thickness in the direction perpendicular to the
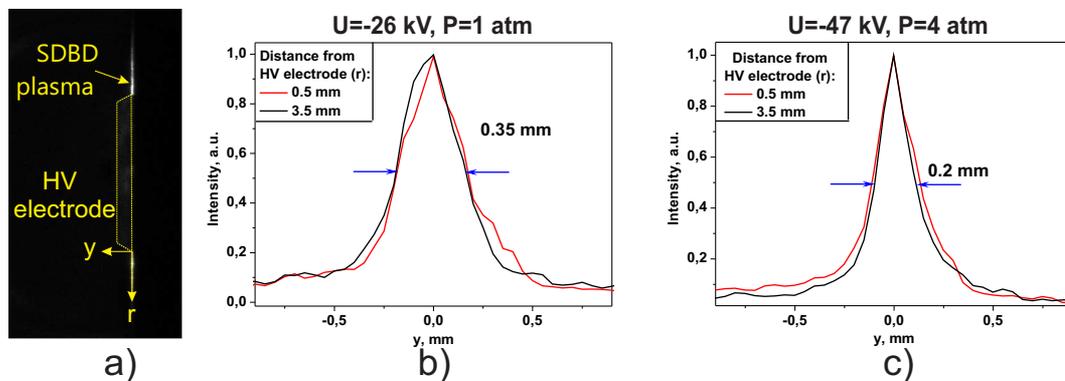
Figure 5.12: (a) Side view intensity distribution in air; (b) and (c) are normalized intensity profiles of the discharge in y-direction for P = 1 bar, U = −26 kV (streamer discharge) and P = 4 bar and U = −47 kV (filamentary discharge) respectively.
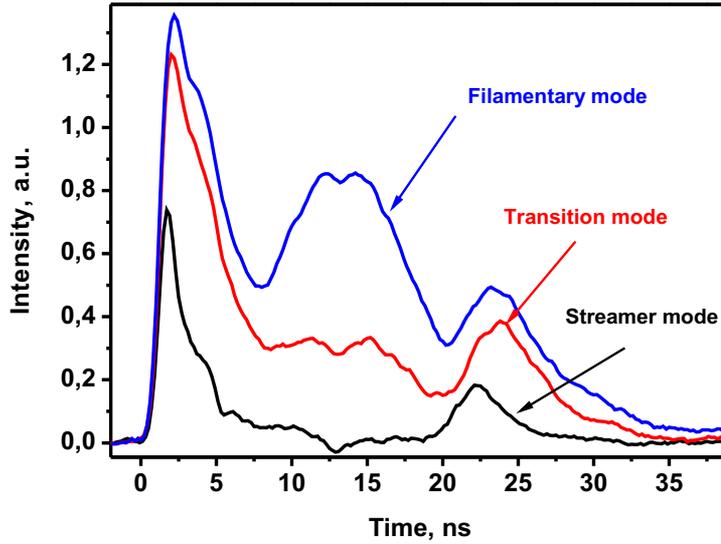
Figure 5.13: Emission profiles of $\lambda = 337.1$ nm for $P = 3$ bar: (1) quasi-uniform mode, $U_1 = -36$ kV; (2) transition mode, $U_2 = -46$ kV; and (3) filamentary mode, $U_3 = -55$ kV. Emission collected from the ring diaphragm between 2 and 4 mm from the HV electrode [46].

dielectric surface. Figure 5.12(a) demonstrates a typical side view of the discharge.

Figures 5.12(b) and (c) present the distributions of the normalized emission intensity in the direction y perpendicular to the surface at different distances r from the HV electrode. These experiments were not specially dedicated to the measurements of intensity distribution in the direction perpendicular to the electrodes or to the measurements of a fine structure of the discharge. Although a special case has been taken, by the rotation of the whole electrode system, to get a minimum possible thickness, these measurements should be considered as an experimental estimate of the upper limit of the thickness of a plasma layer. A characteristic optical thickness of the discharge comprises $100 - 400$ μm and practically does not change with the distance from the high–voltage electrode, that is along a plasma channel. The distribution of the emission in the direction perpendicular to the dielectric surface is smooth, with a single well–pronounced maximum. It should be noted that no significant changes were observed for different gas mixtures. The most pronounced difference is related to the decrease of the thickness of a plasma layer with pressure, which seems to be reasonable.

So, the intensity in the filaments is significantly ($\sim$50 times) higher than the intensity of streamers and the intensity of the discharge between filaments. As it was mentioned above, the emission of the surface nanosecond discharge at the

considered conditions is mainly due to the emission of the 2^+ system of molecular nitrogen. However, according to previous results described in [46] and represented in figure 5.13, the time intensity profile of the (0-0) band of $N_2(C^3\Pi_u)$–$N_2(B^3\Pi_g)$ transition does not demonstrate the sharp, a few tens times, intensity increase of the 2^+ system emission. If the intensity increase does not come from the molecular nitrogen emission, where does it come from?

5.2.2 Emission spectra of streamer and filamentary nSDBD

To understand why the intensity of the filaments is much higher than the intensity of streamers, it is necessary to compare the spectral structure of both type of the discharge. The emission spectra of the streamer and filamentary discharge are represented in figure 5.14(a). The spectra were recorded in the range $280 - 450$ nm. The camera gate was 50 ns, e.g. the spectra were accumulated within the whole HV pulse duration including trailing edge and early afterglow ($15 - 20$ ns after pulse). The presented in figure 5.14(a) and (b) spectra were obtained from the entire surface/volume occupied by the discharge. The frontal window of the high pressure chamber was placed 20 cm from the entrance slit of the spectrometer and the emission of the discharge was focalized on the slit with $f = 7$ cm fused silica lens. The number of accumulation during the spectra acquisitions was 100. The backgrounds for all presented spectra were subtracted. Since the filaments are not tied to a fixed location on the HV electrode edge, the spectra represent the sum of spectra corresponding to filaments and inter–filamentary space.

Figure 5.14(a) represents the normalized emission spectra of the streamer (black curve, $U = -47$ kV, $P = 2$ bar) and the filamentary (red curve, $U = -47$ kV, $P = 6$ bar) discharges in air. The obtained spectra are not calibrated on the transmission function of the spectral system. The emission spectrum of the streamer discharge consists of the second positive system of molecular nitrogen in the considered spectral range. As far as the spectrum of the 2^+ system of N_2 appears during the first nanoseconds of the discharge, we conclude that the $N_2(C^3\Pi_u)$ excitation is mainly due to direct electron impact, and so, the electric fields in the streamer discharge are relatively high, in a reasonable agreement with the results of the previous chapter.

Two different types of emission can be separated in the filamentary discharge: the emission of molecular bands, mainly of the 2^+ system of N_2, and the cw emission. Continuum emission in visible and UV-parts of spectra has been observed earlier in high power nanosecond discharges [126–128], initiated in atmospheric pressure air between two metal electrodes separated by 1-2 cm, by high voltage pulses of units-tens of nanoseconds in duration and 150-250 kV in amplitude. Typically, at these conditions the atomic lines corresponding to materials of electrodes are
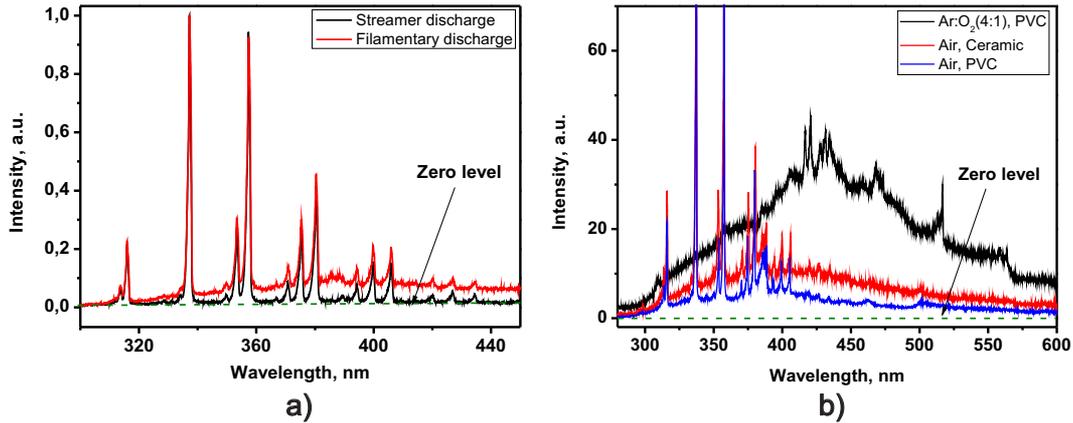
Figure 5.14: (a) **Normalized emission spectra of the streamer ($P = 2$ bar) and filamentary ($P = 6$ bar) discharge (U=-47 kV); (b) Emission spectra of the filamentary discharge in Ar/O_2 and in air. Two dielectric layers are compared: (i) ceramics and (ii) PVC. Applied voltages are $U = -47$ kV in air and $U = -40$ kV in Ar/O_2. Pressures of both gases was $P = 6$ *bar*. The spectra are not corrected to the sensitivity function of the optical system.**

clearly observed [126]. This is confirmed [129] by a direct comparison, at the same conditions, of nanosecond discharge and nano- and femtosecond optical breakdowns caused by action of laser generation on the gas. Somewhat more "soft" spectra were observed in [127] presenting a broadband radiation detected in visible range of spectra in discharge in ambient pressure developing in 3 cm gap under the voltage pulse 90 kV in amplitude, where no materials of electrodes are detected but the lines of ionized nitrogen atoms are clearly seen. Similar spectra, with atomic N-ions lines dominated over the cw emission, were observed in [49] in emission of constricted SDBD powered by a burst of unipolar pulses 400 μs in duration and 20 kV in amplitude. It should be noted that the most of presented spectrum are so-called review spectrum not calibrated for the spectral sensitivity of the system, and the decay in the UV-region is because of the transmission of optics. High-voltage nanosecond discharges excited in open atmosphere at high overvoltages generate [126] high energy runaway electrons and secondary X-ray bremsstrahlung. X-ray doses of the order of magnitude $60 - 200$ μR/shot have been reported in [128] for $250 - 270$ kV discharge in atmospheric pressure air.

There are several known reasons of CW spectrum appearance: (i) the emission spectra of some molecular bands (continuum of molecular hydrogen, NO_2^* emission); (ii) heavy polyatomic molecules with a large number of internal degrees of freedom;
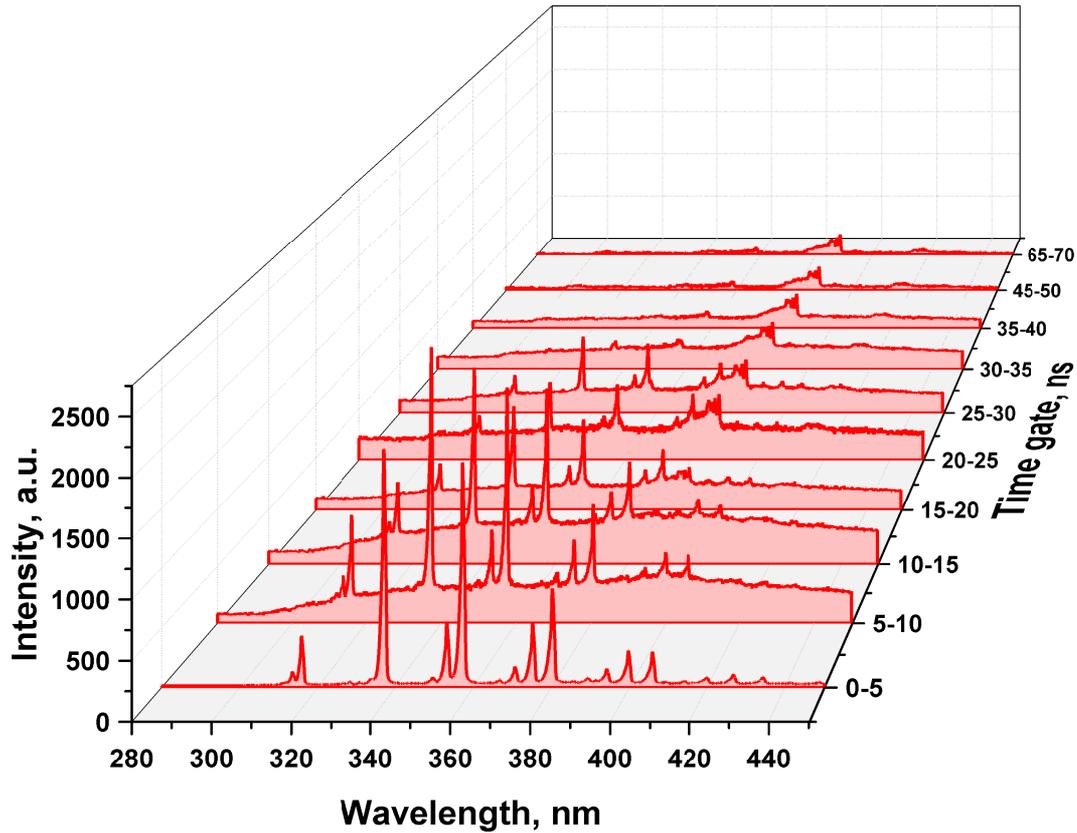
Figure 5.15: Time resolved emission spectra of filamentary discharge in air ($P = 6$ bar, $U = -47$ kV). Camera gate is 5 ns. The spectra are not corrected to the sensitivity function of the optical system.

(iii) Plank spectrum; (iv) bremsstrahlung radiation; (v) recombination emission.

No lines corresponding to the material of electrode were found in the spectra. Further, although after a long time of operation (a few weeks) the "microgrooves" are visibly produced on the surface of the PVC, we do not believe that ablation of the material of the dielectric is a reason of the cw emission. First, the cw spectrum is observed from the very first experiment and in any studied gas mixture. As it is shown in figure 5.14b, the cw spectra are observed in air and in Ar/O_2 (4:1) mixtures. The shape of spectra can be different, but continuum component was detected in all considered gas mixtures (air, N_2, N_2/CH_4, N_2/H_2, Ar/N_2, Ar/O_2, Ar/H_2) and for both polarities of applied pulses. Second, PVC and high temperature ceramics (MACOR) were used as dielectrics. PVC, or Polyvinyl chloride, is produced by polymerization of the vinyl chloride monomer, C_2H_3Cl; ceramics consists of non-organic materials (for MACOR: SiO_2 (46%), Al_2O_3 (16%), MgO (17%), KO_2 (10%), B_2O_3 (7%), F (4%)). The cw spectra obtained with so different dielectrics are identical (see figure 5.14b), and this fact proves that the spectrum does not originate

from damaging the dielectric and producing complex organic molecules.

The question arises, how the spectral structure correlates with the intensity of filaments on ICCD images? Does it appears at the same time moment with filaments? Figure 5.15 demonstrates the spectral composition in range $280-450$ nm of the filamentary discharge in air at different time periods. In order to increase, from one side, the signal/noise ratio and to have, from another side, a good enough temporal resolution, the camera gate was set to 5 ns. The pressure and the applied voltage were $P = 6$ bar and $U = -47$ kV respectively.

The filamentation occurs $5-6$ ns after the discharge start. The first $\Delta t = 5$ ns (0-5 ns on time axes) corresponds to the streamer discharge. Only the bands of the second positive system of N_2 are observed. When the filamentation happens, a well pronounced cw spectrum is detected in the period $5-10$ ns.

Coming back to figure 5.11(c), we see that the sharp emission intensity rise occurs at the time instant of filamentation. By integrating the intensity of the spectra (figure 5.15) over considered wavelength range we get:

$$\frac{\int\limits_{\lambda_1=280}^{\lambda_2=450} I_{5-10}d\lambda}{\int\limits_{\lambda_1=280}^{\lambda_2=450} I_{0-5}d\lambda} \approx 40 \qquad (5.2)$$

so the sharp rise of intensity corresponds to the presence of cw spectrum. The last expression is in a good agreement with the observed ratio (5.1). Both cw spectrum and nitrogen molecular bands can be observed up to $25-30$ ns. Then the second positive system of N_2 disappears and only one molecular band is detected and identified against the cw background. This band appears at time period $15-20$ ns and corresponds to the emission of cyan radical - $CN(B^2\Sigma^+) \rightarrow CN(X^2\Sigma^+)$ in the wavelength range $382-389$ nm. The appearance of the CN violet emission indicates the formation of gaseous CN radicals. The CN radicals are intensively produced and radiate even at very low concentration of carbon containing molecules (f.e. CO_2, CO, CH_4), less that 1000 ppm. It happens because the natural radiative time of CN is very small and at the same time the quenching rate is rather low. Thus, almost all $CN(B^2\Sigma^+)$ radiates and we see well distinguished band in the wavelength range $382-389$ nm. The kinetic of excited CN radicals is well described elsewhere [130–132].

It is seen from figure 5.15, that the highest level of cw is observed during the discharge pulse. Then the cw component decreases significantly within $45-50$ ns and at $65-70$ ns time period there is no more cw component, but only CN bands can still be detected. The vibrational and rotational temperatures formally calculated from the CN emission remain constant during considered time period (70 ns). The
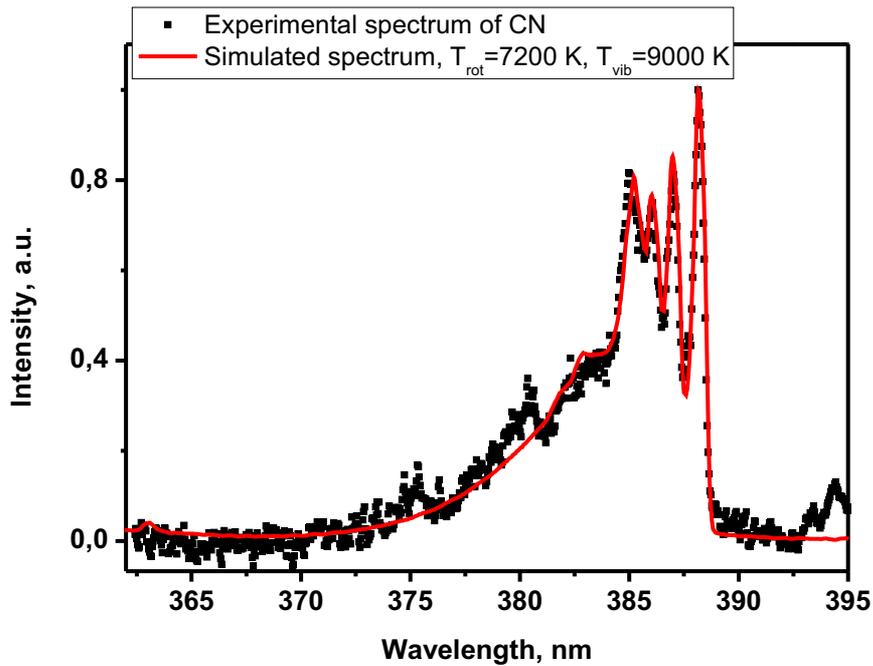
Figure 5.16: Experimental and simulated (SPECAIR) CN emission spectra (T_{vib}=9000 K, T_{rot}= 7200 K, camera delay=30 ns, camera gate=5 ns)

experimental and calculated spectra are shown in figure 5.16.

In some particular cases the investigation of CN violet emission has a great potential since CN can be detected in experiments with hydrocarbon containing mixtures. As far as the signal-to-noise ratio of this molecular violet band is usually one of the highest in hydrocarbon fuel breakdown spectra. Therefore, the CN radicals can be used for diagnostics of hydrocarbon fuels. Also, the chemistry of the CN radical is crucial for understanding the complex nature of NO_x formation. The chemical interaction of CN radicals with H_2O, O_2, C_2H_4 *etc* are considered elsewhere [133–135].

Possible channels of CN production are discussed in numerous papers in flames [131, 134], by photolysis [136], in pulsed discharges [137] and in DBDs [138]. As declared in some investigations of organic material [139, 140], the formation of CN occurs through the four-center reaction $C_2+N_2 \rightarrow$ 2CN. However, some other investigations [141, 142] of hydrocarbons demonstrate that the often cited four-center reaction is very unlikely to be the major CN forming process in considered experiments. Rather, the reactions of $C(^3P)+N_2 \rightarrow CN(B^2\sum^+)+N$, $C(^3P)+N(^4S)+M \rightarrow CN(B^2\sum^+)+M$ and $N(^4S)+CH \rightarrow CN(B,A)+H$ are responsible for the increasing CN concentration in $B^2\sum^+$ state. Indeed, according to [132], in these reactions $CN(B^2\sum^+)$ is produced with high rotational and vibrational population. The ef-
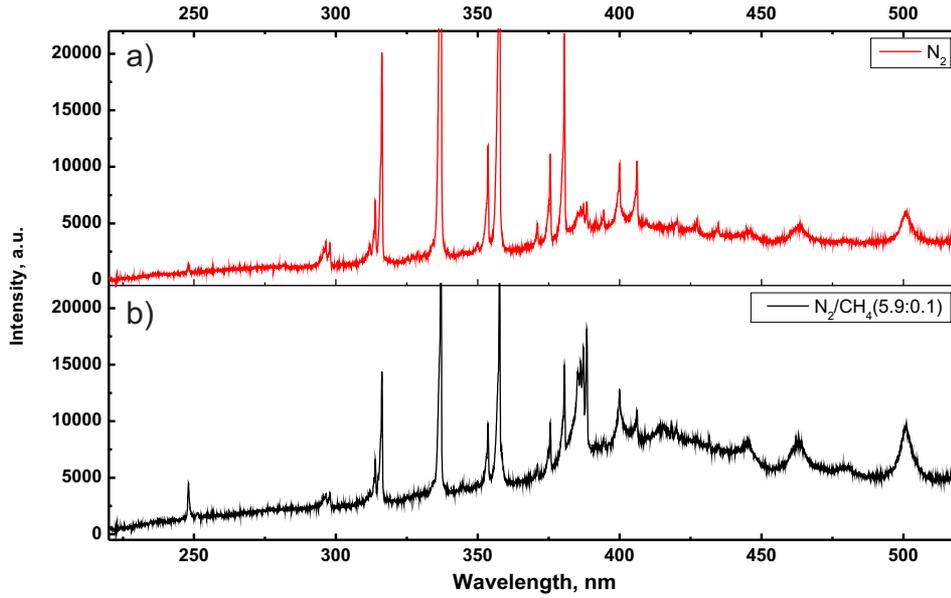
Figure 5.17: Emission spectra in (a) nitrogen and (b) N_2CH_4 mixture (P=6 bar, U=+50 kV, camera gate=50 ns).

fective lifetime of CN radical in our conditions is about $1.4 \cdot 10^{-9}$ s [143]. Since the mean collisional frequency of CN in the considered pressure is about $\sim 10^9$ s^{-1}, it has a time just for few collisions, whereas for R-T relaxation the following radical needs to have a few tens of collisions. Therefore, figure 5.16 does not reflect a real temperature in the discharge.

Figure 5.17 demonstrates the comparison of the emission spectra of the filamentary discharge in nitrogen and in N_2:CH_4 (5.9:0.1) mixture. Pressure and voltage in both cases were equal to 6 bar and +50 kV respectively. The emission of CN is observed in both gases. We assume that there are two possible sources of C-atoms in nitrogen (see figure 5.17(a)): (i) the CO_2 form residual air in the chamber (before the chamber is filled by N_2, it is pumped down to $1-2$ mbar); (ii) C and CH appearance that can be produced from some intermediate species coming from the surface [138].

Analysis of the time resolved laser and emission spectroscopy measurements [138] leads to the conclusion that three main chemi-luminescent mechanisms are active in the CN(B) formation. The first two pathways C+N+M→CN(B)+M and C+N_2 →CN+N are dominant in the post-discharge; the other one, active in the discharge, is the reaction N+CH→CN(B)+H, that becomes considerable with methane additives (see figure 5.17(b)). We assume that for the discharge in N_2:CH_4 mixture the third reaction contributes significantly that increases the fraction of CN emission.
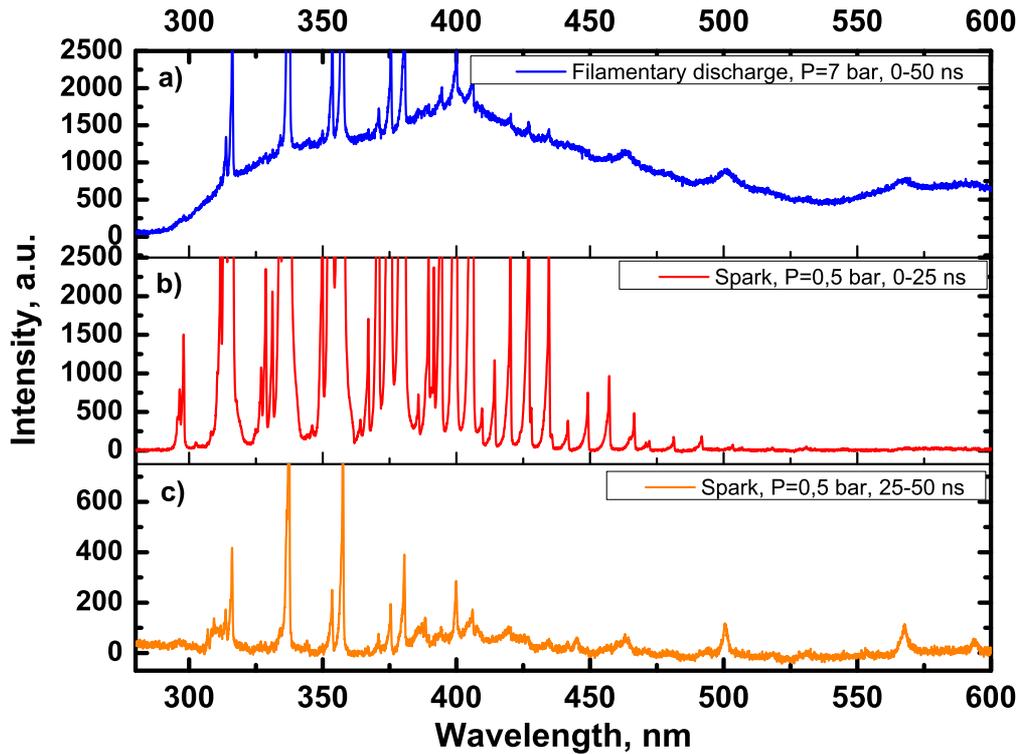
Figure 5.18: Comparison of filamentary discharge (a) and low-pressure spark discharge (b),(c). The spectra are not calibrated to the sensitivity of the optical system.

Figure 5.18 demonstrates the difference of emission spectra of filamentary discharge in air ($P = 6$ bar, $U = -50$ kV) and low–pressure nanosecond spark. The spark discharge was initiated at gas pressure $P = 0.5$ bar. In this case the discharge closes the inter–electrode gap with a single high-current channel. The shot circuit is clearly seen on the discharge oscillograms. The spectrum of the filamentary discharge is accumulated during 50 ns (figure 5.18(a)). For spark, the spectrum was taken in two time periods: (i) first 25 ns correspond to the discharge phase (figure 5.18(b)); (ii) second 25 ns correspond to the afterglow (figure 5.18(c)).

No cw spectrum is detected in the low–pressure spark during the first 25 ns. However, there are a lot of atomic lines and molecular bands which are not observed in filamentary discharge. During the second 25 ns, the intensity decreases significantly and a weak cw component can be seen.

One more important fact is connected with a broadening of the lines of N^+ on the wavelengths 460, 500 and 560 nm. These lines are well pronounced in the spectrum of a low–pressure arc (see figure 5.18(c)). They can be also distinguished in the figure 5.18(a) for the filamentary discharge. The difference is that in the filamentary discharge the broadening is extremely high. Other cases of abnormally

high broadening of the atomic lines in the filaments will be considered further for H– and O–atoms.

5.2.3 Spatial spectral structure of the filaments

Further analysis of the emission picture required a knowledge about spectral distribution of emission in streamers and filaments. To understand a spectral distribution of emission in space, a series of ICCD images with narrow band filters have been taken. The central wavelengths of the filter were selected to transmit "only nitrogen emission" or "only continuum emission". Images were taken for two delays, 0 and 5 ns, and for two ICCD gates, 5 and 20 ns for streamer and filamentary phase of the discharge respectively. Figure 5.19 presents, as a table, typical images taken without and with described filtering.
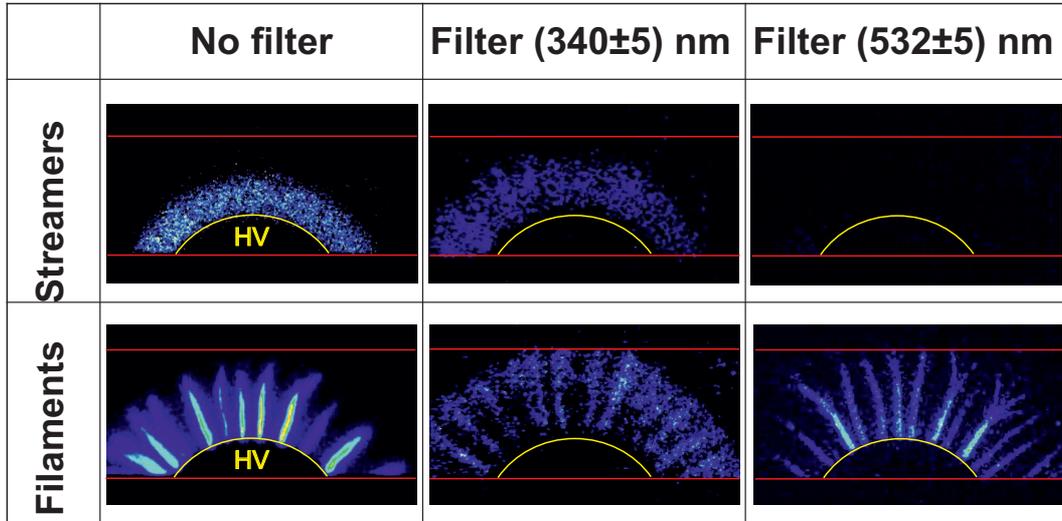
Figure 5.19: ICCD images of streamer and filamentary mode with narrow bandwidth filters. Time delay is 0 ns for the streamer mode and 5 ns for the filamentary mode. Camera gate is 5 ns for streamers and 20 ns for filaments. Synthetic air, $U = -52$ kV, $P = 4$ bar.

The discharge starts and develops during a few first nanoseconds similar to a "classical" nanosecond SDBD in the air–flow configuration at atmospheric pressure [8, 13]. In the filamentary mode two separate zones are clearly seen: the emission of the 2^+ system corresponds to the zone "around and ahead of" each filament, while continuous emission comes from the filament core, or from the filament "channel".

Detailed spectral analysis demanded to fix the position of the filament from experiment to experiment, so the discharge was stabilized in space using the technique suggested in [7]: the high-voltage electrode has been replaced by a toothed wheel with the distance between the teeth compared with a typical distance between the
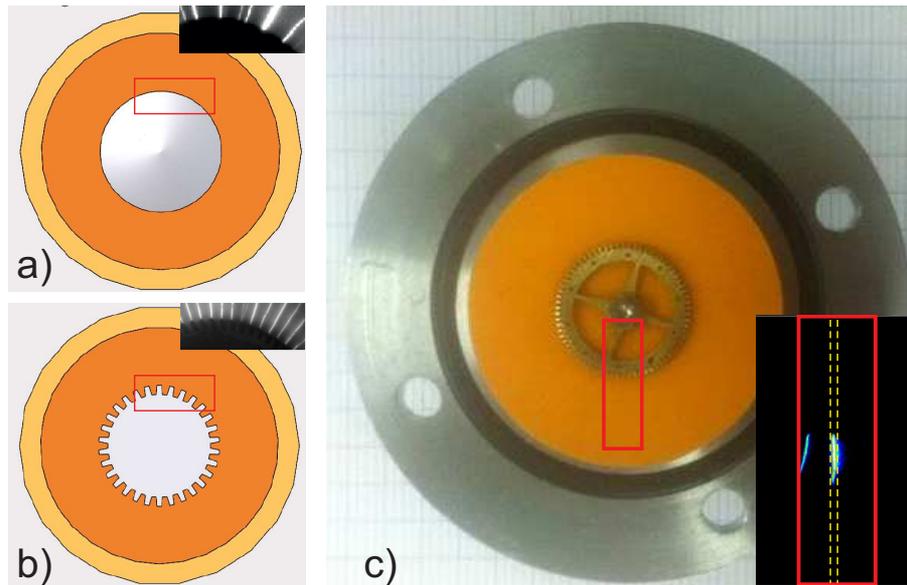
Figure 5.20: Cylindrical electrode system with (a) classical disc and (b) gear–like HV electrode. (c) Photo of the electrode with schematically presented entrance slit (yellow dashed lines) of the spectrometer.

filaments. The electrodes and corresponding discharges are demonstrated in figure 5.20(a) and (b). It is seen that discharge develops almost from every tooth of gear. A filament was selected and the discharge chamber was rotated so that the filament was aligned with the spectrometer slit. The image of electrode system and the relative orientation of the entrance spectrometer slit are shown in figure 5.20(c). The system provided a temporal resolution of 0.5 ns and a spatial of 30 μm/pixel. To our knowledge, this is a first available data on time- and space-resolved emission of the filaments in nSDBD. A typical image of the selected filament obtained with the described system is demonstrated in figure 5.20(c).

Figures 5.21 and 5.22 show the ICCD images of the discharge development (first column), and corresponding "spectral composition" of the discharge in the range $220 - 500$ nm at the same time instances (second column). The entrance slit of the spectrometer was equal to 3 mm for ICCD imaging and 100 μm for taking the spectra to assure the only filament within the slit area. To increase the contrast, both images and 2D spectra are shown in false colors. The gate of the camera was 5 ns. The corresponding time periods, during which signals were accumulated are shown on the left of the ICCD images. The spectra were acquired with the number of accumulation - 100, whereas images were obtained in a single shot regime.

Well pronounced cw spectrum can be seen for both polarities starting from the period $5 - 10$ ns. The camera sensitivity was selected to be the same and without the saturation of MCP during the acquisitions. It is seen that for negative polarity the
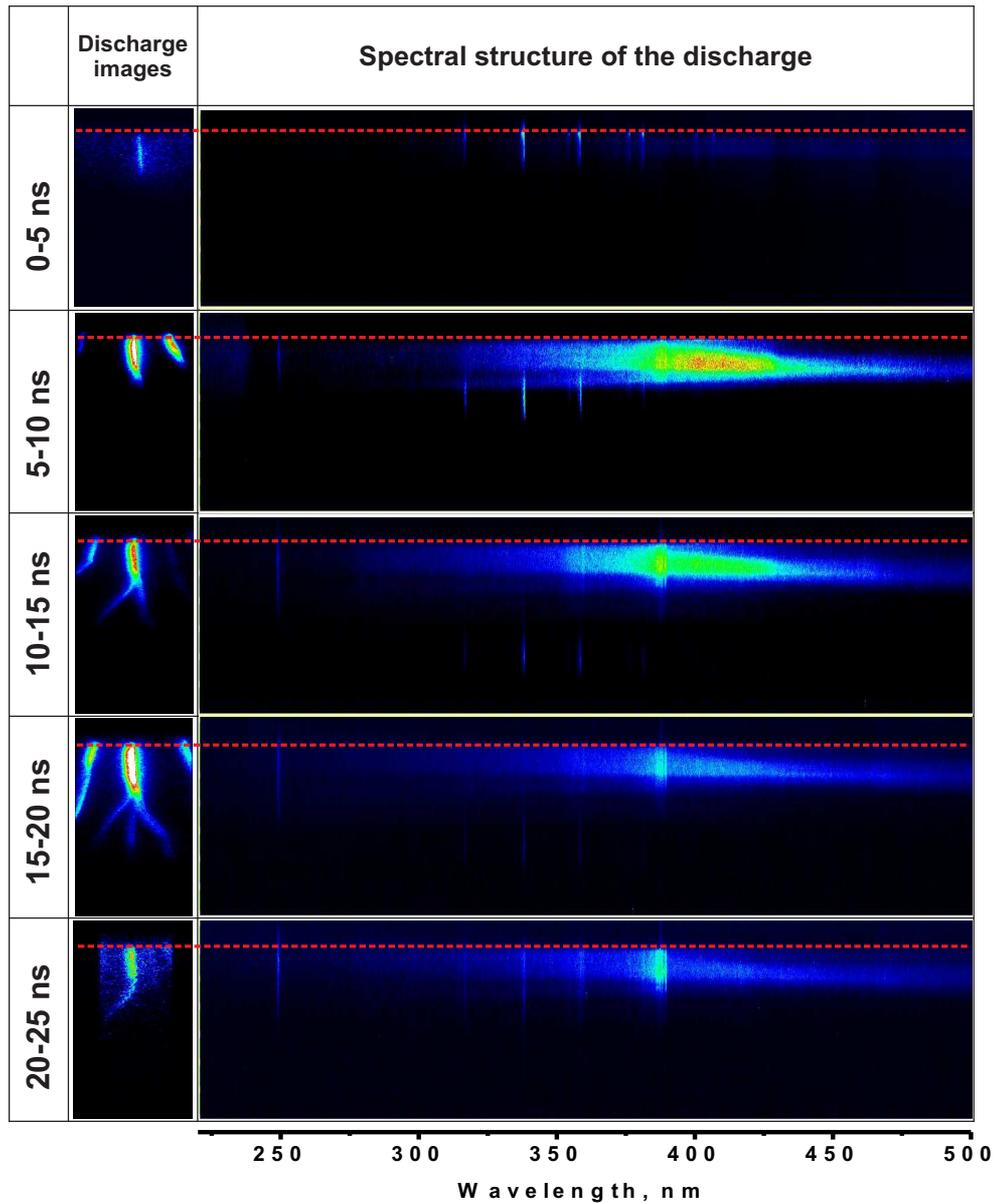
Figure 5.21: ICCD images and time-resolved 2D spectra of the filamentary discharge of negative polarity. Air, $P = 6$ bar, $U = -50$ kV.

absolute intensity of the cw component is higher than for the positive polarity. On the contrary, the intensity of the second positive system (SPS) of molecular nitrogen is higher for positive polarity.

It is clearly seen that the general behavior of positive and negative polarity filaments is similar. From the very beginning, when discharge propagates as a set of streamers, only SPS system can be detected. At $|U| = 50$ kV and $P = 6$ bar the filamentation for both polarities occurs at the period $5 - 7$ ns. So, as far as filaments appear, the cw spectrum is observed. The cw component of spectrum rises abruptly
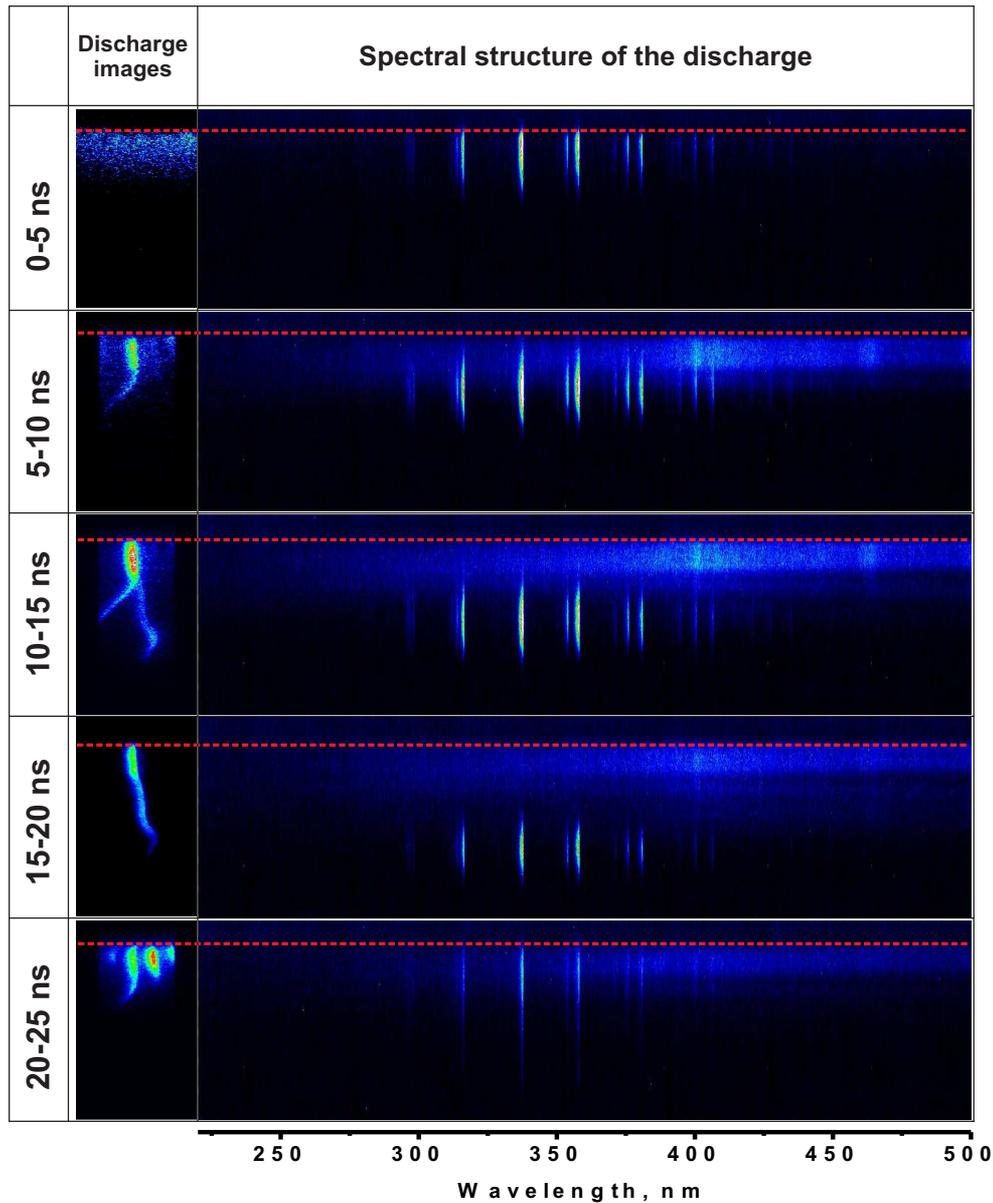
Figure 5.22: ICCD images and time-resolved 2D spectra of the filamentary discharge of positive polarity. Air, $P = 6$ bar, $U = +50$ kV.

and the highest intensity seems to be at the period $5 - 10$ ns.

The most important fact is that the SPS and the cw components of the same 2D spectrum are separated in space. This is especially well seen for the time periods of $10 - 15$ and $15 - 20$ ns. It can be noticed, that cw spectrum comes from the body of filament, starting from the edge of HV electrode (red dashed line) until the distance of few mm away, whereas SPS emission appears at the front of the discharge, that corresponds to the streamer corona that supplies filaments with electrons and provokes the propagation of the filaments from the edge of HV electrode. It can
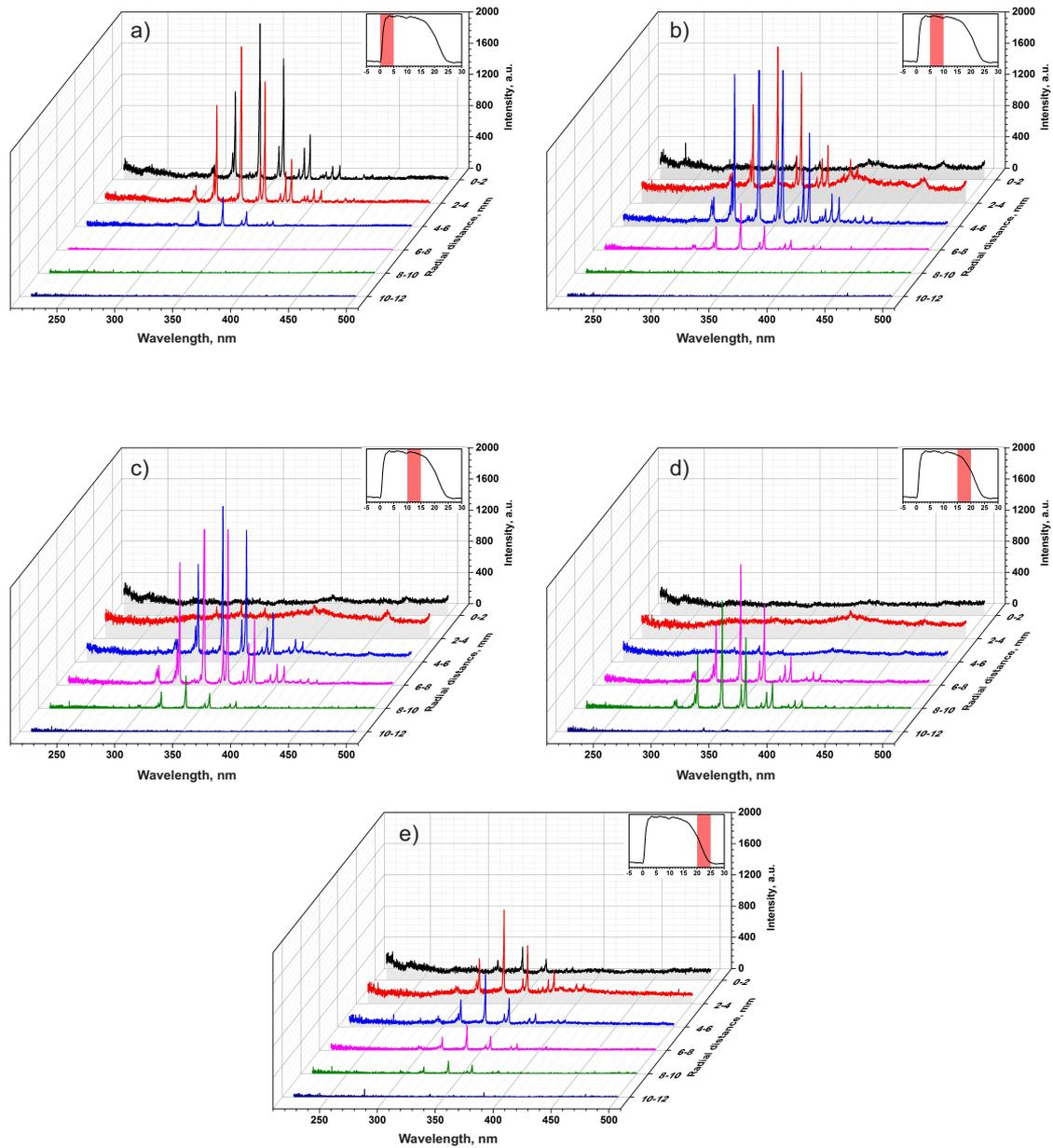
Figure 5.23: Emission spectra of the positive polarity discharge in air. $P = 6$ **bar,** $U = +50$ **kV. The spectra are corrected to the sensitivity function of the optical system.**

be considered, according to data of time period $5 - 10$ ns, that there is a region of overlap of the SPS and the cw. This point must be figured out with higher temporal resolution, but we suppose that it is only because of 5 ns camera gate, during this period the discharge propagates on several millimeters. The camera can record the data, at fixed space region, of discharge front (SPS) and later of filament's body emission (cw).
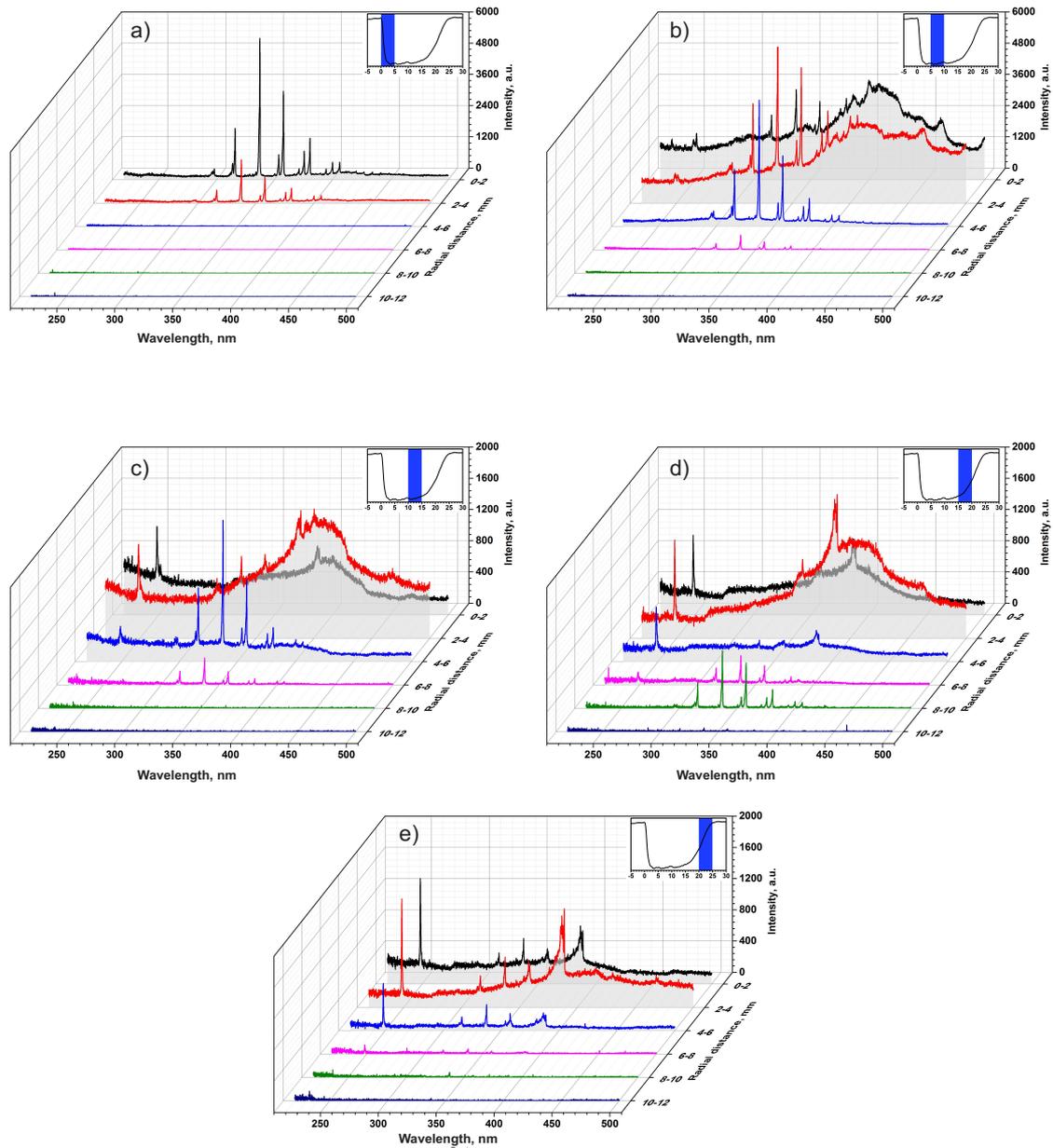
Figure 5.24: Emission spectra of the negative polarity discharge in air.
$P = 6$ **bar,** $U = -50$ **kV. The spectra are corrected to the sensitivity function of the optical system.**

Quantitative treatment of the spectra presented in figures 5.21–5.22 allows more detailed analysis of a spatial–temporal structure of the filament emission. The corresponding spectra of the discharge in synthetic air at pressure 6 bar, corrected on the transmission of the spectral system, are presented in figure 5.23 for positive and figure 5.24 for negative polarity of applied pulses. Each plot presents the discharge emission as a function of wavelength and of the distance from the edge of
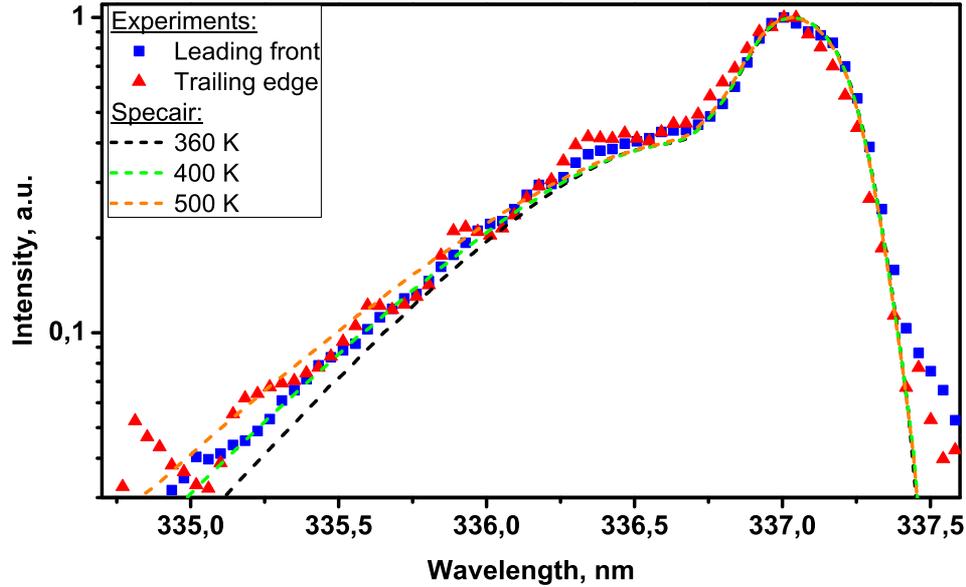
Figure 5.25: **Rotational temperature of 2^+ system (0-0) transition on leading (0-5 ns) and trailing (20-25 ns) edge.**

high–voltage electrode. The spectra are spatially averaged over 2 mm gap. The corresponding gaps are shown in the signatures to the axis. The insert in the right upper corner of each image provides information about the position of the ICCD gate relative to the voltage waveform. The emission of the second positive band of N_2, typical for streamer discharge, is clearly seen in the front of the propagating discharge (figure 5.23(a) and figure 5.24(a)). Start of the filament from the electrode corresponds to the regions $0-2$ and $2-4$ mm where the continuous wavelength spectra can be seen(figure 5.23(b) and figure 5.24(b)). Emission of the first negative system of molecular nitrogen at 391.4 nm was detected in the front of the discharge, that indicates on the presence of high electric fields in the streamer corona of the filament. When the filament is formed, the N_2 emission is replaced by cw emission at the near electrode region (see figure 5.23(c) and figure 5.24(c)). For negative polarity discharge the intensity of the cw emission is systematically $3-4$ times higher than the intensity of the positive polarity discharge, and the shape is somewhat different from the shape of the cw emission of the positive discharge. At the trailing edge of applied pulses the second ionization wave starts from the HV electrode and propagates on the trace of the filament (see section 4.5). The second ionization wave contains emission of the 2^+ system of molecular nitrogen (see figure 5.23(e) and figure 5.24(e)) indicating on the electric field comparable to the fields in the discharge front.

It should be noted that absence of NO(γ) emission, NO($A^2\Sigma^+, v$) $\rightarrow$ NO($X^2\Pi, v'$) + $h\nu$, at $\lambda < 300$ nm means absence of high specific deposited energy. Indeed, NO($A^2\Sigma^+, v$) is produced by electron impact and emits a photon in the reaction N$_2$($A^3\Sigma_u^+$) + NO($X^2\Pi$) $\rightarrow$ N$_2$($X^1\Sigma_g^+, v$) + NO($A^2\Sigma^+, v$). At low energy release, the dissociation degree and so, the NO($X^2\Pi$) and NO($A^2\Sigma^+, v$) densities are low [78].

The observed spectrum is not a Planck emission caused by gas heating. First, the gas temperatures calculated from the rotational temperature of nitrogen, measured on the rise front and on the trailing edge of the pulse, do not differ significantly. Figure 5.25 shows the experimental and calculated with SpecAir [104, 105] emission spectra of 337 nm band of SPS for leading and trailing edge of HV pulses. As one can see for both time instants, T_{rot} in in the range $300 - 500$ K.

Second, the analysis of the radial distribution of the cw emission across the filaments (see figure 5.10) proves that the emission comes from the central part of the channel, not from the filament's surface.

Finally, the most important evidence is a temporal behavior of the cw emission: if this was Planck radiation, it would increase with time corresponding to fast gas heating observed in the nanosecond scale in the discharges with high specific deposited energy [83, 144]. This is not the case: the cw emission goes down within a few tens of nanoseconds, and hydrodynamic expansion on the time scale 50 ns is small to provide significant cooling: for the filament radius $r_f \approx 70$ μm [145] and $T_g = 500$ K, a gas–dynamic time is about 200 ns. Below, the other possible reasons of the cw emission will be analysed.

5.2.4 O- and H- atomic line broadening

Two experimental observations are important for nSDBDs at high pressures and voltages. One of them is an intense cw spectrum. Another one is broadening of atomic lines. As it was discussed above, neither emission of a molecular continuum nor Plank emission are the causes of cw spectra. Absence of a strong gas heating on nanosecond scale means that the energy is spending for processes with high energy thresholds, such as bremsstrahlung and recombination. To check the hypothesis of bremsstrahlung and recombination radiation it is necessary to estimate the electron density in the filaments.

The measurements of the width of selected spectral lines can answer the question about the electron density in the filaments. The experiments were carried out in 5 bar H$_2$:N$_2$=1:4 mixture and in 5 bar O$_2$:Ar=2:3 mixture; the lines of atomic hydrogen (656.3 nm, H$_\alpha$) and of atomic oxygen (777.3 nm, OI(3^5P–3^5S)) have been analyzed. Continuous spectra similar to those measured in air were observed in both mixtures. The time instant of appearance of the emission of atoms coincided
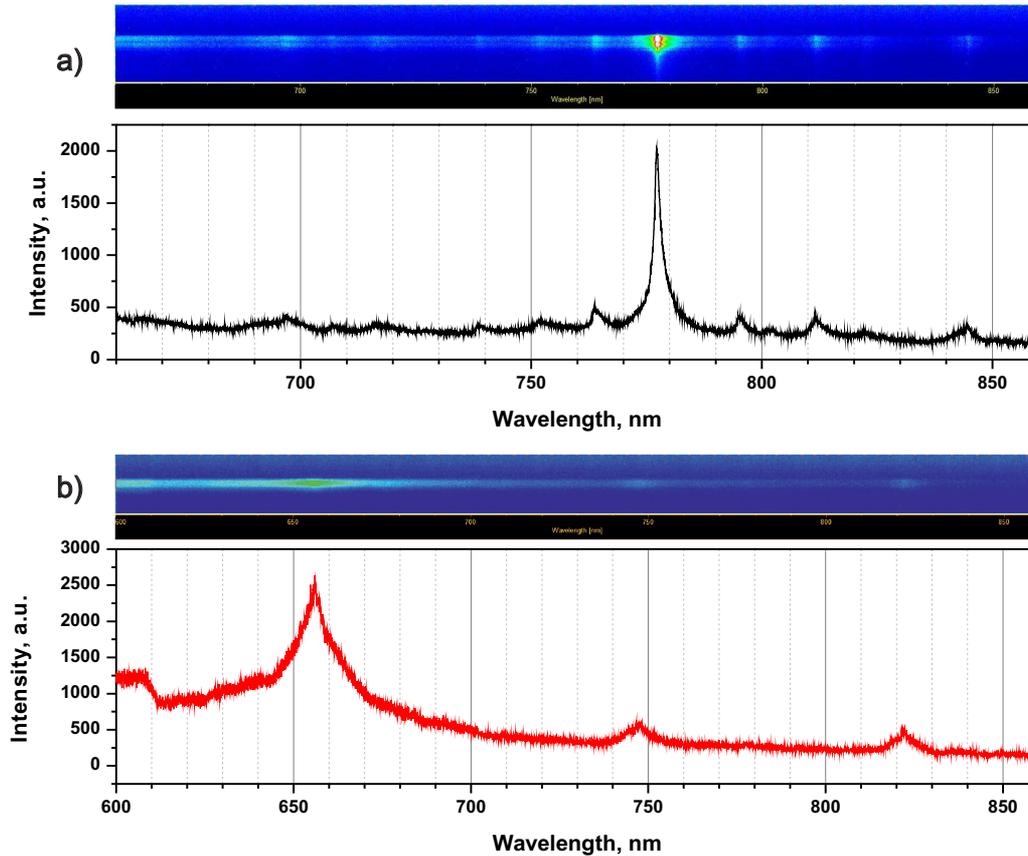
Figure 5.26: Emission spectra of the discharge in (a) O$_2$:Ar (2:3) mixture (660 − 860 nm) and in (b) H$_2$:N$_2$ (1:4) mixture (600 − 860 nm). For both mixtures $P = 5$ bar. Camera gate 20 ns. The spectra are not calibrated to the sensitivity function of the optical system.

with appearance of the cw spectra and were not observed at the regions where cw is absent.

The review spectra of the filamentary discharge are presented in figure 5.26(a) for O$_2$:Ar and (b) for H$_2$:N$_2$ mixtures. These spectra were acquired with 500 nm cut-on filter to avoid the second order of the diffraction grating. As previously, the filaments were fixed in space and aligned with the entrance slit of the spectrometr. The spectra are plotted by averaging of the emission over the entire length of the filament where the cw spectrum exists – 0−6 mm (2D images of spectra are presented above the plots).

Figure 5.27 shows the experimental results of H$_\alpha$ broadening and the technique of the FWHM calculations. As an example the discharge of negative polarity is used. A typical evolution of the line is demonstrated in figure 5.27(a). Camera gate for each event was equal to 5 ns. It is clearly seen how the width of the line decreases with time. The widest line was detected at time instant of 10 ns and its FWHM is
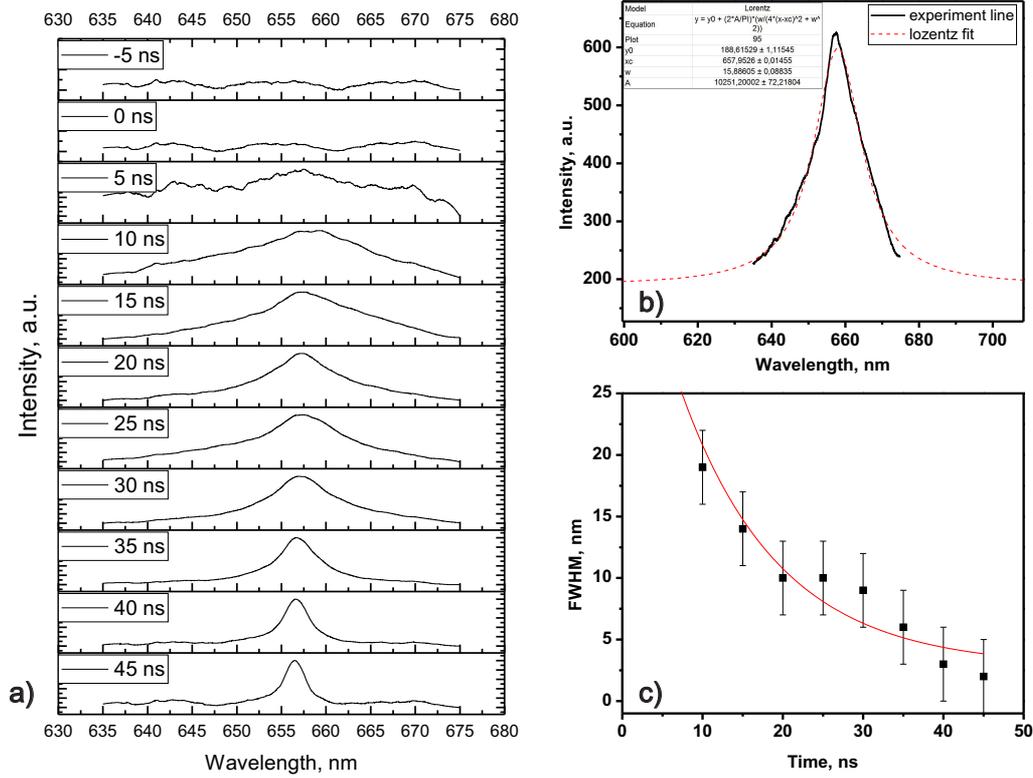
Figure 5.27: (a) H_α lines (656.5 nm) at different time instances. Camera gate is 5 ns; (b) Lorentz fit of the line at 15 ns; (c) FWHM as a function of time.

about 20 nm. The method of fitting is demonstrated in figure 5.27(b). The atomic lines are well fitted by Lorenz function. The values of FWHM in nanometers are shown in figure 5.27(c).

One important point concerning the discharge current can be assumed. Figure 5.28 demonstrates the normalized H_α line for different applied voltages. When the voltage is low enough and no streamer–to–filamentary transition is observed, H_α is not detected in the spectra. However, when the discharge constriction takes place, with increase of voltage the width remains constant. And thus, if we associate the line broadening with Stark effect in the plasma [146, 147], the electron number density as well as the current does not increase with voltage. It coincides with the theory of normal current density [113, 124]. In the theory of cathode layer one of the most important parameter is so–called normal current density j_n. During the discharge constriction state the size of the spot that appears on the vicinity of the high voltage electrode - the diameter of filament, and the number of filaments are set up to have the current density in each channel equal to normal current density
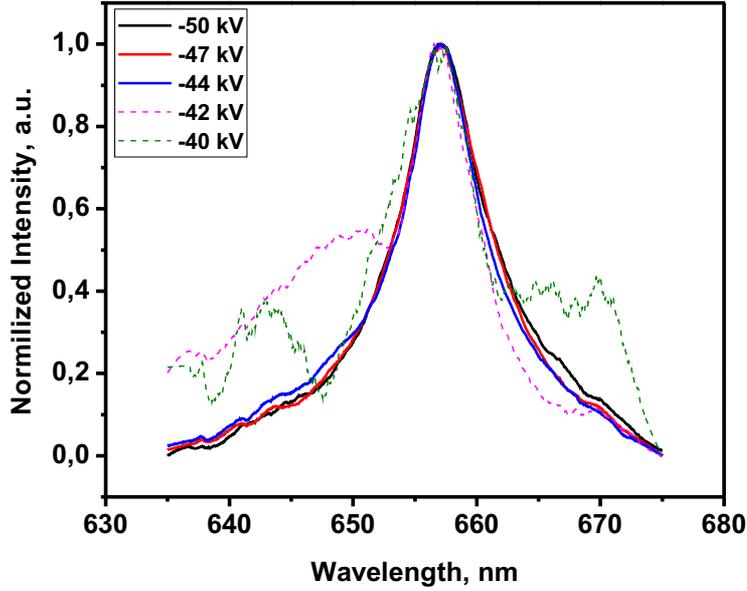
Figure 5.28: Normalized H_α line for different applied voltages.

in the considered conditions:

$$\frac{j_n}{p^2} = \frac{(1+\gamma)(\mu_+ p)U_n^2}{4\pi(pd)_n}. \tag{5.3}$$

where γ is the effective coefficient of secondary emission from the cathode under the action of positive ions, photons, etc.; μ_+ is the mobility of positive ions in the cathode layer; d is characteristic thickness of the cathode layer; index n symbolizes the values that are realized in normal discharge; U_n is a normal potential drop in the cathode layer. The normal drop of the potential can be found as follows: $U_n = A(pd)/(B + ln(pd))$. It does not depend on the amplitude of applied voltage, A and B are the phenomenological constants. Therefore, the normal current density depends on the gas nature and pressure and does not depend on applied voltage, that is confirmed by the constant electron density in the filaments for different voltages on HV electrode (figure 5.28).

One more important point is that the line width remains constant along the filament as it is demonstrated in figure 5.29 for two different time instances, 10 and 25 ns. As an example $OI(3^5P–3^5S)$ line is demonstrated. Indeed, the H_α line behaves in a similar manner. It underlines the fact that the channel has a high conductivity.

Dynamics of the FWHM for 656 nm hydrogen line is given by figure 5.30(a) for both polarities of the pulse, together with the waveforms of voltage on the high voltage electrode and electrical current for negative polarity discharge. The FWHM
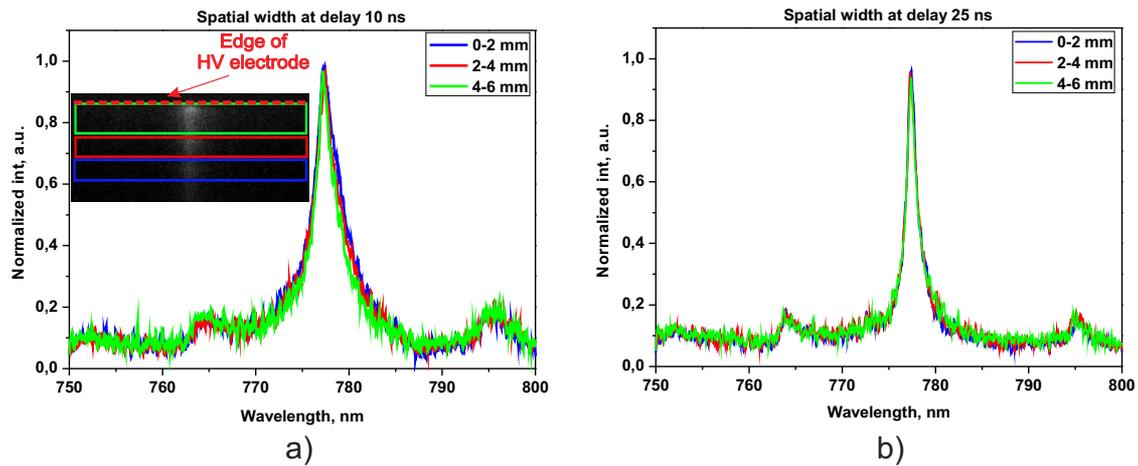
Figure 5.29: Normalized OI line at (a) 10 and (b) 25 ns time instances obtained for different distances from the edge of HV electrode. Applied voltage $U = -40$ kV.
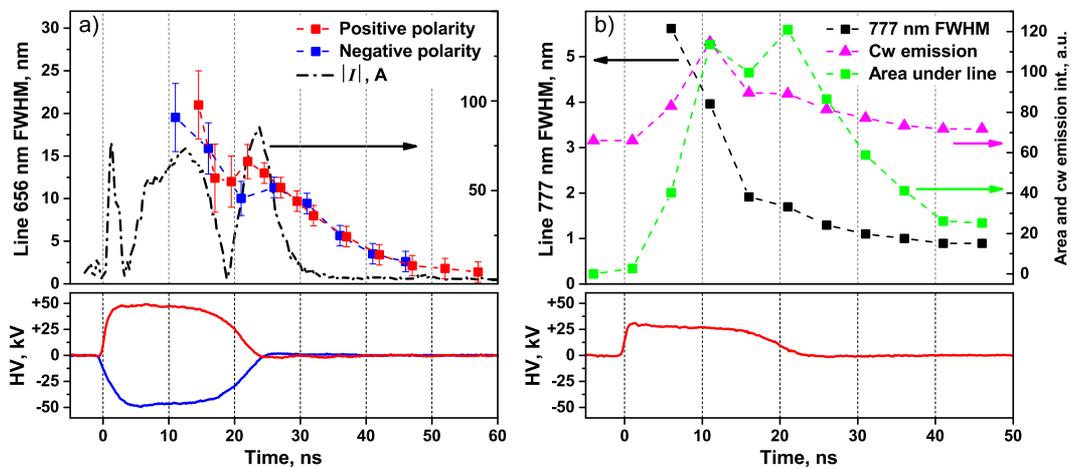
Figure 5.30: FWHMs *vs* time: (a) H_α superimposed with the voltage coming to the electrode and current through the discharge; (b) 777 nm of atomic oxygen superimposed with the voltage waveform, the area under the line and cw emission near 777 nm.

is enormously large in the discharge, ~ 20 nm. Two decays are observed: the first one is in a good correlation with the decay of electrical current, and the second is longer: already in the "current-free" zone, a typical time of 50% decrease of the FWHM is equal $10 - 20$ ns. These numbers are in correlation with figure 5.30(b) presenting the FWHM for 777 nm oxygen line. The FWHM itself is narrower for oxygen, comprising about 6 nm in the discharge, according to the idea that H-atom is more sensitive to a reason of broadening, but the time of 50% decrease the

FWHM after the discharge is equal to 15 ns. Let us note, that at a typical time of change of the electrical current $\tau \sim 1$ ns and electron ion recombination coefficient $\beta \simeq 10^{-7}$ cm^3/s [113], the electron density $n_e \sim (\beta\tau)^{-1} = 10^{16}$ cm^{-3} is high enough to provide a fast decay, of the order of τ, of the electron density. To explain slow decay in early afterglow, the additional mechanisms are needed. Figure 5.30(b) gives also a temporal behavior of continuous emission taken in the vicinity of the atomic oxygen line, and the integral of O-atom emission over the wavelength as a function of time, proportional to O*–atoms density in 3^5P state.

Summary of time-dependent behavior of the experimentally observed values reveals the following evidences: cw emission does not exists at the rising front of the pulse (figure 5.23) and slightly decreases but does not disappear (figure 5.30(b)) at the trailing edge. The cw emission in the filaments and emission of the broad atomic lines appear at the same time instant, a few nanoseconds after the start of a single shot discharge; they come from the same space region. Temporal behavior of the cw emission and of FWHM of the O-atom and H-atom lines is similar: a typical decay after the discharge comprises a few tens of nanoseconds (figure 5.30). Density of excited O-atoms estimated from the integral of emission at 777 nm, has a similar shape but somewhat delayed relative to the maximum of the FWHM, and has a broader maximum. Finally, the intensity of cw emission in the negative polarity discharge is higher than in the positive polarity discharge (compare figure 5.23 and 5.24); and the FWHM of H-atom line is higher in the negative polarity discharge (figure 5.30(a)).

5.2.5 Nature of cw emission and electron density

Two types of emission due to high electron density can be considered at the initial stage of the discharge: bremsstrahlung and recombination radiation. Bremsstrahlung emission originates from acceleration of an electron in Coulomb collisions with ions [148]. Energy per 1 cm^3 per second in SGC system in assumption of Maxwellian EEDF is written as [149]

$$P_b = 1.5 \cdot 10^{-27} Z^2 n_e n_i \sqrt{T_e[\text{K}]}. \tag{5.4}$$

Recombination radiation is a process of emitting of the photon in recombination of ion and electron, and can be expressed as [149]

$$P_r = 5 \cdot 10^{-22} Z^4 n_e n_i \sqrt{1/T_e[\text{K}]}. \tag{5.5}$$

here Z is a charge of ion, n_e, n_i are electron and ion densities respectively, T_e is electron temperature. Equations (5.4) and (5.5) give the equal values of power of
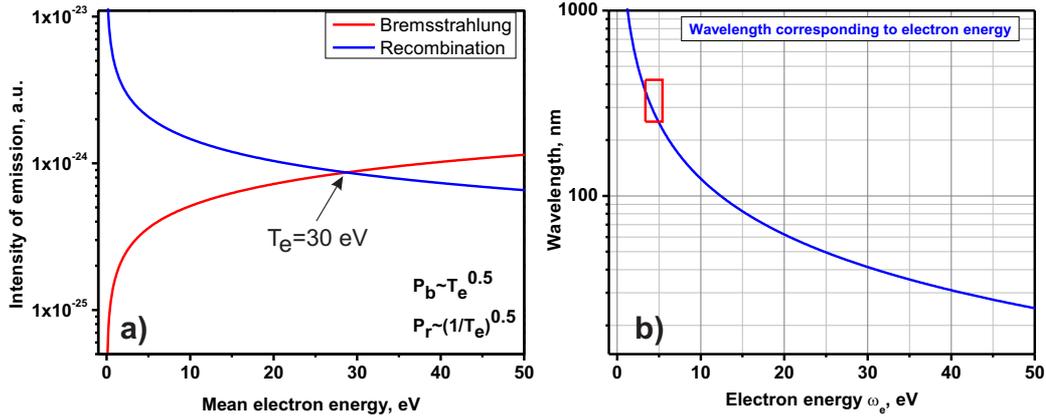
Figure 5.31: (a) Characteristic emission intensity of bremsstrahlung or recombination radiation; (b) The radiation wavelength as a function of the incident electron, $\omega_s = 0$. Red rectangle denotes the region of wavelength observed in the experiment.

radiation at $T_e \approx 30$ eV (see figure 5.31(a)). For the electrons with temperatures less than 30 eV the recombination emission is a few orders of magnitude higher than the bremsstrahlung. At the conditions of the present work, the mean electron energy should be on the level of a few electronvolts. So, it is expected that the recombination radiation will be dominating in the cw spectrum.

The frequencies of bremsstrahlung radiation is in the range $\omega_p < \omega < \omega_e$, where ω_p is a plasma frequency, ω_e is a frequency corresponding to the electron kinetic energy. The recombination radiation is given by the energy of the initially free electron and by the energy of bound electron. The emitting photon has a frequency $\omega = \omega_s + \omega_e$, where ω_s is the energy of final bound state of incident electron. The wavelength corresponding to electron energy assuming that $\omega_s = 0$ is shown in figure 5.31(b). The red rectangle shown the spectral region of our experiments. If the cw spectrum would be given by bremsstrahlung radiation, the plot shown in figure 5.31(b) could be considered as maximal frequency $\omega = \omega_e$ (e.g. minimal wavelength) of bremsstrahlung radiation. We see, that cw spectrum continues to region $\lambda < 200$ nm. So, we could have the situation when we have both bremsstrahlung and recombination radiation if the EEDF is extremely non-Maxwellian with "enrichment" at high–energy region. But this is not the case. We do not see the 2^+ system of molecular nitrogen in the body of the filament, that indicates that E/N and thus T_e is relatively low. Therefore, we believe that cw spectrum is given by the recombination processes.

If we associate the H_α line broadening with Stark effect due to the electric micro–

fields of electrons in plasma, we can estimate the electron density according to analysis described in [146] and applied in [150]. Figure 5.32(a) demonstrates the results of n_e calculations. It is clearly seen either from analysis of the broadening of atomic line, that the electron density in the filaments of nSDBD at elevated pressures is extremely high $n_e \sim 10^{18}$ cm^{-3} and corresponds to high ionisation degree $\sim 1\%$.

High values of n_e from H$_\alpha$ and N–atoms broadening were reported earlier in $P = 1$ atm discharge in N$_2$:H$_2$O mixture for 9 kV and 170 ns pulses [150]. Values up to $n_e = 4 \cdot 10^{18}$ cm^{-3} ($n_e/N > 10\%$) with a long decay rate, $8.6 \cdot 10^6$ s^{-1}, were obtained. The authors explain a long decay by additional production of electrons in the afterglow *via* Penning and associative ionization and remark that the density of excited species should be comparable to n_e. At the same time, our estimates of energy release at so high ionization degree gives too high values of gas heating: $\Delta E = 2.25$ eV in electron–ion recombination of N$_2^+$ [84] and $\Delta E \approx 2$ eV in quenching of N(^2D) [151] results in $T_g = 1500 - 1900$ K at 100 ns, while measured temperature is $T_g \leq 800$ K [150].

Values of $n_e = 2.4 \cdot 10^{17}$ cm^{-3} were obtained in helium mixed with 1% argon and 0.01% hydrogen for 4.5 kV and a duration of electrical current pulse of a few hundreds of nanoseconds [152, 153]. A series of papers [154, 155] considers a nanosecond discharge at voltage amplitude 150 kV, pulse duration 5 ns and discharge gap 2 cm at atmospheric pressure He [154] reporting $n_e = 6 \cdot 10^{16}$ cm^{-3}, and at $1 - 3$ atm of hydrogen reporting, at $P = 1$ atm of H$_2$, $n_e = 2 \cdot 10^{17}$ cm^{-3} respectively.

The intensity of the recombination radiation is determined by the electron density and temperature according to expression (5.5). We know from the experiment that the emission intensity of N$_2$(C$^3\Pi_u \to$B$^3\Pi_g$) transition at $\lambda = 337.1$ nm ($\nu' = 0 \to \nu'' = 0$) is of the same order of magnitude that the intensity of the cw spectrum. If we estimate the absolute intensity of N$_2$(C$^3\Pi_u$) emission at $\Delta\lambda \simeq 3$ nm corresponding to the width of $0 \to 0$ transition, and compare this value to the emission produced by cw radiation in the filament, we can estimate the electron density in the filament. So, estimating the absolute value of intensity we can get an information about electron density. Lets consider the equation of the concentration of the emitting N$_2$(C$^3\Pi_u$):

$$\frac{dN_2(C)}{dt} = k_C(E/N) \cdot n_e \cdot N_2 + N_2(C) \cdot \nu_q. \tag{5.6}$$

at $P = 6$ bar and $T_0 = 300$ K characteristic time of collisional quenching of N$_2$(C$^3\Pi_u$) state by molecular oxygen and nitrogen is $\tau_q = 1/\nu_q \approx 0.1$ ns, that is considerably lower than the characteristic time of intensity changes, e.g.

$$\nu_q \gg \frac{1}{N_2(C)} \frac{dN_2(C)}{dt} \tag{5.7}$$

in this case using the equation (5.6), the concentration of N$_2$(C$^3\Pi_u$) can be rewritten

as:

$$N_2(C) = k_C(E/N) \cdot n_e \cdot N_2/\nu_q \tag{5.8}$$

According to chapter 4, the electric field in the streamer channels $E/N \simeq 70 - 80$ Td and the rate constant of $N_2(C^3\Pi_u)$ excitation by direct electron impact is $k_C \simeq 6 \cdot 10^{-12}$ cm^3/s. The quenching frequency $\nu_q = (k_q^{O_2} \cdot [O_2] + k_q^{N_2} \cdot [N_2]) = 1.12 \cdot 10^{10}$ s^{-1}. The normal current density in the cathode region at $P = 6$ bar and of $T_0 = 300$ K is $j_n \approx 6$ kA/cm^2 [113]. Assuming that the current density in the streamer channel is approximately the same as current density in the cathode layer $j_s \approx j_n$, we obtain, $[N_2(C^3\Pi_u)] = 3 \cdot 10^{12}$ cm^{-3}.

The intensity of (0-0) transition of 2$^+$ system of nitrogen ($\lambda = 337$ nm)

$$Q_C = N_2(C) \cdot F_{FK} \cdot A_{00} \tag{5.9}$$

$F_{FK} = 0.5466$ is a Franck-Condon factor of $N_2(X,\nu = 0) \rightarrow N_2(C,\nu' = 0)$ [156], $A_{00} = 1.3 \cdot 10^7$ s^{-1} is a Einstein coefficient for $(0 - 0)$ transition of 2$^+$ system [156]. The absolute intensity of the considered transition following the expression (5.9) is:

$$Q_C = 3 \cdot 10^{21} \text{quantum/cm}^3/\text{s} \tag{5.10}$$

According to measured time– and spatially-resolved spectra of filaments (see figure 5.24) at $\lambda = 335 - 338$ nm the ratio $Q_C(t = 0 \text{ ns})/Q_{CW}(t = 5 \text{ ns}) \sim (1.5 - 2)$. So, we get:

$$Q_{CW} = (1.5 - 2) \cdot 10^{21} quantum/cm^3/s \tag{5.11}$$

Lets estimate the electron density, which allows to obtain such intensity of recombination emission. The intensity of the recombination radiation for singly charged ions ($Z = 1$) is described by the following expression:

$$Q_{CW}(\omega) = C_0 \cdot \frac{n_e \cdot n_i}{\sqrt{T_e} \cdot \hbar\omega} d\omega, \tag{5.12}$$

where $C_0 = 1.08 \cdot 10^{-38}$ egr·cm$^3\sqrt{K}$=$6.742 \cdot 10^{-27}$ eV·cm$^3\sqrt{K}$ [113], n_e, n_i are the electron and ion densities, T_e is an electron temperature. For $\lambda = 337$ nm $\hbar\omega = 3.6$ eV, thus for $\Delta\lambda = 3$ nm, $d\omega = 2\pi c\Delta\lambda/\lambda^2 = 5 \cdot 10^{13}$ s^{-1}.

Lets consider the intensity of the recombination radiation in the wavelength range $\lambda = (337 \pm 1.5)$ nm as a function of the electron temperature. Figure 5.32(a) demonstrates the results of $Q_{CW(337)}(T_e)$ calculated by equation 5.12 for $n_e = n_i = (1-2) \cdot 10^{18}$ cm^{-3}. It is clearly seen that, in order to get the intensity of recombination emission $Q_{CW(337)} = (1.5 - 2) \cdot 10^{21}$ quantum/cm^3/s in the discharge with $T_e =$
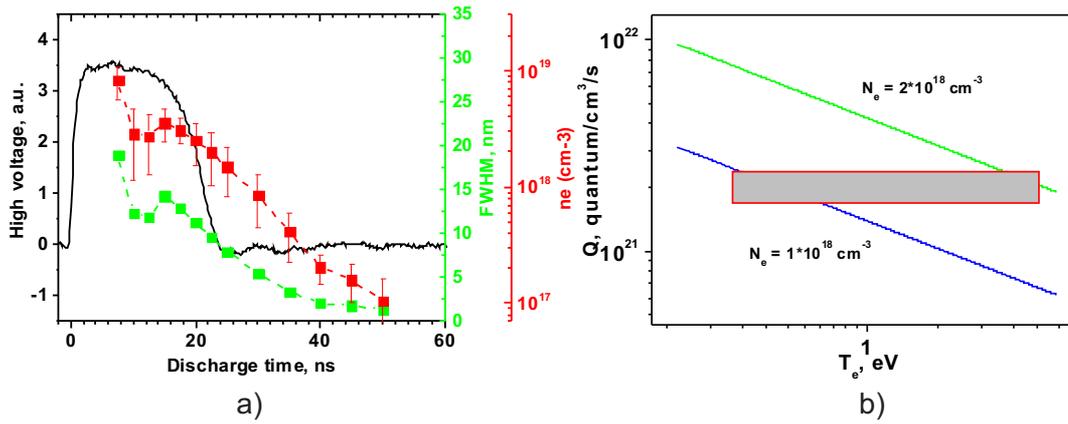
Figure 5.32: (a) Temporal profile of electron density recalculated in assumption of Stark broadening (see explanations in the text) and corresponding applied HV pulse and the width of H_α line; (b) calculated intensity of the recombination emission at the wavelength $\lambda = 337 \pm 1.5$ nm as a function of electrons temperature. Applied voltage $U = -50$ kV, $P = 8$ bar.

$2 - 4$ eV the densities of charged particles must be equal $n_e \approx 2 \cdot 10^{18}$ cm^{-3} and in the afterglow $T_e < 0.5$ eV, $n_e \approx 10^{18}$ cm^{-3}

In spite of a good correlation between n_e values obtained from Stark broadening and estimates of cw/N$_2$ emission intensity, the electron density seems to be too high. We can try to estimate roughly the electron density from the electrical current, assuming that the current per filament is about $(2 - 3)$ A and the radius of the filament is about 70 μm (see chapter 6). The current density is $j = I/S = \sigma \cdot E = en_e v_{dr}$. We can assume that the E/N in the channel is about ~ 10 Td. In such electric field the electron drift velocity is about $\sim 5 \cdot 10^6$ cm/s. Taking into account all these values the electron density is about $(5-8) \cdot 10^{16}$ cm^{-3} that is more than one order of magnitude lower than estimated n_e from line broadening and cw emission. One more argument against such high electron density $(10^{17} - 10^{18}$ cm$^{-3})$ is that the plasma decay rate increases with electron density. The decay is $\tau = 1/(\beta n_e) = 1/(10^{-7} \cdot 10^{18}) = 10^{-11}$ s, however we see the cw spectrum and highly broadened H_α line even in afterglow when $T_e \sim 0.5$ eV during ~ 10 ns.

Although the absolute n_e values obtained from the estimates above need additional verification, it is evident that the appearance of the cw spectra correlates with the appearance of high electron density. The filamentation is a reason of significant increase of the electron density.

5.2.6 The mechanisms of contraction and development of filamentary nSDBD

The basis of filamentation mechanism of the nanosecond SDBD, which is proposed in present work is the appearance of cathode or anode spots on the surface of exposed electrode. According to [113, 157], the normal current density in the cathode layer in air at $P = 6$ bar and $T = 300$ K is about $j_n \approx 6.5$ kA/cm^2. In these conditions the measured value of total current is less than $30 - 40$ A in the streamer mode just before filamentation. If we assume that this current is homogenously distributed in the thin layer with the thickness about 100μm along entire fringe of HV electrode ($2\pi R \approx 6$ cm), the current density will be $j_{el} \leq 0.5$ kA/cm^2, that is considerably lower than normal current density j_n. This is an unstable situation and leads to a discharge rearrangement, fragmentation of the cathode layer and the formation of the system of cathode spots in which the current density will correspond to normal one [157, 158]. The characteristic time of the cathode layer and spots formation in these conditions is determined by the time of plasma polarization in near electrode region that reaches $\sim 5 - 10$ ns.

Currently, there is a number of works [124, 127, 159, 160], where it is shown that the instability of self-sustained volumetric discharge usually begins with the appearance of the cathode/anode spots, followed by the formation of highly conductive plasma channel, which extends from the electrode into the discharge gap. The experiments of [124] showed that the homogeneous plasma column, which is stable against a strong plasma disturbance in the bulk, constricts readily if current spots on the electrodes are formed. The formation of these spots can be induced by weak plasma disturbances created not far from the electrode. Hence strong plasma disturbance located in the middle of the plasma column does not always initiate the discharge constriction but a weak disturbance located not far from the electrode can initiate current spot formation followed by the discharge constriction. The constriction induced by the current spot develops not as the simultaneous shrinking of the plasma column along its entire length but the constriction mode develops in the form of a thin high–current density filament originated from the spot on the electrode. This filament quickly elongates toward the opposite electrode with a typical velocity $10^4 - 10^6$ cm/s.

Similar results were obtained in [159] where contraction of high-current nanosecond discharge in nitrogen takes place at P = 70 Torr and a current density of hundreds of A/cm^2. The research was carried out in the tip–plane electrode system. During the instability development near the cathode layer (at the tip) the plasma channel with high electron density (10^{17} cm^{-3}) was formed. The propagation velocity of the channel reached $10^6 - 10^7$ cm/s. It should be noticed that the ionization

degree in the channel is rather high, whereas the channel propagation velocity a few tens times lower than the velocities observed during the filamentation in our case.

In [127, 160] the contraction of pulsed nanosecond discharge was observed in air and nitrogen at pressures $P = 1 - 6$ bar. The duration of the applied pulse was 3 ns. It was shown that highly conductive channel was produced from the anode or cathode spots, further this channel was propagating to the region of quasi–neutral plasma with the velocities $\geq 10^9$ cm/s.

The role of emission of the electrons from the cathode in discharges with high current density is discussed in [161]. The authors conclude, on the basis of PIC simulations and comparison with experimental study of run–away electrons, that the field emission is the dominant emission mechanism for pulses of duration of 2.5 ns and less, and that the explosive emission seems to be dominant at longer time scale. In the conditions of nanosecond surface DBDs, the high field emission can be caused by peculiarity in so called triple point that takes place in the region of gas-metal-dielectric junction. In this point the emission is stimulated by extremely high values of induced electric field created by the dielectric polarization. This effect is well known in power electronics. This phenomenon leads to a failure of the high-voltage equipment. Due to the high values of electric field at the vicinity of HV electrode, the high current spots and jets can appear.

Velocities of the filaments in the present work are at least two orders of magnitude higher than in [124], nevertheless the mechanism of filamentation seems to be quite similar: on the very first stage, a uniform plasma layer starts from the high-voltage electrode. This layer can be broken on separate streamers within a time scale of parts of nanoseconds; in this case streamer discharge is observed. The filamentation is a kind of instability caused by the appearance at least of one current spot on the high-voltage electrode. If this happens, the filament increases in length because of increase of the electric field in the filament head. The development of adjacent streamers is suppressed. This caused an appearance of the next current spot along the perimeter of the high voltage electrode, and the process develops in similar way until a regular structure of the filaments is formed around the high–voltage electrode. The distance between the spots and so, between the filaments, is regulated by the electric charge in the filament. The picture is similar to installing a mode-locking regime in multi–mode laser generation when the external source, acting on the inter-mode frequency, appears in the system. The process is fast: it can be easily seen at the point of transition (f.e. in air at $P = 3$ bar and $U \approx -50$ kV the transition takes a few nanoseconds); at developed filamentary mode ($P = 6$ bar and $U \approx -50$ kV) this takes less than 1 ns. High electron densities, produced behind the front of the filaments, cause recombination radiation.

The potential of the head region of highly conductive channel, filament, is higher

than the potential that streamer got in the same space point (this potential of streamer head set the charge density that was deposited on the dielectric surface in streamer mode). This leads to the formation of filamentation wave - a wave of overcharging of the dielectric surface, which propagates with higher velocity through streamer channels, and at the same time significantly increasing their conductivity. Since the capacitance charged by filaments during their propagation is rather high, the specific energy that comes into the filaments is also high. The electron density in the secondary ionization wave can be significantly [162, 163] higher, therefore the recombination radiation can make significant contribution to the emission of filamentary discharge.

It should be noticed that a similar effect of the cathode spots formation on the propagation of fast ionization waves was observed in [162]. This paper presents the results of the investigation concerning the waves of charging of capacitance with distributed parameters in the discharge tube with a metal screen. The studies were carried out in nitrogen at $P = 1 - 30$ Torr, the voltage pulse duration was $\tau = 20$ ns, the amplitude of HV pulses was $U = -30$ kV. After the formation of the cathode spots, the appearance of the secondary ionization wave, passing through the channel of primary one, was detected. The electron density and the emission intensity was significantly higher in secondary wave. The velocity of secondary ionization wave reached $V = 10^{10}$ cm/s.

The dielectric surface is charged mostly by the set of streamers. In the case of filamentary phase of the discharge it is charged also by streamers which start from the head of filament. This way of surface charging seems to be optimal since: (i) it provides fast charging of dielectric; (ii) this ensures the charging on a long distance. If the surface would be charged due to the electron drift in the strong radial field, the rate of charging would be much lower and, what is the most important, the charging would occur at relatively small distances - of the order of streamer head's size. Indeed the streamers propagate at much longer distance as far as they try to reach the regions with the lowest electric field (electric potential) values. But for the formation of streamer corona (not homogeneous ionization wave, leading to the "spreading" of the head) the certain conditions concerning the value of electric field in the head of filament must be fulfilled.

5.3 Schlieren spectroscopy of the nSDBD at elevated pressures

Gas heating and electrostatic body force generation are two basic mechanisms controlling the flow by SDBD plasmas. In AC SDBDs the dominant mechanism of the effect on the low–speed flows is associated with ions acceleration in a space charge region of the plasma, so–called electrohydrodynamic (EHD) force [1]. In SDBDs powered by high–voltage nanosecond ($\sim 10 - 100$ ns) pulses, the EHD accelerations can be neglected [164]. It was suggested in [10] that in the case of nanoseconds SDBDs the dominant effect of the discharge on the flow is caused by fase localized heat generation.

In pulse periodic regime [18] it was demonstrated that contracted, filamentary, nSDBD produces more intense shock wave than the quasiuniform plasma layer. Since the physics of either filamentary or streamer SDBD at high pressures was not described before, in literature there is no data describing hydrodynamic effects produced by nSDBD in a single shot regime at elevated gas densities.

5.3.1 Shock wave propagation produced by nSDBD at elevated pressure

Schlieren technique has been used for diagnostics of hydrodynamic and thermal effects of nSDBD. The sensitivity of the camera as well as the intensity of the light source remain the same during all considered experimental cases listed in table 5.1. The aim of the experiments was to compare hydrodynamic perturbations generated by a set of streamers or by a set of filaments. So, 6 different conditions were selected for the experiments. Different pressures and voltage amplitudes resulted in different discharge appearance and deposited energy.

Table 5.1: The range of experimental conditions

Number №	Pressure	Applied voltage	Energy deposition
Case 1	1 bar	-25 kV	11 mJ
Case 2	4 bar	-25 kV	9 mJ
Case 3	4 bar	-50 kV	25 mJ
Case 4	6 bar	-25 kV	8 mJ
Case 5	6 bar	+50 kV	38 mJ
Case 6	6 bar	-50 kV	49 mJ
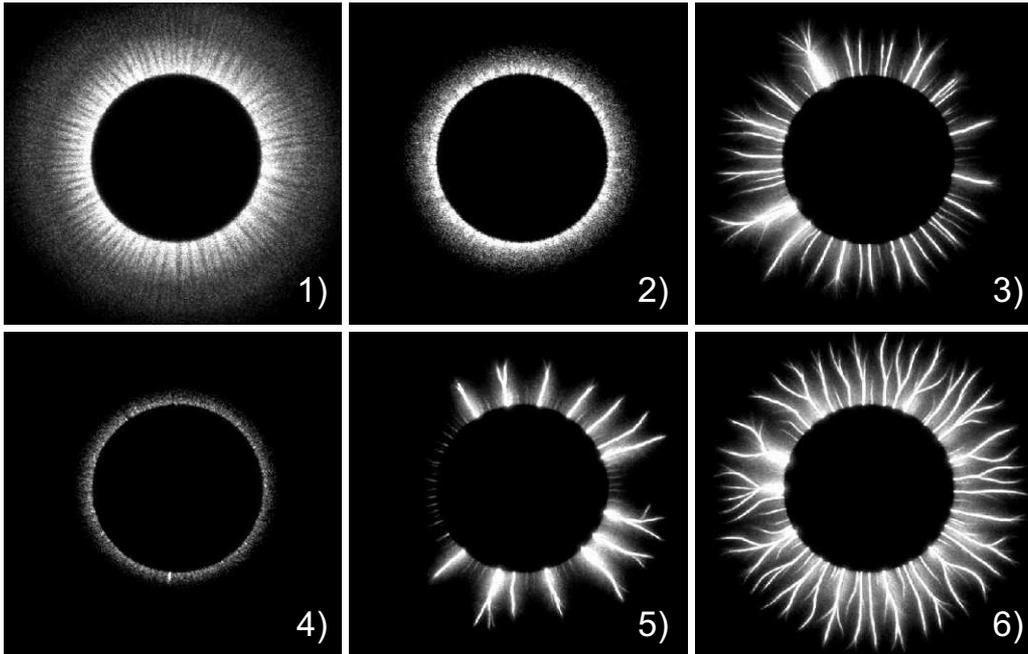
Figure 5.33: Discharge images for investigated cases. Camera gate 20 ns.

The corresponding discharge images are presented in figure 5.33. The streamer discharges were used for cases 1, 2 and 4. The cases 3, 5 and 6 corresponds to filamentary mode. The following conditions have been selected for two reasons: (i) to demonstrate how streamer discharge produces shock wave at fixed voltage but at different pressures (1, 4 and 6 bar). According to equation $E/N \approx U_0/(L_{max} \cdot N) = const$, at higher pressures (higher gas densities) the discharge propagates to smaller distance from HV electrode, reduced electric field remains almost the same; (ii) to compare the perturbations caused by streamer and filamentary discharges. Filamentary discharges were initiated at: $P = 4-6$ bar, $V = -50$ kV and $P = 6$ bar, $V = +50$ kV. These conditions were selected to compare the perturbations of the filamentary discharges of different polarities.

First of all let's consider the perturbations of streamer discharge in synthetic air, at P=1, ambient temperature and applied voltage $U = -25$ kV. This case almost repeats the conditions of chapter 4, except that the electrode in cylindrical symmetry is used here. As it was shown, the shock wave propagates from the plane of electrode, in the direction perpendicular to discharge propagation. During the first few microseconds the wave's velocity slightly exceeds the sound speed, $M = 1.2$. Here the set of images starts from 2 μs (figure 5.34), when shock wave is already generated. As far as the streamer discharge covers the dielectric layer homogenously, the propagating wave can be considered as a plane disk–like wave. The radius of the "disk" is practically equal to the discharge radius.

When pressure in the chamber is 4 bar (figure 5.34), the radius of produced shock
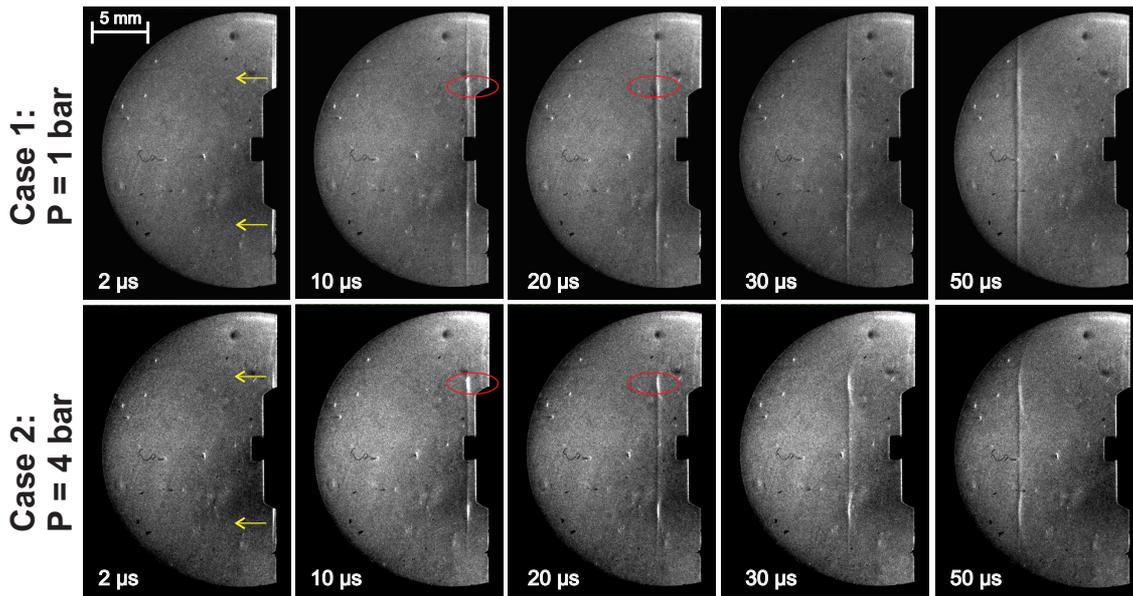
Figure 5.34: Schlieren images of the shock wave propagation. U=-25 kV. Camera gate is 200 ns.

wave is significantly smaller (is about 3 mm) than at P=1 bar (about 10 mm). As far as the conditions of these two experimental series are the same, one can see that the contrast is higher for the case 2 in near electrode region than that of the case 1, emphasised by red ellipses in figure 5.34. The intensity of the perturbation region (wave front) is directly related to the gas density in this region. The higher the contrast, the higher the density deviation from the normal, unperturbed gas. The discharge at $P = 4$ bar propagates at shorter distance, but the energy release in the near cathode region is higher than for $P = 1$ bar. Therefore, the higher contrast for the case of higher gas pressure seems to be reasonable. During the compression wave propagation the redistribution of gas density along entire "disk" volume takes place and finally, within $10 - 20\mu$s the front becomes flat. Starting from 70 μs, compression wave leaves the region visible through optical window. At approximately 200 μs a weak wave, reflected from the frontal optical window, moves in the opposite direction. Comparing the temporal behavior of contrast of reflected waves the wave can be noticed that it dissipates faster at higher pressures.

Case 6, presenting a well-developed filamentary discharge, is given by figure 5.35. The difference with the Schlieren image of the streamer mode (figure 5.34) is following: (i) intense cylindrical wave is produced around each filament; (ii) merging together, these waves produce a single front with the contrast $3 - 4$ times higher than in the streamer case and radius equals to the radius of the filamentary discharge; (iii) the contrast is almost uniform along the entire length of the filaments ($\sim 8 - 10$ mm). The uniformity of the contrast along the filaments confirms the uni-
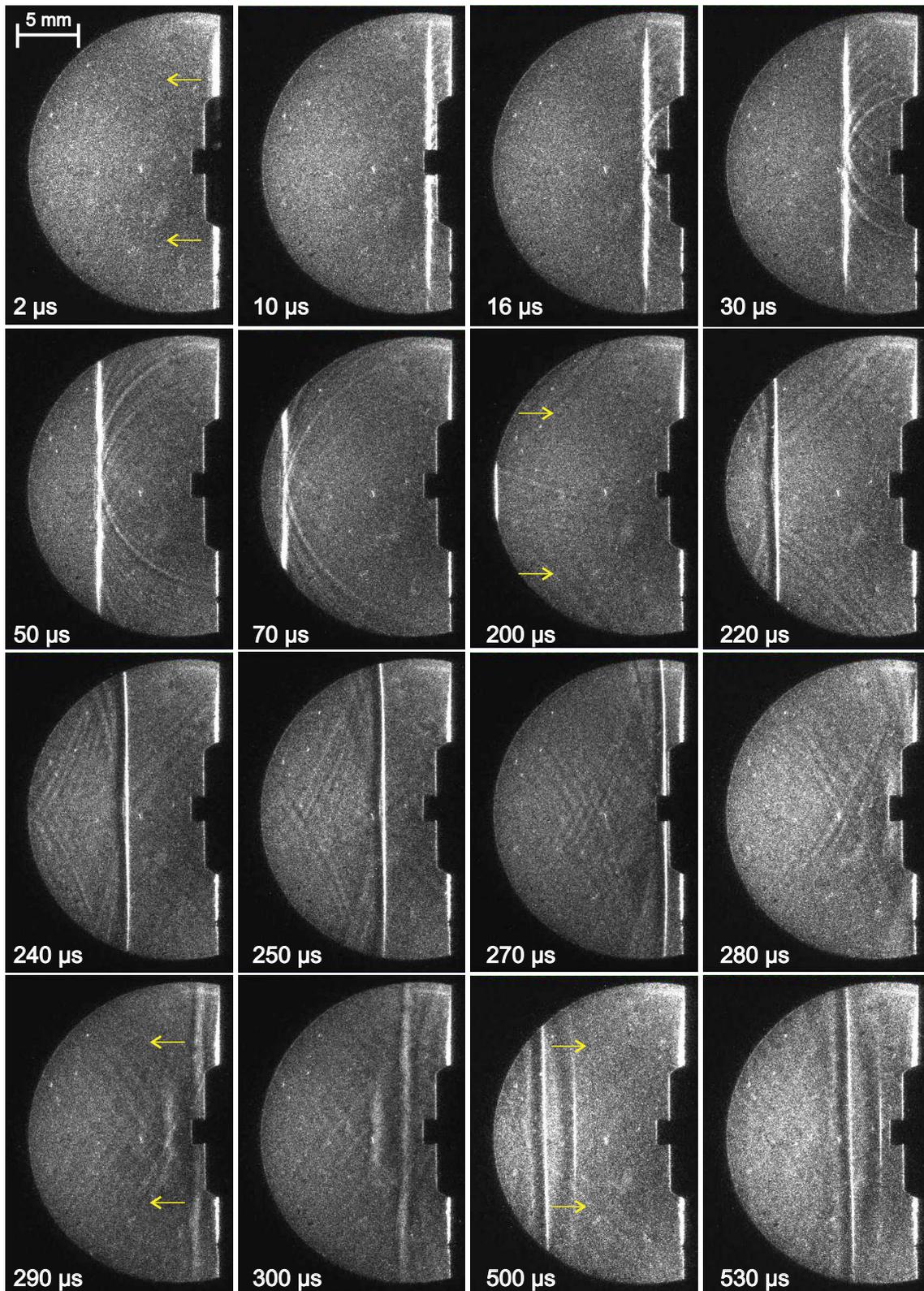
Figure 5.35: Schlieren images of the shock wave propagation. P=6 bar, V=-52 kV. Camera gate 200 ns.
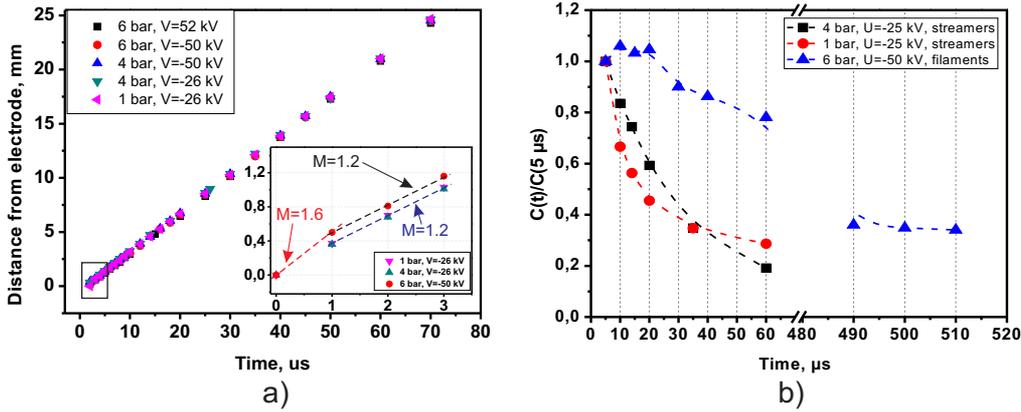
Figure 5.36: (a) Velocities of shock wave propagation at different pressures and applied voltages; (b) Contrast dynamics in the front of compression waves.

formity of parameters (f.e. the uniformity of electron density discussed in previous section) along the channel of the filament.

It is clearly seen that the produced compression wave "oscillates" between the electrode and frontal window of the chamber. The first wave, reflected from the opposite wall, appears ~ 200 μs after discharge initiation. The contrast of this wave remains rather high. This wave returns back to the electrode and even after reflection from dielectric surface it does not decay. The second reflected wave can be seen in ~ 500 μs. Its contrast is also high enough. It emphasizes the high values of power contributed to the compression wave by filamentary discharge. The contrast of the diagnostic system allows to distinguish the propagating waves even after $\sim 700 - 800$ μs.

The velocities of the compression waves in the direction perpendicular to the dielectric are presented in figure 5.36(a). Filamentary discharge produces the shock waves with initial speed $M \geq 1.5 - 1.7$, whereas the propagating velocity of the wave produced by streamer discharge is $M \geq 1.2 - 1.3$. The rates of the waves decay are compared for three considered cases and presented in figure 5.36(b). The relative contrast $\frac{C(t)}{C(5\ \mu s)}$ was analyzed as a function of time, where $C(t) = \frac{\Delta I}{I_0}$, I_0 - is an intensity of the background light at fixed cutoff knife position and $\Delta I = I_{front} - I_0$. Two important features can be emphasized: (i) the decay of the wave during first 60 μs does not exceed 10% for filamentary discharge, whereas the decay of the wave produced by streamers is considerably faster; (ii) for streamer discharges, the rate of wave dissipation is strongly coupled with the gas pressure, and as it was mentioned above, it decays faster for higher pressure.

5.3.2 Pressure in the front of compression wave

Because of a complex 3D morphology of the filamentary discharge in cylindrical configuration, calculation of the exact value of pressure is complicated. Nevertheless, it is possible to make the estimates in assumption that the compression wave has cylindrical symmetry (with respect to z-axes, see figure 5.37), and to describe some hydrodynamic effects from collective perturbation.

The schlieren image gives the information about the local deviations of the refractive index. The perturbation of the refractive index n is a function of the pressure p (or density ρ) in the wave producing this perturbation. The relation between the density and the refractive index is given by the *Gladstone-Dale equation*: where $G(\lambda)$ is a Gladstone-Dale number ($kg^{-1} \cdot m^3$) is defined for air as:

$$n + n_0 - 1 = G(\lambda) \cdot (\rho + \rho_0), \tag{5.13}$$

where $G(\lambda)$ is a Gladstone-Dale number ($kg^{-1} \cdot m^3$) is defined for air as $G(\lambda) = 2.2244 \cdot 10^{-4} \cdot (1 + ((6.7132 \cdot 10^{-8})/\lambda)^2)$, λ is light wavelength in m. As it has been shown, the perturbation propagates from the plane of electrode with the velocity close to the sound speed in air. Therefore the relation between the pressure and the density in the wave front is linear: $\rho = p/c_0^2$, and the refractive index can be expressed as

$$n = G(\lambda)\frac{p}{c_0^2} \tag{5.14}$$

Nonuniform distribution of the refractive index leads to the additional phase shift of the light, ϕ. In the plane xy shown in figure 5.37, the additional optical phase along the light beam is accumulated with light propagation in y-direction. The phase can be written as
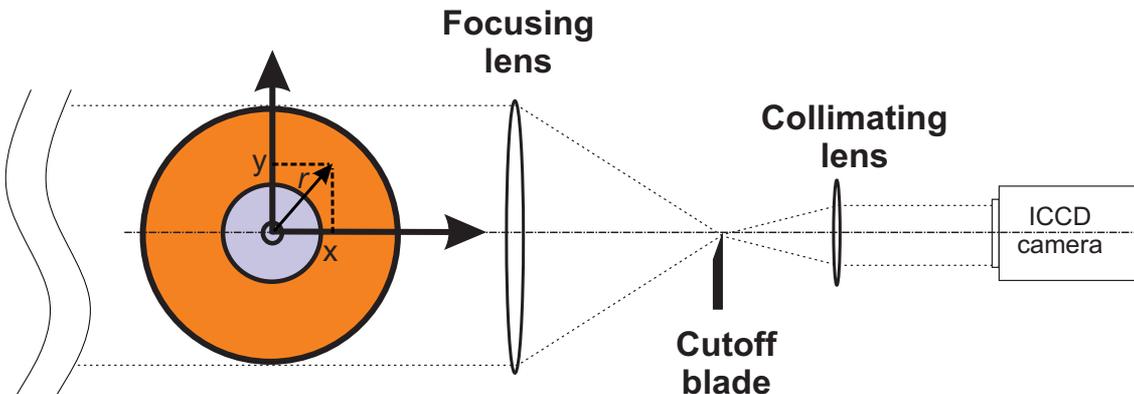
Figure 5.37: Geometry of the considered system.

$$\phi(x) = (2\pi/\lambda) \int_{-\infty}^{+\infty} n(x, y) dy. \tag{5.15}$$

Taken into account the cylindrical symmetry of the acoustic wave, the phase can be written as

$$\phi = \frac{2\pi}{\lambda} \int_0^{+\infty} 2n(r) dy = \frac{2\pi}{\lambda} \int_x^{+\infty} \frac{2n(r) r dr}{\sqrt{r^2 - x^2}} \tag{5.16}$$

where $r = \sqrt{x^2 + y^2}$ is a radius in the plane of the propagating wave. The equation (5.16) is the direct Abel transform [165] of the function $n(r)$. Then, by using the inverse Abel transform and the expression $s = \lambda\phi/2\pi$, where s is optical path with the phase shift ϕ, we get:

$$n(r) = -\frac{1}{2\pi} \int_r^{+\infty} \frac{ds}{dx} \frac{dx}{\sqrt{x^2 - r^2}}. \tag{5.17}$$

In the experiments, the intensity distribution is measured in the plane xz, that is perpendicular to image plane in figure 5.37. The intensity of the schlieren image formed by the light beam after the optical knife, is proportional to the deviation angle on the optical inhomogeneities [106]. Taking into account the cylindrical symmetry of the wave front, the deviation angle can be written as: $\varepsilon = \partial s/\partial l$, where $l^2 = x^2 + z^2$ is a radial coordinate in the image plane xz. Therefore, the intensity of the schlieren image is

$$I(l) = -C\frac{\partial s}{\partial l}, \tag{5.18}$$

where C is a unknown constant, and sign "-" shows the orientation of the optical knife with respect to the light beam (dark regions correspond to the higher gas density). If we put the knife from the opposite direction, the dark regions of the schlieren image will become brighter than a reference beam. By integrating the equation (5.18), we get the optical path s:

$$s(l) = \frac{1}{C} \int_l^{+\infty} I(l') dl', \tag{5.19}$$

For pressure estimates we reduce this problem to one–dimensional taking into account the cylindrical symmetry the considering the regions close to z–axis and put $z = 0$. In this case the integration takes place along the x-axis:

$$s(l) = \frac{1}{C} \int_x^{+\infty} I(l') dl', \tag{5.20}$$

Taking into account the equations (5.14), (5.17) and (5.20), we get a ratio between pressure profile and the intensity distribution in the schlieren image:
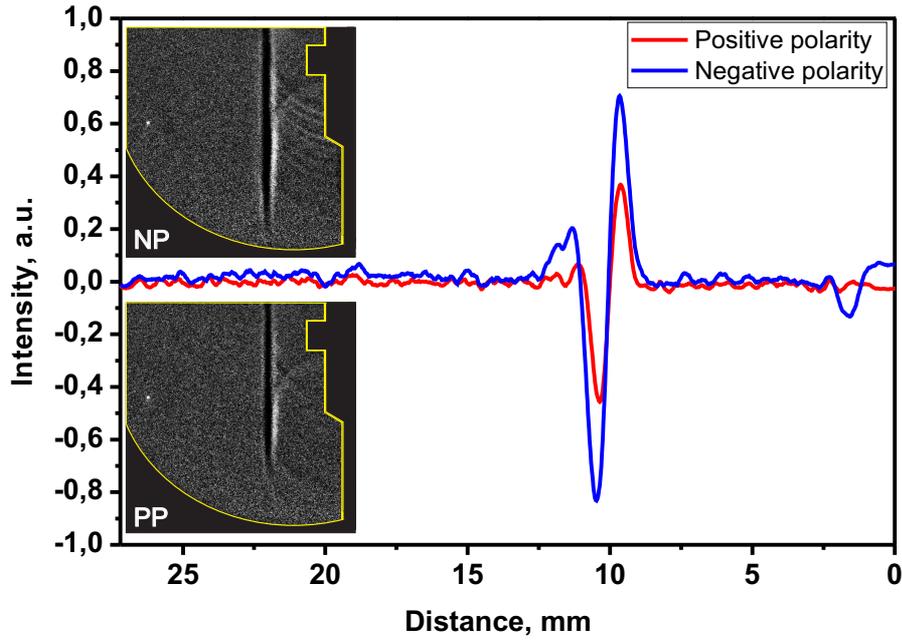
Figure 5.38: The wave produced with positive and negative polarity filamentary discharges in air. $P = 6$ **bar,** $|U| = 50$ **kV. Camera gate** 200 **ns. NP–negative polarity; PP–positive polarity.**

$$p(r) = -\frac{c_0^2}{2\pi GC} \int_r^{+\infty} \frac{d}{dx}(\int_x^{+\infty} I(l')dl')\frac{dx}{\sqrt{x^2 - r^2}}. \tag{5.21}$$

The equation (5.21) contains the unknown constant C, what makes impossible the calculation of absolute pressure profile directly from schlieren image. We can estimate the ratio between the pressure at different conditions.

The dimensionless pressure profiles can be obtained by calculation of the following integral:

$$p(r) \sim \int_r^{+\infty} \frac{d}{dx} \left(\int_x^{+\infty} I(l')dl' \right) \frac{dx}{\sqrt{x^2 - r^2}}. \tag{5.22}$$

For further pressure analysis in the wavefront it is necessary to analyse the wave structure. Figure 5.38 shows the wave profiles produced by positive and negative polarity filamentary discharge. The N–shape profile is clearly seen. It is clearly seen, that wave has N-like form. The corresponding schlieren images are presented in the same plot. The wave profiles are obtained by averaging the 1 mm width region near the edge of the HV electrode. The amplitude of the wave produced by negative polarity discharge is higher than that of the positive polarity. It is difficult to say what is the real reason. Two explanations are possible: (i) the energy release of the

151
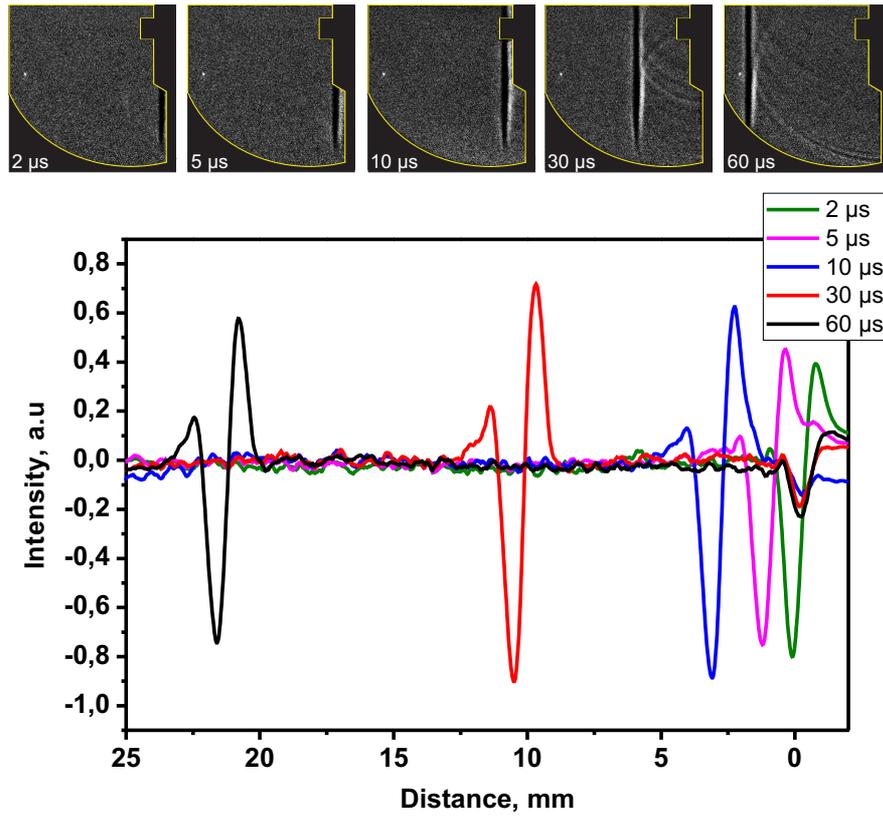
Figure 5.39: Propagation of the N-wave produced by filamentary discharge in air. $P = 6$ **bar,** $U = -50$ **kV. Camera gate** 200 **ns.**

negative polarity discharge is higher than in the positive polarity filaments; (ii) the discharge structure is different according to figure 5.33, cases 5 and 6. We can only conclude that for initiation of the more intense wave in air the negative polarity filamentary discharge should be used.

Figure 5.39 presents a few N–shape profiles for the wave initiated by the filamentary discharge at $P = 6$ bar and $U = -50$ kV. During first $2 - 10$ μs almost flat N–shape wave is formed. The attenuation of the wave amplitude with the distance from the electrode system is weak.

Pressure in the front of the compression wave were compared for different experimental conditions. Four cases were considered: 1) filamentary discharge at $P = 6$ bar and $U = -50$ kV; 2) filamentary discharge at $P = 6$ bar and $U = +50$ kV; 3) streamer discharge at $P = 6$ bar and $U = -25$ kV; 4) streamer discharge at $P = 1$ bar and $U = -25$ kV. The pressure profiles in arbitrary units were restored according to equation (5.22). The radial intensity $|I|$-profiles are plotted in figure 5.40(b). The profiles are averaged over the wavefront thickness as it is shown in figure 5.40(a). The segment of maximum amplitude was selected. Dark region in the insert of schlieren image (figure 5.40(a)) corresponds to the pressure surplus
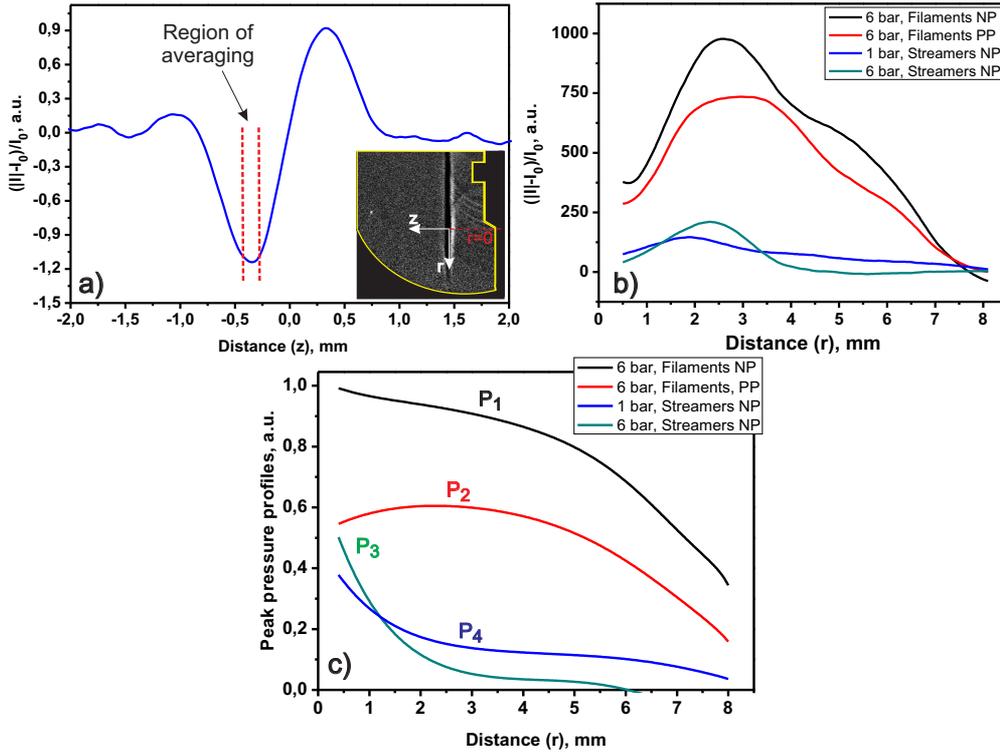
Figure 5.40: (a) N-wave structure. Representation of the region of averaging for pressure analysis; (b) Radial profiles of the contrast. $|I|$- module of intensity in arbitrary units; (c) pressure profiles in arbitrary units (in r–direction).

in the wavefront. All the profiles are plotted for time instant 25 μs after discharge initiation.

Figure 5.40(c) demonstrates the pressure profiles in r-direction. It is clearly seen that both pressure behavior in r-direction and absolute values of pressures are different depending on gas pressure and discharge structure. The maximum of the pressure is in the near electrode region for negative polarity filaments and a few millimeters away from the edge of HV electrode for positive polarity discharge. For streamer discharges the maximum corresponds to the near electrode region and decreases significantly with the distance from HV electrode. The ratio of maximum pressures for considered cases are: $P_1^{max}/P_2^{max}/P_3^{max}/P_4^{max} = 2.7/1.6/1.3/1$. The maximum pressure in the filamentary discharge of negative polarity ($P = 6$ bar), is more than 2 times higher than the pressure in the streamer discharge.

5.3.3   Relaxation of the heated near-electrode region

One more distinctive feature that is present in case 6 and is absent for streamer discharges is the existence of the region of decreased gas density at the near electrode area. Figure 5.41 demonstrates schlieren images of the developing perturbation. The heated channels are rather uniform up to $\approx$100 μs. Starting from 200 μs, the channels become inhomogeneous. These inhomogeneities are related to the decay of heated channels. The changes of the considered region occur much slower comparing to the propagation of generated aforementioned waves. Thus, the camera gate was increased up to 10 μs to increase the signal/noise ratio.
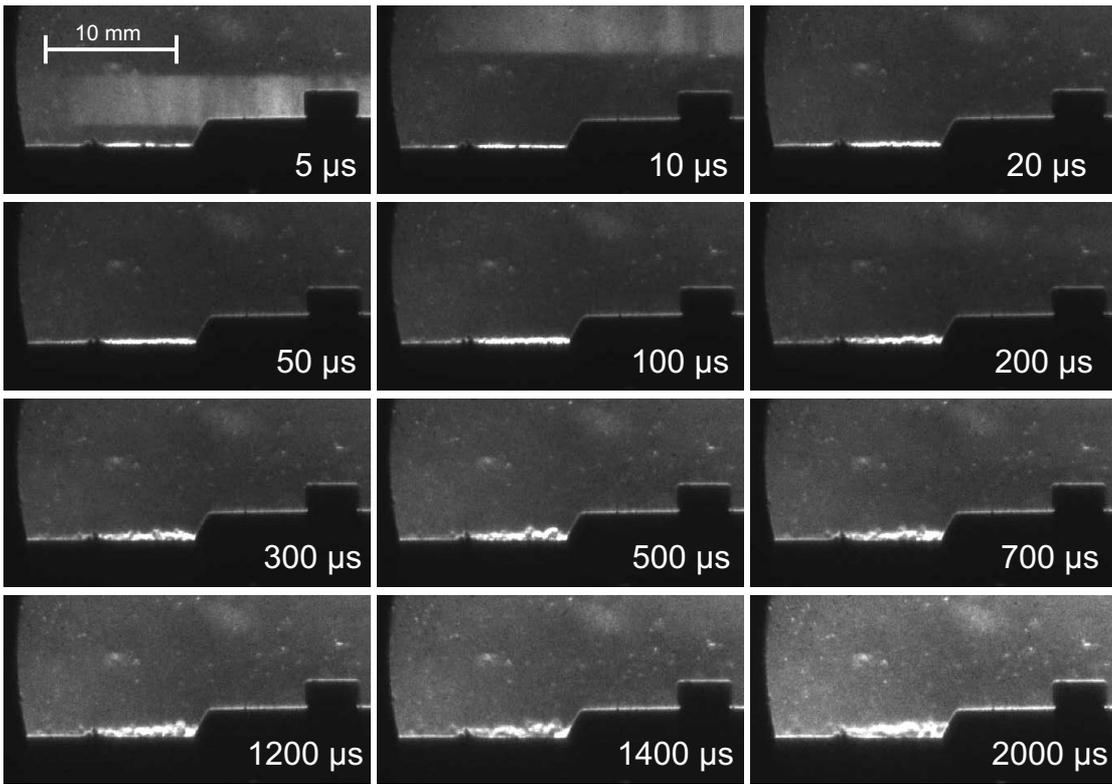
Figure 5.41: Schlieren images of the near electrode heated region. $P = 6$ **bar,** $|U| = 50$ **kV. Camera gate** 10 μ**s.**

Two different perturbations in units and in hundreds of microsecond time scales show us that there are two mechanisms of energy release during and after the discharge initiation. The fast (on a nanosecond time scale) heating mechanism caused primarily by quenching of N_2^* electronic excited states by oxygen molecules: $N_2^*+O_2 \rightarrow N_2+O+O+heat$, results in significant pressure increase in the filament. This sharp pressure increase, with subsequent gas expansion of the filament, is equivalent to high–amplitude pressure perturbation generated by the discharge in gas flows [166]. Quantitative evidence of this expansion is demonstrated in figures 5.34
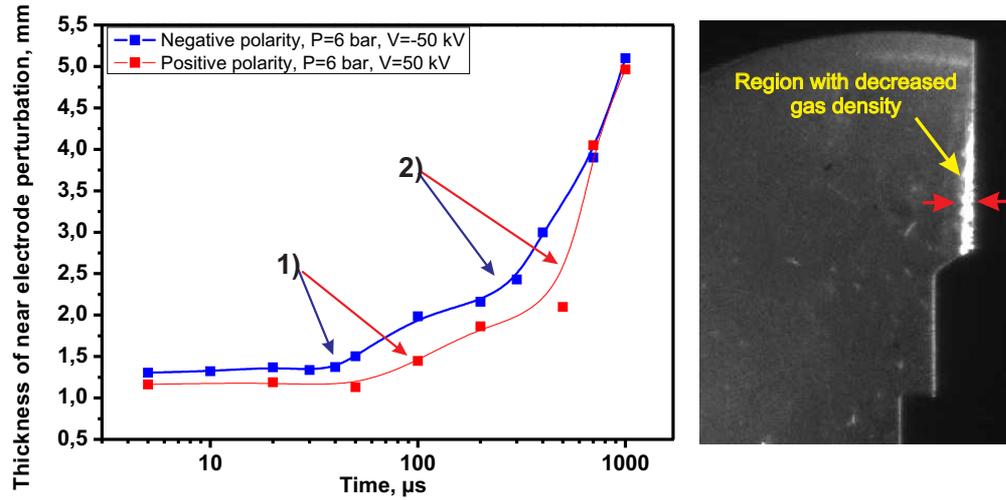
Figure 5.42: Thickness of the near–electrode perturbation as a function of time. $P = 6$ **bar,** $|U| = 50$ **kV. Camera gate is** 10 μ**s.**

and 5.35 which show compression waves origination in the discharge filament and propagating in the direction perpendicular to electrode surface after the discharge pulse.

The subsequent "slow" heating on the time scale of $t \sim 10 - 200$ μs after the discharge pulse is detected only in filamentary discharge mode. It occurs at the same time scale as V-T relaxation of the nitrogen molecules by O_2 and N_2 molecules and also by O-atoms: $N_2(\nu)+O \rightarrow N_2(\nu - 1)+O$.

Spots–like perturbations have been already observed near the surface of dielectric in pulse periodic SDBD a few hundreds of microseconds after the discharge initiation [18]. It was assumed that possible reasons of these perturbations can be a local heating of the dielectric layer and subsequent cooling on considered time scale. This point of view is reasonable for the particular case of the pulse periodic SDBD. But probably, the spatial resolution of the diagnostics system in [18] does not allow to resolve the channel structure as it is demonstrated in figure 5.41. In our conditions for single pulsed nanosecond SDBD dielectric surface is unlikely heated in nanosecond time scale.

The heated near-electrode region expands and transforms to some non–uniform structure of vortices. The pressure in the heated channel is practically equal to the external one, whereas the temperature is higher than the ambient temperature. Since the channel has a source of heat release, it expands without any turbulization. When the heat source does not exist anymore, the temperature in the channels start to decrease. A further temperature decrease occurs at almost constant pressure

that is accompanied by a gas density rise and requires a gas flux from periphery of the channel to the volume. This reverse radial gas flow is unstable and as a result, the turbulent gas flow appears inside the channel. According to the current understanding of the following phenomenon, the main mechanism of the appearance of the hydrodynamic instability is the Rayleigh–Taylor instability.

The development of Rayleigh–Taylor instability in the transition layer of the expanding channel is possible if the channel fringe is moving with deceleration. At the same time, such motion is allowed only if the gradients of pressure and gas density are in opposite directions, e.g. the following condition is satisfied $\nabla p \cdot \nabla \rho < 0$. The expansion of a single heated channel and development of Rayleigh–Taylor instability are analyzed theoretically in [167]. The modeling was performed for a single heated channel of a lighting. The energy release was due to the high current in the lightning plasma. As soon as current drops down, the heating processes terminates and the instability is observed.

In our case the heat source in the afterglow is due to energy transfer from vibrational degrees of freedom. Therefore, the time of turbulization should coincide with the time of VT-relaxation. The most significant process of vibrational relaxation of $N_2(X^1\Sigma_g^+,\nu)$ molecules in nitrogen:oxygen mixtures is the VT relaxation on oxygen atoms $O(^3P)$. The density of $O(^3P)$ atoms was roughly in [46] and reaches rather high values of $[O(^3P)]=10^{18}$ cm^{-3}. The characteristic time of VT relaxation $\tau_{VT} = 1/(k_{VT}[O])$, where $k_{VT} = 4.5 \cdot 10^{-15}(T/300)^{2.1}$ the rate constant of VT relaxation of nitrogen molecules on oxygen atoms taken from [79]. In considered conditions this time is in the range of $100 - 500$ μs.

The plot presented in figure 5.42 shows the thickness of the heated near-electrode region as a function of time. The behavior of the heated region is demonstrated for the positive and the negative polarity filamentary discharges. Two slope changes can be seen in the plot (1 and 2 in the figure). The first one corresponds to the beginning of the channels expansion and the second one - to turbulization of the channels, that correlates with VT-relaxation time. For negative polarity of applied pulses the turbulization starts earlier. As far as the rate constant k_{VT} increases with gas temperature we can conclude that, the temperature in the channel and thus the heat release is higher for negative polarity filaments in air. The turbulization times are equal ~ 200 μs and ~ 500 μs for negative and positive polarity of applied pulses respectively.

5.4 Conclusion

Development of single pulsed nanosecond SDBD has been studied in different gas mixtures for a range of pressures $1 - 12$ bar at ambient temperature. With pressure and/or voltage increase the streamer discharge transforms to filamentary nSDBD. The constriction takes place within a few nanosecond during the applied HV pulse. It was found, that the constriction of the surface nanosecond discharge - filamentation in a single shot regime is a very common phenomenon for any gases and polarities of applied pulses. The current and energy deposition of the discharge are directly related to the gas mixture and the discharge structure.

For the first time the time and spatially resolved spectra of single filament were obtained. The spectral analysis showed that emission spectra of filamentary discharge consist of two components: (i) the second positive system of molecular nitrogen (SPS); (ii) continuous spectrum. It was found, that the SPS emission bands comes only from the head of filaments (streamer corona of filaments), whereas the cw spectrum comes only from the body of filaments. A few lines corresponding to emission of N^+ ion, C-atom and also the violet band of CN-radical have been detected in the body of filaments together with cw components. The main reason of the cw component appearance in filamentary discharge is the recombination radiation. For this case the electron density should be high enough, that is confirmed by broadening of O- and H-atomic lines. According to analysis of emission spectra and current behavior the electron density should be $n_e > 10^{17}$ cm^{-3}. At the same time the electric field in the filament body is relatively low, $E/N \simeq 1 - 5$ Td. It is confirmed by absence of the emission of 2^+ system of molecular nitrogen. There is no significant temperature increase during the discharge in any region of the filament. The mechanism of the discharge constriction is discussed. Theoretical estimates and literature analysis of experimental investigation under different conditions showed that the appearance of anode and cathode high current spots can be suggested as a mechanism of filamentation.

Schlieren spectroscopy have been used to visualize the processes after the discharge initiation in air at elevated pressures. The shock waves that transform within a few microseconds to acoustic waves have been studied for different gas pressures, applied voltages and polarities of applied pulses. It was found that the waves produced by filamentary discharge a few times more intense than the waves produced by streamer discharge. The pressure drop in the wavefront of the filamentary discharge is $2 - 2.5$ times higher than that in streamer discharge. The contrast and thus the pressure drop in the wavefront attenuates during the propagation of the wave initiated by streamers. However, the amplitude of pressure drop remains almost constant while propagating of the wave initiated by filaments. Analysis of the pres-

sure profiles shows that the energy distribution in the propagating waves depends significantly on the polarity of applied pulses and the discharge mode (filaments or streamers).

It was found that the region of decreased gas density is produced after the discharge initiation near the dielectric surface. This layer correspond to the heated channels on the place of the discharge filaments. The thickness of this layer increases with time and $200 - 500$ μs after the discharge initiation, depending on polarity of applied pulses, the channels turbulizates and decays. The turbulization time coincides with a typical time of VT-relaxation of $N_2^*(\nu)$.

Chapter 6

Plasma-assisted ignition of H_2:air mixtures with nSDBD

Initiation and sustaining of combustion of lean mixtures at high gas densities is a challenge for the combustion community. One of the possible solutions is the ignition/combustion assisted by low temperature nonequilibrium plasma, or so–called plasma assisted ignition/combustion (PAI/PAC) [168]. The mechanisms of plasma assisted ignition and combustion [87, 88, 93, 169] include dissociation of molecular species by electron impact, energy transfer from electronically excited species, like $N_2(B^3\Pi_g)$, $N_2(C^3\Pi_u)$, $O(^1D)$ and others to dissociation or to fast increase of gas temperature [79, 82] and partial reforming of fuels [170, 171].

The nanosecond spark discharge could be an efficient tool for ignition at elevated gas densities. It provides a high local energy density. This energy is distributed over the degrees of freedom according to the E/N values. As it is described in [83], it provides both fast gas heating up to ~ 1000 K within a few nanoseconds and efficient excitation of electronic and vibrational states. From the other side, the ignition of combustible mixtures by uniform, distributed over the volume or surface, excitation is the best way to increase the stability and to reduce the combustion time.

The spatial distribution of active species is characterised by discharge morphology. As it was demonstrated in the previous chapters, sustaining homogeneous plasmas at high gas density is a complex technical problem. A lot of conditions should be fulfilled: it is necessary to provide significant pre-ionization of gas mixture by UV or fast electrons [172, 173], to keep the voltage rise time short enough and so to provide the conditions when the local field is higher than the critical ionization

field [174] etc.

In nanosecond SDBD the deposited energy is equally distributed over the set of 100–200 streamers or 40–60 filaments, depending on the conditions described in chapter 5. The nanosecond SDBD was suggested for PAI/PAC [5, 175] due to the fact that a quasi-uniform plasma pattern is produced at elevated pressures in the plane of high voltage electrode for a typical time much shorter than the ignition delay for combustible mixtures; the produced plasma is a non-equilibrium plasma acting on the gas *via* the production of atoms/radicals/excited species and temperature increase due to their recombination and relaxation, and *via* possible hydrodynamic effects. Although the advantages of nSDBD for the initiation of combustion were clearly demonstrated, the discharge in high–pressure combustible mixtures was practically not studied and the picture of ignition of gas mixtures by nSDBD plasma was not clear.

This chapter presents the results of experimental study of plasma-assisted ignition by nanosecond SDBD under stationary initial conditions. The chapter contains four parts. The first one describes the behavior of nSDBD in lean combustible H$_2$:air mixtures $ER = 0.3 - 0.6$. The initial conditions were in the range of pressures $1 - 6$ bar and ambient temperature. The streamer–to–filament transition is discussed. The second part of the chapter is devoted to the morphology and efficiency of the flame initiation by different discharge modes. The influence of the discharge structure and energy deposition on the ignition is demonstrated. The velocity of flame propagation and its hydrodynamics are analyzed in the third part of the chapter. The minimum ignition energy of the discharge and ignition delay time of combustion have been measured and analyzed with the help of kinetic numerical modeling in the last part of the chapter.

6.1 Streamer–to–filament transition of nSDBD in H$_2$:air mixture

Lean hydrogen/air mixtures were selected for the PAI experiments because H$_2$ combustion is one of the most classical and the most studied processes. A large number of experimental results are available for a variety of conditions and experimental installations: constant volume chamber, shock tubes and RCMs. The kinetic mechanisms of hydrogen containing mixtures are well developed. Therefore we can focus on the efficiency of ignition with nSDBD, namely on the morphology of the discharge in H$_2$:air mixtures and on subsequent flame propagation.

Both discharge modes, streamer and filamentary, are of interest for plasma assisted ignition. The conception of the distributed, multi–point ignition at high
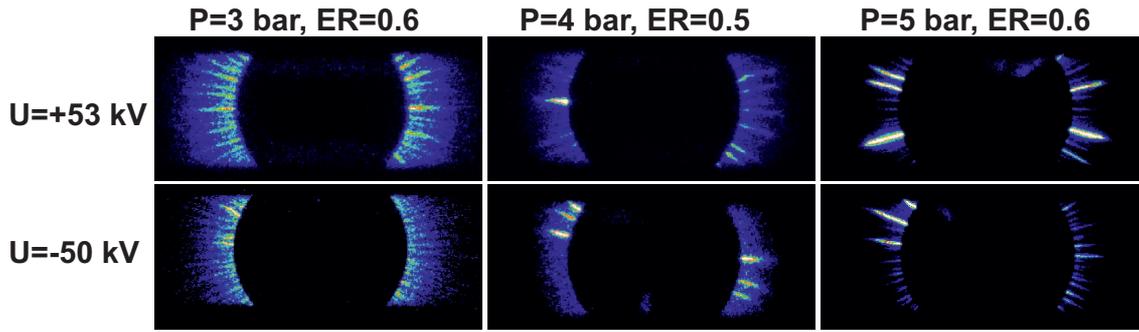
Figure 6.1: Positive and negative polarity discharge in H$_2$:air mixtures. Camera gate 100 ns.

pressures is of particular value. As it was demonstrated, the discharge morphology is directly related to gas density. In real systems such as SI engines, we have to deal with elevated gas pressures. So, to analyze the efficiency of flame initiation with both discharge modes is a very important problem.

Mixtures studied in the previous chapter are not combustible. They may contain fuels (CH$_4$, H$_2$) but without oxidizer, diluted by N$_2$ or Ar. It was demonstrated, that depending on gas composition the discharge structure behaves differently. For example, in air, N$_2$ and N$_2$:H$_2$ the discharges with positive and negative polarity of applied pulses have different threshold parameters $\{P_{th}, U_{th}\}$ for the streamer–to–filamentary transition. If in air, for fixed value of applied voltage, the negative polarity discharge undergoes the contraction at lower pressure (3 bar in our system), the positive polarity discharge transforms to the filamentary mode at higher values of gas pressure (6–7 bar). The opposite situation is observed in nitrogen and N$_2$:H$_2$ mixtures.

The experiments in combustible gases are more complicated. After each experiment the chamber must be evacuated and filled with a new portion of the investigated gas. It is not possible to work in the mode of data accumulation, even for adjustment of the experiment. Figure 6.1 presents integral ICCD images of the discharge in H$_2$/air mixtures with equivalence ratio (ER=0.5-0.6) for the pressures range $3-5$ bar. The discharge was initiated with both positive and negative polarities. The applied voltages were $+53$ and -50 kV. It can be noticed that the regime with well developed filamentary discharge with periodical structure of filaments was not acquired in the considered range of parameters. However, for the case of $U = +53$ kV, $P = 5$ bar and ER=0.6, several filaments can be seen. It suggests that the positive polarity discharge becomes filamentary at lower threshold parameters.

To compare the ignition of H$_2$/air mixture with streamer and filamentary nSDBD we need to select the conditions where we can clearly distinguish streamer and
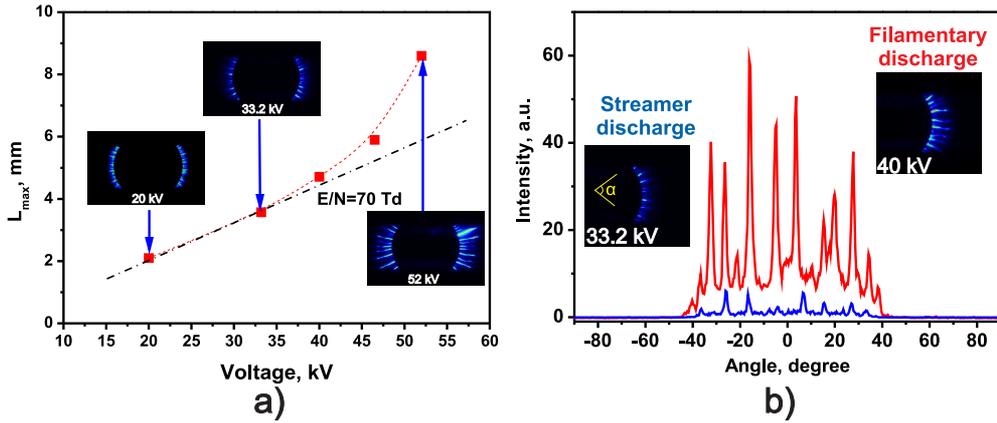
Figure 6.2: **(a) Maximal length of discharge propagation in H$_2$:air mixture as a function of applied voltage.** $P = 6$ **bar,** $T = 300$ **K,** $ER = 0.5$**; (b) comparison of angular distribution of emission intensity for streamers,** $U = +33$ **kV and filaments,** $U = +40$ **kV on the high–voltage electrode.**

well developed filamentary modes of the discharge. To achieve rather developed filamentary regime in H$_2$/air mixture the following conditions were selected: positive polarity of HV pulses, P=6 bar, equivalence ratio $ER = 0.5$.

The difference in the maximal propagation length of streamers and filaments in H$_2$:air ($P = 6$ bar, $ER = 0.5$) mixture is not so well pronounced like for air or nitrogen, the transition between streamer and filamentary modes is smooth. This is illustrated by figure 6.2(a) representing L_{max} as a function of applied voltage. The ICCD images for selected conditions, $U = +20, +33$ and $+52$ kV, are given in the same plot. A streamer discharge is observed for $+20$ and $+33$ kV. At high voltage ($+52$ kV), a filamentary mode is clearly seen in the image. Indeed, two dots without images in figure 6.2(a) for amplitudes $+40$ and $+46.5$ also correspond to filamentary discharge.

The difference between streamer and filamentary mode is clearly seen from the angular (transversal) distribution of emission, see figure 6.2(b). The intensity profiles are plotted as a function of azimuth angle in the plane of the electrode. The angle is marked in the ICCD image as α. The angle α is determined by the opening in the upper flange of the discharge chamber (see the details of the experimental setup in the chapter 3). So, the discharge can be seen just through this peephole. Therefore, in figure 6.2(b) we see a non–zero intensity level in the angle range $[-40, +40]$ degrees. Filamentary mode provides a regular structure of bright emitting channels, with emission intensity $20 - 30$ times higher than emission of a streamer mode at relatively close voltage amplitudes, $+33$ and $+40$ kV. Another possibility to distinct between a streamer and a filamentary mode in lean H$_2$:air mixture is illustrated by

figure 6.2(a): maximal length of propagation, L_{max} in streamer mode are situated on the line $E/N = const \approx 70$ Td, while L_{max} for filaments is noticeably higher.

To understand a correlation between the discharge appearance and the behavior of the ignition pattern, a set of experiments was carried out by varying only the amplitude of the high voltage pulse. A broad optical access provided by HPHT discharge cell allows studying the nSDBD discharge and the following combustion under the same experimental condition that is an important feature of the present experiments.

6.2 Initiation of combustion in the afterglow of nS-DBD in H$_2$:air mixture at elevated pressures

6.2.1 Ignition pattern

Spectral analysis shows that after the discharge, the dominating emission is the emission of OH radical ($\lambda = 306.4$ nm, $A^2\Sigma(v' = 0) \rightarrow X^2\Pi(v'' = 0)$ transition). This molecular band was chosen to study initiation of combustion after the discharge action. The emission spectra obtained during the discharge and during the afterglow with the following flame are demonstrated in figure 6.3. The ignition is triggered by a streamer discharge. Pressure and applied voltage were equal to $P = 3$ bar and $U = -50$ kV respectively. It is clearly seen that during the discharge (first ~ 20 ns) only second positive system of N$_2$ can be observed. When discharge
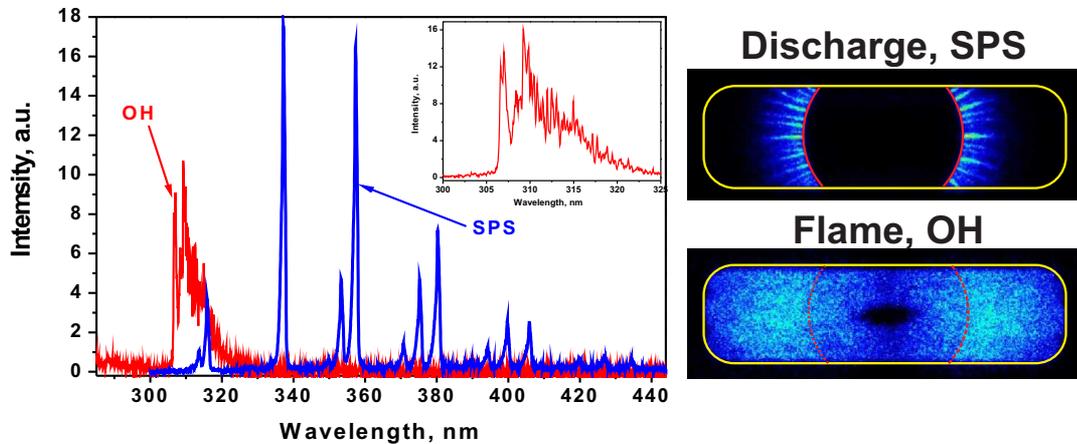
Figure 6.3: Emission spectra of the discharge (blue line) and subsequent flame (red line) in H$_2$:Air mixture; $P = 3$ bar, $U = -50$ kV, $ER = 0.6$; the gate of the camera for discharge 100 ns, for flame 1 ms.
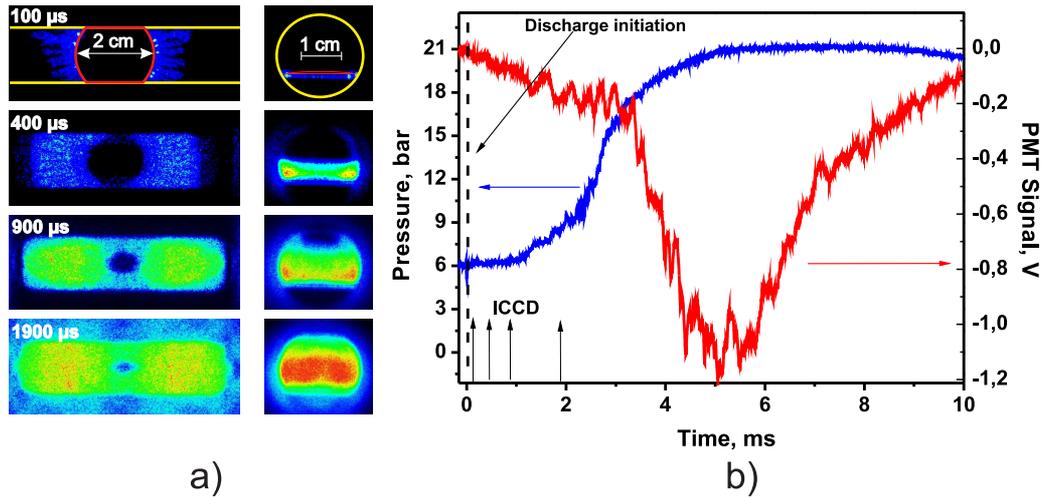
Figure 6.4: (a) ICCD images of frontal and side views of ignition of H₂:air mixture with nSDBD: $U = +53$ kV. $P = 6$ bar, $T = 300$ K, $ER = 0.5$. Camera gate is equal to 50 μs, delay between the discharge and ICCD gate is indicated in each frame; (b) pressure and OH emission as a function of time. Vertical arrows indicate the time instants where the ICCD images were taken.

action terminates, with some delay depending on a set of parameters (P, U, ER) the glow corresponding to the emission of OH–radical takes place. For OH emission spectrum and corresponding ICCD image of the flame, the signal was accumulated during 1 ms. Delay of the camera was 10 μs. It can be noticed that no other lines and bands are present during the flame propagation in the wavelength $220 - 450$ nm. All the emission intensity of the ignition pattern is related to the emission of OH.

ICCD images of OH emission for H₂:air $(ER = 0.5)$ mixture at $P = 6$ bar are presented in figure 6.4(a). Voltage pulse $U = +53$ kV in amplitude is applied to the high–voltage electrode at time instant $t = 0$. Frontal and side ICCD images are synchronized in time, the time instant is marked in the left upper corner of each pair of frames. It is seen that the emission front starts after the discharge from the near–electrode zone, propagates gradually and reaches the upper flange of the discharge chamber in a few milliseconds. OH–emission pattern at $t = 100$ μs (the first frame) is similar in shape to the discharge.

Figure 6.4(b) represents synchronized oscillograms of the KULITE pressure sensor installed in HPHT chamber and OH emission taken with the PMT connected with the Acton spectrometer. Joint analysis of the OH behavior and ICCD images proves that sharp increase of pressure between 2 and 4 ms is accompanied by a sharp increase of intensity of OH emission. So, between 2 and 4 ms the initiation of

combustion in the entire volume of HPHT chamber takes place, and the combustion front expands out of the discharge chamber through the rectangular slit in the upper flange.

6.2.2 Temperature analysis

To study the combustion development at time interval $0-3$ ms, when pressure rise is small but already clearly seen, the spectra of two different molecular transitions were analyzed. The rotational temperatures of hydroxyl radicals and molecular nitrogen were recorded at 306.4 nm and 337.1 nm respectively. OH-emission was available all the time in the discharge afterglow, so the emission spectra of excited hydroxyl radical corresponding to A$^2\Sigma^+$, v'=0 $\to$ X$^2\Pi$, v"=0 transition were recorded at different time instances: $2, 300, 600, 1900$ and 3500 μs after the discharge. To get N$_2$(C$^3\Pi_u \to$ B$^3\Pi_g$) emission, molecular nitrogen was excited by the discharge. The spectra were taken during the main discharge and in the additional probe pulse, initiated only for this kind of measurements 1.9 ms after the main pulse. All theoretical spectra were simulated with SpecAir code [104, 105] with the known slit function of the spectrometer calculated from the broadening of Hg line of a calibration source.

Figure 6.5(a) shows experimental and calculated emission spectra of OH* acquired at different time moments and figure 6.5(b) shows the values of corresponding rotational temperatures. A small inserted plot demonstrates the OH–emission and pressure profiles. Pink and blue rectangular denote the position and with of camera gate while spectra acquisition. For all demonstrated spectra the camera gate was equal to 100 μs. The resolution of the spectral system remains the same for the cases presented in figure 6.5(a) and FWHM of broadening slit function is $\Delta\lambda = 0.64$ nm. Spectra of the same band presented in figure 6.5(c) were obtained with higher resolution and FWHM was equal to $\Delta\lambda = 0.27$ nm.

As it can be seen from figure 6.5(b) the rotational temperature of OH* increases relatively fast. During the period $100-300$ ns its value increases two times. Afterwards it saturates and $T_{rot}^{th} \approx 3500$ K. The fact that during $0-0.1$ ms and $0.5-3$ ms, the OH rotational temperatures are different indicates that a chemical way to get the OH(A$^2\Sigma^+$) changes. The saturation of the rotational temperature means that initially one way of radicals production takes place ($0-0.1$ ms). Then, the second channel appears, starts to dominate ($0.1-0.3$ ms) and later replaces the first one.

It is known that the main reaction responsible for production of OH(A$^2\Sigma^+$) in the discharge later afterglow or in flame is O+H+M=OH(A$^2\Sigma^+$)+M. In this reaction the radical is formed with high rotational energy. The rate constants of quenching of OH(A$^2\Sigma^+$) radicals by H$_2$,O$_2$,H$_2$O molecules are high, on the order of $(2-5)\cdot 10^{-10}$ cm^3/s (see table 6.1), so the quenching of OH(A$^2\Sigma^+$) is faster than
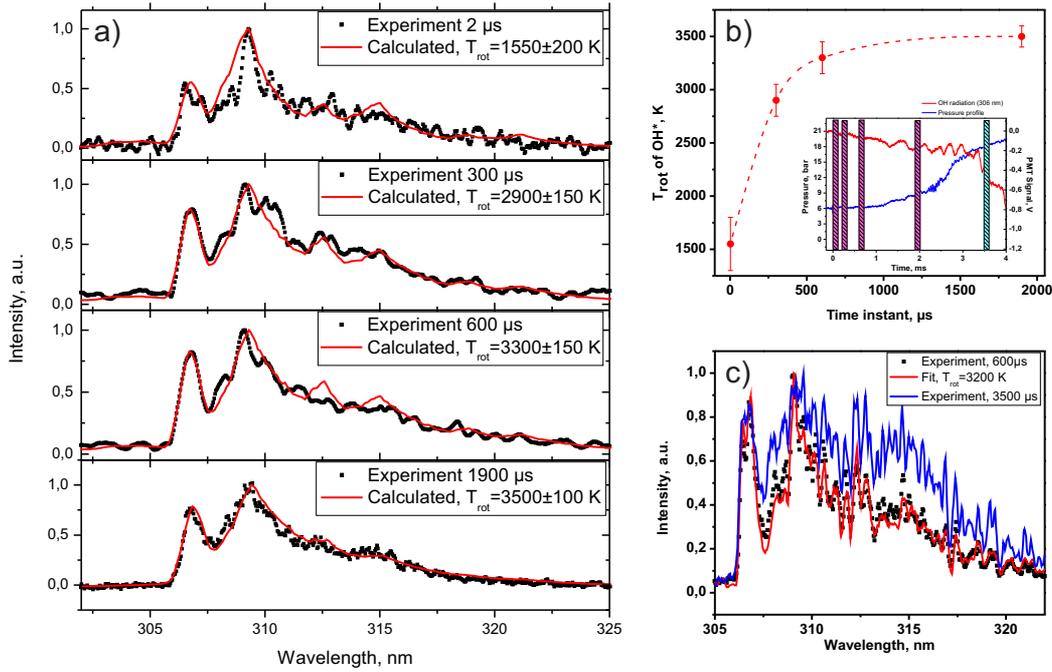
Figure 6.5: **(a) Experimental and calculated emission spectra of OH–radicals at different time moments. Camera gate 100 μs, FWHM of slit function 0.64 nm; (b) Rotational temperature as a function of time. Inserted plot shows the corresponding pressure and OH intensity profiles; (c) Experimental and calculated emission spectra at two time instances 600 and 3500 μs. Camera gate 500 μs, FWHM of slit function 0.27 nm.**

thermalization of the rotational distribution. The intensity of emission and therefore the concentration of radicals increase, the rotational temperature remains the same, and so, does not allow calculating the gas temperature.

Figure 6.5(c) shows the emission spectra of OH(A$^2\Sigma^+$) at 600 and 3500 μs time

Table 6.1: Reactions of production and quenching of excited OH radicals

No	Reaction	Rate constant	Reference
R1	H + O + M $\rightarrow$ OH* + M	$3.3 \cdot 10^{-35} exp(\frac{-3500}{T})$ cm^6/s	[176]
R2	OH* + H$_2$ $\rightarrow$ OH + H$_2$	$(4.6\pm0.2) \cdot 10^{-10}$ cm^3/s	[177]
R3	OH* + O$_2$ $\rightarrow$ OH + O$_2$	$(1.5\pm0.5) \cdot 10^{-10}$ cm^3/s	[177]
R4	OH* + N$_2$ $\rightarrow$ OH + N$_2$	$(1.0\pm0.2) \cdot 10^{-11}$ cm^3/s	[177]
R5	OH* + H$_2$O $\rightarrow$ OH + H$_2$O	$(4.4\pm0.3) \cdot 10^{-10}$ cm^3/s	[177]
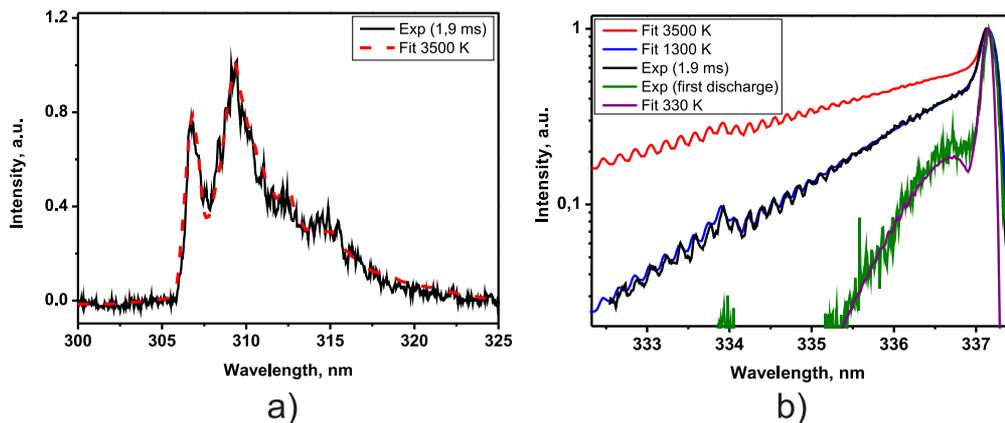
Figure 6.6: Spectra of emission of (a) OH–radical, ICCD gate is 50 μs, delay 1.9 ms after the discharge; and (b) molecular nitrogen, ICCD gate is 1 μs, delays 0 ns and 1.9 ms after the discharge. Fits are calculated with SpecAir software [104, 105].

instances. The calculated spectrum correspond to the temperature close to the saturation value. This spectrum is well superimposed on experimental one at 600 μs time moment. And it is clearly seen that the spectrum of 3500 μs is significantly different with respect to the fitted one. However, it was impossible to fit the experimental spectrum acquired at 3500 μs. It means that this spectrum is highly non–equilibrium. Indeed, at 3.5 ms a thermal conduction cooling of the gas occurs. It means, that the temperatures of the gas, the flame or rotational temperature of OH*, close to the walls of the chamber and the electrode system are lower than the temperatures in the volume. All spectra were obtained along the entire optical window size. So, the experimental spectra can be interpreted as a sum of spectra from different areas of the chamber. If these temperatures are different the resulting spectrum can not be fitted by theoretical one.

To get rotational and further, gas temperature, $N_2(C^3\Pi_u \rightarrow B^3\Pi_g)$ emission during the discharge was used. Figure 6.6(b) demonstrates the experimental and theoretical emission spectra of the N_2 emission. Two consequent discharges were initiated: first, which triggers the ignition of H_2:air mixture, and second, triggering 1.9 ms after the first one. Acquired spectra of molecular nitrogen correspond to rotational temperatures $T_{rot}^C = 330$ K in the discharge and 1300 K at the time instant 1.9 ms.

Excitation of molecular nitrogen in nanosecond discharge takes place mainly due to direct electron impact. In this case the distribution of the rotational levels of $N_2(C^3\Pi_u)$ state remains relatively similar as for ground state of N_2, and so the

recorded rotational temperature of excited nitrogen T_{rot}^C and translational temperature T are linked by the following equation: $T = T_{rot}^X = (B_e^X/B_e^C)T_{rot}^C = 1.1T_{rot}^C$. So, the temperature recorded in H$_2$:air mixture in the vicinity of the discharge (camera gate was 1 μs) is equal to $T = 363$ K, and 1.9 ms after the discharge (camera gate was 50 μs) is equal to $T = 1430$ K, what is close to adiabatic flame temperature for considered experimental conditions, about 1550 K [178].

So, the conclusion from analysis of pressure waveform, ICCD images and emission behavior is that (a) observed emission patterns correspond to initiation of combustion; (b) before the main pressure increase, a system of combustion waves develops and propagates in the discharge chamber, the temperature in the flame zone being close to adiabatic combustion temperature; (c) on the initial stage of the flame initiation ($0 - 100$ μs) the processes of OH(A$^2\Sigma^+$) population differ from the processes during the developed flame.

6.2.3 Three regimes of flame initiation

To analyze a correlation between the discharge appearance and the behavior of the ignition pattern, imaging of combustion was made for the initial period of flame development in the discharge cell for three different amplitudes of the high–voltage pulse. Figure 6.7(a) presents ICCD images of ignition at 20 kV on the high voltage electrode, the total deposited energy being equal to $W = 3$ mJ. These parameters correspond to developed streamer mode of SDBD discharge. The flame starts 300 μs after the discharge as a few ignition kernels developing at the edge of the high-voltage electrode. The kernels expand as spherical combustion waves interacting with each other, forming an irregular structure at $1 - 3$ ms. Despite the fact that discharge energy is distributed equally between the streamers, the ignition starts only from one or several kernels. The number of ignition kernels increases with voltage. This regime of ignition is unstable and extremely sensitive to applied voltage. Even with a slight voltage deviation, the number of kernels and the time of ignition in each kernel change significantly the time of initiation of combustion in entire volume.

When the voltage reaches the value of $U = +33$ kV (deposited energy is $W = 5$ mJ), the combustion kernels are distributed evenly along the edge of the high–voltage electrode, and ignition starts from a quasiuniform structure near the electrode (see figure 6.7(b)). In this case, maximal energy release is presumably concentrated near the high-voltage electrode, whatever polarity is, and synchronous structure of combustion waves propagates with a high visible velocity. Emission from excited OH appears approximately 50 μs after the discharge initiation. The repeatability of the experiments in this mode is high enough: the scattering of ignition delay time did not exceed 10%. This mode of ignition has already been men-
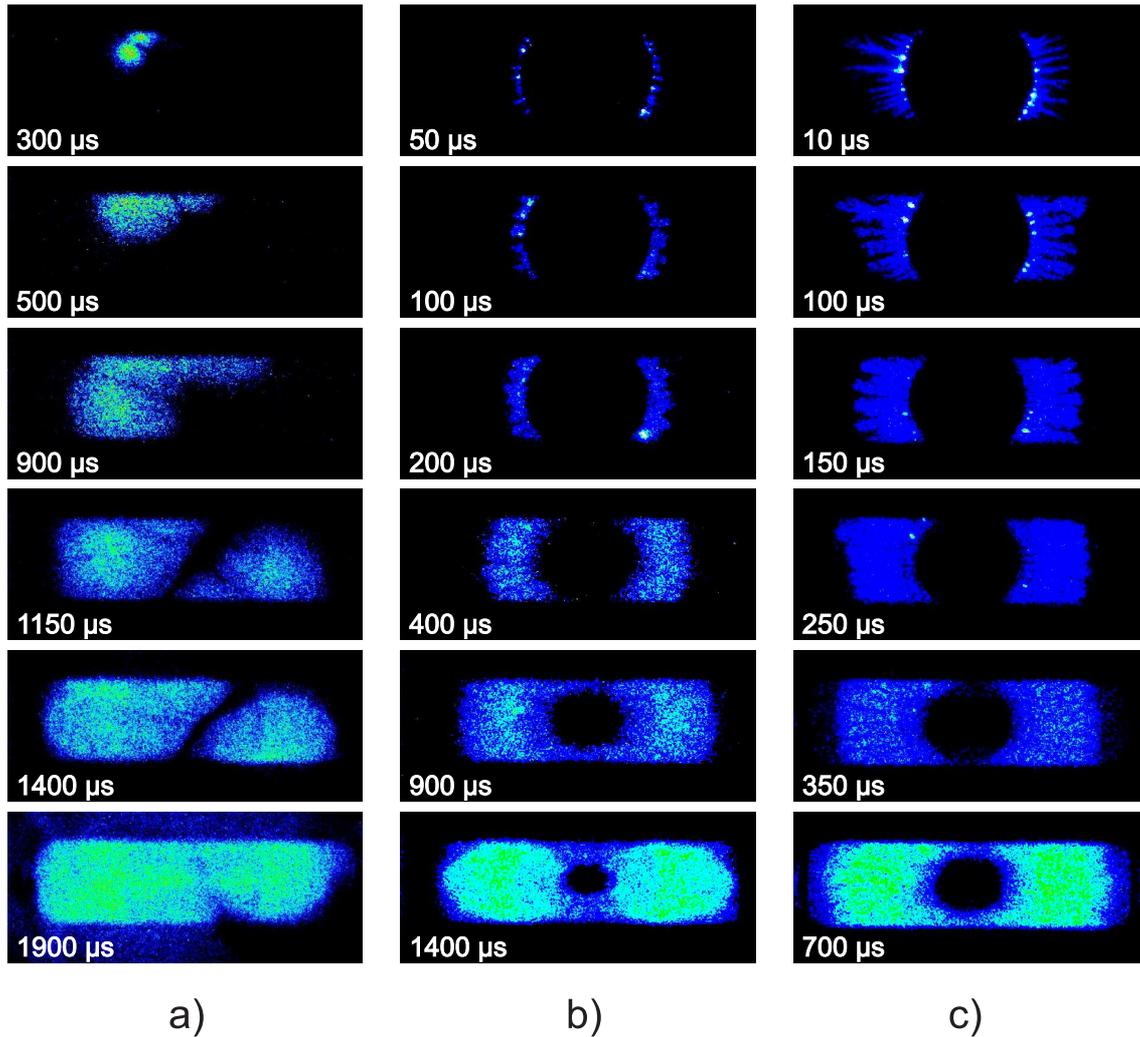
Figure 6.7: Three regimes of ignition of H$_2$:air mixture with nSDBD: (a,b) streamer discharge; (c) filamentary discharge. Voltage on the electrode is equal to (a) $U = +20$ **kV; (b)** $U = +33.2$ **kV; (c)** $U = +53$ **kV.** $P = 6$ **bar,** $T = 300$ **K,** $ER = 0.5$**. Camera gate is equal to 50** μ**s, delay between the discharge and ICCD gate is indicated in each frame.**

tioned in [5] and later in [7], where ignition of stoichiometric C$_2$H$_6$:O$_2$ and C$_2$H$_2$:air mixtures respectively was studied at atmospheric pressure.

The third mode of flame initiation is demonstrated in figure 6.7(c). This regime has not been observed before and corresponds to the ignition by filamentary discharge. The applied voltage was equal to $U = +53$ kV, and total energy deposition was $W = 21$ mJ. In this mode, similarly to streamer mode of the discharge, the initial distribution of energy is inhomogeneous along the discharge channel: a few bright spots in the near–electrode region can be easily seen in the frame corresponding to time period $t < 150$ μs. The bright spots do not expand and decay in
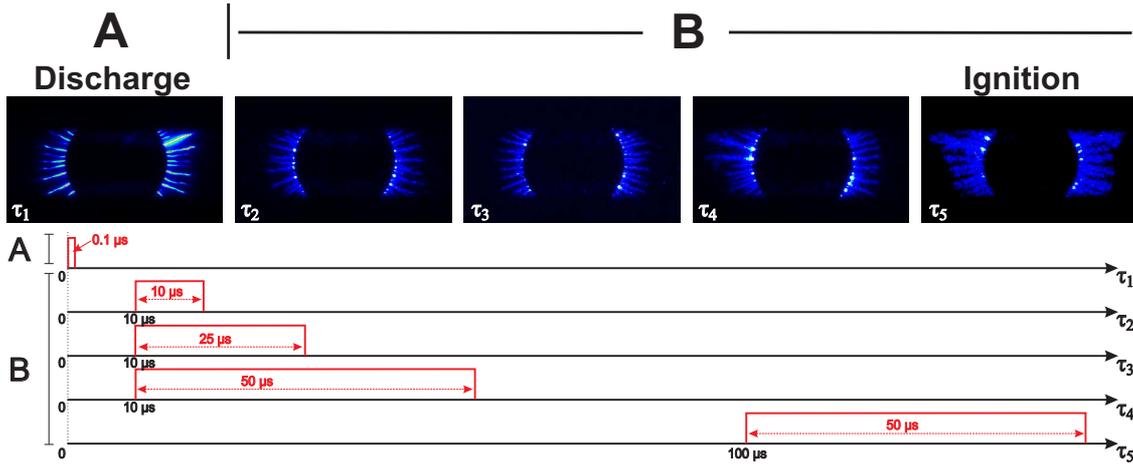
Figure 6.8: Discharge and subsequent ignition along the filamentary channels. $P = 6$ **bar,** $U = +53$ **kV. The camera gate (CG) and delay of the camera trigger (CD) are mentioned in the table.**

$150 - 250\ \mu$s (see figure 6.7(c)) not influencing the morphology of the ignition. Combustion starts along entire length of each filament. We believe that quenching of the bright spots near the electrode can be explained by heat removal to the electrode or by non–sufficient size of the ignition kernel [179]. The ignited channels expand in three directions: (i) in radial direction, that is elongation of the ignition channels; (ii) in azimuthal direction; (iii) in direction perpendicular to the electrode, in the volume of the discharge chamber.

The temperature analysis described above was done for the regime of ignition by filamentary discharge. And it was demonstrated, that during first $\sim 100\ \mu$s the rotational temperature of OH(A$^2\Sigma^+$) state is lower than the T_{rot}^{th} value. The interesting fact can be noticed during the accurate analysis of ignition with filamentary nSDBD. Figure 6.8 demonstrates the filamentary ($U = +53$ kV) discharge – "A" and the following ignition pattern – "B". Camera settings (camera gate and delay) are marked as τ_i in the bottom left corner of each ICCD image. The camera gate and the delay are represented schematically as diagrams below the images. Two conclusions can be done therein: (i) the ignition channels repeat the discharge morphology; (ii) during the first $\sim 100\ \mu$s the ignition channels do not expand. And only at $100 - 150\ \mu$s period the expansion of the ignition pattern can be observed. This time correlates with time of turbulization of heated channel produced by filaments near the surface of dielectric represented by schlieren analysis in the section 5.3.3.

The formed 2D ignition pattern propagates to the volume of combustion chamber. Figure 6.9 demonstrate the images of the flame propagation in the direction perpendicular to the electrode plane. The side–view images help to understand the spatial structure and intensity of the combustion waves for considered three regimes
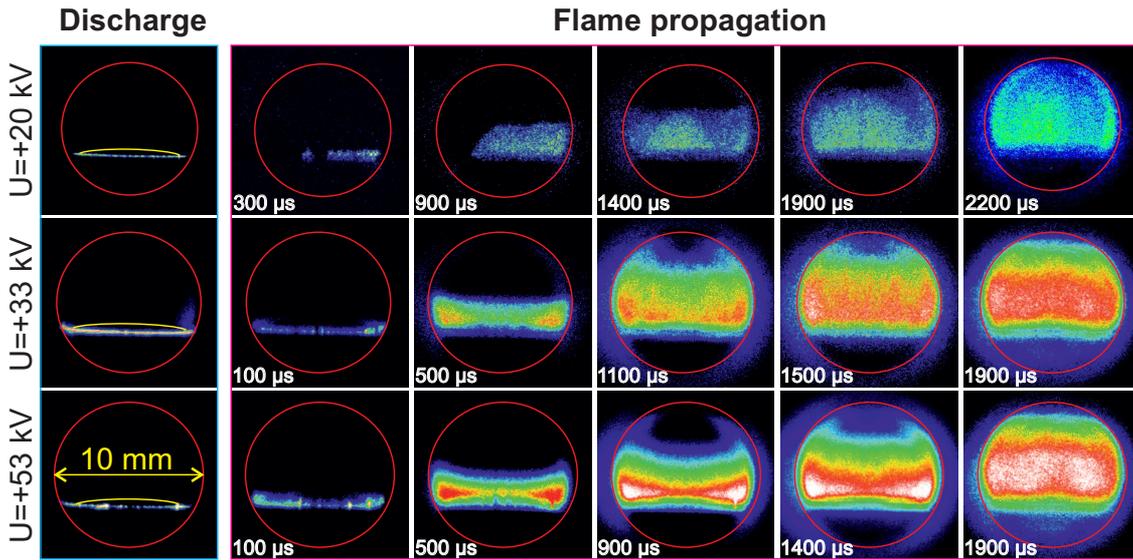
Figure 6.9: Flame propagation (side view). Ignition by three regimes.

of flame initiation. For the case of ignition with streamer discharge $U = +20$ kV, a few distinct ignition kernels are formed a few hundreds of nanoseconds after the discharge initiation. However, for the regimes of uniform ignition along the filaments ($U = +53$ kV) and along the perimeter of the HV electrode ($U = +33$ kV) the combustion waves form a quasi–flat front.

Despite the fact that the combustion waves corresponding to the ignition by filamentary $U = +53$ kV and by streamer $U = +33$ kV discharge, propagate in the volume of the chamber with relatively same velocities, the intensity of the OH emission is higher for filaments. It means that the rate of combustion and thus the efficiency, is higher for the filamentary ignition.
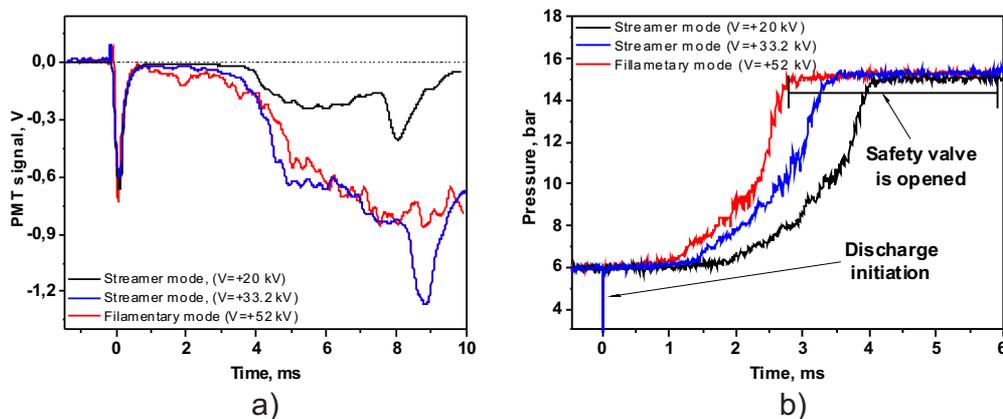
Figure 6.10: (a) OH emission profiles and (b) Pressure profiles for three regimes of flame initiation.

The OH–emission profiles are presented in figure 6.10(a). The photomultiplier is installed in front of the side window of the HPHT chamber. A narrow band interference filter of (310 ± 5) nm is mounted on the PMT. A sharp peak at the very beginning of the intensity profiles corresponds to the emission of nitrogen 2$^+$ system $(v' \rightarrow v'' = 1 - 0)$ and $(v' \rightarrow v'' = 2 - 1)$ transitions. The OH–emission of streamer regimes, both $U = +20$ kV and $U = +33$ kV, appears later than the emission of the flame initiated by filamentary discharge $U = +52$ kV.

Figure 6.10(b) demonstrates the pressure profiles for three regimes of flame initiation. It is clearly seen, that the pressure rise with the smallest delay is observed when filamentary discharge is used. The horizontal shape of profiles $(2.5 - 4$ ms) correspond to the safety valve opening.

6.3 Propagation of combustion wave

Velocities of flame propagation in different directions are summarized in figure 6.11(b-d) for two different modes: streamer discharge at $U = +33$ kV (conditions as in the figure 6.7(b)) and filamentary discharge at $U = +53$ kV (conditions as in the figure 6.7(c)). The details of the geometry are explained by figure 6.11(a). The formation of combustion pattern in the plane of the electrode is quite complex. Figures 6.11(b),(c) present velocity in radial and azimuthal direction respectively. They differ significantly for streamer and filamentary mode. When the 2D pattern of combustion is formed near the electrode, the flame front propagates from the lower end plate of the discharge chamber with velocity 10.3 m/s both for streamer and filamentary discharge modes (figure 6.11(d)). High velocity of propagation corresponds to the fact presented recently in [18] that nanosecond SDBD discharge with high specific delivered energy can produce significant hydrodynamic perturbations. The highest obtained velocity, 14 m/s in radial direction was obtained for filamentary mode of the discharge.

Measured velocities are comparable or higher than the velocity of flame propagation for the given conditions. Velocities of flame propagation in the H$_2$:air mixture (ER=0.5, that is the fraction of hydrogen in the mixture is about 17%, P=6 bar, T$_0$=300 K), can be estimated in the following way. The normal propagation velocity of the flame under the considered conditions is V_n=50 cm/s [180]. The coefficient of expansion is $\rho/\rho_0 \approx T_{max}/T_0 = 5$. Thus, the observed speed of the combustion wave, measured in the experiment, is equal to

$$V^* = V_n \cdot \rho/\rho_0 = 2.5 \text{ m/s.} \tag{6.1}$$

The measured velocity of the combustion wave in the experiments of the present
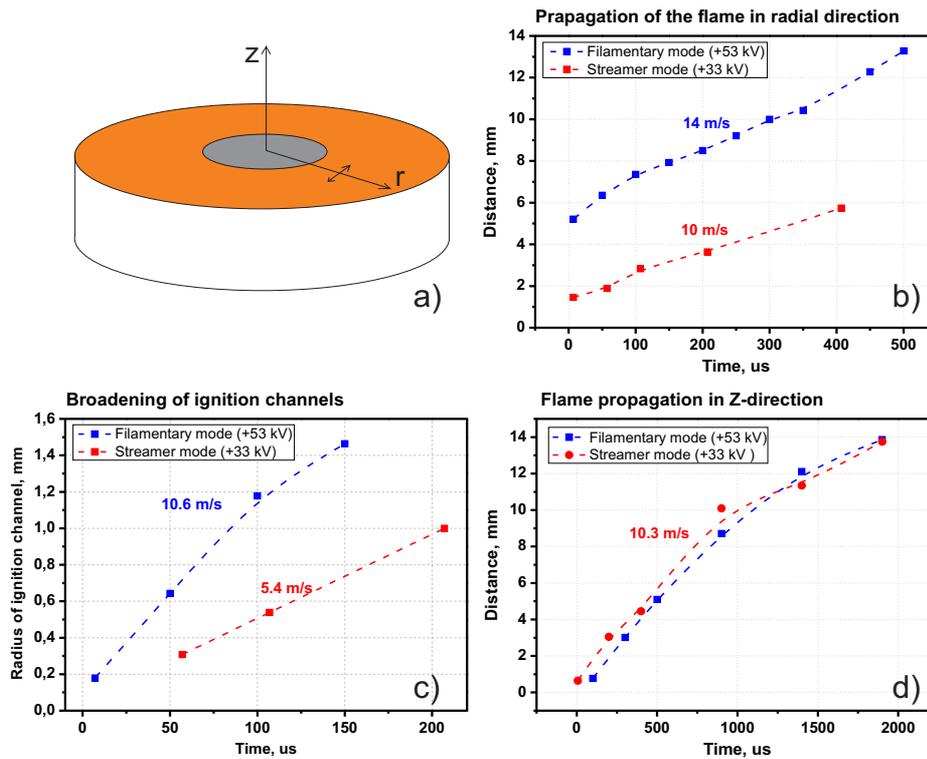
Figure 6.11: Flame velocities. (a) scheme of electrode system and the representation of direction of flame propagation; (b) propagation in radial direction; (c) expansion of ignition channels; (d) flame propagation in the volume of the chamber.

work is $10-14$ m/s (see figure 6.11), that is $4-5$ times higher than V^* value (6.1). It should be noted that high flame velocities achieved in lean mixtures (ER=0.5 in our experimental case) can be an interesting issue for industrial applications.

One of the possible reasons of increasing of combustion wave speed is the turbulization of the flow field in the vicinity of the front of the combustion wave. This may be the result of interactions of weak gas-dynamic perturbations initiated by discharge channels, with the flame front. According to [181], $4-5$ times increase of the velocity of the combustion wave is observed when the rate of turbulent fluctuations in the flame front exceeds 3 m/s.

6.4 Discharge energy needed for ignition. Measurements of MIE

Nanosecond surface dielectric barrier discharge is a 3D structure with a complex distribution of energy over the discharge volume. Nevertheless, observed symmetry

and regular structure of the discharge allow calculation of minimal ignition energy (MIE) on the basis of experimentally measured energy delivered to the discharge. Kinetic modeling is used to estimate the specific energy in discharge filaments needed for ignition and the corresponding spatial characteristics of the plasma channels.

6.4.1   Deposited energy as a function of applied voltage

At $P = 6$ bar and $ER = 0.5$ the mixture ignited at the lowest possible voltage of the generator. To study minimum ignition energy, the experiments were carried out at $P = 3$ bar, $ER = 0.6$ and $P = 5$ bar, $ER = 0.6$. Figure 6.12a presents the total energy deposited into plasma as a function of applied voltage at $P = 3$ bar, $ER = 0.6$ and voltages $U = 20 - 55$ kV on the electrode. An example of the integral ICCD image of the discharge (camera gate is equal to 100 ns, wavelength range is equal to $300 - 800$ nm) for $U = +53$ kV is shown at the left upper corner of the figure. It is clearly seen that at $P = 3$ bar, even at the highest voltage amplitude, the discharge is a streamer discharge, no filament is observed. It is interesting to compare deposited energies at $P = 3$ bar, $ER = 0.6$ to those at $P = 6$ bar,
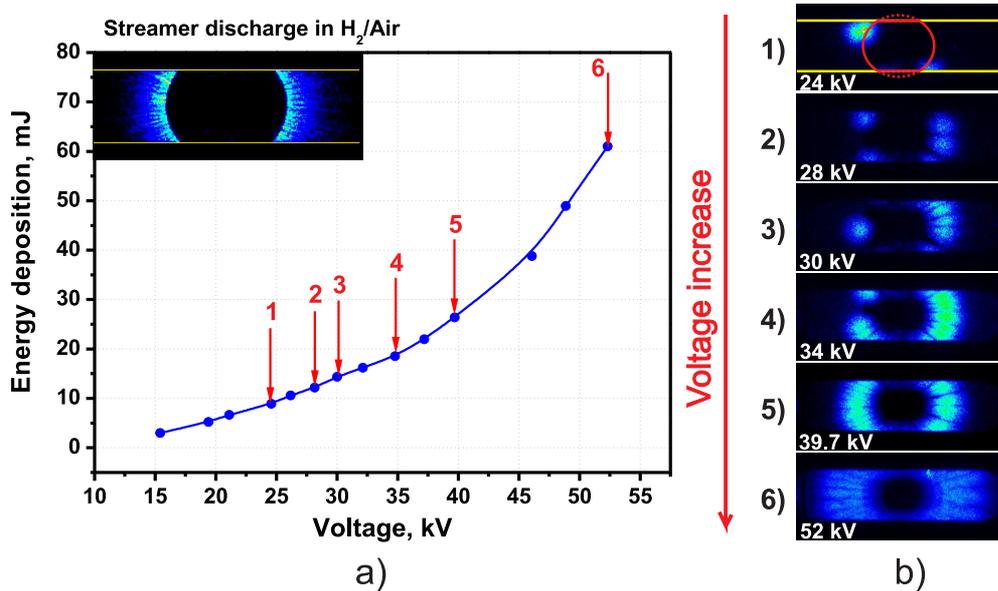
Figure 6.12: **H$_2$:air mixture, $ER = 0.6$, $P = 3$ bar, $T = 300$ K. (a) Total energy deposited in plasma as a function of voltage on the electrodes and the discharge image for $U = +53$ kV on the electrode. Red arrows at the plot show the experimental conditions where ICCD images in the afterglow were taken; (b) Integral ICCD images of emission in the afterglow for different voltages. Camera gate is 500 μs, time delay from the discharge initiation is 5 μs.**

$ER = 0.5$: the energies are higher for 3 bar, the difference increases progressively with voltage, and the ratio of delivered energies at 3 bar and 6 bar is approximately equal to 2/3/6 for 20/30/50 kV of voltage amplitude.

ICCD images of OH emission after the discharge, integrated over 500 μs, are presented in figure 6.12b. To eliminate any emission corresponding to the discharge, the images were taken with $\tau = 5$ μs delay after the discharge initiation. It is clearly seen that the structure of ignition kernels is similar to the structure obtained at higher pressure in the streamer mode of the discharge: (compare with Figure 6.7 a,b): a few kernel are observed at low voltages; with voltage increase, a regular structure appears around the high–voltage electrode. Ignition always appears at the edge of the high–voltage electrode, and the length of the propagation at given time instant is a function of high voltage amplitude. It should be noted that at $P = 3$ bar and $ER = 0.4$ the ignition was unstable, a probability to ignite the mixture at highest used amplitude was not higher than 50%.

6.4.2 Measurements of MIE

Time of initiation of combustion in entire volume, τ_{comb}, was determined as a beginning of a sharp rise of OH emission, corresponding to pressure increase in HPHT chamber (for example in figure 6.4b $\tau_{comb} = 3.3$ ms). The τ_{comb} progressively decreases with deposited energy. This fact is illustrated by figure 6.13, where the time τ_{comb} for $P = 3$ bar and $P = 5$ bar is presented. It is clearly seen from the figure that, when ignition starts in a few points around the electrode, the τ_{comb} is high. With increased energy deposition, τ_{comb} decreases drastically. This part of curve, marked as "1" in figure 6.13, corresponds to increase of number of ignition kernels around the electrode and to beginning of the interaction between separate combustion waves. Ignition of entire volume depends upon the initiation of combustion in each of kernels and by the velocity of the flame propagation. Starting from some value of deposited energy, 13 mJ for 3 bar and 5 mJ for 5 bar, ignition delay time practically does not change with deposited energy. This part, marked as "2", corresponds to a "saturated" chain of ignition kernels along all the perimeter of the high-voltage electrode. In this case, the time τ_{comb} is determined mainly by a flame propagation velocity. Ignition presented in figure 6.13 corresponds to streamer mode of nSDBD discharge.

The ICCD images of combustion pattern on the right hand side of figure 6.12 illustrate the approach used to calculate a minimal ignition energy (MIE). The voltage amplitude was decreased to the threshold U_{min} when combustion appears statistically in a regular way not more than in $1-3$ kernels and the flame propagation, followed by combustion in the whole volume, is observed. We defined that the
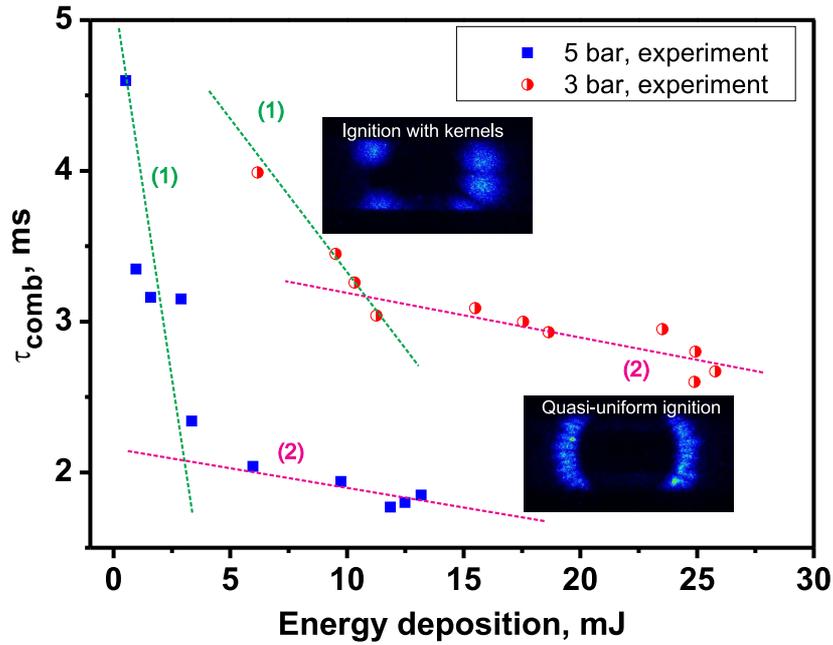
Figure 6.13: Time of initiation of combustion in entire volume as a function of delivered energy for different pressures. H$_2$:air mixture, $ER = 0.6$.

threshold is reached when combustion appeared with 90% probability. The delivered to the discharge energy corresponding to this voltage, W_{min}, was divided by a number of streamers, Z_s at these experimental conditions. Minimum ignition energy for H$_2$:air mixture at ER=0.6 was estimated as 50 μJ at $P = 3$ bar ($W_{min} = 2.8$ mJ, $Z_s \approx 120$) and 20 μJ at $P = 5$ bar ($W_{min} = 1.6$ mJ, $Z_s \approx 80$). Difference of MIE for $P = 3$ bar and 5 bar can be explained by increase of reactivity of combustible mixture at higher pressure. On the other hand, this difference would be not so significant if more realistic energy parameter, namely specific delivered energy, was compared. The MIE for H$_2$:O$_2$ mixture ignited by spark discharge at $ER = 0.6$ at atmospheric pressure is reported to be 50 μJ [178]. A few experiments on MIE measurements for plasma assisted combustion is known. In particular, MIE was measured for transient plasma of nanosecond discharge in point–to–plane geometry for propane- and n–heptane containing mixtures [75]. They reported a value of MIE equal to 17 mJ for stoichiometric mixtures of both hydrocarbons under study.

Although experimentally obtained MIE is in reasonable correlation with the data of other authors, it should be noted that, for plasma assisted ignition, MIE is more complicated parameter than for spark ignition. Indeed, in addition to ideas of critical flame radius and quenching distance, processes of relaxation of nonequilibrium energy must be considered.

6.5 Numerical calculations and analysis of specific deposited energy

The aim of numerical modeling was (i) to analyze kinetics of ignition initiated by nSDBD for conditions close to the experimental conditions of the present work; (ii) to provide, on the basis of calculations, minimum specific energy giving experimentally observed ignition delay time.

The kinetic model used to study plasma–assisted ignition of H_2:air mixtures is described in detail in [181]. The model includes "plasma" reactions, such as electron impact ionization, dissociation and excitation of mixture molecules, ion-molecular reactions, reactions between electronically excited atoms and molecules, as well as "combustion" processes describing ignition of hydrogen/air mixture.

Figure 6.14 presents the results of calculations of gas temperature, densities of atomic species and of excited $OH(A^2\Sigma^+)$ molecules in H_2:air mixture ($ER = 0.5$) in the afterglow of the discharge.The discharge is characterized by reduced electric field $E/N = 200$ Td and specific deposited energy $w = 0.2$ eV/molecile. The calculations were made using model [181], in isobaric approximation.

The decay of O and H-atoms in the near afterglow is relatively fast. The reactions (R6)-(R7) are responsible for decrease of O atoms density:

$$O(^3P) + HO_2 \rightarrow OH + O_2 \qquad \text{(R6)}$$
$$O(^3P) + OH \rightarrow H + O_2 \qquad \text{(R7)}$$
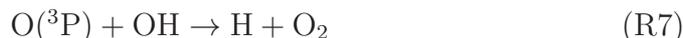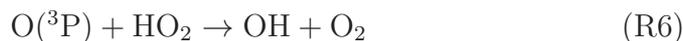
Decay of atomic hydrogen is mainly due to reactions

$$H + O_2 + M \rightarrow HO_2 + M \qquad \text{(R8)}$$
$$H + HO_2 \rightarrow OH + OH \qquad \text{(R9)}$$
$$H + HO_2 \rightarrow H_2 + O_2 \qquad \text{(R10)}$$

In the afterglow of the discharge, the production of electronically excited $OH(A^2\Sigma^+)$ molecules is due to the reaction (R1):

$$H + O + M \rightarrow OH(A^2\Sigma^+) + M,$$

so the kinetic curve of $OH(A^2\Sigma^+)$ "follows" the density of the atomic species. Increase of gas temperature in the afterglow is due to (i) recombination of atoms (R6)-(R10) and (ii) VT - relaxation of molecular nitrogen, $N_2(v)$. At $w = 0.2$ eV/mol and $E/N = 200$ Td, maximal possible vibrational temperature is $T_v(N_2) = 2120$ K. Relaxation takes place mainly in collisions with H_2 and produced H_2O molecules. Typical time of VT-relaxation under the conditions of figure 6.14 is $7 - 8$ μs.
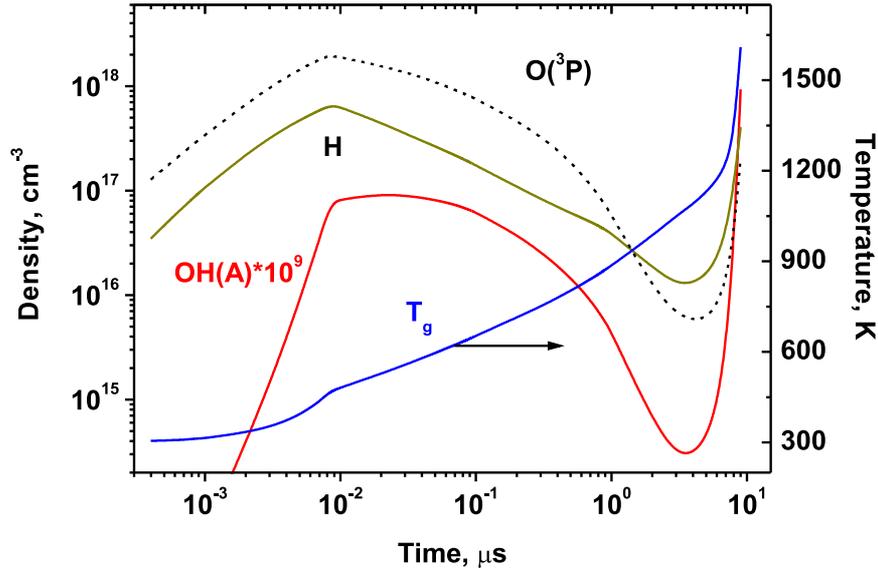
Figure 6.14: Gas temperature, densities of atomic species and of excited OH(A$^2\Sigma^+$) molecules in the afterglow of the discharge in H$_2$:air ($ER = 0.5$) at $= 6$ bar and $T_0 = 300$ K. Specific deposited energy is $w = 0.2$ eV/mol, reduced electric field is $E/N = 200$ Td. Calculations of Dr.Popov [145].

To compare the efficiency of equilibrium and non-equilibrium ignition of H$_2$:air mixtures, the numerical calculations were performed for both autoignition (given as "equilibrium" energy release corresponding to gas heating by the shock wave in the experiments [182]) and ignition by pulsed discharge. For the equilibrium case it was suggested that total deposited energy goes directly to heating of the mixture and initial energy distribution corresponds to the Boltzmann distribution. In nonequilibrium regime the energy is distributed over internal degrees of freedom depending upon E/N. To calculate energy branching, Boltzmann equation for EEDF in two-term approximation has been solved with $BOLSIG+$ code [116, 183].

To compare the simulation results with the measurement data in autoignition mode, the calculations were carried out for the experimental conditions of [182]. The experimental results of [182] represent the ignition delay measured in the shock tube for lean H$_2$:air mixture in the pressure range between 3 and 5 bar. The results of numerical simulation of ignition delay time as a function of specific energy w for H$_2$:air mixture with $ER = 0.44$, $P = 4$ bar (curve 1) and $P = 6$ bar (curve 2) are presented in figure 6.15;

$$w/N = c_p(T - T_0),\tag{6.2}$$

where N and c_p are gas density and specific heat capacity at constant pressure, T
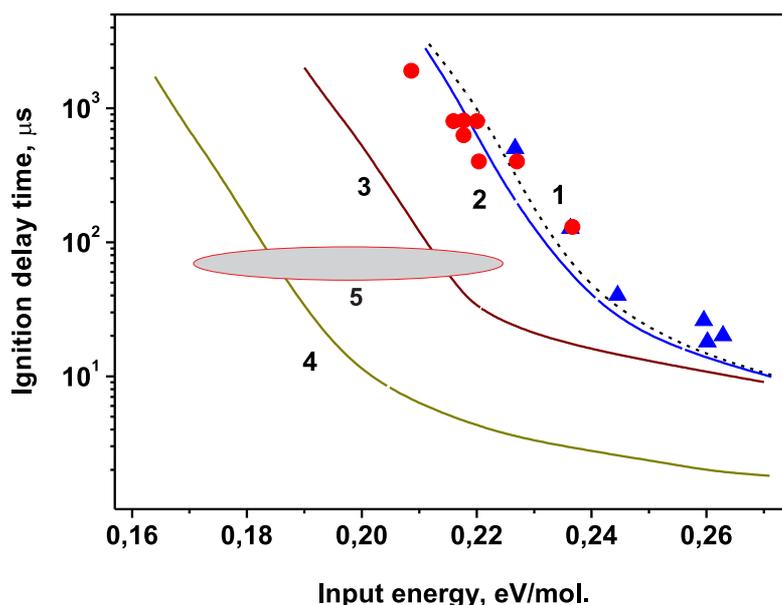
Figure 6.15: The induction time as a function of specific energy. H_2/air mixture, P=4-6 bar, T_0=300 K, ER=0.44-0.5. Results of simulation (curves 1,2) and experimental data (dots) [182] for the conditions when the total energy of the discharge instantly goes to the gas heating; ER = 0.44, P = 4 bar (curve 1), P = 6 bar (curve 2). Curves 3 and 4 correspond to the simulation with real energy distribution over the degrees of freedom at $E/N = 100$ Td (3) and $E/N = 200$ Td (4), ER=0.5, P=6 bar. The shaded area 5 is the experimental data on the induction delay time τ_{ind}=50-70 μs. Calculations of Dr.Popov [145].

is gas temperature behind the shock wave, T_0=300 K is initial temperature of the mixture. Similar calculations, but taking into account nonequilibrium distribution of the discharge energy over degrees of freedom, are also presented in the figure 6.15 for $E/N = 100$ Td (curve 3) and $E/N = 200$ Td (curve 4). In the case of nonequilibrium distribution the part of energy goes to the dissociation of mixture molecules, to vibrational excitation and to gas heating [181]).

At $E/N = 100$ Td almost half of the discharge energy is spent for the excitation of vibrational degrees of freedom of molecular nitrogen $N_2(\nu)$. The characteristic time of VT-relaxation of $N_2(\nu)$ molecules under the following conditions is about hundreds of microseconds [78]), therefore the gas temperature remains relatively low on a timescale less than a characteristic time of VT relaxation. The calculation results underline the fact that in the case of non-equilibrium plasma-assisted ignition the rate of gas heating has a significant impact on the ignition delay.

According to figure 6.15, at $E/N = 100 - 200$ Td the ignition delays τ_{ind}=50-

70 μs correspond to specific energies (0.2$\pm$0.01) eV/mol. The possibility of achieving such values of specific deposited energy can be estimated in the following way. The average maximum length of the filaments calculated from the ICCD images is equal to $< L_{max} > = 4.5$ mm. If the total energy deposition into the volume occupied by the discharge is about $W = 10$ mJ, and the number of channels (filaments) is N_{ch}=50, then the energy per unit length in the channel can be estimated as W_d=0.4 mJ/cm. It was assumed, according to the distribution of emission intensity, that the energy is distributed homogenously along the filaments.

Volume occupied by the discharge can be estimated on the basis of ICCD images. The average maximum length of a filament and the average radius were estimated from the images of the discharge in H$_2$:air; the thickness of the plasma layer was taken from the experimental data for air [46].

If the discharge channel can be presented as a half–cylinder, extended on the dielectric surface, then at $P = 6$ bar, $T = 300$ K and $W_d = 0.4$ mJ/cm to achieve the specific energy of $w = 0.2$ eV/mol, the radius of the cylinder must be around 70 μm ($S_{ch} = 8 \cdot 10^{-5}$ cm^2), which seems to be quite reasonable value. It should be noted that optical radius obtained directly from ICCD images is about 130 μm, that is approximately two times higher. Two possible reasons should be mentioned here. First, the optical radius of the discharge is always larger than the "current" radius [115] corresponding to the distribution of the electron density and so, to maximal energy release. Second, electric fields in the filaments should be low (see chapter 5). The electric fields $100 - 200$ Td are only possible in the filament head. So, if the main energy release in the filamentary mode happens in the filament head, the estimated radius corresponds to the radius of the head of the filament. The possible reason of this distinction is that generally the optical radius of the discharge channels is significantly larger than "current" radius [115] corresponding to the distribution of the electron density.

ICCD data can be used for the estimate of the discharge current assuming that the current density in cathode layer is normal. Normal density of electrical current in cathode layer at $P = 6$ bar and $T = 300$ K is equal to j$_n$=6 kA/cm^2 [113]. Taking the section of the discharge channel equal to S_{ch}=8$\cdot$10^{-5} cm^2 and the number of channels equal to N_{ch}=50, will obtain for the total current $I = 25$ A, which is in a reasonable correlation with the experimentally measured value.

6.6   Conclusion

Discharge and following initiation of combustion were studied in H$_2$:air mixture at $P = 6$ bar, $ER = 0.5$ and ambient initial temperature. It was shown that there is a strong correlation between the discharge appearance and the behavior of the ignition pattern. At lowest voltage, a few ignition kernels appear on the edge of the high-voltage electrode. When voltage increases, the number of ignition kernels increases, and at relatively high applied voltage, combustion starts from a continuous chain of ignition kernels around the high-voltage electrode. At high pressures and/or voltages the flame is initiated by the filamentary discharge. The most distinctive feature of ignition by filamentary nSDBD is that the combustion starts simultaneously from the entire length of each filament. The interaction of combustion waves initiated by separate filaments results in high visible speeds of flame propagation, about 10 m/s, which is a few times higher than the observed speed of combustion wave should be.

Minimum ignition energy, MIE, was measured at low voltages, when combustion starts from a few ignition kernels near the high-voltage electrode. The obtained values are MIE= 50 μJ for 3 bar and ER= 0.6; and MIE= 20 μJ for 5 bar and ER= 0.6. An important role of the spatial distribution of energy release for MIE definition for the case of non-equilibrium plasma discharges is underlined.

Kinetic modeling of plasma assisted ignition for the electric fields typical for nSDBD, $E/N = 100 - 200$ Td, showed that to get the experimentally observed values of the ignition delay, the specific deposited energy in the discharge must be higher than 0.2 eV/mol. This is possible only if the radius of the filament head is less than 70 μm. The conclusion for such a small radius of filaments in nSDBD is new; it seems that high-pressure non-equilibrium surface discharges suggest an opportunity of "self-concentration" of energy in distributed channels. This, in particular, can produce effective hydrodynamic perturbations, both from the discharge and from the interaction of combustion waves. Although hydrodynamic effects need additional investigation, it can be concluded that the obtained system of regular channels of a filamentary nanosecond surface dielectric barrier discharge is an efficient tool for ignition of combustible mixtures at elevated pressures.

Chapter 7

General conclusions

7.1 Contributions of the present work

The work was focused on the experimental study of the single pulsed nanosecond surface dielectric barrier discharge (nSDBD) at atmospheric and elevated gas pressures. The ability of the flame initiation by nSDBD at high pressures is studies in lean H_2:air mixtures.

Discharge investigation at atmospheric pressure

The nSDBD was investigated in atmospheric air using several experimental and numerical techniques. For the nSDBD in ambient air the discharge morphology, electric field, electron density and heat release were analyzed. The parameters of the discharge were compared for identical high–voltage pulses ($U = \pm24$ kV on the electrode, rise time 2 ns, pulse width 20 ns) for cathode–directed and anode–directed streamers. Propagation of negative polarity surface streamer is supported by high ionization in the cathode layer, whereas for positive polarity streamer the main source of active species is the head of the streamer. Optical diameter of the streamers, velocities and maximum propagation lengths significantly depend on polarity of the applied pulses and practically do not depend on geometry and size of the HV electrode.

For the first time, a complete set of parameters of plasma in the channel was obtained for $P = 1$ bar nanosecond surface streamers of negative polarity. It was found, on the basis of ICCD imaging with high temporal ($0 - 5$ ns) and spatial (7 μm/pixel) resolution, that a bulk of plasma after the discharge front is relatively

uniform and the parameters in a given point on the streamer axis can be successfully described by a set of consistent data depending upon time. On the basis of the electrical current, propagation velocity and the intensity of the second positive system of N_2 the time dependent profiles of $E/N(t), n_e(t)$ and of the density of $N_2(C^3\Pi_u)$ were obtained for negative polarity streamers.

Electron densities in the streamer head and in the "body" for positive polarity streamer were calculated from the analysis of the streamer dimensions and propagation velocity. The results of electron density measurements can be summarized in the following way: the average electron densities in the streamer channels for positive and negative polarity nSDBD are equal $(7\pm0.5)\cdot10^{14}$ cm^{-3} and $(1.5\pm0.5)\cdot10^{14}$ cm^{-3} respectively.

The mechanism of the secondary discharge wave appearing at the trailing edge of applied HV pulse is discussed. The experimental results are confirmed by 2D modelling. It is demonstrated that the secondary wave corresponds to the current in the opposite direction with respect to the main discharge. In some particular cases this "reverse" current on the trailing edge can be significant, that supplied additional energy to the discharge.

The analysis of the energy release shows that the temperature increase during the discharge does not exceed $\Delta T \simeq 50$ K for both polarities. Despite the similarity of the structure and velocities of compression wave produced by different polarities of applied pulses, the energy release at the vicinity of the HV electrode is higher in a sub–nanosecond scale, when the HV electrode is cathode.

Discharge investigation at elevated pressures

For elevated gas pressures , the discharge was studied in non–combustible mixtures: air, N_2, N_2:CH_4, N_2:H_2, Ar:O_2, Ar:H_2, Ar. The filamentation was observed for all mixtures containing molecular gases and for both polarities of the high–voltage pulses. The parameters of the transition to contracted phase, $\{P_{th}, U_{th}\}$, depend on the gas nature and polarity of the applied pulse. We conclude that the filamentation is the common and general phenomenon for the nanosecond surface discharges at high pressures. The energy deposition per channel in filaments is at least one order of magnitude higher than in the streamer mode. Produced regular structure of the discharge channels with "concentrated" specific energy is of particular interest for high–pressure combustion applications. For the first time, plasma parameters in the channel of a filamentary nSDBD have been studied.

It was found from the detailed analysis of the discharge intensity that the intensity of filaments is significantly $(40-50$ times$)$ higher than the intensity of streamers. Time and spatial–resolved emission spectra of the filament were obtained. The intense broad cw spectrum was detected in the "body" of the filament. At the same

time, no bands of 2^+ system of molecular nitrogen were observed. The emission of molecular nitrogen takes place only in the head region of the filament. The absence of 2^+ system in the channel indicates on relatively low E/N values $\sim 10 - 20$ Td, whereas the electric field in the head region of the filament remains high.

It was suggested that cw spectrum appears due to the recombination emission. For this case, the electron density should be very high, $\sim 10^{18}$ cm^{-3}. Such high values of n_e correlate with the estimations of Stark broadening of H$_\alpha$ line, but in contradiction with kinetics: observed plasma decay is $10 - 20$ ns, that is much longer than predicted theoretically ($\sim 10^{-11}$ s). In spite of observed contradictions, we can conclude that the electron density in filaments is a least $2 - 3$ orders of magnitude higher than in the streamers.

High energy release in the filament was confirmed by analysis of hydrodynamic effects. The compression wave produced by filamentary nSDBD propagates with high velocities (about $M = 1.7$) at the very beginning and decreases to approximately sound speed within a few μs. The pressure drop in the front of the compression waves is ~ 3 times higher when the wave is produced by filamentary nSDBD. More intense heat release is observed near the dielectric surface for the case of filamentary nSDBD.

Initiation of combustion with nSDBD

It was demonstrated that nSDBD in a single shot regime is able to ignite lean, $ER = 0.3 - 0.6$, H$_2$:air mixtures at elevated gas pressures, $P = 1 - 6$ bar and ambient initial temperatures. The parameters of transition to filamentary mode were found in order to compare the ignition of combustible mixtures by streamer and filamentary nSDBD.

It was found that depending on deposited energy and discharge mode three different regimes of flame initiation can be observed: (i) for low deposited energies, $4 - 8$ mJ, the flame starts from a few ignition kernels that appear in the vicinity of HV electrode. With increase of the amplitude of applied voltage the number of ignition kernels increases; (ii) when energy deposition is high enough, ~ 10 mJ, but the discharge is still in streamer mode, the quasiuniform ignition of the combustible mixtures occurs along the perimeter of HV electrode; (ii) when the discharge is filamentary and energy deposition is about $15 - 22$ mJ, the ignition starts uniformly along entire lengths of the filaments.

The velocities of flame propagation were measured. It was found that interaction between the combustion waves corresponding to each filament accelerates the resulting combustion wave velocity. The highest velocity of flame propagation was observed for the ignition along the filaments and was equal ~ 15 m/s at $P = 6$ bar and $ER = 0.5$.

From the analysis of the ignition kinetics it was found that, in order to have observed values of the ignition delay for filamentary discharge, the specific deposited energy should be as high as $0.2 - 0.4$ eV/molecule. High values of specific energy release in the filaments obtained from combustion kinetics are in a good correlation with parameters of filamentary nSDBD measured in non–combustible mixtures.

7.2 Perspectives and future work

The results presented in the present Thesis significantly improve already existing knowledge about nSDBD at atmospheric and elevated gas pressures. However, some questions such as spatial distribution of the electric field in both streamer and filamentary nSDBD, the dependence of plasma parameters on the gas composition, the ignition of heavy hydrocarbons and biofuels by nSDBD remain open. As a start of continuation of this thesis, the spatial and temporal resolution can be improved. The next stage of the experiments is related to acquisition of the spatial distribution of the intensity of second positive and first negative systems to obtain the electric field distribution across and along the streamer in atmospheric air. The "flat" configuration need to be adapted for high pressure experiments to perform the same analysis for the discharge at high pressures.

To obtain the independent information about the electron density in the filaments a set of experiments will be carried out using Shack–Hartmann wavefront sensor and double wavelength light sources. This method demonstrated [184] the measurements of $n_e = 10^{14} - 10^{15}$ cm^{-3} with a signal–to–noise ratio of ≥ 10. So, the technique is well adapted to measure $n_e > 10^{15}$ cm^{-3}.

Additional experiments on the surface charge distribution are planned. The surface charge can be measured by implantation the sensors in the dielectric. Such diagnostics, named Kelvin probe, was used to measure the surface charge density distribution in [18]. The preliminary experiments were performed and showed that rather trustful results can be obtained in our conditions.

To get more precise experimental data, Schlieren system needs to be modified and calibrated. The system can be significantly improved by using high power spatially and temporally stable light source and spherical mirrors instead of the lenses used in the thesis. The propagation velocities of the compression waves should be analyzed with higher spatial and temporal resolution to clarify the speed values at the beginning stages. The improved Schlieren system will be also used for the detailed analysis of the interaction of a few combustion waves that should be a key point for the improvement of combustion processes.

The discharge behavior was analysed for different gas pressures, whereas the

temperature was unchanged ~ 300 K. During the present work, high–pressure high–temperature (HPHT) chamber was developed. However, no results at elevated gas temperatures are presented herein. As far as the temperature distribution in the chamber will be studied, the experiments of both discharge behavior and flame initiation at elevated gas temperatures will be performed.

Finally, the ignition of hydrocarbons and especially heavy hydrocarbons that are the major part of motor fuel and raw materials in industrial organic synthesis are of particular interest. It was demonstrated [93, 103] that low temperature plasma can be an efficient tool for triggering a low temperature combustion chemistry. It was shown [93, 95] that NTC region can be significantly modified and even completely suppressed by the action of non–equilibrium plasma. Study of temporal and spatial dynamics of plasma–assisted ignition of heavy hydrocarbons at high pressures is a very important question. New advanced techniques, as laser collision–induced fluorescence (LCIF) [185] and femtosecond LIF/TALIF [186] can be promising for 2D mapping of electron density and quenching–free measurements of chemical intermediates respectively. Discharge chemistry, combustion chemistry and hydrodynamics should be linked together to get an answer about plasma efficiency and optimisation for these particular conditions.

Appendix

List of Publications

Publications in reviewed journals

1. Optical emission spectrum of high pressure filamentary nanosecond surface dielectric barrier discharge. S.A. Shcherbanev, A. Yu. Khomenko, S.A. Stepanyan, N.A. Popov, S.M. Starikovskaia. Plasma Sources Science and Technology Letters. 26 (2017) 02LT01 (7pp).

2. Ignition of high pressure lean H_2:air mixture along the multiple channels of nanosecond surface discharge. S.A. Shcherbanev, N.A. Popov, S.M. Starikovskaia Combustion & Flame Journal 176 (2017) 272–284.

3. Emission Spectroscopy of Partial Discharges in Air-filled Voids in Unfilled Epoxy S A Shcherbanev, I U Nadinov, P Auvray; S M Starikovskaia; S Pancheshnyi; L G Herrmann; *IEEE Transactions on Dielectrics and Electrical Insulation 1219-1227 2016.*

4. A comparative experimental kinetic study of spontaneous and plasma-assisted cool flames in a rapid compression machine G. Vanhove , M. A. Boumehdi, S.A. Shcherbanev, Y. Fenard, P. Desgroux, S. M. Starikovskaia *Proc.Comb. Instit.1540-7489 2016.*

5. Dielectric barrier discharge for multipoint plasma–assisted ignition at high pressures. S.A. Shcherbanev, S.A. Stepanyan, N.A. Popov and S.M. Starikovskaia, Phyl. Trans. A 2015 DOI: 10.1098/rsta.2014.0342.

6. 5) Evolution of nanosecond surface dielectric barrier discharge for negative polarity of voltage pulse. V R Soloviev, V M Krivtsov, S A Shcherbanev, S M Starikovskaia J. Phys. D: Appl. Phys.26 (2017) 014001 (12pp).

Conference proceedings

1. Ignition and combustion sustained by low temperature plasmas. S. Shcherbanev and S. Starikovskaia. *3rd International Conference on Ignition Systems; Berlin 2016*

2. Plasma assisted ignition with nanosecond surface dielectric barrier discharge.

Two modes of nanosecond surface discharge. S.Shcherbanev, N.Popov, S.Starikovskaia. *Gaseous Electronics Conference 2016, Bochum Germany*

3. High-voltage nanosecond surface dielectric barrier discharges at high pressures: physics and applications. S.A.Shcherbanev, S.A.Stepanyan, N.A.Popov, S.M. Starikovskaia, *Moscow WSMPA Conference 2016.*

4. Plasma assisted ignition of hydrogen/air mixtures at high pressures with nanosecond SDBD discharge. S.A.Shcherbanev, N.A.Popov, S.M. Starikovskaia *54rd AIAA Aerospace Science Meeting and Exhibit paper AIAA-2016*

5. Nanosecond surface discharges for plasma assisted ignition at elevated gas densities. Development and energy distribution of nanosecond surface dielectric barrier discharge. S.A. Shcherbanev, S.M. Starikovskaia *Fundamentals of Aerodynamic Flow and Combustion Control by Plasmas ATW 2015 Les Houches.*

6. Energy balance in surface nanosecond dielectric barrier discharge. Plasma-assisted ignition of heavy hydrocarbons at high pressures. S. A. Shcherbanev, S. A. Stepanyan, M. A. Boumehdi, G. Vanhove, P. Desgroux, S. M. Starikovskaia *53rd AIAA Aerospace Science Meeting and Exhibit (Orlando, FL, 5-10 January 2015) paper AIAA-2015-0668.*

7. High–pressure nanosecond discharges for plasma–assisted combustion S.A. Shcherbanev, N.Lepikhin, A.V.Klochko, S.A.Stepanyan, N.A.Popov, S.M.Starikovskaia *53rd AIAA Aerospace Science Meeting and Exhibit (Orlando, FL, 5-10 January 2015) paper AIAA-2015-0412.*

8. Two modes of optical emission in partial discharges, S A Shcherbanev, I U Nadinov, P Auvray; S M Starikovskaia; S Pancheshnyi; L G Herrmann; *Belgium, Antwerp, 5-10 July. International Symposium on Plasma Chemistry 2015*

9. Development and energy distribution of nanosecond surface dielectric barrier discharge. Initiation of combustion. S. A. Shcherbanev, S. M. Starikovskaia, Belgium, Antwerp, 5-10 July. *International Symposium on Plasma Chemistry 2015*

10. Development of the nanosecond surface dielectric barrier discharge in air for different electrode system configurations S. A. Shcherbanev, S. M. Starikovskaia, *Greifswald, Germany, ESCAMPIG 2014* ID- 629.

11. Plasma–Assisted Cool Flames in a Rapid Compression Machine, M.A. Boumehdi, S. Shcherbanev, S, Stepanyan, P. Desgroux, S.M. Starikovskaia, G. Vanhove, *Europeen combustion meeting* 2015

Résumé

Plasmas non-équilibre est l'un des outils les plus attrayants et prometteurs pour de nombreuses applications assistés par plasma. La production d'espèces actives (espèces excitées, des radicaux, des photons de haute énergie couvrant UV et IR gamme spectrale) est importante pour le contrôle de la pollution de gaz, traitement de surface, les actionneurs de plasma pour l'application de l'aérodynamique, des applications biomédicales et plus récemment le domaine de la médecine de plasma. Pour les densités de gaz atmosphérique et élevée le courant dominant des applications des plasmas non-thermiques est l'inflammation des mélanges combustibles ou Ignition assistée par plasma (IAP).

Décharges de surface à barrière diélectriques (DSBD), largement utilisé pour le contrôle de l'écoulement aérodynamique, ont été récemment suggéré comme initiateurs distribués de la combustion dans les différents systèmes. Une possibilité d'utiliser les DSBD comme les allumeurs à pression aussi élevée que dizaines de bars a été démontrée au cours des 4-5 dernières années. Au moment du début de la thèse, l'ensemble des données expérimentales sur la décharge et d'inflammation des combustibles avec DSBD était assez pauvre et insuffisant pour une analyse détaillée. Par conséquent, l'étude expérimentale de la DSBD à des densités de gaz atmosphériques et élevées et l'étude de l'initiation de flamme par DSBDs nanosecondes ont fait l'objet de la thèse présentée.

Les résultats de la thèse sont présentés en trois parties. Dans la première partie le nDSBD dans un régime single shot regime (de prise de vue unique ???) à l'air atmosphérique est étudiée. L'analyse du dépôt d'énergie, le courant de décharge, la distribution d'intensité et de libération d'énergie est réalisée en conséquence. Les impulsions de polarité positive et négative sont utilisées pour produire la décharge de surface. La physique des streamers de polarité positive et négative est discutée. Pour les deux polarités de la haute tension la densité d'électrons et le champ électrique réduite sont estimés et comparés avec des calculs et/ou des résultats de la modélisation 2D.

La deuxième partie est consacrée à l'étude des nDSBD à des pressions élevées, jusqu'à 12 bar, dans différents mélanges de gaz (N_2, air, N_2:CH_4, N_2:H_2, Ar:O_2, etc.). Deux formes morphologiquement différents de la nDSBD sont considérées: une DBD streamer «classique» à des pressions et des tensions relativement basses, et une DBD filamentaire à des pressions et/ou des tensions élevées. La spectroscopie d'émission est utilisée pour obtenir des données quantitatives sur la décharge à haute pression (de 1 à 12 bar). Les raisons possibles de la filamentation de décharge est décrite.

Finally, the third part describes the experiments of plasma-assisted ignition with nanosecond SDBD at elevated pressures. Enfin, la troisième partie décrit les expériences d'ignition assistée par plasma avec nDSBD à des pressions élevées. La morphologie de décharge dans les mélanges combustible pauvres (H2:air) et après l'allumage sont étudiés. La comparaison de l'inflammation par décharge filamentaire et streamer à la pression 1-6 bar est effectué. Modélisation cinétique d'allumage assistée par plasma pour les champs électriques typiques pour nDSBD (E/N=100 Td) est utilisé pour l'analyse des données expérimentales. Étude complexe des décharges à la pression atmosphérique, la décharge à haute pression et l'allumage permet description détaillée de l'allumage à haute pression distribué dans l'espace par plasma non - équilibre.

Décharge à la pression atmosphérique

Le nSDBD a été étudié dans l'air atmosphérique en utilisant plusieurs techniques expérimentales et numériques. Pour la nSDBD dans l'air ambiant, on a analysé la morphologie de la décharge, le champ électrique, la densité électronique et le dégagement de chaleur. Les paramètres de la décharge ont été comparés pour des impulsions à haute tension identiques (U = ± 24 kV sur l'électrode, temps de montée 2 ns, largeur d'impulsion 20 ns) pour des streamers dirigés par cathode et dirigés par anode. La propagation du streamer surfacique à polarité négative est supportée par une forte ionisation dans la région de cathode, alors que pour le streamer de polarité positive, la source principale d'espèce active est la tête du streamer. Le diamètre optique des streamers, les vitesses et les longueurs maximales de propagation dépendent sensiblement de la polarité des impulsions appliquées et ne dépendent pratiquement pas de la géométrie et de la taille de l'électrode d'haute tension.

Pour la première fois, on a obtenu un ensemble complet de paramètres de plasma dans le canal des streamers surfacique de polarité négative à P = 1 bar. On a découvert, sur la base de l'imagerie ICCD à haute résolution temporelle (0-5 ns) et spatiale (7 μm/pixel), que le volume de plasma après le front de décharge est relativement uniforme et les paramètres en un point donné sur le streamer peut être décrit avec succès par un ensemble de données cohérentes en fonction du temps. A partir du courant électrique, de la vitesse de propagation et de l'intensité du système second positif de N_2, on obtient les profils dépendant du temps de E/N(t), n_e(t) et de densité de $N_2(C^3\Pi_u)$ pour le streamer négative.

On a calculé les densités d'électrons dans la tête et dans le "corps" d'un streamer positive à partir de l'analyse des dimensions du streamer et de la vitesse de propagation. Les résultats des mesures de la densité électronique peuvent être résumés de la manière suivante: les densités électroniques moyennes dans les canaux du streamer pour la polarité positive et négative sont égales $(7\pm0.5)\cdot10^{14}\,cm^{-3}$ et $(1.5\pm0.5)\cdot10^{14}\,cm^{-3}$ respectivement.

Le mécanisme de l'onde secondaire de la décharge apparaissant au bord de fuite de l'impulsion HV appliquée est discuté. Les résultats expérimentaux sont confirmés par la modélisation 2D. Il est démontré que l'onde secondaire correspond au courant dans la direction opposée par rapport à la décharge principale. Dans certains cas particuliers, ce courant "inverse" sur le bord de fuite peut être important, ce qui fournit de l'énergie supplémentaire à la décharge.

L'analyse de la libération d'énergie montre que l'augmentation de la température pendant la décharge n'excède pas $\Delta T \simeq 50$ K pour les deux polarités. Malgré la similarité de la structure et des vitesses de l'onde de compression produite par différentes polarités d'impulsions appliquées, la libération d'énergie au voisinage de l'électrode HT est plus élevée dans une échelle de sous-nanoseconde, lorsque l'électrode HT est une cathode.

Décharge à haute pression

Pour des pressions de gaz élevées, la décharge a été étudiée dans des mélanges non combustibles: air, N_2, N_2:CH_4, N_2:H_2, Ar:O_2, Ar:H_2, Ar. La filamentation a été observée pour tous les mélanges contenant des gaz moléculaires et pour les deux polarités des impulsions à haute tension. Les paramètres de la transition vers phase contractée $\{P_{th}, U_{th}\}$, dépendent de la nature du gaz et de la polarité de l'impulsion appliquée. Nous concluons que la filamentation est le phénomène commun et général des décharges surfaciques nanosecondes à haute pression. Le dépôt d'énergie par canal dans les filaments est au moins un ordre de grandeur plus élevé que dans le mode streamer. La structure régulière des canaux de décharge avec une énergie spécifique "concentrée" est particulièrement intéressante pour les applications de combustion à haute pression. Pour la première fois, des paramètres plasmatiques dans le canal d'un nSDBD filamenteux ont été étudiés.

On a trouvé à partir de l'analyse détaillée de l'intensité de décharge que l'intensité des filaments est significativement (40-50 fois) supérieure à l'intensité des streamers. On a obtenu des spectres d'émission du filament. On a détecté le spectre large et intense dans le "corps" du filament. En même temps, on n'a observé aucune bande de 2+ système de diazote. L'émission d'azote moléculaire n'a lieu que dans la zone de tête du filament. L'absence de système 2+ dans le canal indique des valeurs E/N relativement faibles ~10-20 Td alors que le champ électrique dans la région de tête du filament reste élevé.

Il a été suggéré que le spectre cw apparaît en raison de l'émission de recombinaison. Pour ce cas, la densité électronique devrait être très élevée, ~10^{18} cm^{-3}. Ces valeurs élevées sont en corrélation avec les estimations de Stark élargissement de ligne de H, mais ne sont pas en contradiction avec la cinétique: la décroissance plasmatique observée est 10-20 ns, ce qui est beaucoup plus long que prévu théoriquement (~10-11 s). Malgré les contradictions observées, on peut conclure que la densité électronique dans les filaments est au moins 2-3 ordres de grandeur plus élevée que dans les streamers.

La libération d'énergie élevée dans le filament a été confirmée par l'analyse des effets hydrodynamiques. L'onde de compression produite par le nSDBD filamentaire se propage avec des vitesses élevées (environ M = 1,7) au tout début et diminue à environ la vitesse du son en quelques μs. La chute de pression à l'avant des ondes de compression est ~3 fois plus élevée lorsque l'onde est produite par nSDBD filamentaire. Une libération de chaleur plus intense est observée près de la surface diélectrique pour le cas du nSDBD filamentaire.

Démarrage de la combustion avec nSDBD

Il a été montré que la nSDBD dans le régime mono-pulse est capable d'allumer des mélanges pauvres, ER=0.3-0.6, H$_2$:air à des pressions de gaz élevées, P=1-6 bars et températures ambiantes initiales. Les paramètres de transition vers le mode filamentaire ont été trouvés afin de comparer l'inflammation des mélanges combustibles par les modes streamer et filamentaire.

On a constaté que, selon l'énergie déposée et le mode de décharge, on peut observer trois régimes différents de déclanchement de la flamme: (i) pour des énergies faiblement, 4-8 mJ, la flamme commence à partir de quelques noyaux apparaissant à proximité de l'électrode HT. Avec l'augmentation de l'amplitude de la tension appliquée, le nombre de noyaux d'allumage augmente; (ii) lorsque le dépôt d'énergie est suffisamment élevé, ~10 mJ, mais la décharge est toujours en mode streamer, l'allumage quasi-uniforme se produit le long du périmètre de l'électrode HT; (iii) lorsque la décharge est filamenteuse et que le dépôt d'énergie est d'environ 15 à 22 mJ, l'allumage commence uniformément sur toute la longueur des filaments.

Les vitesses de propagation des flammes ont été mesurées. On a constaté que l'interaction entre les ondes de combustion correspondant à chaque filament accélère la vitesse d'onde de combustion résultante. La vitesse la plus élevée de propagation de la flamme a été observée pour l'allumage le long des filaments et était égale ~15 m/s à P = 6 bar et ER = 0.5.

A partir de l'analyse de la cinétique d'allumage, on a constaté que, pour avoir des valeurs observées du délai d'inflammation pour la décharge filamentaire, l'énergie déposée spécifique devrait être aussi élevée que 0,2-0,4 eV/molécule. Des valeurs élevées de libération d'énergie spécifique dans les filaments obtenus à partir de la cinétique de combustion sont en bonne corrélation avec les paramètres de nSDBD filamentaire mesurés dans des mélanges non combustibles.

List of Figures

Bibliography

[1] Moreau E 2007 Airflow control by non-thermal plasma actuators *Journal of Physics D: Applied Physics* **40** 605

[2] Corke T C, Post M L and Orlov D M 2009 Single dielectric barrier discharge plasma enhanced aerodynamics: physics, modeling and applications *Experiments in Fluids* **46** 1–26

[3] Thomas F O, Corke T C, Iqbal M, Kozlov A and Schatzman D 2009 Optimization of Dielectric Barrier Discharge Plasma Actuators for Active Aerodynamic Flow Control *AIAA Journal* **47** 2169–2178

[4] Benard N and Moreau E 2014 Electrical and mechanical characteristics of surface AC dielectric barrier discharge plasma actuators applied to airflow control *Experiments in Fluids* **55** 1846

[5] Kosarev I N, Khorunzhenko V I, Mintoussov E I, Sagulenko P N, Popov N A and Starikovskaia S M 2012 A nanosecond surface dielectric barrier discharge at elevated pressures: time-resolved electric field and efficiency of initiation of combustion *Plasma Sources Science and Technology* **21** 045012

[6] Boumehdi M A, Stepanyan S A, Desgroux P, Vanhove G and Starikovskaia S M 2015 Ignition of methane- and n-butane-containing mixtures at high pressures by pulsed nanosecond discharge *Combustion and Flame* **162** 1336 – 1349

[7] Anokhin E M, Kuzmenko D N, Kindysheva S V, Soloviev V R and Aleksandrov N L 2015 Ignition of hydrocarbon:air mixtures by a nanosecond surface dielectric barrier discharge *Plasma Sources Science and Technology* **24** 045014

[8] Shcherbanev S A, Stepanyan S A, Popov N A and Starikovskaia S M 2015 Dielectric barrier discharge for multi-point plasma-assisted ignition at high pressures *Philosophical Transactions of the Royal Society of London A: Mathematical, Physical and Engineering Sciences* **373**

[9] Vincent-Randonnier A, Larigaldie S, Magre P and Sabel'nikov V 2007 Plasma assisted combustion: effect of a coaxial DBD on a methane diffusion flame *Plasma Sources Science and Technology* **16** 149

[10] Starikovskii A Y, Nikipelov A A, Nudnova M M and Roupassov D V 2009 SDBD plasma actuator with nanosecond pulse-periodic discharge *Plasma Sources Science and Technology* **18** 034015

[11] Benard N, Zouzou N, Claverie A, Sotton J and Moreau E 2012 Optical visualization and electrical characterization of fast-rising pulsed dielectric barrier discharge for airflow control applications *Journal of Applied Physics* **111** 033303

[12] Takashima K, Yin Z and Adamovich I V 2013 Measurements and kinetic modeling of energy coupling in volume and surface nanosecond pulse discharges *Plasma Sources Science and Technology* **22** 015013

[13] Nudnova M M, Aleksandrov N L and Starikovskiy A Y 2010 Influence of polarity on the properties of surface nanosecond barrier discharge in atmospheric air *Plasma Physics Reports* **36** 94–103

[14] Soloviev V R, Konchakov A M, Krivtsov V M and Aleksandrov N L 2008 Numerical simulation of a surface barrier discharge in air *Plasma Physics Reports* **34** 594–608

[15] Soloviev V R and Krivtsov V M 2009 Surface barrier discharge modelling for aerodynamic applications *Journal of Physics D: Applied Physics* **42** 125208

[16] Gibalov V I and Pietsch G J 2000 The development of dielectric barrier discharges in gas gaps and on surfaces *Journal of Physics D: Applied Physics* **33** 2618

[17] Gibalov V I and Pietsch G J 2012 Dynamics of dielectric barrier discharges in different arrangements *Plasma Sources Science and Technology* **21** 024010

[18] Leonov S B, Petrishchev V and Adamovich I V 2014 Dynamics of energy coupling and thermalization in barrier discharges over dielectric and weakly conducting surfaces on μs to ms time scales *Journal of Physics D: Applied Physics* **47** 465201

[19] Zhu Y, Takada T, Sakai K and Tu D 1996 The dynamic measurement of surface charge distribution deposited from partial discharge in air by Pockels effect technique *Journal of Physics D: Applied Physics* **29** 2892

[20] Stollenwerk L 2009 Interaction of current filaments in dielectric barrier discharges with relation to surface charge distributions *New Journal of Physics* **11** 103034

[21] Stollenwerk L, Laven J G and Purwins H G 2007 Spatially Resolved Surface-Charge Measurement in a Planar Dielectric-Barrier Discharge System *Phys. Rev. Lett.* **98**(25) 255001

[22] Hoder T, Brandenburg R, Basner R, Weltmann K D, Kozlov K V and Wagner H E 2010 A comparative study of three different types of barrier discharges in air at atmospheric pressure by cross-correlation spectroscopy *Journal of Physics D: Applied Physics* **43** 124009

[23] Sokolova M B, Kozlov K V, Krivov S A, Samoylovich V G and Tatarenko P A 2008 Study of surface discharge emission in the dry air. *JETP Letters* **35**

[24] Paris P, Aints M, Laan M and Valk F 2004 Measurement of intensity ratio of nitrogen bands as a function of field strength *Journal of Physics D: Applied Physics* **37** 1179

[25] Paris P, Aints M, Valk F, Plank T, Haljaste A, Kozlov K V and Wagner H E 2005 Intensity ratio of spectral bands of nitrogen as a measure of electric field strength in plasmas *Journal of Physics D: Applied Physics* **38** 3894

[26] Stepanyan S A, Soloviev V R and Starikovskaia S M 2014 An electric field in nanosecond surface dielectric barrier discharge at different polarities of the high voltage pulse: spectroscopy measurements and numerical modeling *Journal of Physics D: Applied Physics* **47** 485201

[27] Soloviev V R and Krivtsov V M 2014 Mechanism of streamer stopping in a surface dielectric barrier discharge *Plasma Physics Reports* **40** 65–77

[28] Likhanskii A V, Shneider M N, Macheret S O and Miles R B 2007 Modeling of dielectric barrier discharge plasma actuators driven by repetitive nanosecond pulses *Physics of Plasmas* **14** 073501

[29] Zhu Y, Wu Y, Cui W, Li Y and Jia M 2013 Modelling of plasma aerodynamic actuation driven by nanosecond SDBD discharge *Journal of Physics D: Applied Physics* **46** 355205

[30] Bonaventura Z, Bourdon A, Celestin S and Pasko V P 2011 Electric field determination in streamer discharges in air at atmospheric pressure *Plasma Sources Science and Technology* **20** 035012

[31] Boeuf J P, Lagmich Y, Unfer T, Callegari T and Pitchford L C 2007 Electro-hydrodynamic force in dielectric barrier discharge plasma actuators *Journal of Physics D: Applied Physics* **40** 652

[32] Lagmich Y, Callegari T, Pitchford L C and Boeuf J P 2008 Model description of surface dielectric barrier discharges for flow control *Journal of Physics D: Applied Physics* **41** 095205

[33] Boeuf J P, Lagmich Y and Pitchford L C 2009 Contribution of positive and negative ions to the electrohydrodynamic force in a dielectric barrier discharge plasma actuator operating in air *Journal of Applied Physics* **106** 023115

[34] Likhanskii A V, Shneider M N, Macheret S O and Miles R B 2008 Modeling of dielectric barrier discharge plasma actuator in air *Journal of Applied Physics* **103** 053305

[35] Likhanskii A, Semak V, Opaits D, Shneider M, Miles R and Macheret S 2009 The role of the photoionization in the numerical modeling of the DBD plasma actuator *47th AIAA Aerospace Sciences Meeting including The New Horizons Forum and Aerospace Exposition* Aerospace Sciences Meetings (American Institute of Aeronautics and Astronautics) URL 2009-841

[36] Forte M, Jolibois J, Pons J, Moreau E, Touchard G and Cazalens M 2007 Optimization of a dielectric barrier discharge actuator by stationary and non-stationary measurements of the induced flow velocity: application to airflow control *Experiments in Fluids* **43** 917–928

[37] Soloviev V, Krivtsov V, Konchakov A and Malmuth N 2008 Surface Barrier Discharge Simulation in Air for Constant Applied Voltage *46th AIAA Aerospace Sciences Meeting and Exhibit* Aerospace Sciences Meetings (American Institute of Aeronautics and Astronautics) URL 2008-1378

[38] Kim W, Do H, Mungal M G and Cappelli M A 2007 On the role of oxygen in dielectric barrier discharge actuation of aerodynamic flows *Applied Physics Letters* **91** 181501

[39] Leonov S, Opaits D, Miles R and Soloviev V 2010 Time-resolved measurements of plasma-induced momentum in air and nitrogen under dielectric barrier discharge actuation *Physics of Plasmas* **17** 113505

[40] Soloviev V R 2012 Analytical estimation of the thrust generated by a surface dielectric barrier discharge *Journal of Physics D: Applied Physics* **45** 025205

[41] Babaeva N Y, Tereshonok D V and Naidis G V 2016 Fluid and hybrid modeling of nanosecond surface discharges: effect of polarity and secondary electrons emission *Plasma Sources Science and Technology* **25** 044008

[42] Starikovskaia S, Allegraud K, Guaitella O, Kosarev I, Mintusov E, Pendleton S J, Popov N, Sagulenko P and Rousseau A 2010 Surface Discharges: Possible Applications for Plasma-Assisted Ignition and Electric Field Measurements *48th AIAA Aerospace Sciences Meeting Including the New Horizons Forum and Aerospace Exposition* Aerospace Sciences Meetings (American Institute of Aeronautics and Astronautics) URL 2010-1587

[43] Carlier M, Corre C, Minetti R, Pauwels J F, Ribaucour M and Sochet L R 1991 Autoignition of butane: A burner and a rapid compression machine study *Symposium (International) on Combustion* **23** 1753 – 1758

[44] Minetti R, Ribaucour M, Carlier M, Fittschen C and Sochet L 1994 Experimental and modeling study of oxidation and autoignition of butane at high pressure *Combustion and Flame* **96** 201 – 211

[45] Anikin N B, Gersen S, Mokhov A V and Levinsky H B 2005 *Combura 2005 Book of abstracts* p 31

[46] Stepanyan S A, Starikovskiy A Y, Popov N A and Starikovskaia S M 2014 A nanosecond surface dielectric barrier discharge in air at high pressures and different polarities of applied pulses: transition to filamentary mode *Plasma Sources Science and Technology* **23** 045003

[47] Zavershinskii I P, Klimov A I, Makaryan V G, Molevich N E, Moralev I A and Porfir'ev D P 2011 Structure of RF capacitive discharge in swirl airflow at atmospheric pressure *Technical Physics Letters* **37** 1120–1123

[48] Akishev Y, Aponin G, Balakirev A, Grushin M, Karalnik V, Petryakov A and Trushkin N 2013 Spatial–temporal development of a plasma sheet in a surface dielectric barrier discharge powered by a step voltage of moderate duration *Plasma Sources Science and Technology* **22** 015004

[49] Houpt A W and Leonov S B 2016 Charge Transfer in Constricted Form of Surface Barrier Discharge at Atmospheric Pressure *Journal of Thermophysics and Heat Transfer* 1–9

[50] Kof L and Starikovskii A Y 1996 Oxygen–hydrogen mixtures ignition under the high-voltage ionization wave conditions at high temperatures 26th Int. Symp. on Combustion (Naples, Italy, 1996) *Work-in-Progress Papers*

[51] Starikovskaia S M 2014 Plasma-assisted ignition and combustion: nanosecond discharges and development of kinetic mechanisms *Journal of Physics D: Applied Physics* **47** 353001

[52] Yin Z, Montello A, Carter C D, Lempert W R and Adamovich I V 2013 Measurements of temperature and hydroxyl radical generation/decay in lean fuel–air mixtures excited by a repetitively pulsed nanosecond discharge *Combustion and Flame* **160** 1594 – 1608

[53] Li T, Adamovich I V and Sutton J A 2013 A Burner Platform for Examining the Effects of Non-Equilibrium Plasmas on Oxidation and Combustion Chemistry *Combustion Science and Technology* **185** 990–998

[54] Yin Z, Pulcini A, Adamovich I V and Lempert W R 2014 Time-Resolved Measurements of Temperature and Species Concentrations Distributions in Ar-Based Mixtures Excited by a Nanosecond Pulse Discharge *52nd Aerospace Sciences Meeting* AIAA SciTech (American Institute of Aeronautics and Astronautics) URL `2014-1361`

[55] Stepanyan S, Vanhove G, Desgroux P and Starikovskaia S 2013 Time-resolved electric field measurements in nanosecond surface dielectric discharge. Comparison of different polarities. Ignition of combustible mixtures by surface discharge in a rapid compression machine. *51st AIAA Aerospace Sciences Meeting including the New Horizons Forum and Aerospace Exposition* Aerospace Sciences Meetings (American Institute of Aeronautics and Astronautics) URL `2013-1053`

[56] Shcherbanev S A, Stepanyan S A, Boumehdi M A, Vanhove G, Desgroux P and Starikovskaia S M Energy balance in surface nanosecond dielectric barrier discharge. Plasma–assisted ignition of heavy hydrocarbons at high pressures. *Proc. of 53rd AIAA Aerospace Sciences Meeting Kissimmee, Florida* AIAA–2015–2587

[57] Starikovskaya S M, Aleksandrov N L, Kosarev I N, Kindysheva S V and Starikovskii A Y 2009 Ignition with low-temperature plasma: Kinetic mechanism and experimental verification *High Energy Chemistry* **43** 213–218

[58] Anikin N B, Starikovskaia S M and Starikovskii A Y 2006 Oxidation of saturated hydrocarbons under the effect of nanosecond pulsed space discharge *Journal of Physics D: Applied Physics* **39** 3244

[59] Starikovskaia S M, Starikovskii A Y and Zatsepin D V 2001 Hydrogen oxidation in a stoichiometric hydrogen-air mixture in the fast ionization wave *Combustion Theory and Modelling* **5** 97–129

[60] Anikin N, Starikovskaia S and Starikovskii A 2004 Study of the oxidation of alkanes in their mixtures with oxygen and air under the action of a pulsed volume nanosecond discharge *Plasma Physics Reports* **30** 1028–1042

[61] Belaia V and Starikovskiy A 2014 Nanbosecond discharge ignition of lean C_2H_6-containing mixtures at elevated temperatures *52nd Aerospace Sciences Meeting* AIAA SciTech (American Institute of Aeronautics and Astronautics) pp AIAA 2014–1181

[62] Ombrello T, Won S H, Ju Y and Williams S 2010 Flame propagation enhancement by plasma excitation of oxygen. Part I: Effects of O_3 *Combustion and Flame* **157** 1906 – 1915

[63] Ombrello T, Won S H, Ju Y and Williams S 2010 Flame propagation enhancement by plasma excitation of oxygen. Part II: Effects of $O_2(a^1\Delta_g)$ *Combustion and Flame* **157** 1916 – 1928

[64] Sun W, Won S H and Ju Y 2014 In situ plasma activated low temperature chemistry and the S-curve transition in DME/oxygen/helium mixture *Combustion and Flame* **161** 2054 – 2063

[65] Kosarev I N, Pakhomov A I, Kindysheva S V, Anokhin E M and Aleksandrov N L 2013 Nanosecond discharge ignition in acetylene-containing mixtures *Plasma Sources Science and Technology* **22** 045018

[66] Bak M S, Do H, Mungal M G and Cappelli M A 2012 Plasma-assisted stabilization of laminar premixed methane/air flames around the lean flammability limit *Combustion and Flame* **159** 3128 – 3137

[67] Bak M S, kyun Im S, Mungal M G and Cappelli M A 2013 Studies on the stability limit extension of premixed and jet diffusion flames of methane, ethane, and propane using nanosecond repetitive pulsed discharge plasmas *Combustion and Flame* **160** 2396 – 2403

[68] Wu L, Lane J, Cernansky N, Miller D, Fridman A and Starikovskiy A 2011 Plasma-assisted ignition below self-ignition threshold in methane, ethane, propane and butane-air mixtures *Proceedings of the Combustion Institute* **33** 3219 – 3224

[69] Starikovskiy A, Rakitin A, Correale G, Nikipelov A, Urushihara T and Shiraishi T 2012 Ignition of hydrocarbon-air mixtures with non-equilibrium plasma at elevated pressures *50th AIAA Aerospace Sciences Meeting including the New Horizons Forum and Aerospace Exposition* Aerospace Sciences Meetings (American Institute of Aeronautics and Astronautics) URL 2012-828

[70] Singleton D, Pendleton S J and Gundersen M A 2011 The role of non-thermal transient plasma for enhanced flame ignition in C 2 H 4 –air *Journal of Physics D: Applied Physics* **44** 022001

[71] Pendleton S J, Bowman S, Carter C, Gundersen M A and Lempert W 2013 The production and evolution of atomic oxygen in the afterglow of streamer discharge in atmospheric pressure fuel/air mixtures *Journal of Physics D: Applied Physics* **46** 305202

[72] Gundersen M, Singleton D, Kuthi A, Lin Y and Sanders J 2012 Transient plasma for marine diesel GHG abatement *China Maritime Week*

[73] Pendleton S J, Montello A, Carter C, Lempert W and Gundersen M A 2012 Vibrational and rotational CARS measurements of nitrogen in afterglow of streamer discharge in atmospheric pressure fuel/air mixtures *Journal of Physics D: Applied Physics* **45** 495401

[74] Bentaleb S, Blin-Simiand N, Jeanney P, Magne L, Moreau N, Pasquiers S and Tardiveau P 2015 Ignition of Lean Air/Hydrocarbon Mixtures at Low Temperature by a Single Corona Discharge Nanosecond Pulse *AerospaceLab*

[75] Tardiveau P, Bentaleb S, Jeanney P, Jorand F and Pasquiers S 2012 Comparative Study of Air-Propane and Air-Heptane Mixtures Ignition by Nanosecond Pulsed Discharges *International Journal of Plasma Environmental Science & Technology* **6** 130–134

[76] Nalbandyan A B 1946 Photochemical oxidation of hydrogen *J. Phys. Chem.* **20** 1259–72

[77] Popov N A 2007 The effect of nonequilibrium excitation on the ignition of hydrogen-oxygen mixtures *High Temperature* **45** 261–279

[78] Popov N A 2016 Kinetics of plasma-assisted combustion: effect of non-equilibrium excitation on the ignition and oxidation of combustible mixtures *Plasma Sources Science and Technology* **25** 043002

[79] Popov N A 2011 Fast gas heating in a nitrogen-oxygen discharge plasma: I. Kinetic mechanism *Journal of Physics D: Applied Physics* **44** 285201

[80] Popov N A 2016 Pulsed nanosecond discharge in air at high specific deposited energy: fast gas heating and active particle production *Plasma Sources Science and Technology* **25** 044003

[81] Shkurenkov I and Adamovich I V 2016 Energy balance in nanosecond pulse discharges in nitrogen and air *Plasma Sources Science and Technology* **25** 015021

[82] Aleksandrov N L, Kindysheva S V, Nudnova M M and Starikovskiy A Y 2010 Mechanism of ultra-fast heating in a non-equilibrium weakly ionized air discharge plasma in high electric fields *Journal of Physics D: Applied Physics* **43** 255201

[83] Rusterholtz D L, Lacoste D A, Stancu G D, Pai D Z and Laux C O 2013 Ultra-fast heating and oxygen dissociation in atmospheric pressure air by nanosecond repetitively pulsed discharges *Journal of Physics D: Applied Physics* **46** 464010

[84] Mintoussov E I, Pendleton S J, Gerbault F G, Popov N A and Starikovskaia S M 2011 Fast gas heating in nitrogen–oxygen discharge plasma: II. Energy exchange in the afterglow of a volume nanosecond discharge at moderate pressures *Journal of Physics D: Applied Physics* **44** 285202

[85] Lavid M and Stevens J G 1985 Photochemical ignition of premixed hydrogenoxidizer mixtures with excimer lasers *Combustion and Flame* **60** 195 – 202

[86] Bozhenkov S, Starikovskaia S and Starikovskii A 2003 Nanosecond gas discharge ignition of H_2- and CH_4-containing mixtures *Combustion and Flame* **133** 133 – 146

[87] Aleksandrov N L, Kindysheva S V and Kochetov I V 2014 Kinetics of low-temperature plasmas for plasma-assisted combustion and aerodynamics *Plasma Sources Science and Technology* **23** 015017

[88] Adamovich I V, Li T and Lempert W R 2015 Kinetic mechanism of molecular energy transfer and chemical reactions in low-temperature air-fuel plasmas *Philosophical Transactions of the Royal Society of London A: Mathematical, Physical and Engineering Sciences* **373**

[89] Konnov A A 2015 On the role of excited species in hydrogen combustion *Combustion and Flame* **162** 3755 – 3772

[90] Sun W, Uddi M, Won S H, Ombrello T, Carter C and Ju Y 2012 Kinetic effects of non-equilibrium plasma-assisted methane oxidation on diffusion flame extinction limits *Combustion and Flame* **159** 221 – 229

[91] Sun W 2013 *Non-equilibrium plasma assisted combustion* Ph.D. thesis Department of Mechanical and Aerospace Engineering, Princeton University

[92] Sun W, Won S H, Ombrello T, Carter C and Ju Y 2013 Direct ignition and S-curve transition by in situ nano-second pulsed discharge in methane/oxygen/helium counterflow flame *Proceedings of the Combustion Institute* **34** 847 – 855

[93] Ju Y and Sun W 2015 Plasma assisted combustion: Dynamics and chemistry *Progress in Energy and Combustion Science* **48** 21 – 83

[94] Won S H, Jiang B, Dievart P, Sohn C H and Ju Y 2015 Self-sustaining n-heptane cool diffusion flames activated by ozone *Proceedings of the Combustion Institute* **35** 881 – 888

[95] Filimonova E A 2015 Discharge effect on the negative temperature coefficient behaviour and multistage ignition in C_3H_8 -air mixture *Journal of Physics D: Applied Physics* **48** 015201

[96] Bellenoue M, Labuda S, Ruttun B and Sotton J 2007 Spark plug and corona abilities to ignite stoichiometric and lean methane/air mixtures *Combustion Science and Technology* **179** 477–496

[97] Castela M, Stepanyan S, Fiorina B, Coussement A, Gicquel O, Darabiha N and Laux C A 3-D DNS and experimental study of the effect of the recirculating flow pattern inside a reactive kernel produced by nanosecond plasma discharges in a methane-air mixture *Proceedings of the Combustion Institute* –

[98] Xu D, Lacoste D and Laux C 2015 Ignition of Quiescent Lean Propaneв:Air Mixtures at High Pressure by Nanosecond Repetitively Pulsed Discharges *Plasma Chemistry and Plasma Processing* 1–19

[99] Pilla G, Galley D, Lacoste D A, Lacas F, Veynante D and Laux C O 2006 Stabilization of a Turbulent Premixed Flame Using a Nanosecond Repetitively Pulsed Plasma *IEEE Transactions on Plasma Science* **34** 2471–2477

[100] Rapp V H, DeFilippo A, Saxena S, Chen J Y, Dibble R W, Nishiyama A, Moon A and Ikeda Y 2012 Extending Lean Operating Limit and Reducing Emissions of Methane Spark-Ignited Engines Using a Microwave-Assisted Spark Plug

[101] Wolk B, DeFilippo A, Chen J Y, Dibble R, Nishiyama A and Ikeda Y 2013 Enhancement of flame development by microwave-assisted spark ignition in constant volume combustion chamber *Combustion and Flame* **160** 1225 – 1234

[102] Healy D, Donato N, Aul C, Petersen E, Zinner C, Bourque G and Curran H 2010 n-Butane: Ignition delay measurements at high pressure and detailed chemical kinetic simulations *Combustion and Flame* **157** 1526 – 1539

[103] Vanhove G, Boumehdi M A, Shcherbanev S, Fenard Y, Desgroux P and Starikovskaia S 2016 A comparative experimental kinetic study of spontaneous and plasma-assisted cool flames in a rapid compression machine *Proceedings of the Combustion Institute* –

[104] Laux C. O., Fletcher D. et al (Rhode-Saint-Genese, Belgium: Von Karman Institute) 2002 *Radiation and nonequilibrium collisional-radiative models Physico-Chemical Modeling of High Enthalpy and Plasma Flows* (von Karman Institute Lecture Series 2002-07)

[105] Laux C O, Spence T G, Kruger C H and Zare R N 2003 Optical diagnostics of atmospheric pressure air plasmas *Plasma Sources Science and Technology* **12** 125

[106] Settles G S 2001 *Schlieren and Shadowgraph techniques* (Springer)

[107] Vasiliev L 1968 *Shadowgraphy methods* (Nauka, Moscow (in Russian))

[108] Roth J R, Sherman D M and Wilkinson S P 2000 Electrohydrodynamic Flow Control with a Glow-Discharge Surface Plasma *AIAA Journal* **38** 1166–1172

[109] Artana G, Juan D, Luc L, Moreau E and Gerard T 2002 Flow Control with Electrohydrodynamic Actuators *AIAA Journal* **40** 1773–1779

[110] Briels T M P, Kos J, Winands G J J, van Veldhuizen E M and Ebert U 2008 Positive and negative streamers in ambient air: measuring diameter, velocity and dissipated energy *Journal of Physics D: Applied Physics* **41** 234004

[111] Guaitella O, Marinov I and Rousseau A 2011 Role of charge photodesorption in self-synchronized breakdown of surface streamers in air at atmospheric pressure *Applied Physics Letters* **98** 071502

[112] Starikovskiy A and Aleksandrov N 2011 *Nonequilibrium plasma aerodynamics* (INTECH Open Access Publisher)

[113] Raizer Y P 1991 *Gas Discharge Physics* (New York: Springer)

[114] Pancheshnyi S, Starikovskaia S and Starikovskii A 2000 Collisional deactivation of $N_2(C^3\Pi_u, v = 0, 1, 2, 3)$ states by N_2, O_2, H_2 and H_2O molecules *Chemical Physics* **262** 349 – 357

[115] Babaeva N Y and Naidis G V 1996 Two-dimensional modelling of positive streamer dynamics in non-uniform electric fields in air *Journal of Physics D: Applied Physics* **29** 2423

[116] http://www.bolsig.laplace.univ-tlse.fr/

[117] Bazelyan E M and Raizer Y P 1997 *Spark discharge* (CRC press)

[118] Naidis G V 2006 On photoionization produced by discharges in air *Plasma Sources Science and Technology* **15** 253

[119] Flitti A and Pancheshnyi S 2009 Gas heating in fast pulsed discharges in N_2-O_2 mixtures *Eur. Phys. J. Appl. Phys.* **45** 21001

[120] Simek M, Babick V, Clupek M, DeBenedictis S, Dilecce G and Sunka P 1998 Excitation of $N_2(C^3\Pi_u)$ and $NO(A^2\Sigma^+)$ states in a pulsed positive corona discharge in N_2, N_2-O_2 and N_2-NO mixtures *Journal of Physics D: Applied Physics* **31** 2591

[121] Gat E, Gherardi N, Lemoing S, Massines F and Ricard A 1999 Quenching rates of $N_2(C,v)$ vibrational states in N_2 and He glow silent discharges *Chemical Physics Letters* **306** 263 – 268

[122] Xu D A, Shneider M N, Lacoste D A and Laux C O 2014 Thermal and hydrodynamic effects of nanosecond discharges in atmospheric pressure air *Journal of Physics D: Applied Physics* **47** 235202

[123] Stepanyan S A 2014 *Nanosecond surface dielectric barrier discharge at high pressures for plasma assisted combustion* Ph.D. thesis Ecole Polytechnique

[124] Akishev Y, Karalnik V, Kochetov I, Napartovich A and Trushkin N 2014 High-current cathode and anode spots in gas discharges at moderate and elevated pressures *Plasma Sources Science and Technology* **23** 054013

[125] Shcherbanev S A, Khomenko A Y, Stepanyan S A, Popov N A and Starikovskaia S M 2016 Features of optical emission spectrum of high pressure filamentary nanosecond surface dielectric barrier discharge *PSST Letters*

[126] Babich L P, Loiko T V and Tsukerman V A 1990 High-voltage nanosecond discharge in a dense gas at a high overvoltage with runaway electrons *Soviet Physics Uspekhi* **33** 521–540

[127] Shao T, Tarasenko V F, Zhang C, Lomaev M I, Sorokin D A, Yan P, Kozyrev A V and Baksht E K 2012 Spark discharge formation in an inhomogeneous electric field under conditions of runaway electron generation *Journal of Applied Physics* **111** 023304

[128] Babich L P and Loiko T V 2010 Peculiarities of detecting pulses of runaway electrons and X-rays generated by high-voltage nanosecond discharges in open atmosphere *Plasma Physics Reports* **36** 263–270

[129] Prokopiev V E, Ivanov N G, Krivonosenko D A and Losev V F 2013 Elementary physical processes in the regions of filamentation and optical breakdown at propagation of the femtosecond laser pulse with a wavelength 950 nm in atmospheric pressure air *Izvestia vuzov* **11** 60—65

[130] Katayama D H, Miller T A and Bondybey V E 1979 Radiative decay and radiationless deactivation in selectively excited CN *The Journal of Chemical Physics* **71** 1662–1669

[131] Iwai T, Savadatti M I and Broida H P 1967 Mechanisms of Populating Electronically Excited CN in Active Nitrogen Flames *The Journal of Chemical Physics* **47** 3861–3874

[132] Evenson K M and Broida H P 1966 Measurements of Collisional Energy Transfer between Rotational Energy Levels in CN *The Journal of Chemical Physics* **44** 1637–1641

[133] Jacobs A, Wahl M, Weller R and Wolfrum J 1988 Kinetic studies of the reaction of CN with H_2O from 518 to 1027 K *Chemical Physics Letters* **144** 203 – 207

[134] Luque J, Jeffries J, Smith G, Crosley D and Scherer J 2001 Combined cavity ringdown absorption and laser-induced fluorescence imaging measurements of CN(B-X) and CH(B-X) in low-pressure CH_4-O_2-N_2 and CH_4-NO-O_2-N_2 flames *Combustion and Flame* **126** 1725 – 1735

[135] Saidani G, Kalugina Y, Gardez A, Biennier L, Georges R and Lique F 2013 High temperature reaction kinetics of CN (v= 0) with C_2H_4 and C_2H_6 and vibrational relaxation of CN (v= 1) with Ar and He *The Journal of chemical physics* **138** 124308

[136] Reisler H, Mangir M and Wittig C 1980 The kinetics of free radicals generated by IR laser photolysis. II. Reactions of $C_2(X^1\Sigma_g^+)$, $C_2(a^3\Pi_u)$, $C_3(X^1\Sigma_g^+)$ and $CN(X^2\Sigma^+)$ with O_2 *Chemical Physics* **47** 49 – 58

[137] Pintassilgo C D, Guerra V, Guaitella O and Rousseau A 2014 Study of gas heating mechanisms in millisecond pulsed discharges and afterglows in air at low pressures *Plasma Sources Science and Technology* **23** 025006

[138] Dilecce G, Ambrico P F, Scarduelli G, Tosi P and Benedictis S D 2009 CN($B^2\Sigma^+$) formation and emission in a N_2-CH_4 atmospheric pressure dielectric barrier discharge *Plasma Sources Science and Technology* **18** 015010

[139] Vivien C, Hermann J, Perrone A, Boulmer-Leborgne C and Luches A 1998 A study of molecule formation during laser ablation of graphite in low-pressure nitrogen *Journal of Physics D: Applied Physics* **31** 1263

[140] St-Onge L, Sing R, Béchard S and Sabsabi M 1999 Carbon emissions following 1.064 μm laser ablation of graphite and organic samples in ambient air *Applied Physics A* **69** S913–S916

[141] Ma Q and Dagdigian P J 2011 Kinetic model of atomic and molecular emissions in laser-induced breakdown spectroscopy of organic compounds *Analytical and Bioanalytical Chemistry* **400** 3193–3205

[142] Fernandez-Bravo A, Delgado T, Lucena P and Laserna J J 2013 Vibrational emission analysis of the CN molecules in laser-induced breakdown spectroscopy of organic compounds *Spectrochimica Acta Part B: Atomic Spectroscopy* **89** 77 – 83

[143] Huber K P and Herzberg G 1979 *Molecular Spectra and Molecular Structure IV. Constants of diatomic molecules* (VNR)

[144] Klochko A V, Lemainque J, Booth J P and Starikovskaia S M 2015 TALIF measurements of oxygen atom density in the afterglow of a capillary nanosecond discharge *Plasma Sources Science and Technology* **24** 025010

[145] Shcherbanev S A, Popov N A and Starikovskaia S M 2016 Ignition of high pressure lean H2:air mixtures along the multiple channels of nanosecond surface discharge. *Combustion and Flame*

[146] Marco A Gigososa Manuel A Gonzalez V C 2003 Computer simulated Balmer-alpha, -beta and -gamma Stark line profiles for non-equilibrium plasmas diagnostics *Spectrochimica Acta Part B: Atomic Spectroscopy* **58** 1489 – 1504

[147] Lisica V S 1977 Stark broadening of hidrogen lline in plasma *Uspekhi Fizicheskikh Nauk*

[148] Landau L and Lifshitz E 1989 *Quantum mechanics* (M: Nauka)

[149] Artsimovich A A and Sagdeev R Z 1979 *Plasma Physics for Physicists* (M: Atomizdat)

[150] van der Horst R M, Verreycken T, van Veldhuizen E M and Bruggeman P J 2012 Time-resolved optical emission spectroscopy of nanosecond pulsed discharges in atmospheric-pressure N_2 and N_2/H_2O mixtures *Journal of Physics D: Applied Physics* **45** 345201

[151] Galvao B R L, Braga J P, Belchior J C and C V A J 2014 Electronic Quenching in N(2D) + N_2 Collisions: A State-Specific Analysis via Surface Hopping Dynamics *Journal of Chemical Theory and Computation* **5** 1872–1877

[152] Huang B D, Zhu X M, Takashima K and Pu Y K 2013 The spatial–temporal evolution of the electron density and temperature for a nanosecond microdischarge *Journal of Physics D: Applied Physics* **46** 464011

[153] Huang B D, Takashima K, Zhu X M and Pu Y K 2014 The influence of the repetition rate on the nanosecond pulsed pin-to-pin microdischarges *Journal of Physics D: Applied Physics* **47** 422003

[154] Yatom S, Stambulchik E, Vekselman V and Krasik Y E 2013 Spectroscopic study of plasma evolution in runaway nanosecond atmospheric-pressure He discharges *Phys. Rev. E* **88**(1) 013107

[155] Yatom S and Krasik Y E 2014 Plasma density evolution during nanosecond discharge in hydrogen gas at $(1-3)*10^5$Pa pressure *Journal of Physics D: Applied Physics* **47** 215202

[156] Gilmore F R, Laher R R and Espy P J 1992 Franck–Condon Factors, r-Centroids, Electronic Transition Moments, and Einstein Coefficients for Many Nitrogen and Oxygen Band Systems *Journal of Physical and Chemical Reference Data* **21** 1005–1107

[157] Meek J 1953 JD Craggs Electrical breakdown of gases Oxford

[158] Sigmond R S 1965 Evidence of a high-pressure cathode gas sheath in an arc discharge of short duration *Proceedings of the Physical Society* **85** 1269

[159] Korolev Y D 1985 Pulsed breakdowns is gases *JTP* **55** 1216

[160] Sorokin D A, Lomaev M I, Banokina T I and Tarasenko V F 2014 Determination of the electron concentration and temperature, as well as the reduced electric field strength, in the plasma of a high-voltage nanosecond discharge

initiated in atmospheric-pressure nitrogen by a runaway electron beam *Technical Physics* **59** 1119–1126

[161] Levko D, Yatom S, Vekselman V and Krasik Y E 2012 Electron emission mechanism during the nanosecond high-voltage pulsed discharge in pressurized air *Applied Physics Letters* **100** 084105

[162] Asinovskii E Iand Markovetz V V, Polyakov D N, Ulyanov A M and Filyugin I V 1985 On the nature of the X-ray radiation in the wave breakdown *High Temperature Physics* **23** 606–608

[163] Vasilyak L M, Kostyuchenko S V, Kudryavtsev N N and Filyugin I V 1994 Fast ionisation waves under electrical breakdown conditions *Physics-Uspekhi* **37** 247

[164] Little J, Takashima K, Nishihara M, Adamovich I and Samimy M 2012 Separation Control with Nanosecond-Pulse-Driven Dielectric Barrier Discharge Plasma Actuators *AIAA Journal* **50** 350–365

[165] Bracewell R N 2000 *The Fourier Transform and its Applications* third edition ed

[166] Nishihara M, Takashima K, Rich J W and Adamovich I V 2011 Mach 5 bow shock control by a nanosecond pulse surface dielectric barrier discharge *Physics of Fluids* **23** 066101

[167] Aleksandrov N L, Bazelyan E M and Shneider M N 2000 Effect of continuous current during pauses between successive strokes on the decay of the lightning channel *Plasma Physics Reports* **26** 893–901

[168] Starikovskaia S M 2006 Plasma assisted ignition and combustion *Journal of Physics D: Applied Physics* **39** R265

[169] Starikovskiy A and Aleksandrov N 2013 Plasma-assisted ignition and combustion *Progress in Energy and Combustion Science* **39** 61 – 110

[170] Kim W, Mungal M G and Cappelli M A 2010 The role of in situ reforming in plasma enhanced ultra lean premixed methane/air flames *Combustion and Flame* **157** 374 – 383

[171] Nagaraja S, Sun W and Yang V 2015 Effect of non-equilibrium plasma on two-stage ignition of n-heptane *Proceedings of the Combustion Institute* **35** 3497 – 3504

[172] Shao T, Zhang C, Niu Z, Yan P, Tarasenko V F, Baksht E K, Burahenko A G and Shut'ko Y V 2011 Diffuse discharge, runaway electron, and x-ray in atmospheric pressure air in an inhomogeneous electrical field in repetitive pulsed modes *Applied Physics Letters* **98** 021503

[173] Chen S, Heijmans L C J, Zeng R, Nijdam S and Ebert U 2015 Nanosecond repetitively pulsed discharges in N_2-O_2 mixtures: inception cloud and streamer emergence *Journal of Physics D: Applied Physics* **48** 175201

[174] Tardiveau P, Moreau N, Bentaleb S, Postel C and Pasquiers S 2009 Diffuse mode and diffuse-to-filamentary transition in a high pressure nanosecond scale corona discharge under high voltage *Journal of Physics D: Applied Physics* **42** 175202

[175] Starikovskaia S M, Allegraud K, Guaitella O, Kosarev I, Mintusov E, Pendleton S, Popov N, Sagulenko P and Rousseau A Surface discharges: possible applications for plasma-assisted ignition and electric field measurements *Proc. of 48th AIAA Aerospace Sciences Meeting (4 - 7 Jan 2010, Orlando, Florida)* AIAA–2010–1587

[176] Hidaka Y, Takuma H and Suga M 1985 Shock-tube study of the rate constant for excited hydroxyl OH*$(A^2\Sigma^+)$ formation in the nitrous oxide-molecular hydrogen reaction *The Journal of Physical Chemistry* **89** 4903–4905

[177] Fairchild P W, Smith G P and Crosley D R 1983 Collisional quenching of OH*$(A^2\Sigma^+)$ at elevated temperatures *The Journal of Chemical Physics* **79** 1795–1807

[178] Lewis B and Von Elbe G 1987 *Combustion, flames and explosions of gases. Third edition* (Academic Press, Inc.,Orlando, FL)

[179] Ombrello T Pulse-to-Pulse Coupling for Ignition in Cross-Flow Using Nanosecond-Pulsed High-Frequency Discharge *Proc. 54th AIAA Aerospace Sciences Meeting (San Diego, California, CA, 4–8 January 2016)* pp 2016–1210

[180] Gelfand B, Popov O and Chayvanov B 2008 *Hydrogen. Parameters of combustion and explosion* (PhysMatLit (in russian))

[181] Popov N A 2008 Effect of a pulsed high-current discharge on hydrogen-air mixtures *Plasma Physics Reports* **34** 414–430

[182] Wang B, Olivier H and Gronig H 2003 Ignition of shock-heated H_2-air-steam mixtures *Combustion and Flame* **133** 93 – 106

[183] Hagelaar G J M and Pitchford L C 2005 Solving the Boltzmann equation to obtain electron transport coefficients and rate coefficients for fluid models *Plasma Sources Science and Technology* **14** 722

[184] Inada Y, Matsuoka S, Kumada A, Ikeda H and Hidaka K 2012 Shack–Hartmann type laser wavefront sensor for measuring two-dimensional electron density distribution over extinguishing arc discharge *Journal of Physics D: Applied Physics* **45** 435202

[185] Weatherford B R, Barnat E V and Foster J E 2012 Two-dimensional laser collision-induced fluorescence measurements of plasma properties near an RF plasma cathode extraction aperture *Plasma Sources Science and Technology* **21** 055030

[186] Barnat E V 2016 Diagnostic tools for multi-dimensional plasmas *GEC, Bochum, Germany*

Titre : Décharge Filamentaire Nanoseconde en Surface à Barrière Diélectrique. Transition Streamer-Filamentaire et Application pour Combustion Assistée par Plasma

Mots clés : Décharge Nanoseconde Surfacique, Combustion Assistée par Plasma

Résumé : Plasmas non-équilibre est l'un des outils les plus attrayants et prometteurs pour de nombreuses applications assistés par plasma. La production d'espèces actives (espèces excitées, des radicaux, des photons de haute énergie couvrant UV et IR gamme spectrale) est importante pour le contrôle de la pollution de gaz, traitement de surface, les actionneurs de plasma pour l'application de l'aérodynamique, des applications biomédicales et plus récemment le domaine de la médecine de plasma. Pour les densités de gaz atmosphérique et élevée le courant dominant des applications des plasmas non-thermiques est l'inflammation des mélanges combustibles ou Ignition assistée par plasma (IAP).

Décharges de surface à barrière diélectriques (DSBD), largement utilisé pour le contrôle de l'écoulement aérodynamique, ont été récemment suggéré comme initiateurs distribués de la combustion dans les différents systèmes. Une possibilité d'utiliser les DSBD comme les allumeurs à pression aussi élevée que dizaines de bars a été démontrée au cours des 4-5 dernières années. Au moment du début de la thèse, l'ensemble des données expérimentales sur la décharge et d'inflammation des combustibles avec DSBD était assez pauvre et insuffisant pour une analyse détaillée. Par conséquent, l'étude expérimentale de la DSBD à des densités de gaz atmosphériques et élevées et l'étude de l'initiation de flamme par DSBDs nanosecondes ont fait l'objet de la thèse présentée.

Les résultats de la thèse sont présentés en trois parties. Dans la première partie le nDSBD dans un régime single shot regime (de prise de vue unique ???) à l'air atmosphérique est étudiée. L'analyse du dépôt d'énergie, le courant de décharge, la distribution d'intensité et de libération d'énergie est réalisée en conséquence. Les impulsions de polarité positive et négative sont utilisées pour produire la décharge de surface. La physique des streamers de polarité positive et négative est discutée. Pour les deux polarités de la haute tension la densité d'électrons et le champ électrique réduite sont estimés et comparés avec des calculs et/ou des résultats de la modélisation 2D.

La deuxième partie est consacrée à l'étude des nDSBD à des pressions élevées, jusqu'à 12 bar, dans différents mélanges de gaz (N_2, air, N_2:CH_4, N_2:H_2, Ar:O_2, etc.). Deux formes morphologiquement différents de la nDSBD sont considérées: une DBD streamer «classique» à des pressions et des tensions relativement basses, et une DBD filamentaire à des pressions et/ou des tensions élevées. La spectroscopie d'émission est utilisée pour obtenir des données quantitatives sur la décharge à haute pression (de 1 à 12 bar). Les raisons possibles de la filamentation de décharge est décrite.

Finally, the third part describes the experiments of plasma-assisted ignition with nanosecond SDBD at elevated pressures. Enfin, la troisième partie décrit les expériences d'ignition assistée par plasma avec nDSBD à des pressions élevées. La morphologie de décharge dans les mélanges combustible pauvres (H2:air) et après l'allumage sont étudiés. La comparaison de l'inflammation par décharge filamentaire et streamer à la pression 1-6 bar est effectué. Modélisation cinétique d'allumage assistée par plasma pour les champs électriques typiques pour nDSBD (E/N=100 Td) est utilisé pour l'analyse des données expérimentales. Étude complexe des décharges à la pression atmosphérique, la décharge à haute pression et l'allumage permet description détaillée de l'allumage à haute pression distribué dans l'espace par plasma non - équilibre.

Title: Filamentary surface dielectric barrier discharge at elevated pressures. Streamer-to-filament transition and application for plasma assisted combustion.

Keywords : Surface nanosecond discharge, Plasma assisted combustion

Abstract : Non-equilibrium plasma is one of the most attractive and promising tool for many plasma-assisted applications. Production of active species (excited species, radicals, high energetic photons covering UV and IR spectral range) is important for gas pollution control, surface treatment, plasma actuators for aerodynamics application, biomedical applications and more recently the field of plasma medicine. For atmospheric and elevated gas densities the mainstream of the non-thermal plasma applications is the ignition of combustible mixtures or so-called Plasma-Assisted Ignition (PAI).

Surface dielectric barrier discharges (SDBDs), widely used for aerodynamic flow control, were recently suggested as distributed initiators of combustion in different systems. A principal possibility of using the SDBD igniters at as high pressure as tens of bars has been demonstrated during the last 4-5 years. At the moment of the beginning of the thesis, the set of experimental data on the discharge and of ignition of fuels with SDBD was insufficient for detailed analysis. Therefore, the experimental study of the surface DBD at atmospheric and elevated gas densities and the study of flame initiation with nanosecond SDBD were the object of the presented thesis.

The results in the Thesis are presented in three parts. In the first part the nSDBD in a single shot regime at atmospheric air is investigated. The analysis of energy deposition, discharge current, intensity distribution and consequent energy release is performed. The positive and negative polarity pulses are used to produce surface discharge. The physics of anode and cathode-directed streamers is discussed. For both polarities of the applied pulses the electron density and reduced electric field are estimated and compared with calculations and/or 2D modeling results.

The second part is devoted to the study of nSDBD at elevated pressures, up to 12 bar, in different gas mixtures (N_2, air, N_2:CH_4, N_2:H_2, Ar:O_2, etc.). Two morphologically different forms of the nSDBD are considered: a "classical" streamer DBD at relatively low pressures and voltages, and a filamentary DBD at high pressures and/or voltages. The emission spectroscopy is used to obtain quantitative data about the discharge at high pressures (1–12 bar). The possible nature of the discharge filamentation is described.

Finally, the third part describes the experiments of plasma-assisted ignition with nanosecond SDBD at elevated pressures. The discharge morphology in lean combustible (H_2:air) mixtures and following ignition of the mixtures are studied. The comparison of ignition by filamentary and streamer discharge at the pressures 1–6 bar is performed. Kinetic modeling of plasma assisted ignition for the electric fields typical for nSDBD, E/N=100−200 Td is used for analysis of experimental data. Complex study of the discharges at atmospheric pressure, discharge at high pressures and ignition allow detailed description of the high-pressure, distributed in space ignition by non–equilibrium plasma.